A UNITED STATES DEPARTMENT OF COMMERCE PUBLICATION

Physics and Chemistry

SECTION A

JOURNAL OF RESEARCH

NATIONAL BUREAU OF STANDARDS

Volume 74A
Number 1
Jan.–Feb. 1970

J. Res. Nat. Bur. Stand. (U.S.), A
CODEN: JNBAA 74A (1) 1–139 (1970)

XUM

Journal of Research

of the

National Bureau of Standards

A. Physics and Chemistry

Jan.–Feb. • 1970

VOLUME • 74A

NUMBER • 1

Editor: C. W. Beckett

Associate Editor: D. D. Wagman

Publication dates:
Feb. 1, Apr. 1, June 1, Aug. 1, Oct. 1, Dec. 1, 1970

JOURNAL OF RESEARCH

The National Bureau of Standards Journal of Research reports research and development in the fields of activity shown at right. Also included from time to time are survey articles on topics closely related to the Bureau's scientific and technical program.

The Journal is published in three separate sections as follows:

A. Physics and Chemistry

Contains papers of interest primarily to scientists working in these fields. Issued six times a year. Annual subscription: domestic, $9.50; foreign $11.75. Single copy, varies.

B. Mathematical Sciences

Presents studies and compilations designed mainly for the mathematician and the theoretical physicist. Issued quarterly. Annual subscription: domestic, $5.00; foreign, $6.25. Single copy, $1.25.

C. Engineering and Instrumentation

Reports research and development results of interest chiefly to the engineer and the applied scientist. Issued quarterly. Annual subscription: domestic, $5.00; foreign, $6.25. Single copy, $1.25.

U.S. DEPARTMENT OF COMMERCE
Maurice H. Stans, Secretary
NATIONAL BUREAU OF STANDARDS
Lewis M. Branscomb, Director

The National Bureau of Standards [1] was established by an act of Congress March 3, 1901. Today, in addition to serving as the Nation's central measurement laboratory, the Bureau is a principal focal point in the Federal Government for assuring maximum application of the physical and engineering sciences to the advancement of technology in industry and commerce. To this end the Bureau conducts research and provides central national services in four broad program areas. These are: (1) basic measurements and standards, (2) materials measurements and standards, (3) technological measurements and standards, and (4) transfer of technology.

The Bureau comprises the Institute for Basic Standards, the Institute for Materials Research, the Institute for Applied Technology, the Center for Radiation Research, the Center for Computer Sciences and Technology, and the Office for Information Programs.

THE INSTITUTE FOR BASIC STANDARDS provides the central basis within the United States of a complete and consistent system of physical measurement; coordinates that system with measurement systems of other nations; and furnishes essential services leading to accurate and uniform physical measurements throughout the Nation's scientific community, industry, and commerce. The Institute consists of an Office of Measurement Services and the following technical divisions:

Applied Mathematics — Electricity — Metrology — Mechanics — Heat — Atomic and Molecular Physics — Radio Physics [2] — Radio Engineering [2] — Time and Frequency [2] — Astrophysics [2] — Cryogenics. [2]

THE INSTITUTE FOR MATERIALS RESEARCH conducts materials research leading to improved methods of measurement standards, and data on the properties of well-characterized materials needed by industry, commerce, educational institutions, and Government; develops, produces, and distributes standard reference materials; relates the physical and chemical properties of materials to their behavior and their interaction with their environments; and provides advisory and research services to other Government agencies. The Institute consists of an Office of Standard Reference Materials and the following divisions:

Analytical Chemistry — Polymers — Metallurgy — Inorganic Materials — Physical Chemistry.

THE INSTITUTE FOR APPLIED TECHNOLOGY provides technical services to promote the use of available technology and to facilitate technological innovation in industry and Government; cooperates with public and private organizations in the development of technological standards, and test methodologies; and provides advisory and research services for Federal, state, and local government agencies. The Institute consists of the following technical divisions and offices:

Engineering Standards — Weights and Measures — Invention and Innovation — Vehicle Systems Research — Product Evaluation — Building Research — Instrument Shops — Measurement Engineering — Electronic Technology — Technical Analysis.

THE CENTER FOR RADIATION RESEARCH engages in research, measurement, and application of radiation to the solution of Bureau mission problems and the problems of other agencies and institutions. The Center consists of the following divisions:

Reactor Radiation — Linac Radiation — Nuclear Radiation — Applied Radiation.

THE CENTER FOR COMPUTER SCIENCES AND TECHNOLOGY conducts research and provides technical services designed to aid Government agencies in the selection, acquisition, and effective use of automatic data processing equipment; and serves as the principal focus for the development of Federal standards for automatic data processing equipment, techniques, and computer languages. The Center consists of the following offices and divisions:

Information Processing Standards — Computer Information — Computer Services — Systems Development — Information Processing Technology.

THE OFFICE FOR INFORMATION PROGRAMS promotes optimum dissemination and accessibility of scientific information generated within NBS and other agencies of the Federal Government; promotes the development of the National Standard Reference Data System and a system of information analysis centers dealing with the broader aspects of the National Measurement System, and provides appropriate services to ensure that the NBS staff has optimum accessibility to the scientific information of the world. The Office consists of the following organizational units:

Office of Standard Reference Data — Clearinghouse for Federal Scientific and Technical Information [3] — Office of Technical Information and Publications — Library — Office of Public Information — Office of International Relations.

[1] Headquarters and Laboratories at Gaithersburg, Maryland, unless otherwise noted; mailing address Washington, D.C. 20234.
[2] Located at Boulder, Colorado 80302.
[3] Located at 5285 Port Royal Road, Springfield, Virginia 22151.

Order all publications from the Superintendent of Documents
U.S. Government Printing Office, Washington, D.C. 20402

Use of funds for printing this publication approved by the Director of the Bureau of the Budget (June 22, 1966).

XUM

JOURNAL OF RESEARCH of the National Bureau of Standards—A. Physics and Chemistry
Vol. 74A, No. 1, January–February 1970

Standardization of Cesium-137 Gamma-Ray Sources in Terms of Exposure Units (Roentgens)

T. P. Loftus

Center for Radiation Research, National Bureau of Standards, Washington, D.C. 20234

(October 7, 1969)

^{137}Cs γ-ray sources, which have been proposed by the Public Health Service as a substitute for radium in the treatment of malignant diseases, require suitable calibration if consistency is to be achieved in radiation treatment.

Several ^{137}Cs sources were calibrated using a graphite cavity ionization chamber in an open-air geometry. The contribution of scatter from the room surfaces was calculated and the source measurements corrected for this effect.

A large-volume aluminum-walled ionization chamber was designed and fabricated for use in routine calibrations. This chamber will be used as a means for intercomparison of the source to be calibrated with one of the standards.

Key words: Calibration; cavity ionization chamber; cesium-137; exposure rate; scattered radiation; standardization.

1. Introduction

Gamma radiation has been used successfully for many years in the treatment of malignant disease. Extensive use of radium has brought about the development of many treatment plans, and much dosimetry data has been accumulated. Attendant on the use of radium are some serious problems which derive from the fact that its first daughter product is the gas radon which, if introduced into the body and retained, has serious toxic effects. Because of the difficulties associated with the use of radium, the Public Health Service has proposed [1][1] that ^{137}Cs be used as a substitute in cancer therapy. Some source leakage had been experienced in the early use of ^{137}Cs, but, with improved encapsulation techniques, this problem has largely been solved. In addition, the isotope can now be incorporated into physiologically inert material. ^{137}Cs is inexpensive, has a relatively long half-life, good characteristics as a radium substitute, and requires less shielding than radium.

The Public Health Service proposal of ^{137}Cs as a substitute for radium has had favorable acceptance, though both suppliers and users have lacked satisfactory standards for determining source exposure rates. The National Bureau of Standards has been requested on various occasions to provide source calibrations, and, with the support of the Public Health Service, has carried out the work required to establish such a service.

Several small ^{137}Cs sources were measured in an open-air geometry using a graphite cavity ionization chamber. The effect of scattering from the room surfaces was computed and the measured exposure rates reduced accordingly. The standardized sources are to be used for comparison with unknowns submitted for calibration. A specially designed spherical, aluminum-walled ionization chamber of large volume has been fabricated and will be used for intercomparison calibrations.

Calibrations of ^{137}Cs sources will be performed for exposure rates ranging from a few to a few hundred milliroentgens per hour at 1 m.

2. Exposure Measurements Using Cavity Ionization Chambers

The instrument ordinarily used for measurements of x or gamma radiation, in terms of exposure units (roentgens), is the standard free-air ionization chamber. The chamber presently available at the National Bureau of Standards is designed for measurements of radiation generated by x-ray tube potentials of up to 250 kv, and is inadequate for measurements of the 662-keV gamma rays of ^{137}Cs. Therefore it was necessary to use the principle of cavity ionization for these measurements and a cavity chamber which fulfills the requirements of the Bragg-Gray theory. Briefly, these are (1) the chamber must be small with respect to the distance between the source and chamber to minimize the variation of radiation intensity over the chamber dimensions; (2) the chamber gas cavity

[1] Figures in brackets indicate the literature references at the end of this paper.

XUM

must be small to ensure that only a small fraction of the electron energy is dissipated in traversing the cavity, and to minimize the contribution to the ionization by direct interaction of the gamma rays with the gas; and (3) the chamber wall material must be sufficiently thick to establish electronic equilibrium and exclude electrons generated from other sources.

Consider a graphite chamber of volume V with air of density ρ. If a charge Q is collected, the specific ionization in the chamber is $Q/\rho V$ charge per unit mass. The corresponding energy deposited in the air of the cavity is found by multiplying by W, the average energy per ion pair (or per unit charge). Using the Bragg-Gray cavity principle, the energy absorbed in the graphite wall is obtained by multiplying by ${}_mS^C_{\text{air}}$, the ratio of the mass stopping power of carbon to that of air. Then the corresponding energy which would be absorbed in the wall if it were air instead of graphite is obtained by multiplying by $[\mu_{en}/\rho]^{\text{air}}_C$, the ratio of the mass energy-absorption coefficient of air to that of carbon. The corresponding ionization in air is obtained by dividing by W. So the ionization per unit mass of free air, in the absence of the chamber, is given by

$$\frac{Q}{\rho V}\,{}_mS^C_{\text{air}}[\mu_{en}/\rho]^{\text{air}}_C.$$

Since 1 roentgen $=2.578\times10^{-4}$ C/kg of free air at *STP*, and the density of air is 1.293 kg/m^3 at *STP*, the exposure rate in roentgens per second is given by

$$\dot{X}=\frac{3\times10^3 I}{V}\frac{T}{273.2}\frac{1.013}{P}\,{}_mS^C_{\text{air}}[\mu_{en}/\rho]^{\text{air}}_C\ R/s$$

where I is the chamber current in amperes, V is the volume in m^3, T is the temperature in degrees Kelvin, and P is the pressure in bar (1.013 bar = 760 mm Hg.)

Several corrections must be applied to the measurements in order to comply with the requirements of an experimental realization of the roentgen. For the cavity chamber, these corrections account for wall absorption, saturation, and stem scatter.

3. Cavity Chamber Description and Corrections

The cavity ionization chamber, used to measure the exposure rates from the ^{137}Cs sources, is spherical in shape with an external diameter of 20.7 mm. This chamber is one of three spherical graphite chambers designed by Wyckoff [2], all of which have the same outer diameter but different inner diameters. The wall absorption correction is determined by measuring for each chamber the ionization per unit volume at a constant gamma-ray exposure rate, and plotting it against wall thickness. These data, supplemented by absorption data available from other types of graphite chambers, are extrapolated to a zero wall condition to determine the wall-absorption correction for each chamber.

The intermediate-volume chamber (designated as VIII), used for these measurements, has a wall thickness of 4 mm and its derived wall correction is 2.5 percent. This value is reduced slightly since extrapolation to a zero wall condition actually over-estimates the correction, and the extrapolation should be only to the mean center of electron production. An estimate of the reduction required in the absorption correction has been provided by Wyckoff [3]. From measurements of electronic equilibrium requirements for ^{60}Co and ^{137}Cs gamma rays in a parallel-plate pressure chamber, and the calculations of Roesch [4] and Aglintsev [5], he computed the required reduction in the absorption correction to be 0.2 percent for ^{137}Cs gamma rays and carbon-walled cavity chambers. The saturation correction for the exposure rates encountered in these measurements is 0.2 percent and the correction for scatter from the supporting stem and shank of the chamber is 0.1 percent.

The mean mass stopping power ratio, ${}_mS^C_{\text{air}}$, used in the calculation of exposure rate is 1.010. This value was computed for ^{137}Cs gamma rays by Burlin [6] using an average exitation potential of 78.4 eV for carbon and the Spencer-Attix theory.

The ratio of the mass energy-absorption coefficients for air and carbon [7] differs from unity by less than 0.1 percent for the gamma rays of ^{137}Cs and is taken to be unity in the calculations.

The air volume of chamber VIII was determined by differential weighing using water to fill the cavity. The volume determined in this manner includes the small volume in the neck of the chamber. The value for the volume used in the computations is this measured volume minus the volume of the collection electrode. For the electrode used at the time of these measurements, the net chamber volume was 1.130 cm^3.

4. ^{137}Cs Sources

Eight sources were used in this project. Three sources were designed primarily for nondestructive testing of materials, density gauging, and research projects. The nominal activities of these three sources are 5, 50, and 500 mCi. The sources are doubly encapsulated in stainless steel with both inner and outer capsules sealed by heliarc welding. The outer capsule is 13.5 mm long with an outer diameter of 7.1 mm. The inside active diameter is 4.3 mm with the active length varying with the activity of the source. The end wall thickness is 1.0 mm.

Since this same capsule design is used for source strengths up to one curie, it was necessary to determine the acutal length of each source. The sources were radiographed and it was found that the lengths of the active volumes were about 4, 6, and 7 mm for the 5, 50, and 500 mCi sources respectively. These results are uncertain by about 1 mm due to fogging of the x-ray film by the source radiation. While the active material of the 5-mCi source appears to be localized in the active volume to three distinct particles, the larger sources seem to be uniformly filled although the fogging precludes an examination in detail.

Five sources of a medical type were obtained for study, calibration, and in order to provide a complete range of source activities as standards for routine calibrations. These sources are doubly sealed in nickel-plated stainless-steel capsules and needles, with nominal activities of 2.5, 7.5, 25, 60, and 100 mCi. Radiographs of these sources indicate they are all uniformly filled. A detailed study using densitometric methods however was not carried out for confirmation.

5. Open-Air Geometry Source Measurements

The exposure-rate measurements were carried out in an open-air geometry to minimize the contribution of scattered radiation to the measured ionization. The room was 9 m long, 6 m wide, and 4.5 m high. To minimize scattering from the supporting devices, the source was laid in a thin plastic trough which was supported above the floor by a long thin-walled plastic tube. The chamber was supported horizontally above the source by a plastic rod which extended approximately 1.3 m out from a ring stand. Mirror-image measurements with another ring stand and support rod showed no significant scatter contribution to the chamber reading from the stand.

Most of the exposure measurements were carried out for a source-to-chamber distance of approximately 0.5 m. For this geometry, the source and chamber were located symmetrically in the room, the chamber being 2 m from the ceiling and the source 2 m from the floor. In subsequent measurements, where there was a distance of 1 m between source and chamber, the chamber position remained the same and the source trough was lowered.

The distance between the source and ion chamber was determined by means of a cathetometer placed about 3 m from the source-detector line and supported by sturdy steel tables 1.5 m above the floor. The preamplifier of the vibrating-reed electrometer was located about 2.5 m from the source and protected from the radiation by a lead house. The operator and the measurement equipment were protected from the radiation by mobile lead shields.

Part of the measured ionization is caused by radiation scattered from the walls, ceiling, and floor of the laboratory, and an estimate of its effect must be made in order to make an absolute determination of the direct exposure rate from the source. The scatter contribution can be calculated using data published by Berger [8], which provides dose-reflection coefficients for gamma rays incident on concrete slabs. The reflected dose D_R, from the concrete floor of the laboratory, was computed using the equation

$$D_R = \frac{NE_0\mu_{en}R_d}{r^2}$$

where $R_d = R_d(\theta,\ \varphi/E_0,\ \theta_0)$ is Berger's reflection coefficient, a dimensionless number;

$$N = N_0 \cos\theta_0 \delta A/4\pi r_0^2;$$

and μ_{en} is the mass energy-absorption coefficient for air at the gamma-ray energy E_0. N_0 is the number of photons emitted per second by an isotropic source located a distance r_0 from the scattering area δA, while r is the distance from δA to the detector (see fig. 1). Berger's data are tabulated in terms of the cosine of the source obliquity angle θ_0, the cosine of the obliquity of emergence θ, and the azimuthal variable φ which is measured with respect to the direction of incidence in the plane of the floor.

The particular geometry of source and detector with respect to the floor allows a simplification of the computations, since the azimuthal angle φ is always 180 degrees. The data for the reflection coefficient may therefore be plotted versus the cosine of the emergence obliquity with the cosine of the incidence obliquity as a parameter.

The differential area δA is a ring on the floor, with its center on the vertical through the chamber and source. For computational purposes, it was useful to develop an analytical solution for δA in terms of the vertical distance to the floor S_0, and the source obliquity angle θ_0. With reference to figure 1 it can be shown that

$$\delta A = 2\pi S_0^2\left[\frac{\sec^2\theta_0}{2}\right]_{\theta_{01}}^{\theta_{02}}.$$

In addition, it is convenient to solve for r_0 and r in terms of S_0, θ_0, and S.

Then for the reflecting area defined by angles θ_{01} and θ_{02}

$$D_R = \frac{N_0E_0\mu_{en}R_d}{4S_0^2}\,\frac{(\sec^2\theta_{02}-\sec^2\theta_{01})\cos^3\theta_0}{\tan^2\theta_0+\dfrac{S^2}{S_0^2}}.$$

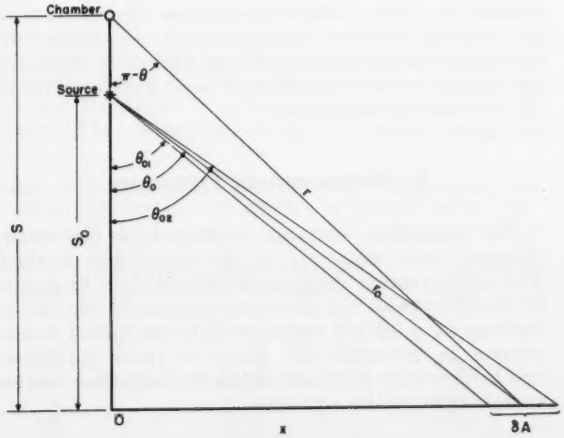

FIGURE 1. *Relationship of angles of γ-ray incidence on the area δA and scatter from δA back to the cavity chamber.*

The appropriate R_d factor can be read from a plot of Berger's tabulated data when the cos θ is found from

$$\theta = \pi + \tan^{-1}\left(\frac{S_0 \tan \theta_0}{S}\right).$$

The computation was made for five-degree intervals out to a distance on the floor equal to the radius of a circle of area equal to the area of the rectangular floor. The scattered radiation contribution from the floor area was found to be 0.14 percent for the 0.5 m source-to-chamber distance. The same approach was used for calculating the contributions from each sidewall, even though in this case the azimuthal angle is not exactly 180 degrees. The sum of the percentage scatter contributions from all room surfaces is 0.46 percent.

As an independent check on the above calculations, an upper limit to the scatter contribution can be estimated using a method proposed by Eisenhauer [9] in which an image source technique is used for calculating the reflection of gamma rays from concrete slabs. The ratio of the scattered dose to the primary dose is given as a function of the ratio of the distance of the source from the detector to the distance of an image source from the detector, and a constant which is dependent on the properties of the medium and the energy of the radiation. Thus

$$\frac{D_s}{D_0} = \frac{(S-S_0)^2}{(S+S_0)^2} R_{PT}.$$

For the detector-source-floor geometry of this experiment $S-S_0=0.50$ m and $S+S_0=4.50$ m. The scatter contribution, calculated from these data and Chilton's [10] R_{PT} value of 0.161 for ^{137}Cs gamma rays, is 0.2 percent. This value compares favorably with the value of 0.14 percent derived from Berger's data for the same geometry.

The percentage contribution to the chamber reading, due to scattered radiation from the floor, was also computed from Berger's data for a source-to-chamber distance of 1 m in the above-described geometry. The calculation showed that the scatter contribution to the chamber reading was essentially unchanged by this slight change in geometry, as a result of which the percentage scatter contribution increased by a factor of 4 for the 1-m separation.

6. Measurement Procedure

The ionization currents produced in the cavity chamber were measured by the rate-of-drift method. The measurement consists of determining, by means of a null method, the time Δt required for the charge buildup on a known capacitor C to produce a known change in potential ΔV. Each of these quantities can be precisely determined and the ionization current computed from the equation

$$I = C\frac{\Delta V}{\Delta t}.$$

To reduce source handling, the measurement procedure was to determine the background current (which includes leakage) at the collection potential and polarity to be used, and then take sightings on the top and bottom of the ion chamber with the cathetometer. The cathetometer was lowered to the expected position of the source, the source placed in the trough and then sightings taken on the top and bottom of the source with the cathetometer. Eight current measurements were performed and the polarity of the collection potential was then reversed. After a sufficient time lapse to allow for soakage at the new polarity, another eight measurements were made. The source was then returned to its container and the background current measured for the polarity last used. Averaging of the background drift rates, determined for both positive and negative collection potentials, eliminates background ionization produced in those extracameral volumes where the current does not change sign.

Four sources were measured for a distance of 0.50 m between source and chamber and the largest source was measured at a distance of 1 m. The data resulting from all these measurements are given in table 1.

TABLE 1. *Summary of ^{137}Cs open air exposure-rate measurements with all data corrected to August 24, 1967*

Measurement No.	Nominal source activity (mCi)	Nominal chamber-to-source distance (meters)	Measured $\dot{X}$ multiplied by D^2 ($mR \cdot m^2 \cdot h^{-1}$)	Average $\dot{X}D^2$ ($mR \cdot m^2 \cdot h^{-1}$)	Avg. $\dot{X}D^2$ corrected for room scatter ($mR \cdot m^2 \cdot h^{-1}$)
1	500	0.5	137.9_4		
2	500	.5	137.6_2	137.8_3	137.2_0
3	500	.5	137.9_2		
4	500	.5	137.3_6		
5	500	.5	136.8_2	137.1_4	136.5_1
6	500	.5	137.2_4		
7	500	1.0	139.5_8		
8	500	1.0	140.0_3	139.8_0	137.2_7
10	50	0.5	15.0_5		
11	50	.5	14.8_9	14.9_7	14.9_0
12	5	.5	1.3_4		1.3_3
13	100	.5	36.1_1		35.9_4

Measurements 1 through 3 in table 1 were performed approximately one year before the 4 through 6 measurements. The elapsed time between measurements 10 and 11 was nine months. The decay corrections used to correct all the data to the August 24, 1967 date were computed on the basis of a 26.68-year half-life [11]. The good agreement between measurements made at such long intervals of time indicates that ^{134}Cs contamination is insignificant. The agreement between the two groups of measurements for the "500" source at 0.5 m is within 0.5 percent, and the ratio of the aver-

age value for the "500" source at one meter to the average value for 0.5 m is 1.003.

In order to correlate source measurements at 0.5 and 1 m distances, it is necessary to account for air attenuation and scatter. For 0.6-Mev gamma rays and short source-to-detector distances, the buildup factor equals $1+\mu D \sim e^{\mu D}$ [12], where μ is the linear attenuation coefficient and D is the distance from the source. At the same time the attenuation of the primary radiation goes as $e^{-\mu D}$. The product of these two corrections is not significantly different from unity.

7. Ion Chambers for Routine Measurements

A 2.5 liter ionization chamber was fabricated from aluminum alloy with the insulators designed to minimize charge soakage and extracameral effects. The chamber consists of two spun aluminum hemispheres welded together with a hole 6 mm in diameter at one point in the weld to allow entrance of a copper collection electrode 3 mm in diameter. The inside diameter of the spherical chamber is approximately 170 mm, and the wall thickness is 1.6 mm. The collection electrode is about 140 mm long.

The large spherical chamber is supported by a polystyrene cylinder, shown in figure 2, which also serves as the high-voltage insulator. The high-voltage connection is made through a phosphor-bronze spring (not shown) inserted between the sphere and the high-voltage insulator. The sphere and cylinder are cemented together with an epoxy resin. In the high-voltage insulator all surfaces which can be "seen" by the collection electrode have been made conducting with colloidal graphite. The high-voltage insulating surface is recessed behind the conducting surfaces. A type-83 connector with high-quality insulation is used for mounting the collection electrode and as the guard ring. No charge soakage effects have been observed in this chamber.

The large air volume of the aluminum chamber is required to allow measurement of low-activity sources. The chamber background current is about 10^{-14} A which is consistent with the radiation background of about 0.03 mR/h. For the "5" source located one meter from the chamber, the background current is about 3 percent of the reading.

The chamber is mounted on a steel plate which is supported on a track in the radium range. The source to be intercompared, and the standard, are alternately placed in a plastic trough at the same height as the center of the chamber and at an appropriate distance away. The trough can be rotated through 180° to test for possible nonuniform source loading and this is ordinarily done in the course of a calibration.

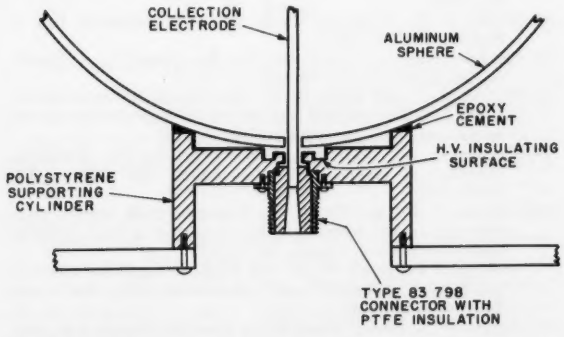

FIGURE 2. *Polystyrene cylinder which serves as (1) a support for the spherical aluminum chamber, (2) a high-voltage insulator, and (3) a means for mounting the guard ring and collection electrode.*

The heavy lines indicate where the polystyrene surfaces have been coated with colloidal graphite to make them conductive.

8. Calibration of Working Standards

When sources are submitted for calibration, it is convenient to use working standards of approximately the same activity for the comparison-type measurements. These working standards should be self consistant so that subsequent intercomparisons of calibrated sources will show no discrepancy beyond the estimated uncertainty when consideration is given to the precision of the combined measurements. Therefore, although several sources were measured in the open-air geometry, the "500" source was chosen to be the reference source for all the working standards since the relatively large ion current it generated allowed the most precise measurements. The average of the eight "500" source measurements, appropriately corrected for room scatter, was $136.9_6 mR \cdot m^2 \cdot h^{-1}$ on the reference date and this value was used for calibration of the working standards. The intercomparisons were carried out using the large aluminum chamber and a vibrating-reed electrometer. The same source-to-chamber distance was used for all the measurements although the source activities differed by a factor of about 100. This was made possible by changing the feedback capacitance of the vibrating-reed electrometer by the addition of accurately calibrated air capacitors.

The results of these intercomparisons are given in table 2. For those sources which were calibrated in open-air condition, the ratios of the two calibration values are also given in table 2. The agreement between the calibrations for the larger sources is within one percent but there is a large difference for the "5" source. The calibration of the "5" source using the

TABLE 2. *Comparison of source calibrations referenced to "500" source, using the aluminum chamber, and open-air calibrations*

Source	Working standard calibrations referenced to "500" source ($mR \cdot m^2 \cdot h^{-1}$)	Ratio: $\frac{\text{open-air cal}}{\text{"500" ref cal}}$
500	136.9_6	1.000
50	14.79	1.007
5	1.27_6	1.04
100	36.15	0.994
60	19.48	.....
25	8.23	.....

XUM

aluminum chamber, with the "500" source as the reference, is believed to be the more reliable since the background and leakage correction under these conditions is a smaller fraction of the reading.

Seven intercomparisons of the "500" and "50" sources were carried out using the aluminum chamber and electrometer system. Using these data an estimate of the standard deviation of the ratios of the ion currents developed in the chamber, is computed to be 0.7 percent.

The calibration of a ^{137}Cs source for the range of exposure rates considered here is believed to have an overall uncertainty of 3.2 percent. The contribution of systematic errors to this percentage, computed from the values given in table 3, is 1.2 percent. This value is equal to the square root of the sum of the squares of the estimated maximum uncertainties for the quantities given in the table.

The largest uncertainties given in table 3 are for the stopping power correction, the wall absorption correction and the volume determination. In the case of the stopping power correction the calculations of Burlin [6] produce values for the carbon-to-air ratio which are identical with those of Spencer-Attix and both agree with the experimental determinations of Whyte [13] for ^{60}Co gamma rays. The accuracy of Whyte's measurements is 0.5 percent and Burlin's calculated values are within his experimental uncertainty of 2 percent. Therefore an uncertainty of 0.5 percent is assigned to this correction.

The wall absorption correction, determined experimentally, is 0.6 percent per mm and 0.8 percent per mm for one-cm^3 and 50-cm^3 spherical chambers respectively. These corrections are determined from data for a set of three chambers each. Therefore 1 percent is taken as the estimated uncertainty for this correction since this is approximately the difference in the percentage corrections for a 4-mm wall.

The cavity chamber volumes were determined by differential weighing of the chambers, using water to fill the cavity. The range of the volume determinations for these chambers is 0.3 percent.

Each of the other quantities contributing to the systematic error, and entering into the cavity chamber measurement of the "500" source exposure rate, is believed to be known to 0.1 percent.

TABLE 3. *Estimated maximum uncertainties in the cavity chamber calibration of a ^{137}Cs Source*

Factor	Est. max. uncertainty
	Percent
Wall absorption correction	1.0
Stopping power correction	0.5
Capacity, potential and time	.1
Recombination	.1
Temperature	.1
Pressure	.1
Chamber volume	.3
Center of electron production correction	.1
Room scattering correction	.1

The random error contribution to the overall uncertainty is computed from three times the square root of the sum of the squares of the percent standard deviations of the various measurements. This includes the cavity chamber measurements of the "500" source, the intercomparison of the "500" source with the working standard sources and finally, the intercomparison of a working standard with a source to be calibrated for the user. In the case of the working standard calibrations the percent standard deviation is for the mean of several sets of measurements whereas the percent standard deviation for the calibration of the user's source is for one set of measurements.

$$\text{Overall uncertainty} = \sqrt{1.4} + 3\sqrt{0.11^2 + 0.26^2 + 0.6^2}$$
$$= 3.2 \text{ percent}$$

where the values given under the square root signs are in the order described above.

The author wishes to acknowledge the considerable assistance of Mr. J. T. Weaver in the measurements and scattering computations, and also Dr. Robert Loevinger for his many helpful suggestions in the editing of this report.

This work was supported by the U.S. Public Health Service whose contract officer, Mr. James Cooper, was most cooperative and helpful during the course of the measurements.

9. References

[1] Medical uses of radium and radium substitutes, U.S. Public Health Service Publication No. 999–RH–16 July 1965.

[2] Report of the International Commission on Radiological Units and Measurements (ICRU), Nat. Bur. Stand. (U.S.), Handb. 78, 99 pages, (Jan. 1959). See p. 19.

[3] Wyckoff, H. O., Measurements of cobalt-60 and cesium-137 gamma rays with a free-air chamber, Nat. Bur. Stand. (U.S.), 64C, (Eng. and Instr.), No. 2, 87–97 (Apr.–June 1967).

[4] Roesch, W. C., Dose for nonelectronic equilibrium conditions. Radiation Research **9**, 399 (1958).

[5] Aglintsev, K. K., and Ostromukhova, G. P., The distribution of ionization along a beam of gamma radiation and the determination of radiation dose with normal ionization chambers, The Soviet Journal of Atomic Energy **6**, No. 1, 33 (1959).

[6] Burlin, T. E., A general theory of cavity ionization, Brit. J. Radiol., **39**, 727 (1966).

[7] Physical Aspects of Irradiation, Nat. Bur. Stand. (U.S.), Handb. 85, 114 pages (March 1964). See p. 3.

[8] Berger, M. J., and Morris, E. E., Dose albedo and transmission coefficients for cobalt-60 and cesium-137 gamma rays incident on concrete slabs, unpublished report.

[9] Eisenhauer, C., An image source technique for calculating reflection of gamma rays or neutrons, Health Phys. **11**, 1145 (1965).

[10] Chilton, A. B., and Fu, C. Y., Exposure field from a point isotropic source located at the surface of a thick concrete slab, U. of Illinois. Urbana, Ill. (1966).

[11] Gorbics, S. G., Kunz, W. E., and Nash, A. E., New values for half-lives of cesium-137 and cobalt-60 nuclides, Nucleonics **21**, No. 1, 63 (1963).

[12] Berger, M. J., Energy deposition in water by photons from point isotropic sources, Journal of Nuclear Medicine Supp. No. 1, 15 (1968).

[13] Whyte, G. N., Measurement of the Bragg-Gray stopping-power correction. Rad. Res. **6**, 371 (1957).

(Paper 74A1–577)

JOURNAL OF RESEARCH of the National Bureau of Standards—A. Physics and Chemistry
Vol. 74A, No. 1, January–February 1970

Calculations of Zn II $3d^9 4s5s$ and Ag I $4d^9 5s6s$, and Some New Levels in these Spectra

William C. Martin and Jack Sugar

Institute for Basic Standards, National Bureau of Standards, Washington, D.C. 20234

(August 28, 1969)

Results of intermediate-coupling calculations are given for Zn II $3d^9 4s5s$ and Ag I $4d^9 5s6s$. A $[(4d^9)J_1, (5s6s)J_{11}]J$ coupling scheme is appropriate for the latter. New $3d^9 4s(^3D)5s\ ^2D_{2\frac{1}{2}}$ and $3d^9 4s(^1D)5s\ ^2D_{2\frac{1}{2}}$ levels were found in Zn II, and a few other additions and revisions are given for the analysis. The combinations of the new levels $3d^9(^2D)4s4p(^3P^\circ)\ ^4F^\circ_{4\frac{1}{2}}$ in Zn II and $4d^9(^2D)5s5p(^3P^\circ)\ ^2F^\circ_{2\frac{1}{2}}$ in Ag I are also listed.

Key words: Atomic spectra; energy levels; silver; zinc.

1. Introduction

A recent fitting of some d^9sp configurations to intermediate coupling theory provided useful comparisons of experimental with predicted levels in several spectra [1].[1] We also made similar calculations for Zn II $3d^9 4s5s$ and Ag I $4d^9 5s6s$. The results of these d^9ss calculations are reported here, along with the supporting combinations for a few new or revised level positions found during the course of the d^9sp and d^9ss work. Some new wavelength measurements for Zn II in the vacuum ultraviolet, and redetermined energy level positions based partially on these measurements, are given in an accompanying paper [2].

2. Zn II

Our first few energy-matrix diagonalization and level-fitting iterations [1] for Zn II $3d^9 4s4p$ indicated that the position previously listed [3] for $^4F^\circ_{4\frac{1}{2}}$ was incorrect. A search with Dick's [4] line list yielded the new level and combinations for $^4F^\circ_{4\frac{1}{2}}$ shown in table 1. The line at 54538.3 cm^{-1} arising from $4p'\ ^4F^\circ_{4\frac{1}{2}} - 5s'\ ^4D_{3\frac{1}{2}}$ was apparently not resolved on Dick's plates from a line at 54541.1 cm^{-1} ($4s^2\ ^2D_{2\frac{1}{2}} - 4f\ ^2F^\circ$). The quoted wavenumbers are from new observations [2] where the two lines are well resolved and show different excitation characteristics, each proper for the assigned classification.

The $3d^9 4s(^3D)5s\ ^2D_{2\frac{1}{2}}$ level at 164998.9 cm^{-1} in table 1 also replaces a previous level that did not fit the calculation. The results of fitting intermediate coupling theory [2] to Zn II $3d^9 4s5s$ are given in tables 2 and 3. The five parameter values in table 3 are determined by only seven known levels. It is seen, however, that these values scale well with the corresponding values[3] for Cu I $3d^9 4s5s$ where all eight levels are known. A check on the value of $G_2(3d^9, 4s)$ for Zn II is given by the fact that it is only slightly less that the value 1914 cm^{-1} for Zn III $3d^9 4s$. The presence of the $5s$ electron has little effect on the $3d$–$4s$ interaction, in agreement with a similar comparison of these two configurations in Cu I and Cu II, respectively.

The $3d^9 4s(^1D)5s\ ^2D_{2\frac{1}{2}}$ level in table 2 was also found by searching near the position predicted in earlier diagonalizations. Some combinations of this new level are given in table 1.

[1] Figures in brackets indicate the literature references at the end of this paper.

[2] The d^9ss energy matrices were calculated independently for this work. They include an additive constant A, related to the configuration center of gravity (c.g.) as follows:

$$A = (\text{c.g.}) + \tfrac{1}{4}[G_2(ds) + G'_2(ds) + G_0(ss)].$$

A description of the procedure for least-squares fitting of level positions to obtain energy parameter values is given by Racah [5]. We use the term "rms error" to describe the level fits. This is defined as

$$\left[\left(\sum_{i=1}^{N} \delta_i^2\right)/(N-M)\right]^{1/2},$$

where δ is the difference between the experimental and calculated level positions, N is the number of experimental levels entered into the fitting procedure, and M is the number of free parameters.

[3] Our fitted values for the Cu I parameters are in agreement with those recently published by Wilson [6].

TABLE 1. *Combinations of some* Zn II *levels*

All but four of these levels were given by Crooker and Dick [3]. The positions have been redetermined, partly on the basis of new observations [2]. Wavenumbers of lines with intensities in parentheses are from [2], and the others are from [4].

			$3d^9 4s(^3D)5s$		$(^1D)5s$	$3d^9 4s4d$?			$3d^9 4s(^3D)6s$	
			$^4D_{3½}$	$^2D_{2½}$	$^2D_{2½}$	$1_{3½}$	$7_{3½}$	$12_{3½}$	$21_{4½}$	$^4D_{3½}$
			161318.4	164998.9[a]	167624.4[a]	169150.5[b]	171643.0[b]	173003.1	173561.9[a]	191198.
			(80)	20	6	(100)	(50)	5		1
$3d^9(^2D)4s4p(^3P^o)$	$^4P^o_{2½}$	103701.6	57616.7	[c]61298.4	63923.5	65448.7	67941.2	69301.9		87496.4
			(150)			(100)	(40)	5	(80)	8
	$^4F^o_{4½}$	[a]106779.9	54538.3			62370.8	64863.2	66223.2	66782.0	84421.8
			(40)			8	(40)	(12)	(30)	1
	$^4F^o_{3½}$	106852.4	54466.0			62297.7	64790.8	66151.0	66708.8	84344.8
			10			3		(40)		
	$^4F^o_{2½}$	107268.6	54050.0			61883.1		65734.3		
			12		10	10		15		0
	$^2F^o_{2½}$	110672.3	50646.6		56952.6	58477.8		62330.7		80523.5
			(50)			60(5)	(60)	25	(100)	2
	$^4D^o_{3½}$	110867.2	50451.3			58283.2	60776.0	62135.3	62694.9	80331.1
			25		8	18	2	15		00
	$^4D^o_{2½}$	111743.0	49576.1		55881.3	57407.6	59899.9	61259.9		79454.6
			30	60	(15)	25	15		20	
	$^2F^o_{3½}$	112409.7	48909.6	52589.4	[d]55214.9	56741.0	59233.3		61151.7	
					75					
	$^2P^o_{1½}$	113499.2			54125.4					
					10					
	$^2D^o_{1½}$	114045.0			53580.1					
			10	50	75			2		1
	$^2D^o_{2½}$	114833.9	46485.3	50166.4	52791.1			58168.8		76363.8
				50W	[e]30					
$3d^9(^2D)4s4p(^1P^o)$	$^2F^o_{3½}$	130014.3		34984.3	37609.0					
				100W	15					
	$^2D^o_{2½}$	131650.9		33348	35973					
				30W	30					
	$^2F^o_{2½}$	133145.8		31851	34480					

[a] New level.
[b] J-value of level changed here.
[c] Line also classified by another transition [3].
[d] Line newly resolved from stronger neighboring line [2].
[e] Line also classified by Zn III transition [4].

TABLE 2. *Calculated energy levels for* Zn II $3d^9 4s5s$

The last column gives the percentage of the leading eigenvector component in the scheme of the first column.

Term	J	Experimental cm^{-1}	Calculated cm^{-1}	E–C cm^{-1}	LS %
$3d^9 4s(^3D)5s\ ^4D$	3½	161318	161322	−4	100
	2½	162070	162068	2	85
	1½	162897	162892	5	74
	0½	164070	164070	0	100
$(^3D)5s\ ^2D$	2½	164999	164999	0	88
	1½	165277	165279	−2	46
$(^1D)5s\ ^2D$	2½	167624	167624	0	92
	1½		169268		57

TABLE 3. *Energy parameter values for three* d^9msns *configurations*

Unit is cm^{-1}

	Zn II $3d^9 4s5s$	Cu I $3d^9 4s5s$	Ag I $4d^9 5s6s$
A	166409.6 ± 4	65964.3 ± 3	84199.3 ± 20
$G_2(d, ms)$	1884.8 ± 4	1550.0 ± 3	1874 ± 102
$G^1_2(d, ns)$	291.4 ± 4	158.9 ± 3	197.5 ± 27
$G_0(ms, ns)$	1812.0 ± 6	1021.9 ± 3	886 ± 19
ζ_d	1099.1 ± 3	826.0 ± 2	1818 ± 10
rms error[2]	5	4	25

3. Ag I

The $4d^9 5s6s$ configuration in this atom begins 18306 cm^{-1} above the Ag II ($4d^{10}\ ^1S$) limit. The levels having $J = 1\frac{1}{2}$ or $2\frac{1}{2}$ are thus broadened by autoionization into the $4d^{10}\epsilon d\ ^2D$ continuum. This mixing with the continuum may help account for the larger standard errors on the parameter values we obtained for Ag I $4d^9 5s6s$ (table 3). The same seven levels are known experimentally as for Zn II, but the level rms error is 25 cm^{-1} for Ag I. The value for the Ag I parameter with the largest standard error, $G_2(4d, 5s) = 1874 \pm 102$ cm^{-1}, compares well with the Ag II value 1942 cm^{-1} obtained directly from the experimental levels of $4d^9 5s$. Both values may be affected by neglect of configuration interaction, since the Ag II value for G_2 given by a general treatment [7] of $(4d+5s)^n$ is 2045 ± 17 cm^{-1}.

The calculated levels are given in table 4. On inspection of the experimental levels, we noticed that whereas the $4d^9 5s(^3D)6s\ ^2D$ and ^4D terms overlap badly, the levels appeared to fall into separated terms based on the coupling scheme $[(d^9)J_I, (ss)J_{II}]J$. As may be seen in table 4, the latter scheme is indeed more appropriate than LS coupling. The $J_I J_{II}$ percentage compositions were obtained by a transformation from the $(d^9 s)s$ LS scheme of our matrices.[4] For those six levels having coupling-dependent purity, the average purity in $J_I J_{II}$ coupling is 82 percent, as compared with 62 percent in the LS scheme.

TABLE 4. *Calculated energy levels for* Ag I $4d^9 5s6s$

The largest component in each of the two coupling schemes is given for each level.

Name $[(4d^9)J_I, (5s6s)J_{II}]$	J	Experimental cm^{-1}	Calculated cm^{-1}	E–C cm^{-1}	$J_I J_{II}$ %	Term	LS %
$[2\frac{1}{2}, 1]$	$3\frac{1}{2}$	79413	79424	−11	100	$4d^9 5s(^3D)6s\ ^4D$	100
	$2\frac{1}{2}$	80164	80175	−11	84	^4D	65
	$1\frac{1}{2}$	81266	81242	24	87	^4D	48
$[2\frac{1}{2}, 0]$	$2\frac{1}{2}$	82070	82066	4	79	$4d^9 5s(^3D)6s\ ^2D$	68
$[1\frac{1}{2}, 1]$	$0\frac{1}{2}$	83983	83969	14	100	$4d^9 5s(^3D)6s\ ^4D$	100
	$1\frac{1}{2}$	84594	84606	−12	79	^4D[a]	49
	$2\frac{1}{2}$	86484	86490	−6	82	$4d^9 5s(^1D)6s\ ^2D$	81
$[1\frac{1}{2}, 0]$	$1\frac{1}{2}$		87429		81	$4d^9 5s(^1D)6s\ ^2D$	64

[a] The LS name for this level would be $(^3D)^2D$, which comprises 41 percent of the calculated composition.

The $J_I J_{II}$ term structure of this configuration is apparent in figure 1. There is no overlapping of the four terms, and the largest of the interactions contributing to the structure, the $4d^9$ spin-orbit interval $2\frac{1}{2}\ \zeta_d$, is nicely exhibited.

As a result of our calculations [1] *for Ag* I $4d^9 5s5p$ we found a new level $4d^9(^2D)5s5p(^3P^\circ)\ ^2F^\circ_{2\frac{1}{2}}$ (designated $5p'\ ^2F^\circ_{2\frac{1}{2}}$). Five combinations are given in table 5 for this level, three of the lines not having been previously classified [8]. The character of these lines shows the level to be wide, as expected because of autoionization. The circumstance that its strongest expected transition, to $4d^9 5s^2\ ^2D_{1\frac{1}{2}}$, is masked by the much stronger resonance line at 3382.89 Å probably explains previous failure to find this level. Some other results of the $4d^9 5s5p$ work as it affected line classifications are also given in table 5. The levels of $4d^9 5s6s$ are given LS names in this table to make it consistent with Shenstone's full line list.

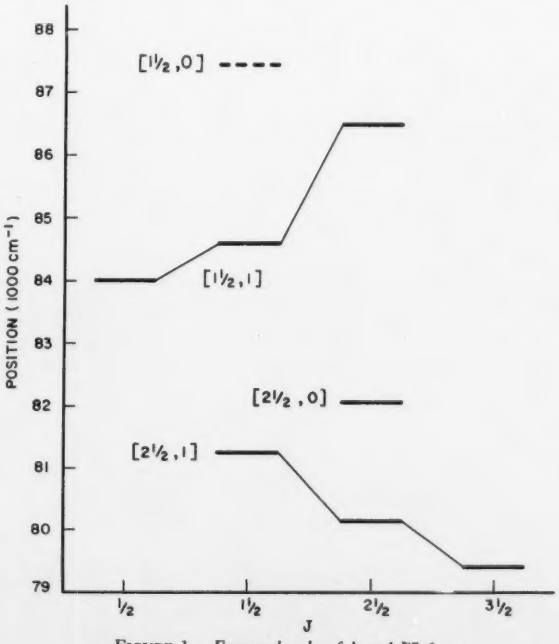

FIGURE 1. *Energy levels of* Ag I $4d^9 5s6s$.

The connected levels form terms in the $[(4d^9)J_I, (5s6s)J_{II}]J$ coupling scheme appropriate for this configuration. The $[1\frac{1}{2}, 0]$ level has not been observed.

[4] This transformation was actually accomplished by first diagonalizing the matrices with all parameters zero except ζ_d and G_0 (ss). See [5].

TABLE 5. *Classifications of some* Ag I *lines*

Wavelengths and intensities are from Shenstone [8]. Configurations and parentages for the levels are indicated by use of the designation scheme of AEL [8]. Notes:

A. Name of the $4d^9 5s5p$ level involved in transition was changed in [1].
B. Line was previously listed as doubly classified, with one of the transitions belonging to the now rejected level at 62934 cm^{-1}
C. New classification.

λ(air) Å	Int.[a]	σ(vac) cm^{-1}	Classification	Note
6010.1	5U	16634.	$5p'\ ^2D^\circ_{1\frac{1}{2}} - 6s'\ ^4D_{2\frac{1}{2}}$	A
5801.92	5U	17230.9	$5p'\ ^4D^\circ_{2\frac{1}{2}} - 6s'\ ^4D_{3\frac{1}{2}}$?[b]	B
5637.01	5U	17735.0	$5p'\ ^2D^\circ_{1\frac{1}{2}} - 6s'\ ^4D_{1\frac{1}{2}}$	A
4917.5	10UU	20330.	$5p'\ ^2F^\circ_{2\frac{1}{2}} - 6s'\ ^2D_{1\frac{1}{2}}$	C
4888.21	20	20451.7	$5p'\ ^2D^\circ_{1\frac{1}{2}} - 6s'\ ^4D_{\frac{1}{2}}$	A
4745.93	2U	21064.8	$5p'\ ^2D^\circ_{1\frac{1}{2}} - 6s'\ ^2D_{1\frac{1}{2}}$	A
4615.69	30U	21659.2	$5p'\ ^4P^\circ_{1\frac{1}{2}} - 6s'\ ^4D_{2\frac{1}{2}}$	B
4499.50	1U	22218.5	$5p'\ ^2F^\circ_{2\frac{1}{2}} - 6s''\ ^2D_{2\frac{1}{2}}$	C
4354.7	5UU	22957.	$5p'\ ^2F^\circ_{3\frac{1}{2}} - 17$ $5p'\ ^2F^\circ_{2\frac{1}{2}} - 14_{2\frac{1}{2}}$	C
3542.608	50	28219.76	$5p'\ ^4F^\circ_{4\frac{1}{2}} - 12$?[b]	B
3469.16	30	28817.2	$5s^2\ ^2D_{1\frac{1}{2}} - 5p'\ ^2D^\circ_{1\frac{1}{2}}$	A
3382.893	1000R	29552.04	$5s\ ^2S_{\frac{1}{2}} - 5p\ ^2P^\circ_{\frac{1}{2}}$ $5s^2\ ^2D_{1\frac{1}{2}} - 5p'\ ^2F^\circ_{2\frac{1}{2}}$	C
2938.42	20U	34022.	$5s^2\ ^2D_{2\frac{1}{2}} - 5p'\ ^2F^\circ_{3\frac{1}{2}}$	C
λ(vac)				
1574.02	5	63531.6	$5s\ ^2S_{\frac{1}{2}} - 5p'\ ^2D^\circ_{1\frac{1}{2}}$	A
1507.37	50RUU	66341.	$5s\ ^2S_{\frac{1}{2}} - 5p'\ ^2D^\circ_{1\frac{1}{2}}$	A

[a] The letter "U" was used in [8] for wide lines (German *unscharf*).

[b] Classification given as questionable by Shenstone [8]. The strong line at 3542.6 Å does not have the wide character expected for transitions from the autoionizing $5p'\ ^2F^\circ_{2\frac{1}{2}}$ level. No classification has been found for this line except that given. (The three combinations of the even level 12 of Shenstone were given with question marks, so presumably the level itself was considered doubtful.)

4. References

[1] Martin, W. C., and Sugar, J., J. Opt. Soc. Am.
[2] Martin, W. C., and Kaufman, V., J. Res. Nat. Bur. Stand. (U.S.). **74A,** No. 1, 11 (Jan.–Feb. 1970).
[3] Crooker, A. M., and Dick, K. A., Can. J. Phys. **46,** 1241 (1968).
[4] Dick, K. A., The Spark Spectra of Zinc (Ph. D. Thesis, University of British Columbia, 1966).
[5] Racah, G., Bull. Res. Council Israel **8F,** No. 1, 1 (1959).
[6] Wilson, M., J. Phys. **B2,** 524 (1969).
[7] Shadmi, Y., Bull. Res. Council Israel **9F,** 141 (1961).
[8] Shenstone, A. G., Phys. Rev. **57,** 894 (1940). See also C. E. Moore, Atomic Energy Levels, Nat. Bur. Stand. (U.S.), Circ. 467, Vol. III, 282 pages (1958).

(Paper 74A1–578)

JOURNAL OF RESEARCH of the National Bureau of Standards—A. Physics and Chemistry
Vol. 74A, No. 1, January–February 1970

New Vacuum Ultraviolet Wavelengths and Revised Energy Levels in the Second Spectrum of Zinc (Zn II)

William C. Martin and Victor Kaufman

Institute for Basic Standards, National Bureau of Standards, Washington, D.C. 20234

(September 23, 1969)

Spectra from sliding spark discharges between zinc electrodes and from a hollow-cathode source were photographed in the range 2105–1400 Å with the NBS 10.7 m vacuum spectrograph. New measurements of 130 Zn II lines in this region, combined in some cases with previous measurements in the air region, were used to derive revised positions for the known levels. Wavelengths calculated from these levels are given for 267 lines in the region 2570–730 Å. The line list also includes unclassified Zn II lines below 2570 Å, based on the most complete description of this spectrum [A. M. Crooker and K. A. Dick, Can. J. Phys. **46**, 1241 (1968)]. A few additions to the line list of Crooker and Dick above 2700 Å are given. The line and level lists take into account recent work at the National Bureau of Standards on the Zn II analysis.

Key words: Atomic energy levels of Zn II; ionized zinc; spectral wavelengths of Zn II.

1. Introduction

An improved description of the Zn II spectrum has recently been given by Crooker and Dick [1],[1] who also extended and revised the earlier analyses [2, 3]. From a combination array made in connection with a theoretical fitting of some Zn II levels [4, 5], we decided that a resolution of several blends in the vacuum ultraviolet spectrum was needed. It appeared likely that the resolution available in this laboratory was sufficiently greater than that obtained by Crooker and Dick to make worthwhile a reobservation of Zn II in the indicated region. The resulting new wavelengths are reported here, together with a list of revised energy levels partially based on them.

2. Observations

The spectra were photographed with the NBS 10.7 m Eagle-mounting vacuum spectrograph. A 1200 grooves/mm grating used in the first order gave a plate factor of 0.78 Å/mm. One source was a sliding spark between zinc electrodes, in series with an auxiliary rotating spark gap and appropriate inductance, resistance, and capacitance charged to 500 V [6]. Three different exposures were made:[2]

S_1, hot spark	2105–1714 Å
S_2, mild spark	2105–1714 Å
S_3, mild spark	2105–1400 Å.

The hot spark gave the stronger lines of Zn IV and Zn III and also gave our most complete Zn II spectrum. The mild sparks showed no Zn IV lines, and were strong sources of Zn I and of Zn II lines having low or medium excitation energies. Spectra for standard wavelengths (C I, N I, and Ge I[7]) were photographed only on the S_3 spectrograms. Zinc wavelengths obtained from this exposure were the principal standards for reducing the other two exposures.

We also obtained measurements of spectra from a water-cooled aluminum hollow-cathode source that contained zinc (as an impurity in the aluminum) and copper, silicon, and germanium (for standard wavelengths [7]). The discharge current was 0.8 A through a carrier gas of helium at about 2 torr. Each of five different exposures (3 to 30 min) covered the range 2105–1400 Å.

[1] Figures in brackets indicate the literature references at the end of this paper.

[2] Typical circuit parameters for hot and mild sparks are given in [6]. We used peak currents varying from several hundred amperes (S_1) to a few amperes (S_2).

3. Line List and Level Values

Table 1 contains more than 300 Zn II lines in the range 2570–730 Å. Crooker and Dick [1] have obtained by far the most complete spectrum in this region, and the observed wavelengths for about two-thirds of these lines are taken from their list. The observed wavelengths for 130 lines are from our measurements (2105–1400 Å, with a number 1–4 in the first column). We derived most of the level values in table 2 using these new measurements combined with a few previous measurements at longer wavelengths where this appeared consistent or was necessary. The calculated wavelengths given for the 267 classified lines in table 1 were obtained from the revised levels. They are recommended as the most accurate wavelengths now available for Zn II in this region. An "X" in the calculated-wavelength column indicates that the corresponding level separation was based entirely on the observed wavelength for this transition.

The resulting wavelengths are categorized as follows (numbers correspond to those in the first column of Table 1):

1. The observed wavelength is from the hollow-cathode source. Most of these lines were measured in each of two to five different exposures. The estimated uncertainty of the calculated wavelength is ±0.002 Å. (The different measurements for a single line usually agreed to within ±0.001 Å, but this precision was not maintained in the accuracy as indicated by the Ritz principle.)

2. All the above applies except that the observed wavelength is based on a single measurement of a weak line. The observed wavelength still usually agrees with the (preferred) calculated value to within 0.003 Å.

3. This indicates a line of the (2) type except that the corresponding energy level difference is based on this one measurement. The wavelength is probably accurate to ±0.003 Å.

4. The observed wavelength is from our sliding spark sources. The Ritz-principle consistency of these lines is considerably poorer than for the hollow-cathode wavelength (see below). The observed and calculated wavelengths for unblended lines are different by about 0.005 Å on the average, and by more than 0.015 Å for a few lines. Most of the calculated wavelengths should be in error by less than 0.01 Å.

No number in the first column. The observed wavelength is from [1] or [9]. The calculated wavelengths for most of these lines are based on level differences derived from our sliding-spark measurements; the corresponding probable error is less than 0.01 Å.

The rms deviation of the standard wavelengths (from smooth reduction curves) for the spark spectrograms was about 0.002 Å. The much larger error for the resulting zinc measurements (type 4 lines, above) is not too surprising, since we had only one independent measurement of the spark spectrum against well-known reference wavelengths. The accuracy for some Zn II lines was also reduced by their width or diffuseness. More accurate wavelength measurements for some Zn II lines from a spark source would probably not be justified, because of sensitivity to Stark shifts. The $6f\,^2F^\circ$ levels, for example, are depressed by about 1 cm^{-1} in the sliding-spark discharge. This accounts for most of the disagreement between the calculated and observed wavelengths for the line at 1430.27 Å.

Except for the even levels above the limit, most of the level values in table 2 are consistent with the best observations to ±0.2 cm^{-1}. Values are given to two decimal places for some levels that appeared consistent to within ±0.1 cm^{-1}. Most of the levels above the limit are probably in error by less than 0.5 cm^{-1}.

The revised levels give improved agreement between the calculated and the more accurately measured wavelengths over the entire spectrum. Disagreements between calculated and observed wavenumbers are much reduced (from ~ 2 cm^{-1} in [1]) for several accurately measured air-region lines connecting $3d^{10}f$ and $3d^{10}d$ levels. The new wavelengths in the region 2000–2103 Å, which contains the basic $3d^{10}4s - 3d^{10}4p$ transitions and also the $3d^{10}4p - 3d^{10}4d$ multiplet, are systematically longer than the values in [1] by more than 0.03 Å. Thus the revised values for the $4p\,^2P^\circ$ and $4d\,^2D$ levels are less than the values in [1] by about 0.7 cm^{-1} and 1.7 cm^{-1}, respectively. This accounts for a systematic difference (between the two lists) for all excited levels except those of the $3d^{10}f$ and $3d^{10}g$ configurations. The systematic difference that exists between our levels and the values of Shenstone and Gibson [2, 3] is smaller and in the opposite direction.

Estimated relative intensities[3] and line characteristics from several different sources are given in table 1, since they often help confirm the analysis. Comparing intensities of Zn II lines from the hot spark (S_1) and the mild sparks (S_2, S_3), we find in S_1 an enhancement of lines from levels above the ionization limit. Some of the weaker lines that appeared only in S_1 were clearly broadened relative to other lines, and the classifications indicate that this width arises from autoionization. We note especially that transitions from the four $3d^9 4s(^3D)5s$ levels having $J = 1\frac{1}{2}$ or $2\frac{1}{2}$ are always wide, analogous to the Cu I spectrum [8]. These same autoionizing transitions are quite strong in Dick's source E_1 and very weak or not observed in E_2.[4]

An example of the usefulness of these excitation characteristics is the classification of the line at 1833.573 Å. We began this work mainly to attempt a resolution of this $4p'\,^4F^\circ_{4\frac{1}{2}} - 5s'\,^4D_{3\frac{1}{2}}$ transition from the $4s^2\,^2D_{2\frac{1}{2}} - 4f\,^2F^\circ$ line. The relative intensities of 1833.573 Å in S_1 and S_2, S_3 (as compared, for example, with the now resolved transition from $4f\,^2F^\circ$) show that it arises from a level above the limit. However, the level is not observably autoionization-broadened. These characteristics are consistent with a transition

[3] The relative intensities of 42 lines observed in the hollow-cathode spectrum were similar to those in the mildest spark (S_2) spectrum, and are not given in table 1.

[4] In the region above 2385 Å, E_1 and E_2 in the table are Dick's [9] intensities I_4 and I_5, respectively; below 2385 Å, E_1 and E_2 are his intensities I_1 and I_2, respectively. Our statements about relative intensities refer to I_1 and I_2. Three autoionizing lines with apparently comparable intensities in these two sources are probably blends (see notes to table 1).

TABLE 1. Zn II *spectrum below 2570 Å*

Sources of the observed wavelengths and accuracies of the calculated wavelengths are indicated by numbers in the first column, as explained in the text. New classifications are indicated by an asterisk (*). The letters refer to footnotes, where it is explained that a few lines of Zn III or of doubtful ionization stage are also listed. Relative intensity estimates: E_1 and E_2 are from different exposures of electrodeless discharge sources, as given by Dick [9], and the other three exposures are described in the text. Numbers under the heading "S_2, S_3" are approximate geometric means of the relative intensities from these two sources. Self-reversed lines are indicated by "R" and haziness (in [9]) by "H". Lines with intensities followed by "W" were so diffuse (on our plates) as to suggest autoionization broadening.

Notes	λ(air), Å		Intensity				σ, cm⁻¹	Classification
	obs.	calc.	E_1	E_2			obs.	
	2567.975	.976	50	30			38929.5	$4d\ ^2D_{2\frac{1}{2}} - 7f\ ^2F^\circ_{3\frac{1}{2}}$
a	2567.795	.798	50	10			38932.3	$4d\ ^2D_{2\frac{1}{2}} - 7f\ ^2F^\circ_{2\frac{1}{2}}$
	2564.456	.461	30	30			38982.9	$4d\ ^2D_{1\frac{1}{2}} - 7f\ ^2F^\circ_{2\frac{1}{2}}$
	2557.947	.948	1000	1000			39082.13	$4p\ ^2P^\circ_{1\frac{1}{2}} - 5s\ ^2S_{1\frac{1}{2}}$
*	2545.0	.00	5				39281.	$7p\ ^2P^\circ_{1\frac{1}{2}} - 5s''\ ^2D_{2\frac{1}{2}}$
b*	2527.96	8.01?	50	15			39545.8	$4d\ ^2D_{2\frac{1}{2}} - 9p\ ^2P^\circ_{1\frac{1}{2}}$?
	2506.69	.70	10	5			39881.2	$4s^2\ ^2D_{1\frac{1}{2}} - 4p'\ ^4P^\circ_{1\frac{1}{2}}$
	2501.990	.990	1000	1000			39956.14	$4p\ ^2P^\circ_{\frac{1}{2}} - 5s\ ^2S_{\frac{1}{2}}$
	2439.5	.53	15				40979.6	$4s^2\ ^2D_{2\frac{1}{2}} - 4p'\ ^4P^\circ_{2\frac{1}{2}}$
	2435.76	.79	15	10			41042.5	$4d\ ^2D_{2\frac{1}{2}} - 8f\ ^2F^\circ$
	2433.131	.11	5	1			41086.8	$4s^2\ ^2D_{1\frac{1}{2}} - 4p'\ ^4P^\circ_{\frac{1}{2}}$
	2432.74	.73	10	5			41093.4	$4d\ ^2D_{1\frac{1}{2}} - 8f\ ^2F^\circ_{2\frac{1}{2}}$
	2390.078	×	20	30			41826.9	$4s^2\ ^2D_{1\frac{1}{2}} - 4p'\ ^4F^\circ_{2\frac{1}{2}}$
	2383.923	.949	30	15			41934.9	$5s\ ^2S_{1\frac{1}{2}} - 4p''\ ^2P^\circ_{1\frac{1}{2}}$
	2346.685	.68	20	12			42600.3	$4s^2\ ^2D_{2\frac{1}{2}} - 4p'\ ^4P^\circ_{1\frac{1}{2}}$
	2336.493	.48	2	0H			42786.1	$4s^2\ ^2D_{1\frac{1}{2}} - 4p'\ ^4F^\circ_{1\frac{1}{2}}$
*	2273.150	.175	50	10			43978.2	$5s\ ^2S_{1\frac{1}{2}} - 8p\ ^2P^\circ_{\frac{1}{2}}$
*	2212.402	.437	3	1			45185.7	$5s\ ^2S_{1\frac{1}{2}} - 8p\ ^2P^\circ_{1\frac{1}{2}}$
	2210.176	.201	60	15			45231.2	$4s^2\ ^2D_{1\frac{1}{2}} - 4p'\ ^2F^\circ_{2\frac{1}{2}}$
	2203.511	.453	15	5			45368.0	$5s\ ^2S_{1\frac{1}{2}} - 4p''\ ^2P^\circ_{\frac{1}{2}}$
	2163.475	.511	6	8			46207.4	$5s\ ^2S_{1\frac{1}{2}} - 4p''\ ^2D^\circ_{1\frac{1}{2}}$
	2159.060	.085	2	2			46301.9	$4s^2\ ^2D_{1\frac{1}{2}} - 4p'\ ^4D^\circ_{2\frac{1}{2}}$
	2150.539	.58	10	6			46485.3	$4p'\ ^2D^\circ_{2\frac{1}{2}} - 5s'\ ^4D_{3\frac{1}{2}}$
b	2147.419	.43	75	20R			46552.9	$4s^2\ ^2D_{1\frac{1}{2}} - 4p'\ ^4D^\circ_{1\frac{1}{2}}$
	2122.741	.775	75	12			47094.0	$4s^2\ ^2D_{1\frac{1}{2}} - 4p'\ ^4D^\circ_{\frac{1}{2}}$
c	2116.318	.35	5	10			47236.9	$4p'\ ^2D^\circ_{2\frac{1}{2}} - 5s'\ ^4D_{2\frac{1}{2}}$
	λ(vac), Å		Intensity					
	obs.	calc.	E_1	E_2	S_1	S_2, S_3		
1	2102.844	.842	200	200R	400	400	47554.65	$4p\ ^2P^\circ_{1\frac{1}{2}} - 4d\ ^2D_{1\frac{1}{2}}$
1	2100.604	×	300	300R	700	700	47605.36	$4p\ ^2P^\circ_{1\frac{1}{2}} - 4d\ ^2D_{2\frac{1}{2}}$
3	2085.511	×	30	15	2	2	47949.88	$4s^2\ ^2D_{2\frac{1}{2}} - 4p'\ ^4F^\circ_{2\frac{1}{2}}$
	2082.191	.246	4				48026.3	$4p'\ ^2D^\circ_{1\frac{1}{2}} - 5s'\ ^4D_{2\frac{1}{2}}$
4	2081.115	.111	25	18	3	3	48051.2	$4s^2\ ^2D_{1\frac{1}{2}} - 4p'\ ^2P^\circ_{\frac{1}{2}}$
4b	2080.596	.600	50	20	8W		48063.2	$4p'\ ^2D^\circ_{2\frac{1}{2}} - 5s'\ ^4D_{1\frac{1}{2}}$
3	2077.070	×	20	15		1	48144.74	$4s^2\ ^2D_{2\frac{1}{2}} - 4p'\ ^4D_{3\frac{1}{2}}$
1	2064.887	.890	200	300R	600	600	48428.80	$4p\ ^2P^\circ_{\frac{1}{2}} - 4d\ ^2D_{1\frac{1}{2}}$
1	2062.662	.664	300	500R	1200R	1200R	48481.04	$4s\ ^2S_{1\frac{1}{2}} - 4p\ ^2P^\circ_{\frac{1}{2}}$
1	2057.471	.470		25R	80	80	48603.36	$4s^2\ ^2D_{1\frac{1}{2}} - 4p'\ ^2D^\circ_{1\frac{1}{2}}$
	2045.594		5	3			48885.6	
	2044.588	.626	30	12			48909.6	$4p'\ ^2F^\circ_{3\frac{1}{2}} - 5s'\ ^4D_{3\frac{1}{2}}$
1	2039.962	×	60	25R	50	50	49020.52	$4s^2\ ^2D_{2\frac{1}{2}} - 4p'\ ^4D^\circ_{2\frac{1}{2}}$
	2037.479		8	8			49080.3	
	2029.543	.556	35	12			49272.2	$4s^2\ ^2D_{2\frac{1}{2}} - 4p'\ ^4D^\circ_{1\frac{1}{2}}$
1	2026.137	.136	300	500R	1500R	1500R	49355.00	$4s\ ^2S_{1\frac{1}{2}} - 4p\ ^2P^\circ_{1\frac{1}{2}}$
	2017.099	.129	25	15			49576.1	$4p'\ ^4D^\circ_{2\frac{1}{2}} - 5s'\ ^4D_{3\frac{1}{2}}$
4b	2013.616	.677	15	15	2W		49661.9	$4p'\ ^2F^\circ_{3\frac{1}{2}} - 5s'\ ^4D_{2\frac{1}{2}}$

TABLE 1. Zn II *spectrum below 2570 Å*—Continued

Notes	λ(vac), Å		Intensity				σ, cm^{-1}	Classification
	obs.	calc.	E_1	E_2	S_1	S_2, S_3	obs.	
1	2012.590	×	100	35R	80	80	49687.22	$4s^2\ ^2D_{2\frac{1}{2}}-4p'\ ^2F^\circ_{3\frac{1}{2}}$
b	1998.977	.998	25				50025.6	$4p'\ ^2D^\circ_{1\frac{1}{2}}-5s'\ ^4D_{1\frac{1}{2}}$
	1996.922	.973	50				50077.1	$4p'\ ^4D^\circ_{1\frac{1}{2}}-5s'\ ^4D_{2\frac{1}{2}}$
*	1993.367	.424	50				50166.4	$4p'\ ^2D^\circ_{2\frac{1}{2}}-5s'\ ^2D_{2\frac{1}{2}}$
4	1986.988	7.001	100	1	3W		50327.4	$4p'\ ^4D^\circ_{\frac{1}{2}}-5s'\ ^4D_{2\frac{1}{2}}$
	1985.608	.620	70				50362.4	$4p'\ ^4D^\circ_{3\frac{1}{2}}-5s'\ ^4D_{1\frac{1}{2}}$
4	1982.426	.430	10		4		50443.2	$4p'\ ^2D^\circ_{2\frac{1}{2}}-5s'\ ^2D_{1\frac{1}{2}}$
4	1982.111	.113	100	20	50	12	50451.3	$4p'\ ^4D^\circ_{3\frac{1}{2}}-5s'\ ^4D_{3\frac{1}{2}}$
	1977.494	.422?	5	10			50569.1	$4p'\ ^2P^\circ_{1\frac{1}{2}}-5s'\ ^4D_{1\frac{1}{2}}$?
	1977.159	.175	25				50577.6	$4p'\ ^2P^\circ_{1\frac{1}{2}}-5s'\ ^4D_{1\frac{1}{2}}$
	1974.467	.485	12	8			50646.6	$4p'\ ^2F^\circ_{2\frac{1}{2}}-5s'\ ^4D_{3\frac{1}{2}}$
1	1969.404	.405	100	35R	80	80	50776.78	$4s^2\ ^2D_{2\frac{1}{2}}-4p'\ ^2P^\circ_{1\frac{1}{2}}$
4	1964.538	.532	80		3W		50902.6	$4p'\ ^4D^\circ_{1\frac{1}{2}}-5s'\ ^4D_{1\frac{1}{2}}$
	1954.872	.881	75				51154.2	$4p'\ ^4D^\circ_{2\frac{1}{2}}-5s'\ ^4D_{1\frac{1}{2}}$
4	1952.999	3.014	80		3W		51203.3	$4p'\ ^4D^\circ_{3\frac{1}{2}}-5s'\ ^4D_{2\frac{1}{2}}$
	1951.911	.902	60				51231.8	$4p'\ ^2D^\circ_{1\frac{1}{2}}-5s'\ ^2D_{1\frac{1}{2}}$
2	1948.459	.460	30	15	1		51322.61	$4s^2\ ^2D_{2\frac{1}{2}}-4p'\ ^2D^\circ_{1\frac{1}{2}}$
	1945.583	.608	60				51398.5	$4p'\ ^2F^\circ_{2\frac{1}{2}}-5s'\ ^4D_{2\frac{1}{2}}$
	1940.413	.421	40				51535.4	$4p'\ ^4D^\circ_{\frac{1}{2}}-5s'\ ^4D_{1\frac{1}{2}}$
	1931.073	.091	40				51784.7	$4p'\ ^2P^\circ_{1\frac{1}{2}}-5s'\ ^2D_{1\frac{1}{2}}$
III	1929.774		} 100	40R	{ 80		51819.5	
3	1929.670	.669			{ 3	3	51822.33	$4s^2\ ^2D_{1\frac{1}{2}}-4f\ ^2F^\circ_{2\frac{1}{2}}$
4	1920.271	.278	70	5H	2		52076.0	$4p'\ ^4D^\circ_{1\frac{1}{2}}-5s'\ ^4D_{1\frac{1}{2}}$
III	1919.068		} 100	{ 20	120		52108.6	
1	1918.962	×		{ 50R	100	100	52111.51	$4s^2\ ^2D_{2\frac{1}{2}}-4p'\ ^2D^\circ_{2\frac{1}{2}}$
	1914.806	.803	60				52224.6	$4p'\ ^2F^\circ_{2\frac{1}{2}}-5s'\ ^4D_{1\frac{1}{2}}$
*	1901.523	.531	60				52589.4	$4p'\ ^2F^\circ_{3\frac{1}{2}}-5s'\ ^2D_{2\frac{1}{2}}$
	1896.056	.015	2				52741.1	$4p'\ ^4D^\circ_{\frac{1}{2}}-5s'\ ^2D_{1\frac{1}{2}}$
*	1894.259	.282	75	8			52791.1	$4p'\ ^2D^\circ_{2\frac{1}{2}}-5s''\ ^2D_{2\frac{1}{2}}$
4	1872.128		100		10W		53415.2	
	1867.994	.968	40				53533.4	$4p'\ ^4D^\circ_{2\frac{1}{2}}-5s'\ ^2D_{1\frac{1}{2}}$
*	1866.366	.390	10				53580.1	$4p'\ ^2D^\circ_{1\frac{1}{2}}-5s''\ ^2D_{2\frac{1}{2}}$
4	1866.077		100	1	7WW		53588.	
4	1864.117		100		15WW		53644.7	
	1857.274	.279	5				53842.4	$4p'\ ^4F^\circ_{1\frac{1}{2}}-5s'\ ^4D_{2\frac{1}{2}}$
	1850.140	.146	10	6			54050.0	$4p'\ ^4F^\circ_{2\frac{1}{2}}-5s'\ ^4D_{3\frac{1}{2}}$
*	1847.562	.568	75	5			54125.4	$4p'\ ^2P^\circ_{1\frac{1}{2}}-5s''\ ^2D_{2\frac{1}{2}}$
1	1836.654	.653	75	15	4	30	54446.84	$4s^2\ ^2D_{1\frac{1}{2}}-6p\ ^2P^\circ_{\frac{1}{2}}$
4	1836.007	.008	70	15	40	2	54466.0	$4p'\ ^4F^\circ_{3\frac{1}{2}}-5s'\ ^4D_{3\frac{1}{2}}$
2	1834.268	.267	40	12	1	1	54517.66	$4s^2\ ^2D_{1\frac{1}{2}}-6p\ ^2P^\circ_{1\frac{1}{2}}$
4 *	1833.573	.567	}		{150	50	54538.3	$4p'\ ^4F^\circ_{4\frac{1}{2}}-5s'\ ^4D_{3\frac{1}{2}}$
3	1833.481	{ .485	} 100	25R	{			{ $4s^2\ ^2D_{2\frac{1}{2}}-4f\ ^2F^\circ_{3\frac{1}{2}}$
		{ .465	}		{ 25	40	54541.06	{ $4s^2\ ^2D_{2\frac{1}{2}}-4f\ ^2F^\circ_{2\frac{1}{2}}$
	1831.376	.341	80				54603.8	$4p'\ ^2F^\circ_{2\frac{1}{2}}-5s'\ ^2D_{1\frac{1}{2}}$
4	1816.479		80		1W		55051.6	
	1813.170	.159	1				55152.0	$4p'\ ^2D^\circ_{2\frac{1}{2}}-4_{2\frac{1}{2}}$
4 *	1811.105	.112			15W		55214.9	$4p'\ ^2F^\circ_{3\frac{1}{2}}-5s''\ ^2D_{2\frac{1}{2}}$
4	1811.008	.014			80W		55217.9	$4p'\ ^4F^\circ_{3\frac{1}{2}}-5s'\ ^4D_{2\frac{1}{2}}$
4	1797.643	.643	100		20W		55628.4	$4p'\ ^4F^\circ_{2\frac{1}{2}}-5s'\ ^4D_{1\frac{1}{2}}$
	1796.701		15	5			55657.6	
	1795.160		5				55705.3	
4	1790.759	.760	80	1H	15		55842.2	$4p'\ ^4F^\circ_{1\frac{1}{2}}-5s'\ ^4D_{1\frac{1}{2}}$
*	1789.509	.504	8				55881.3	$4p'\ ^4D^\circ_{2\frac{1}{2}}-5s''\ ^2D_{2\frac{1}{2}}$
	1787.384	.358	00				55947.7	$4p'\ ^2P^\circ_{1\frac{1}{2}}-3_{2\frac{1}{2}}$
	1775.024	.012	3	1H			56337.3	$4p'\ ^2D^\circ_{2\frac{1}{2}}-6_{2\frac{1}{2}}$
	1774.040	.050	75				56368.5	$4p'\ ^4P^\circ_{1\frac{1}{2}}-5s'\ ^4D_{1\frac{1}{2}}$
	1762.395	.400	25	5			56741.0	$4p'\ ^2F^\circ_{3\frac{1}{2}}-1_{3\frac{1}{2}}$

TABLE 1. Zn II *spectrum below 2570 Å*—Continued

Notes	λ(vac), Å		Intensity				σ, cm^{-1}	Classification
	obs.	calc.	E_1	E_2	S_1	S_2, S_3	obs.	
4	1762.243				10	1	56745.9	
4d	1762.223		80	2H	10		56746.5	
4	1762.191	.195			10		56747.5	$4p'\ ^4P^\circ_{1\frac{1}{2}}-5s'\ ^4D_{2\frac{1}{2}}$
4	1762.151				20	2	56748.8	
	1756.665		2	3			56926.1	
*	1755.847	.862	10				56952.6	$4p'\ ^2F^\circ_{2\frac{1}{2}}-5s''\ ^2D_{2\frac{1}{2}}$
	1752.358	.373	3	0			57066.0	$4p'\ ^2D^\circ_{1\frac{1}{2}}-5_{\frac{1}{2}}$
	1751.806			5			57083.9	
1	1747.124	.125	75	25R	80	80	57236.92	$4s^2\ ^2D_{2\frac{1}{2}}-6p\ ^2P^\circ_{1\frac{1}{2}}$
	1742.285		20	5			57395.9	
	1741.930	.933	18	12			57407.6	$4p'\ ^4D^\circ_{3\frac{1}{2}}-1_{3\frac{1}{2}}$
4	1737.895	.882	50	3	40		57540.9	$4p'\ ^4P^\circ_{1\frac{1}{2}}-5s'\ ^4D_{1\frac{1}{2}}$
	1736.889	.886	60				57574.2	$4p'\ ^4P^\circ_{1\frac{1}{2}}-5s'\ ^4D_{1\frac{1}{2}}$
	1736.825	.817		0H			57576.3	$4p'\ ^2F^\circ_{3\frac{1}{2}}-4_{2\frac{1}{2}}$
4	1735.607	.605	80	20R	80	40	57616.7	$4p'\ ^4P^\circ_{2\frac{1}{2}}-5s'\ ^4D_{3\frac{1}{2}}$
		.581						$4p'\ ^2P^\circ_{1\frac{1}{2}}-5_{1\frac{1}{2}}$
	1732.953	.961	25				57705.0	$4p'\ ^4D^\circ_{2\frac{1}{2}}-3_{2\frac{1}{2}}$
	1730.619	.626	2	0H			57782.8	$4p'\ ^2D^\circ_{1\frac{1}{2}}-8_{1\frac{1}{2}}$
	1724.364	.376	2				57992.4	$4p'\ ^4D^\circ_{1\frac{1}{2}}-4_{2\frac{1}{2}}$
	1723.901	.885	2				58008.0	$4p'\ ^4F^\circ_{2\frac{1}{2}}-5s'\ ^2D_{1\frac{1}{2}}$
	1719.136	.124	2				58168.8	$4p'\ ^2D^\circ_{2\frac{1}{2}}-12_{3\frac{1}{2}}$
	1718.182	.173	1				58201.1	$4p'\ ^2D^\circ_{2\frac{1}{2}}-13_{2\frac{1}{2}}$
	1716.935	.936	1				58243.3	$4p'\ ^4D^\circ_{2\frac{1}{2}}-4_{2\frac{1}{2}}$
			E_1	E_2	S_3			
4	1715.760	.757	60	12	5		58283.2	$4p'\ ^4D^\circ_{3\frac{1}{2}}-1_{3\frac{1}{2}}$
	1715.388	.370	1	0			58295.8	$4p'\ ^2D^\circ_{1\frac{1}{2}}-11_{2\frac{1}{2}}$
	1714.457	.431	15	1H			58327.5	$4p'\ ^2P^\circ_{1\frac{1}{2}}-8_{1\frac{1}{2}}$
	1714.270	.246		0			58333.9	$4p'\ ^2P^\circ_{\frac{1}{2}}-8_{1\frac{1}{2}}$
	1713.251	.253	50	00			58368.6	$4p'\ ^4P^\circ_{2\frac{1}{2}}-5s'\ ^4D_{2\frac{1}{2}}$
b	1710.052	.039	10	1			58477.8	$4p'\ ^2F^\circ_{2\frac{1}{2}}-1_{3\frac{1}{2}}$
	1709.243	.231		0			58505.4	$4p'\ ^2D^\circ_{2\frac{1}{2}}-14_{2\frac{1}{2}}$
b	1707.191	.195	20				58575.8	$4p'\ ^4D^\circ_{\frac{1}{2}}-5_{1\frac{1}{2}}$
	1704.577	.550	00				58665.6	$4p'\ ^2P^\circ_{1\frac{1}{2}}-9_{2\frac{1}{2}}$
e*	1702.836	.820?	2	00			58725.6	$4p'\ ^2D^\circ_{2\frac{1}{2}}-20_{2\frac{1}{2}}$?
b	1702.210	.203	10				58747.2	$4p'\ ^4P^\circ_{1\frac{1}{2}}-5s'\ ^4D_{1\frac{1}{2}}$
		.177						$4p'\ ^4P^\circ_{1\frac{1}{2}}-5s'\ ^2D_{1\frac{1}{2}}$
	1701.766	.783	12	0			58762.5	$4p'\ ^4F^\circ_{3\frac{1}{2}}-6_{2\frac{1}{2}}$
	1701.398	.392	4				58775.2	$4p'\ ^2F^\circ_{2\frac{1}{2}}-3_{2\frac{1}{2}}$
	1699.471	.458	3				58841.8	$4p'\ ^2P^\circ_{1\frac{1}{2}}-11_{2\frac{1}{2}}$
	1691.592	.584	1				59115.9	$4p'\ ^2D^\circ_{1\frac{1}{2}}-5_{1\frac{1}{2}}$
	1691.470	.501	1				59120.2	$4p'\ ^4D^\circ_{3\frac{1}{2}}-4_{2\frac{1}{2}}$
b	1689.818	.837	25	2			59178.0	$4p'\ ^4D^\circ_{1\frac{1}{2}}-6_{2\frac{1}{2}}$
b	1688.240	.240	15	5			59233.3	$4p'\ ^2F^\circ_{3\frac{1}{2}}-7_{3\frac{1}{2}}$
	1686.502	.489	25				59294.3	$4p'\ ^2D^\circ_{1\frac{1}{2}}-14_{2\frac{1}{2}}$
	1685.942	.943	5				59314.0	$4p'\ ^2F^\circ_{2\frac{1}{2}}-4_{2\frac{1}{2}}$

TABLE 1. Zn II *spectrum below 2570 Å*—Continued

Notes	λ(vac), Å		Intensity				σ, cm⁻¹	Classification
	obs.	calc.	E_1	E_2	S_3	---	obs.	
	1682.698	.692	5				59428.4	$4p'\ ^2D^\circ_{2\frac{1}{2}} - 6_{2\frac{1}{2}}$
	1679.667	.653	5	1			59535.6	$4p'\ ^2P^\circ_{1\frac{1}{2}} - 13_{2\frac{1}{2}}$
	1671.313	.310	20				59833.2	$4p'\ ^4D^\circ_{1\frac{1}{2}} - 8_{1\frac{1}{2}}$
	1669.453	.449	2				59899.9	$4p'\ ^4D^\circ_{2\frac{1}{2}} - 7_{3\frac{1}{2}}$
	1668.585	.563	1				59931.0	$4p'\ ^2F^\circ_{3\frac{1}{2}} - 11_{2\frac{1}{2}}$
	1667.911	.934	5	00			59955.2	$4p'\ ^4P^\circ_{1\frac{1}{2}} - 5s'\ ^2D_{1\frac{1}{2}}$
f	1664.326	.320					60084.4	$4p'\ ^4D^\circ_{2\frac{1}{2}} - 8_{1\frac{1}{2}}$
4	1658.251	.254	60		4		60304.5	$4p'\ ^4D^\circ_{3\frac{1}{2}} - 6_{2\frac{1}{2}}$
	1655.020	.007	30				60422.2	$4p'\ ^4D^\circ_{2\frac{1}{2}} - 9_{2\frac{1}{2}}$
f	1652.931	.912					60498.6	$4p'\ ^2F^\circ_{2\frac{1}{2}} - 6_{2\frac{1}{2}}$
4	1650.208	.206	20		6		60598.4	$4p'\ ^4D^\circ_{2\frac{1}{2}} - 11_{2\frac{1}{2}}$
4	1645.386	.392	50		60		60776.0	$4p'\ ^4D^\circ_{3\frac{1}{2}} - 7_{3\frac{1}{2}}$
	1641.257	.225	2				60928.9	$4p'\ ^2F^\circ_{3\frac{1}{2}} - 14_{2\frac{1}{2}}$
4	1638.242	.243	20		3		61041.0	$4p'\ ^4D^\circ_{1\frac{1}{2}} - 13_{2\frac{1}{2}}$
*	1635.277	.264	20				61151.7	$4p'\ ^2F^\circ_{3\frac{1}{2}} - 21_{4\frac{1}{2}}$
	1635.180	.181	20	3			61155.3	$4p'\ ^2F^\circ_{2\frac{1}{2}} - 8_{1\frac{1}{2}}$
	1632.390	.384	15				61259.9	$4p'\ ^4D^\circ_{2\frac{1}{2}} - 12_{3\frac{1}{2}}$
4	1631.534	.526	12	3	8		61292.0	$4p'\ ^4D^\circ_{2\frac{1}{2}} - 13_{2\frac{1}{2}}$
	1631.364	.393 .361	20				61298.4	$4p'\ ^4P^\circ_{2\frac{1}{2}} - 5s'\ ^2D_{2\frac{1}{2}}$ $4p'\ ^4D^\circ_{3\frac{1}{2}} - 9_{2\frac{1}{2}}$
4	1630.114	.111	25		5		61345.4	$4p'\ ^4D^\circ_{1\frac{1}{2}} - 14_{2\frac{1}{2}}$
	1626.200	.191	3				61493.1	$4p'\ ^2F^\circ_{2\frac{1}{2}} - 9_{2\frac{1}{2}}$
	1624.020	.022	30				61575.6	$4p'\ ^4P^\circ_{2\frac{1}{2}} - 5s'\ ^2D_{1\frac{1}{2}}$
	1623.479	.461	40	1			61596.1	$4p'\ ^4D^\circ_{2\frac{1}{2}} - 14_{2\frac{1}{2}}$
	1621.552	.555	40				61669.3	$4p'\ ^2F^\circ_{2\frac{1}{2}} - 11_{2\frac{1}{2}}$
3	1618.968	.968	40	1	15		61767.74	$4s^2\ ^2D_{1\frac{1}{2}} - 5f\ ^2F^\circ_{2\frac{1}{2}}$
4e *	1617.675	.675?	60		40		61817.1	$4p'\ ^4D^\circ_{2\frac{1}{2}} - 20_{2\frac{1}{2}}$?
	1615.949	.981	3	1			61883.1	$4p'\ ^4F^\circ_{2\frac{1}{2}} - 1_{3\frac{1}{2}}$
4d	1614.364		40	1	10		61943.9	
4	1611.866		50	8R	25		62039.9	
	1609.390	.376	25	5R			62135.3	$4p'\ ^4D^\circ_{3\frac{1}{2}} - 12_{3\frac{1}{2}}$
4	1608.819		40	15R	70		62157.4	
	1608.555	.542	10				62167.6	$4p'\ ^4D^\circ_{3\frac{1}{2}} - 13_{2\frac{1}{2}}$
4	1606.082		25	12R	60		62263.3	
	1605.196	.185	8	5R			62297.7	$4p'\ ^4F^\circ_{3\frac{1}{2}} - 1_{3\frac{1}{2}}$
	1604.347	.343	15				62330.7	$4p'\ ^2F^\circ_{2\frac{1}{2}} - 12_{3\frac{1}{2}}$
4	1603.508	.515	30	0	3		62363.3	$4p'\ ^2F^\circ_{2\frac{1}{2}} - 13_{2\frac{1}{2}}$
4 *	1603.315	.320	30	15R	100		62370.8	$4p'\ ^4F^\circ_{4\frac{1}{2}} - 1_{3\frac{1}{2}}$
g *	1597.801	.859?	40	5R	5		62586.0	$4p''\ ^2F^\circ_{3\frac{1}{2}} - 6s'\ ^2D_{2\frac{1}{2}}$?
4	1597.556	.564	50	5R	15W		62595.6	$4p'\ ^4F^\circ_{3\frac{1}{2}} - 3_{2\frac{1}{2}}$
	1596.076		10				62653.7	
4	1595.732	.723	30	8R	20		62667.2	$4p'\ ^2F^\circ_{2\frac{1}{2}} - 14_{2\frac{1}{2}}$
4 *	1595.027	.031	40	10R	100		62694.9	$4p'\ ^4D^\circ_{3\frac{1}{2}} - 21_{4\frac{1}{2}}$
f	1594.448	.446					62717.6	$4p'\ ^4F^\circ_{2\frac{1}{2}} - 4_{2\frac{1}{2}}$
4 *	1590.133	.134?	25	10R	25		62887.8	$4p'\ ^2F^\circ_{2\frac{1}{2}} - 20_{2\frac{1}{2}}$?
2	1589.777	./80	30	10R	50		62901.90	$4s^2\ ^2D_{1\frac{1}{2}} - 7p\ ^2P^\circ_{1\frac{1}{2}}$
	1588.754	.721		3R			62942.4	$4p'\ ^4F^\circ_{1\frac{1}{2}} - 6_{2\frac{1}{2}}$
3	1585.368	×	25	15R	100		63076.84	$4s^2\ ^2D_{1\frac{1}{2}} - 7p\ ^2P^\circ_{\frac{1}{2}}$
	1583.933	.935	15				63134.0	$4p'\ ^4F^\circ_{3\frac{1}{2}} - 4_{2\frac{1}{2}}$
	1575.810		10				63459.4	
4	1572.991		90	8R	40WW		63573.2	
*	1564.369	.387	6	3			63923.5	$4p'\ ^4P^\circ_{2\frac{1}{2}} - 5s''\ ^2D_{2\frac{1}{2}}$
4	1559.466	.454	20	2R	10W		64124.5	$4p'\ ^4P^\circ_{1\frac{1}{2}} - 3_{2\frac{1}{2}}$
3	1555.764		25	12R	100		64277.10	
4	1554.740	.746	20		6		64319.4	$4p'\ ^4F^\circ_{3\frac{1}{2}} - 6_{2\frac{1}{2}}$
4	1554.225		15	1	6		64340.7	

TABLE 1. Zn II *spectrum below 2570 Å*—Continued

Notes	λ(vac), Å		Intensity				σ, cm⁻¹	Classification
	obs.	calc.	E_1	E_2	S_3	---	obs.	
3	1550.936	.937	25	10R	80		64477.19	$4s^2\ ^2D_{2½}-5f\ ^2F°_{3½}$
4	1548.957	.971	15		3W		64559.6	$4p'\ ^4F°_{2½}-8_{1½}$
4	1548.434	.426	20	5R	20		64581.4	$4p'\ ^4P°_{1½}-5_{1½}$
4	1547.800		20	5R	20		64607.8	
4	1546.650		25	12R	100		64655.9	
4	1546.460	.465	20	10R	10		64663.8	$4p'\ ^4P°_{1½}-4_{2½}$
4	1545.087		20	8R	2		64721.3	
4	1544.922		25	15R	50		64728.2	
4	1543.428	.434	25	10R	40		64790.8	$4p'\ ^4F°_{3½}-7_{3½}$
4	1543.037	.034	25	10R	50		64807.3	$4p'\ ^4F°_{1½}-13_{2½}$
4	1542.531		20	10R	2WW		64828.5	
4 *	1541.707	.709	30	12R	40		64863.2	$4p'\ ^4F°_{4½}-7_{3½}$
4	1540.895	.901	35	15R	80		64897.3	$4p'\ ^4F°_{2½}-9_{2½}$
2	1540.120	.122	30	10R	50		64930.01	$4s^2\ ^2D_{1½}-4p''\ ^2P°_{1½}$
4	1536.726	.738	25	10R	20		65073.4	$4p'\ ^4F°_{2½}-11_{2½}$
4	1535.823	.818	30	15R	30		65111.7	$4p'\ ^4F°_{1½}-14_{2½}$
1	1535.081	.085	40	40R	200		65143.14	$4p\ ^2P°_{1½}-6s\ ^2S_{1½}$
4	1531.394	.422	25	8R	3W		65300.0	$4p'\ ^4P°_{1½}-8_{1½}$
4	1531.088	.082	30	8R	30		65313.0	$4p'\ ^4F°_{3½}-9_{2½}$
*	1530.620	.639?	25				65333.0	$4p'\ ^4F°_{1½}-20_{2½}$?
4	1528.759		25	5R	9		65412.5	
4	1528.550		30	10R	40		65421.5	
4	1527.915	.910	30	15R	100		65448.7	$4p'\ ^4P°_{2½}-1_{3½}$
	1527.236		20	10R			65477.8	
	1527.125		25	10R			65482.5	
4	1526.969	.972	30	10R	15		65489.2	$4p'\ ^4F°_{3½}-11_{2½}$
1	1523.903	.903	40	30R	150		65620.97	$4s^2\ ^2D_{2½}-7p\ ^2P°_{1½}$
4	1521.276	.271	50	8R	40		65734.3	$4p'\ ^4F°_{2½}-12_{3½}$
4	1520.998	1.003	40	8R	15		65746.3	$4p'\ ^4P°_{2½}-3_{2½}$
4	1520.527	.526	40	10R	50		65766.7	$4p'\ ^4F°_{2½}-13_{2½}$
	1520.022	.039	25				65788.5	$4p'\ ^4P°_{1½}-5_{1½}$
4	1518.631	.628	30		3		65848.8	$4p'\ ^4P°_{1½}-6_{2½}$
1	1514.763	.761	50	15R	120		66016.93	$4p\ ^2P°_{1½}-6s\ ^2S_{1½}$
4	1514.479		30	8R	25		66029.3	
4	1513.522	.519	20	8R	20		66071.1	$4p'\ ^4F°_{2½}-14_{2½}$
4	1511.718		{ 30	8R	15		66149.9	
4	1511.694	.700			12		66151.0	$4p'\ ^4F°_{3½}-12_{3½}$
2	1510.363	.362	40	15R	150		66209.25	$4s^2\ ^2D_{1½}-4p''\ ^2D°_{2½}$
*	1510.045	.045	5				66223.2	$4p'\ ^4F°_{4½}-12_{3½}$
4	1508.645	.644	40	8R	70		66284.6	$4p'\ ^4P°_{2½}-4_{2½}$
4	1504.034	.044	5		5		66487.9	$4p'\ ^4F°_{3½}-14_{2½}$
4	1503.653	.649	35	5R	25		66504.7	$4p'\ ^4P°_{1½}-8_{1½}$
4h	1503.109		30	5R	20		66528.8	
4e, i*	1499.077	.077?	{ 5		{ 20		66707.7	$4p'\ ^4F°_{3½}-20_{2½}$?
4i *	1499.052	.037					66708.8	$4p'\ ^4F°_{3½}-21_{4½}$
4 *	1497.410	.410	40	8R	80		66782.0	$4p'\ ^4F°_{4½}-21_{4½}$
	1496.001	.043	5	1			66844.9	$4p'\ ^4P°_{1½}-9_{2½}$
1 *	1493.133	×	40	25R	300		66973.27	$4s^2\ ^2D_{1½}-8p\ ^2P°_{½}$
4	1492.121	.119	25		30		67018.7	$4p'\ ^4P°_{1½}-11_{2½}$
2	1488.926	.927	10	10R	120		67162.50	$4s^2\ ^2D_{1½}-6f\ ^2F°_{2½}$
1	1486.065	×	40	40R	700		67291.81	$4s^2\ ^2D_{2½}-4p''\ ^2F°_{3½}$
4	1482.139	.140	30	10R	80		67470.1	$4p'\ ^4P°_{2½}-6_{2½}$
1	1478.216	.216	50	30R	300		67649.11	$4s^2\ ^2D_{2½}-4p''\ ^2P°_{1½}$
1	1477.016	.015	60	30R	400		67704.07	$4s^2\ ^2D_{1½}-4p''\ ^2F°_{2½}$
4	1471.862	.857	30	8R	50		67941.2	$4p'\ ^4P°_{2½}-7_{3½}$

367-409 OL-70—2

TABLE 1. Zn II *spectrum below 2570 Å*—Continued

Notes	λ(vac), Å		Intensity				σ, cm^{-1}	Classification
	obs.	calc.	E_1	E_2	S_3	---	obs.	
	1470.222	.218	2				68016.9	$4p'\ ^4P^\circ_{1\frac{1}{2}}-14_{2\frac{1}{2}}$
4	1467.867	.868	25		4		68126.1	$4p'\ ^4P^\circ_{2\frac{1}{2}}-8_{1\frac{1}{2}}$
4 *	1466.697	.696	30	5R	15		68180.4	$4s^2\ ^2D_{1\frac{1}{2}}-8p\ ^2P^\circ_{1\frac{1}{2}}$
1	1462.743	×	50	15R	150		68364.71	$4s^2\ ^2D_{1\frac{1}{2}}-4p''\ ^2P^\circ_{1/2}$
	1460.616	.620	12				68464.3	$4p'\ ^4P^\circ_{2\frac{1}{2}}-9_{2\frac{1}{2}}$
1	1457.422	.423	40	8R	100		68614.31	$4p\ ^2P^\circ_{1\frac{1}{2}}-5d\ ^2D_{1\frac{1}{2}}$
1	1456.907	×	50	10R	500		68638.56	$4p\ ^2P^\circ_{1\frac{1}{2}}-5d\ ^2D_{2\frac{1}{2}}$
1	1450.778	.779	50	30R	700		68928.53	$4s^2\ ^2D_{2\frac{1}{2}}-4P''\ ^2D^\circ_{2\frac{1}{2}}$
1	1445.042	×	60	30R	700		69202.14	$4s^2\ ^2D_{1\frac{1}{2}}-4p''\ ^2D^\circ_{1\frac{1}{2}}$
	1442.962	.970	5				69301.9	$4p'\ ^4P^\circ_{2\frac{1}{2}}-12_{3\frac{1}{2}}$
1	1439.091	.091	60	30R	500		69488.31	$4p\ ^2P^\circ_{\frac{1}{2}}-5d\ ^2D_{1\frac{1}{2}}$
1	1430.992	.991	50	25R	150		69881.59	$4s^2\ ^2D_{2\frac{1}{2}}-6f\ ^2F^\circ_{2\frac{1}{2}}$
4	1430.285	.268	10		15		69916.1	$4s^2\ ^2D_{2\frac{1}{2}}-6f\ ^2F^\circ_{3\frac{1}{2}}$
2	1419.982	.984	50	25R	200		70423.43	$4s^2\ ^2D_{2\frac{1}{2}}-4p''\ ^2F^\circ_{2\frac{1}{2}}$
*	1419.416	.427	3	3R			70451.5	$4s^2\ ^2D_{1\frac{1}{2}}-7f\ ^2F^\circ_{2\frac{1}{2}}$
3 *	1410.443	×	60	15R	100		70899.71	$4s^2\ ^2D_{2\frac{1}{2}}-8p\ ^2P^\circ_{1\frac{1}{2}}$
4j *	1407.259				7		71060.1	
4j	1407.215		50	5R	3		71062.3	
4j *	1407.189	×			2		71063.7	$4s^2\ ^2D_{1\frac{1}{2}}-9p\ ^2P^\circ_{1\frac{1}{2}}$?
	1390.372	.408	40	5R			71923.2	$4s^2\ ^2D_{2\frac{1}{2}}-4p''\ ^2D^\circ_{1\frac{1}{2}}$
b	1366.682	.728 .678	60	20R			73169.9	$4s^2\ ^2D_{2\frac{1}{2}}-7f\ ^2F^\circ_{3\frac{1}{2}}$ $4s^2\ ^2D_{2\frac{1}{2}}-7f\ ^2F^\circ_{2\frac{1}{2}}$
*	1355.332	.328?	25				73782.7	$4s^2\ ^2D_{2\frac{1}{2}}-9p\ ^2P^\circ_{1\frac{1}{2}}$?
	1323.909		30				75533.9	
	1309.521	.517		1			76363.8	$4p'\ ^2D^\circ_{2\frac{1}{2}}-6s'\ ^4D_{3\frac{1}{2}}$
	1306.741	.763	5				76526.3	$4p\ ^2P^\circ_{1\frac{1}{2}}-7s\ ^2S_{1/2}$
	1277.523	.538	40	10R			78276.5	$4p\ ^2P^\circ_{1\frac{1}{2}}-6d\ ^2D_{1\frac{1}{2}}$
	1277.306	.324	60				78289.8	$4p\ ^2P^\circ_{1\frac{1}{2}}-6d\ ^2D_{2\frac{1}{2}}$
	1265.065						79047.3	
	1263.412	.430	40	15R			79150.7	$4p\ ^2P^\circ_{\frac{1}{2}}-6d\ ^2D_{1\frac{1}{2}}$
	1258.581	.574	00				79454.6	$4p'\ ^4D^\circ_{2\frac{1}{2}}-6s'\ ^4D_{3\frac{1}{2}}$
	1244.848	.852	2	3			80331.1	$4p'\ ^4D^\circ_{3\frac{1}{2}}-6s'\ ^4D_{3\frac{1}{2}}$
	1241.874	.840		0			80523.5	$4p'\ ^2F^\circ_{2\frac{1}{2}}-6s'\ ^4D_{3\frac{1}{2}}$
	1240.625	.638?	3				80604.5	$4p'\ ^4D^\circ_{1\frac{1}{2}}-6s'\ ^2D_{2\frac{1}{2}}$?
	1211.841	.800	25	5R			82519.1	$4p\ ^2P^\circ_{1\frac{1}{2}}-8s\ ^2S_{1/2}$
	1206.525		30	15R			82882.6	
	1197.149	.126	40	10R			83531.8	$4p\ ^2P^\circ_{1\frac{1}{2}}-7d\ ^2D_{2\frac{1}{2}}$
	1193.231		60	20R			83806.1	
	1192.961						83825.0	
	1185.610	.598	1				84344.8	$4p'\ ^4F^\circ_{3\frac{1}{2}}-6s'\ ^4D_{3\frac{1}{2}}$
	1184.858	.840	40				84398.3	$4p\ ^2P^\circ_{1\frac{1}{2}}-7d\ ^2D_{1\frac{1}{2}}$
*	1184.528	.580	8				84421.8	$4p'\ ^4F^\circ_{4\frac{1}{2}}-6s'\ ^4D_{3\frac{1}{2}}$
	1183.488		2				84496.0	
	1171.943	.929?	1	5			85328.4	$4p'\ ^4F^\circ_{2\frac{1}{2}}-6s'\ ^2D_{2\frac{1}{2}}$?
	1153.398	.379	25	5			86700.3	$4p\ ^2P^\circ_{1\frac{1}{2}}-8d\ ^2D_{2\frac{1}{2}}$
	1152.139		4	5			86795.1	
	1142.904	.904	1				87496.4	$4p'\ ^4P^\circ_{2\frac{1}{2}}-6s'\ ^4D_{3\frac{1}{2}}$
	1141.955	.932	20	5H			87569.1	$4p\ ^2P^\circ_{1/2}-8d\ ^2D_{1\frac{1}{2}}$
	1138.524						87833.0	
	1126.611	.602	8	2H			88761.8	$4p\ ^2P^\circ_{1\frac{1}{2}}-9d\ ^2D_{2\frac{1}{2}}$
	1115.657	.660	15	8H			89633.3	$4p\ ^2P^\circ_{\frac{1}{2}}-9d\ ^2D_{1\frac{1}{2}}$
	986.516	.525	12	8			101366.8	$4s\ ^2S_{1/2}-5p\ ^2P^\circ_{\frac{1}{2}}$
	984.139	.142	20	10			101611.7	$4s\ ^2S_{1/2}-5p\ ^2P^\circ_{1\frac{1}{2}}$
	971.699			2			102912.5	
	949.455	.462	5	10			105323.6	$4s\ ^2S_{1/2}-4p'\ ^4P^\circ_{1\frac{1}{2}}$

TABLE 1. Zn II *spectrum below 2570 Å*—Continued

Notes	λ(vac), Å		Intensity			σ, cm^{-1}	Classification
	obs.	calc.	E_1	E_2	---	obs.	
f	938.719	.713				106528.2	$4s\ ^2S_{1/2}-4p'\ ^4P^o_{1/2}$
f	923.969	.976				108228.7	$4s\ ^2S_{1/2}-4p'\ ^4F^o_{1\frac{1}{2}}$
	892.914	.903	2	10		111992.9	$4s\ ^2S_{1/2}-4p'\ ^4D^o_{1\frac{1}{2}}$
f	888.620	.613				112534.0	$4s\ ^2S_{1/2}-4p'\ ^4D^o_{1/2}$
	881.060	.064	1	15		113499.6	$4s\ ^2S_{1/2}-4p'\ ^2P^o_{1\frac{1}{2}}$
	833.600	.616		1H		119961.6	$4s\ ^2S_{1/2}-6p\ ^2P^o_{1\frac{1}{2}}$
	779.163	.159	6	10		128342.9	$4s\ ^2S_{1/2}-7p\ ^2P^o_{1\frac{1}{2}}$
	778.112	.098	2	5		128516.2	$4s\ ^2S_{1/2}-7p\ ^2P^o_{1/2}$
	767.050	.038	7	5		130369.6	$4s\ ^2S_{1/2}-4p''\ ^2P^o_{1\frac{1}{2}}$
*	755.223	.202	4	5		132411.2	$4s\ ^2S_{1/2}-8p\ ^2P^o_{1/2}$
	747.358	.349	3	5		133804.7	$4s\ ^2S_{1/2}-4p''\ ^2P^o_{3/2}$
	742.720	.700	1	3		134640.2	$4s\ ^2S_{1/2}-4p''\ ^2D^o_{1\frac{1}{2}}$
*	732.605	.572?	00	1		136499.2	$4s\ ^2S_{1/2}-9p\ ^2P^o_{1\frac{1}{2}}$?

[a] A Zn I line also at this position belongs to a multiplet having negligible intensity in E_1. (In the region above 2400 Å, E_1 corresponds to I_4 in [9].)

[b] Given in [1] or [9] as blend of Zn II and Zn III transitions. This explains an anomalously strong intensity in E_2 for three autoionizing Zn II lines.

[c] Either a blend or the classification is incorrect. The indicated Zn II transition should not be observed in E_2.

[III] Zn III line now resolved from nearby Zn II line.

[d] Line belongs to either Zn II or Zn III. The close group at 1762.2 Å has three resolved lines; our interpretation of measurements from three exposures (S_1, S_2, and S_3) is that the group comprises four different lines.

[e] Line assigned to Zn II only on the basis of a questionable classification.

[f] Weak line from spark exposure I_3 [9]. (Intensities from this source are not listed here.)

[g] Wavelength from [1]; line is blended with a ghost on S_3 plate.

[h] Line is given as blend of Zn IV and Zn II in [1]; the new wavelength is entirely due to an unclassified Zn II transition.

[i] The E_1 intensity appears to be too low.

[j] Interpretation of group not certain. There appear to be three lines, as given, with a possibility that the strongest (1407.259 Å) is either double or self-reversed.

TABLE 2. *Energy levels of* Zn II

All positions were redetermined in this investigation. The authorities for all except a few new levels are listed by Crooker and Dick [1], who also suggest that the numbered high even levels belong mainly to the $3d^9 4s4d$ configuration.

Configuration	Designation	J	Level (cm^{-1})
Even levels			
$3d^{10}4s$	$4s\ ^2S$	$\frac{1}{2}$	0.00
$3d^9 4s^2$	$4s^2\ ^2D$	$2\frac{1}{2}$	62722.45
		$1\frac{1}{2}$	65441.64
$3d^{10}5s$	$5s\ ^2S$	$\frac{1}{2}$	88437.15
$3d^{10}4d$	$4d\ ^2D$	$1\frac{1}{2}$	96909.74
		$2\frac{1}{2}$	96960.40
$3d^{10}6s$	$6s\ ^2S$	$\frac{1}{2}$	114498.02
$3d^{10}5d$	$5d\ ^2D$	$1\frac{1}{2}$	117969.32
		$2\frac{1}{2}$	117993.61
$3d^{10}7s$	$7s\ ^2S$	$\frac{1}{2}$	125880.0
$3d^{10}5g$	$5g\ ^2G$	$4\frac{1}{2}$	127310.8
		$3\frac{1}{2}$	127310.9
$3d^{10}6d$	$6d\ ^2D$	$1\frac{1}{2}$	127630.6
		$2\frac{1}{2}$	127643.7
$3d^{10}8s$	$8s\ ^2S$	$\frac{1}{2}$	131876.9
$3d^{10}6g$	$6g\ ^2G$	$3\frac{1}{2}, 4\frac{1}{2}$	132683.9
$3d^{10}7d$	$7d\ ^2D$	$1\frac{1}{2}$	132880.6
		$2\frac{1}{2}$	132888.4
$3d^{10}9s$	$9s\ ^2S$	$\frac{1}{2}$	135423.3
$3d^{10}7g$	$7g\ ^2G$	$3\frac{1}{2}, 4\frac{1}{2}$	135923.8
$3d^{10}8d$	$8d\ ^2D$	$1\frac{1}{2}$	136051.9
		$2\frac{1}{2}$	136056.8
$3d^{10}9d$	$9d\ ^2D$	$1\frac{1}{2}$	138114.0
		$2\frac{1}{2}$	138117.5
Zn III $3d^{10}\ ^1S_0$	Limit		144892.6
$3d^9 4s(^3D)5s$	$5s'\ ^4D$	$3\frac{1}{2}$	161318.4
		$2\frac{1}{2}$	162070.3
		$1\frac{1}{2}$	162897.0
		$\frac{1}{2}$	164070.1
$3d^9 4s(^3D)5s$	$5s'\ ^2D$	$2\frac{1}{2}$	[a] 164998.9
		$1\frac{1}{2}$	165277.1
$3d^9 4s(^1D)5s$	$5s''\ ^2D$	$2\frac{1}{2}$	[a] 167624.4
	1	$3\frac{1}{2}$	[b] 169150.5
	3	$2\frac{1}{2}$	169447.7
	4	$2\frac{1}{2}$	169986.3
	5	$\frac{1}{2}$	171110.5
	6	$2\frac{1}{2}$	171171.6
	7	$3\frac{1}{2}$	[b] 171643.0
	8	$1\frac{1}{2}$	171827.6
	9	$2\frac{1}{2}$	172165.7
	11	$2\frac{1}{2}$	172341.5
	12	$3\frac{1}{2}$	173003.1
	13	$2\frac{1}{2}$	173035.3
	14	$2\frac{1}{2}$	173339.8
	20	$2\frac{1}{2}$?	[c] 173560.7?
	21	$4\frac{1}{2}$	[a] 173561.9
$3d^9 4s(^3D)6s$	$6s'\ ^4D$	$3\frac{1}{2}$	191198.0
$3d^9 4s(^3D)6s$	$6s'\ ^2D$	$2\frac{1}{2}$	[b] 192598. ?
Odd levels			
$3d^{10}4p$	$4p\ ^2P^\circ$	$\frac{1}{2}$	48481.00
		$1\frac{1}{2}$	49355.04
$3d^{10}5p$	$5p\ ^2P^\circ$	$\frac{1}{2}$	101365.9
		$1\frac{1}{2}$	101611.4
$3d^9(^2D)4s4p(^3P^\circ)$	$4p'\ ^4P^\circ$	$2\frac{1}{2}$	103701.6
	$4p'\ ^4P^\circ$	$1\frac{1}{2}$	105322.7
	$4p'\ ^4P^\circ$	$\frac{1}{2}$	106528.8
	$4p'\ ^4F^\circ$	$4\frac{1}{2}$	[a] 106779.9
	$4p'\ ^4F^\circ$	$3\frac{1}{2}$	106852.4
	$4p'\ ^4F^\circ$	$2\frac{1}{2}$	107268.6
	$4p'\ ^4F^\circ$	$1\frac{1}{2}$	108227.9
	$4p'\ ^2F^\circ$	$2\frac{1}{2}$	110672.3
	$4p'\ ^4D^\circ$	$3\frac{1}{2}$	110867.2
	$4p'\ ^4D^\circ$	$2\frac{1}{2}$	111743.0
	$4p'\ ^4D^\circ$	$1\frac{1}{2}$	111994.3
	$4p'\ ^2F^\circ$	$3\frac{1}{2}$	112409.7
	$4p'\ ^4D^\circ$	$\frac{1}{2}$	112534.9
	$4p'\ ^2P^\circ$	$\frac{1}{2}$	[d] 113492.9
	$4p'\ ^2P^\circ$	$1\frac{1}{2}$	113499.2
	$4p'\ ^2D^\circ$	$1\frac{1}{2}$	114045.03
	$4p'\ ^2D^\circ$	$2\frac{1}{2}$	114833.95
$3d^{10}4f$	$4f\ ^2F^\circ$	$3\frac{1}{2}$	117263.4
		$2\frac{1}{2}$	117264.0
$3d^{10}6p$	$6p\ ^2P^\circ$	$\frac{1}{2}$	119888.51
		$1\frac{1}{2}$	119959.34
$3d^{10}5f$	$5f\ ^2F^\circ$	$3\frac{1}{2}$	127199.6
		$2\frac{1}{2}$	127209.4
$3d^{10}7p$	$7p\ ^2P^\circ$	$1\frac{1}{2}$	128343.44
		$\frac{1}{2}$	128518.5
$3d^9(^2D)4s4p(^1P^\circ)$	$4p''\ ^2F^\circ$	$3\frac{1}{2}$	130014.26
	$4p''\ ^2P^\circ$	$1\frac{1}{2}$	130371.57
	$4p''\ ^2D^\circ$	$2\frac{1}{2}$	131650.93
$3d^{10}8p$	$8p\ ^2P^\circ$	$\frac{1}{2}$	[a] 132414.9
$3d^{10}6f$	$6f\ ^2F^\circ$	$2\frac{1}{2}$	132604.09
		$3\frac{1}{2}$	132639.4
$3d^9(^2D)4s4p(^1P^\circ)$	$4p''\ ^2F^\circ$	$2\frac{1}{2}$	133145.76
$3d^{10}8p$	$8p\ ^2P^\circ$	$1\frac{1}{2}$	[a] 133622.1
$3d^9(^2D)4s4p(^1P^\circ)$	$4p''\ ^2P^\circ$	$\frac{1}{2}$	133806.3
	$4p''\ ^2D^\circ$	$1\frac{1}{2}$	134643.8
$3d^{10}7f$	$7f\ ^2F^\circ$	$3\frac{1}{2}$	135889.9
		$2\frac{1}{2}$	135892.6
$3d^{10}9p$	$9p\ ^2P^\circ$	$1\frac{1}{2}$	[c] 136505.3?
$3d^{10}8f$	$8f\ ^2F^\circ$	$3\frac{1}{2}$	138002.1
		$2\frac{1}{2}$	138003.3

[a] New level from [4] or [5]. [b] J-value changed [5]. [c] Tentative new level. [d] This level was first located by Shenstone and Gibson [2, 3]. Its combinations were correctly listed in [1], although an erroneous position occurred in the level table.

from $5s'\ ^4D_{3\frac{1}{2}}$, and the new $4p'\ ^4F^\circ_{4\frac{1}{2}}$ level [4, 5] was confirmed by the resolution and character of its strongest combination.[5]

Thirty of the classifications in table 1 are due to work reported in [4] and [5]. A few other new classifications are also listed.

Some previous ambiguities as to the spectrum assignments of certain lines are now resolved. None of the lines in table 1 has any appreciable intensity due to Zn IV in our sources. It appears from Dick's ionization stage assignments [9] that the experimental behavior of the weaker lines classified by Zn II levels was consistent with the classifications but, in itself, was often not conclusive. For the stronger lines a good separation of Zn II and Zn III was obtained [9]. Our sources allow a separation of Zn II and Zn I in the region above 1715 Å for roughly this same group, and all the unclassified lines assigned to Zn II in this region are thus separated from both Zn III and Zn I. Below 1715 Å there is no definite separation of weaker Zn II lines from possible Zn I lines.

Most of the unclassified lines in table 1 were observed by Crooker and Dick in one of their electrodeless discharges and assigned to Zn II on the basis of excitation behavior. Wavelengths for some additional unclassified lines that had Zn II character in a spark source may be found in [1]. Most of the lines previously classified by levels regarded as tentative (or now rejected) are not included in table 1, since they were not assigned to Zn II on the basis of excitation characteristics alone. Conversely, the table includes some new assignments to Zn II made on the basis of classifications by new levels.

Table 3 gives some classified lines above 2700 Å that should be added to the list of Crooker and Dick [1] for completeness.

TABLE 3. *Some additions to the* Zn II *line list of Crooker and Dick [1]*

Unless otherwise noted, observations are from [9], with *E* and *S* corresponding to electrodeless-discharge and spark intensities, respectively, as in [1]. Diffuse lines are denoted by "D".

Note	λ(air), Å	*E*	*S*	σ, cm^{-1}	Classification
a	6842.32			14610.9	$5d\ ^2D_{2\frac{1}{2}}-6f\ ^2F^\circ_{2\frac{1}{2}}$
b	6396.98	1		15628.1	$5d\ ^2D_{2\frac{1}{2}}-8p\ ^2P^\circ_{1\frac{1}{2}}$?
a	5586.22	100	1	17896.2	$5d\ ^2D_{2\frac{1}{2}}-7f\ ^2F^\circ_{3\frac{1}{2}}$
a	5585.21			17899.5	$5d\ ^2D_{2\frac{1}{2}}-7f\ ^2F^\circ_{2\frac{1}{2}}$
c	5577.71	(50)		17923.5	$5d\ ^2D_{1\frac{1}{2}}-7f\ ^2F^\circ_{2\frac{1}{2}}$
b	3514.19	15		28448.0	$8p\ ^2P^\circ_{1\frac{1}{2}}-5s'\ ^4D_{2\frac{1}{2}}$?
a	3304.80			30250.3	$4d\ ^2D_{2\frac{1}{2}}-5f\ ^2F^\circ_{2\frac{1}{2}}$
b	3279.72	10		30481.7	$8p\ ^2P^\circ_{\frac{1}{2}}-5s'\ ^4D_{1\frac{1}{2}}$?
d	3276.57	20		30511.0	$5p\ ^2P^\circ_{\frac{1}{2}}-8s\ ^2S_{\frac{1}{2}}$
e	3153.44	30D	2	31702.2	$4p''\ ^2P^\circ_{1\frac{1}{2}}-5s'\ ^4D_{2\frac{1}{2}}$
b	3138.7	30D		31851.	$4p''\ ^2F^\circ_{2\frac{1}{2}}-5s'\ ^2D_{2\frac{1}{2}}$
b	2997.8	50		33348.	$4p''\ ^2D^\circ_{2\frac{1}{2}}-5s'\ ^2D_{2\frac{1}{2}}$
e	2964.3	10D		33725.	$7p\ ^2P^\circ_{1\frac{1}{2}}-5s'\ ^4D_{2\frac{1}{2}}$
b	2857.59	50D	5	34984.3	$4p''\ ^2F^\circ_{3\frac{1}{2}}-5s'\ ^2D_{2\frac{1}{2}}$
f	2738.46	10		36506.1	$5p\ ^2P^\circ_{1\frac{1}{2}}-9d\ ^2D_{2\frac{1}{2}}$
f	2720.42			36748.1	$5p\ ^2P^\circ_{\frac{1}{2}}-9d\ ^2D_{1\frac{1}{2}}$

[a] Wavelength, classification from G. v. Salis, Ann. Physik [4] **76**, 145 (1925).
[b] Classification involves new level from [4] or [5]. Lines with questionable classifications may not belong to Zn II.
[c] Wavelength from Shenstone and Gibson [3]. Intensity is a guess for unblended Zn II line, as actual line was blended with a strong Zn III line in [9].
[d] Classified by v. Salis.
[e] Upper level found by Crooker and Dick [1].
[f] Both wavelengths are from [3], for consistency. The 2738 Å transition was listed in [1].

[g] The line previously given for this transition, 1816.479 Å, [1] cannot arise from $5s'\ ^4D_{2\frac{1}{2}}$. Since this line is strong in E_1, does not appear in E_2, and is wide and weak (relative to E_1) in S_1, it arises from an (unknown) autoionization-broadened level.

4. Comments on Levels

The $nf(^2F^\circ_{3\frac{1}{2}}-{}^2F^\circ_{2\frac{1}{2}})$ intervals obtained from the levels in table 2 are:[6]

$4f$	-0.6 cm^{-1}
$5f$	-9.8
$6f$	$+35.3$
$7f$	-2.7
$8f$	-1.2

Although *f* series with all or mostly negative intervals are frequently observed, this behavior has not been satisfactorily explained. It does seem clear that it is not generally due to interaction with known configurations. Such interactions can, in some cases, account for irregular variations of the intervals along the series. The $4p''\ ^2F^\circ$ levels in Zn II are so positioned that interaction with them probably explains the relatively large positive interval of the $6f\ ^2F^\circ$ term[7] and the increased negative interval of $5f\ ^2F^\circ$.

It seems best to rely entirely on the three-member *g* series for the ionization energy. The Ritz formula yields a value of 144892.6 cm^{-1} for Zn III $3d^{10}\ ^1S_0$ relative to the ground level of Zn II. An uncertainty of ±2 cm^{-1} should take into account the effect of any errors in the levels.

All Zn II levels that appear to be well established are given in table 2. A few levels listed by Crooker and Dick [1] are omitted. Several of these were undesignated even levels (lying above the limit) given as questionable in [1]. (We have retained the originally assigned numbers as names for the remaining such levels.) The other deletions, and all except two of the new levels (both tentative), result from previously described work [4, 5].

5. References

[1] Crooker, A. M., and Dick, K. A., Can. J. Phys. **46**, 1241 (1968). This paper includes an account of previous investigations of Zn II.

[2] Moore, C. E., Atomic Energy Levels, Nat. Bur. Stand. (U.S.), Circ. 467, Vol. II, 259 pages (1952). References to publications on Zn II earlier than [1] are given.

[6] Some oversights regarding the 7*f* term in the level and line lists of [1] have been corrected. We also used data from references in table 3 to help determine some *nf* levels.

[7] The inference that $6f\ ^2F^\circ$ has the most perturbed of these intervals is consistent with its position nearest to a perturbing $3d^94s4p$ level, $4p''\ ^2F^\circ_{2\frac{1}{2}}$. The observed $3d^94s^2\ ^2D-3d^{10}nf\ ^2F^\circ$ multiplets (forbidden in the pure configuration approximation) probably arise mainly from the small interaction of the $3d^{10}nf$ series with $3d^94s4p$. Thus, on our spectrograms, the $4s^2\ ^2D_{2\frac{1}{2}}-6f\ ^2F^\circ_{2\frac{1}{2}}$ transition at 1430.992 Å is the strongest observed line belonging to any of these multiplets.

[3] Shenstone, A. G., and Gibson, L. E., unpublished material. (The main results of this analysis were given in [2].)
[4] Martin, W. C., and Sugar, J., J. Opt. Soc. Am. **59,** 1266 (1969). The present paper was given as the source of the experimental values for some levels and wavenumbers in Tables III, VI, and XII of this reference. These values were based on preliminary measurement of a zinc spark spectrogram. In some cases they differ by more than 1 cm^{-1} from the much more accurate values reported here.
[5] Martin, W. C., and Sugar, J., J. Res. Nat. Bur. Stand. (U.S.), **74A,** (Phys. and Chem) No. 1, 7 (Jan.–Feb. 1970).
[6] Sugar, J., J. Opt. Soc. Am. **53,** 831 (1963).
[7] Kaufman, V., and Andrew, K. L., J. Opt. Soc. Am. **52,** 1223 (1962); Kaufman, V., and Ward, J. F., J. Opt. Soc. Am. **56,** 1591 (1966); Kaufman, V., and Ward, J. F., Appl. Opt. **6,** 43 (1967); Radziemski, L. J., Andrew, K. L., Kaufman, V., and Litzén, U., J. Opt. Soc. Am. **57,** 336 (1967).
[8] Shenstone, A. G., Phil. Trans. Roy. Soc. (London) [A] **241,** 297 (1948).
[9] Dick, K. A., The Spark Spectra of Zinc (Ph. D. Thesis, University of British Columbia, 1966).

(Paper 74A1–579)

JOURNAL OF RESEARCH of the National Bureau of Standards—A. Physics and Chemistry
Vol. 74A, No. 1, January–February

CIE 1960 UCS Diagram and the Müller Theory of Color Vision

Deane B. Judd and Gary T. Yonemura

**Institute for Basic Standards, National Bureau of Standards,
Washington, D.C. 20234**

(September 11, 1969)

A close relationship has been shown to exist between the second stage of the Müller theory and the MacAdam 1937 (u, v)-diagram recommended in 1960 by the CIE for interim use as a chromaticity diagram having approximately uniform scales. By considering normal vision as a combination of protanopia and tritanopia as suggested by the Müller second stage, a more general measure of the perceived size of a chromaticity difference is developed than the length of the line connecting the two chromaticity points. The general measure is the square root of the sum of the squares of the angles subtended by the line at the convergence points of the chromaticity confusion lines for protanopia and tritanopia, respectively. By this measure the chromatic sensibility to wavelength change in the spectrum is accounted for quantitatively not only for protanopic and tritanopic vision, but also for normal vision including the secondary maximum of sensibility in the neighborhood of 420 nm.

Key words: Chromaticity; color; perception; protanopia; tritanopia; vision.

1. Introduction

In a paper on Recent Developments of Thomas Young's Color Theory, delivered in 1886 before the British Association in Birmingham, A. König [1][1] stated that "it ought not to be difficult in the construction of a chromaticity diagram so to modify the adopted arbitrary assumptions that the separation of two points on it would give a measure for the difference in sensation between the colors corresponding to them, ..." In 1932 one of us [2] drew attention to the fact that the (r, g)-chromaticity diagram based on the so-called "OSA excitation curves" yields some approach to uniform chromaticity scales, and in 1935 a Maxwell triangle yielding approximately uniform chromaticity scales (known as the UCS diagram) was defined [3] by reference to the colorimetric coordinate system recommended by the International Commission on Illumination (CIE) [4].

In 1937 MacAdam [5] showed that essentially the same chromaticity spacing could be achieved by plotting the v-chromaticity coordinate against the u-coordinate in a rectangular coordinate system based on the simple transformation of tristimulus values, X, Y, Z in the 1931 CIE colorimetric coordinate system:

$$U = (2/3)X$$
$$V = Y$$
$$W = -0.5X + 1.5Y + 0.5Z. \quad (1)$$

The V-function, like the Y-function, is equal to the standard spectral luminous efficiency function. The (u, v)-chromaticity coordinates are related to the 1931 CIE tristimulus values, X, Y, Z and to the chromaticity coordinates, x, y in this simple way:

$$u = 4X/(X + 15Y + 3Z) = 4x/(-2x + 12y + 3)$$
$$v = 6Y/(X + 15Y + 3Z) = 6y/(-2x + 12y + 3). \quad (2)$$

In 1939 Breckenridge and Schaub [6] developed a variation of the UCS diagram in which the equi-energy point was made the origin of a rectangular coordinate system (known as the RUCS diagram), and applied it to the specification of the colors of signal lights (railway, highway, marine, and airplane traffic) [7]. In 1942 Scofield, Judd, and Hunter [8] published the definition of the "alpha-beta" diagram that first, like the RUCS diagram, placed achromatic colors at the origin, second could be approximated closely by simple functions of the readings, A, G, B obtained from a photoelectric tristimulus colorimeter through amber, green and blue tristimulus filters, respectively, and finally gave a chromaticity spacing more in accord with Wright's study [9] of the RUCS diagram than any previously formulated diagram.

In 1945 the Committee on Colorimetry [10] made use of a method devised by MacAdam [11] to derive a rectangular-coordinate UCS diagram having the same spacing as the Judd UCS diagram, and this diagram is included in the final report of the committee [12].

In 1944 Farnsworth [13] described a rectilinear uniform chromaticity scale diagram designed so as to

[1] Figures in brackets indicate the literature references at the end of this paper.

make the Munsell value 5, chroma 10 locus [14] approximate a circle. In 1949 Neugebauer [15] made use of the MacAdam 1937 (u, v)-diagram in a form representing achromatic object colors at the origin by plotting $v-v_0$ against $u-u_0$, where u_0, v_0 are the chromaticity coordinates of the illuminant. This form of UCS diagram has been known as the MacAdam-Neugebauer diagram. In 1959 Sugiyama and Fukuda [16] defined still another UCS diagram by adjusting the spacing to accord maximally with that of the Munsell color system [14] and with the MacAdam ellipses [17].

In 1960, the CIE recommended the 1937 MacAdam (u, v)-diagram [18] for use whenever a projective transformation of the CIE (x, y)-diagram is desired to give chromaticity spacing perceptually more nearly uniform than the (x, y)-diagram itself. In the third edition of the International Lighting Vocabulary, the diagram defined by eq (2) is called the "CIE 1960 UCS diagram."

König's idea of a uniform-chromaticity-scale diagram has thus received wide-spread attention and has come to fruition in the form of an international recommendation after 75 years. It should not be supposed, however, that the separation of two points on the recommended UCS diagram is an exact measure of the perceived size of the difference between the chromaticities represented by the points; this separation is an approximate measure. The degree of approximation, however, has been shown by Wyszecki and Wright [19] to be sufficient for many practical purposes, and this degree is probably close to the highest achievable by projective transformation of the 1931 CIE (x, y)-diagram. Less restricted types of transformation should permit improved agreement with the experimental facts; and plane diagrams for this purpose derived by nonlinear transformations have achieved some success; see, for example, those derived by Sinden [20], Adams [21], Moon and Spencer [22], Farnsworth [23], Glasser et al. [24], Nickerson, Judd, and Wyszecki [25], and Saunderson and Milner [26]. The Munsell renotation system [14] itself is equivalent to a series of diagrams derived by nonlinear transformation of the (x, y)-diagram, one for each level of Munsell value, and if the Euclidian distance element derived by Godlove [27] is used, these are UCS diagrams plottable on planes.

Further refinements of these empirical models not subject to the restriction of being plottable on a plane have been derived; see, for example, Nickerson [28], MacAdam [29], Friele [30], and Chickering [31].

In 1949 one of us [32] derived response functions for the three stages of the Müller theory of color vision and showed how the chromatic response functions of the second stage could be combined with the standard spectral luminous-efficiency function, $\bar{y}(\lambda)$, to account for the minimum perceptible luminance purity determined by Priest and Brickwedde [33], and by Purdy [34]. The two chromatic response functions of the second stage correspond to a yellowish red (yR) process whose negative is bluish green (bG) and a greenish yellow (gY) process whose negative is reddish blue (rB). The failure of the (yR−bG)-process accounts in the Müller theory for protanopia; that of the (gY−rB)-process, for tritanopia. These response functions are defined in terms of the tristimulus values, $\bar{x}(\lambda)$, $\bar{y}(\lambda)$, $\bar{z}(\lambda)$, of the spectrum in the 1931 CIE system [4] by the equations:

$$\begin{aligned} \mathrm{yR}(\lambda) &= -\mathrm{bG}(\lambda) = 5.741\bar{x}(\lambda) - 4.601\bar{y}(\lambda) - 1.140\bar{z}(\lambda) \\ \mathrm{gY}(\lambda) &= -\mathrm{rB}(\lambda) = -0.932\bar{x}(\lambda) + 2.751\bar{y}(\lambda) - 1.819\bar{z}(\lambda). \end{aligned} \tag{3}$$

It was shown that the function of wavelength:

$$y(\lambda)/\{[(\mathrm{yR}(\lambda)]^2 + [0.5\mathrm{gY}(\lambda)]^2\}^{1/2}$$

agreed closely with the luminance purity of colors represented by points on a circle on the UCS diagram centered on the achromatic point. Thus, the same type of information derivable from the UCS triangle can be drawn from the yR and gY functions; but the colorimetric coordinate system proposed for the second stage of the Müller theory [32], and formed of these two chromatic response functions combined with the standard spectral luminous-efficiency function $\bar{y}(\lambda)$ yields a chromaticity diagram with scales departing maximally from perceputal uniformity because the diagram is degenerate. From eq (3) we see that the sum of the three functions chosen:

$$\mathrm{yR}(\lambda) + \mathrm{gY}(\lambda) + \bar{y}(\lambda) = 4.809\bar{x}(\lambda) - 0.850\bar{y}(\lambda) - 2.959\bar{z}(\lambda)$$

is positive for the long-wave part of the spectrum and negative for the short-wave portion; so for some intermediate wavelength this sum, the denominator of the fraction defining the chromaticity coordinates, is equal to zero, and the corresponding chromaticity point is located indefinitely far from points representing other chromaticities on this diagram.

This paper will show how to fit the yR(λ) and gY(λ) functions into a coordinate system yielding a UCS diagram, and will present a new distance element for the perceptibility of chromaticity differences based on the Müller theory of color vision.

2. Protanopic and Tritanopic Intersection Points as Primaries

Equation (3) defines the chromatic processes of the Müller theory in terms of the tristimulus values, $\bar{x}(\lambda)$, $\bar{y}(\lambda)$, $\bar{z}(\lambda)$, of the spectrum; that is, as functions of wavelength. If a heterogeneous stimulus of spectral distribution $S(\lambda)$ is viewed, the tristimulus values, X, Y, Z, correspond to:

$$X = \int_0^\infty S(\lambda)\bar{x}(\lambda)d\lambda,$$

$$Y = \int_0^\infty S(\lambda)\bar{y}(\lambda)d\lambda,$$

$$Z = \int_0^\infty S(\lambda)\bar{z}(\lambda)d\lambda$$

and it follows from eq (3) that the chromatic processes corresponding to this stimulus may be evaluated as

functions of X, Y, Z by substituting in eq (3), X, Y, Z, respectively for $\bar{x}(\lambda)$, $\bar{y}(\lambda)$, $\bar{z}(\lambda)$.

In the second stage of the Müller theory, yR corresponds to the process whose failure reduces the normal trichromatic mechanism to the protanopic variety of dichromatic mechanism, and rB corresponds to the process whose failure produces tritanopia. Luminosity, w-s, corresponds to a direct contribution $L(P_i)$ from the primary processes P_1, P_2, P_3, of the first stage plus contributions associated with the yR and rB chromatic processes. From eq (3a) of the previous paper [32] there may be written:

$$w\text{-}s = 0.0075P_1 + 0.1912P_2 + 0.0013P_3 + 0.0810\text{yR} - 0.0024\text{rB} \qquad (4)$$

whence it follows that the direct contribution $L(P_i)$ to luminosity, w-s, from the primary processes $P_i (i = 1, 2, 3,)$ of the first stage is:

$$L(P_i) = 0.0075P_1 + 0.1912P_2 + 0.0013P_3. \qquad (5)$$

The definition of $L(P_i)$ may be written in terms of the tristimulus values, X, Y, Z, of the color in the 1931 CIE system from the definitions of P_i given in eq (1) of the previous paper [32]:

$$\begin{aligned} \text{P}_1 &= 3.1956X + 2.4478Y - 0.6434Z \\ \text{P}_2 &= -2.5455X + 7.0492Y + 0.4963Z \\ \text{P}_3 &= 0.0000X + 0.0000Y + 5.0000Z \end{aligned} \qquad (6)$$

whence:

$$L(P_i) = -0.463X + 1.366Y + 0.097Z. \qquad (7)$$

A colorimetric coordinate system for the second stage, more in keeping with the Müller theory than that previously proposed [32], may be formed by combining $L(P_i)$ with the chromatic processes yR and rB, thus:

$$\begin{aligned} \text{yR} &= 5.741X - 4.601Y - 1.140Z \\ \text{rB} &= 0.932X - 2.751Y + 1.819Z \\ L(P_i) &= -0.463X + 1.366Y + 0.097Z \end{aligned} \qquad (8a)$$

$$\begin{aligned} X &= 0.2391\ \text{yR} + 0.0967\ \text{rB} + L(P_i) \\ Y &= 0.0810\ \text{yR} - 0.0024\ \text{rB} + L(P_i) \\ Z &= \phantom{0.0810\ \text{yR} - 0.0024\ \text{rB} +}\ 0.4966\ \text{rB} + L(P_i). \end{aligned} \qquad (8b)$$

Consideration of eq (8b) for the reverse transformation will show that the variables, yR, rB, $L(P_i)$, defined in eq (8a), do indeed correspond to the Müller theory. The expression for the tristimulus value Y is seen to correspond to the expression for normal luminosity, w-s, given in eq (4) when the definition of $L(P_i)$ given in eq (5) is taken into account. By setting each pair of columns to zero, it may be shown that the chromaticity point for the yR-primary is at $x = 0.2391/(0.2391 + 0.0810) = 0.747$, $y = 0.0810/(0.2391 + 0.0810) = 0.253$. This point was used in the previous paper [32] to derive eq (10) of that paper. Similarly it is seen that the chromaticity point for the $L(P_i)$ primary is at $x = y = 1/3$, the equi-energy point, which was used to derive eq (7) of that paper. Finally it is seen that the rB primary is at:

$$x = 0.0967/(0.0967 - 0.0024 + 0.4966) = 0.164$$

$$y = -0.0024/(0.0967 - 0.0024 + 0.4966) = -0.004$$

which is close to the point ($x = 0.165$, $y = 0.000$) used in the derivation of eq (11) of that paper. The reason for this slight discrepancy is that formerly the tritanopic intersection point was taken as the intersection of the line $P_1 = P_2$ with the alychne, $y = 0$; the present choice places it at the intersection of this line with what might be called the protanopic alychne, that is, the line corresponding to $L(P_i) = 0$.

Equation (8) without detailed explanation has already been published [35] except that gY was substituted for its equivalent $-$ rB, and the $L(P_i)$-function was labeled W_p for protanopic luminosity. This designation and notation is appropriate for eq (5), as a comparison with W_p from the König theory (see previous eq (14a)) and $(w-s)_p$ from the Müller theory (see previous eq (4a)) shows:

$$\begin{aligned} W_p &= 0.0075P_1 + 0.1902P_2 + 0.0023P_3 \\ L(P_i) &= 0.0075P_1 + 0.1912P_2 + 0.0013P_3 \\ (w-s)_p &= 0.0075P_1 + 0.1921P_2 + 0.0003P_3 \end{aligned}$$

that is, $L(P_i)$ is closely an average of W_p and $(w-s)_p$ both of which have been shown by figure 7 of the previous paper [32] to be satisfactory representatives of protanopic luminosity experimentally determined.

3. UCS Diagram Derived from Müller Second Stage

The chromaticity diagram formed by plotting rB/S_a against yR/S_a, $S_a = \text{yR} + \text{rB} + L(P_i)$, in accord with eq (8a), yields chromaticity scales that are far from uniform. Note that $S_a = 6.210X - 5.986Y + 0.776Z$, although greater than zero near the extremes of the visible spectrum, where Y is much smaller than X or Z, respectively, is less than zero near the middle of the spectrum. It follows that for two wavelengths $S_a(\lambda)$ will be zero, and that the chromaticity diagram is degenerate. To regenerate the diagram, however, it is necessary only to change the scale of $L(P_i)$ by multiplying by any constant larger than that required to make the minimum value of $S(\lambda)$ in the middle of the spectrum be precisely zero. If this factor is very large, the point representing the equi-energy point on the resulting chromaticity diagram will fall indefinitely close to the spectrum locus. We have found that the factor 11.70 causes the equi-energy point to fall between the point for 570 nm (greenish yellow) and that for 430 nm (violet) with closely the same spacing as that of the CIE 1960 UCS diagram; that is, the distance to the 570 nm point is about 0.22 times that

to the point for 430 nm. The definition of the coordinate system with the regenerated and adjusted chromaticity diagram is simply:

$$\begin{aligned} \text{yR} &= 5.741X - 4.601Y - 1.140Z \\ \text{rB} &= 0.932X - 2.751Y + 1.819Z \\ 11.7L(P_i) &= -5.417X + 15.982Y + 1.135Z \end{aligned} \tag{8c}$$

$$\begin{aligned} X &= 0.2391\,\text{yR} - 0.0967\,\text{rB} + 0.0855[11.7L(P_i)] \\ Y &= 0.0810\,\text{yR} - 0.0024\,\text{rB} + 0.0855[11.7L(P_i)] \\ Z &= \qquad\quad 0.4966\,\text{rB} + 0.0855[11.7L(P_i)]. \end{aligned} \tag{8d}$$

All statements previously made regarding eqs (8a) and (8b) apply to eqs (8c) and (8d). The sum $S = \text{yR} + \text{rB} + 11.7L(P_i)$, however, is obviously greater than zero for all parts of the spectrum because first $\bar{x}(\lambda)$, $\bar{y}(\lambda)$, $\bar{z}(\lambda)$ are nowhere in the spectrum less than zero, and second this sum S is seen to be equal to: $1.256X + 8.630Y + 1.814Z$, an expression that has coefficients all greater than zero. By plotting rB/S in rectangular coordinates against yR/S we obtain a chromaticity diagram in which the equi-energy point is at the origin (0, 0) of the coordinate system; the protanopic convergence point, (1, 0); and the tritanopic convergence point, (0, 1). This diagram already bears considerable resemblance to the CIE 1960 UCS diagram because that diagram shows the line connecting the equi-energy point with the protanopic convergence point to be approximately perpendicular to the line connecting the equi-energy point with the tritanopic convergence point. The length of the latter line, however, is only about three-fourths that of the former. To make the (yR/S, rB/S)-diagram agree in spacing more closely with the CIE 1960 UCS diagram, we have plotted 0.42yR/S as abscissa with -0.32rB/S as ordinate; see large circles on figure 1. The solid dots refer to the spectrum locus of the Neugebauer [15] form of the CIE 1960 UCS diagram obtained by plotting $u - u_0$ as abscissa and $v - v_0$ as ordinate, where u_0, v_0 are the chromaticity coordinates (0.2105, 0.3158) of the equi-energy point.

It will be noted that the degree of difference in spacing of the two diagrams is not large enough to have any practical significance. The diagrams have the equi-energy point in common. The diagram yielded by eq (8c) in accord with the second stage of the Müller theory has the protanopic convergence point (0.42, 0.00), and the tritanopic convergence point (0.00, -0.32); the corresponding points are shown as solid dots for the CIE 1960 UCS diagram. It is concluded that the CIE UCS diagram, developed empirically, yields spacing in accord with the second stage of the Müller theory of color vision. The accommodation of the CIE 1960 UCS diagram within the second stage

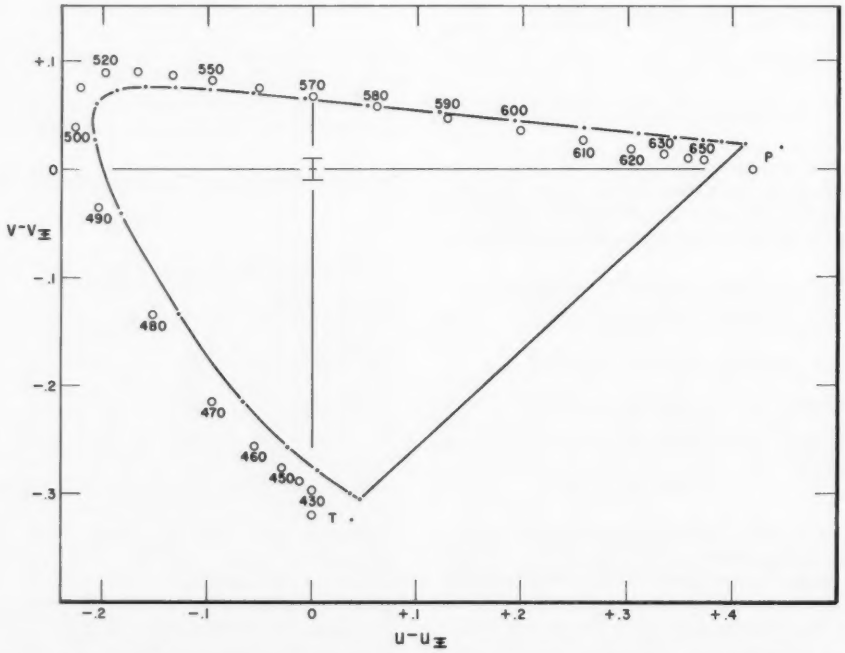

FIGURE 1. *The chromaticity diagram derived in accord with the second stage of the Müller theory (0.42yR/S and −0.32rB/S from eq (8c) plotted in rectangular coordinates) compared with the CIE 1960 UCS diagram in the Neugebauer [15] form obtained by plotting the* (u, v)*-differences from the equi-energy point.*

Note that the spectrum locus on the former diagram (large circles) has a spacing not significantly different from that on the CIE 1960 UCS diagram (dots joined by solid line).

suggests that for the Müller theory the processes determining discrimination of chromatic differences occur in the retina; the third stage must be thought of as the process by which the discriminations made in the retina are recoded for transmission along the optic nerve with no loss of information.

4. Proposed Measure of Perceived Size of Chromatic Differences for Dichromats

If the length of the line connecting two points on a uniform chromaticity diagram is an approximate measure of the size of the chromatic difference perceived for an observer with normal color vision between the chromaticities represented by the two points, what measure is appropriate for dichromatic vision? To a dichromat, the chromaticities represented by any point on any straight line passing through the dichromatic convergence point are all identical. The component of the vector on the UCS diagram along such lines contributes nothing to dichromatic discrimination; only the component orthogonal to the direction of the chromaticity-confusion line counts. It is natural, therefore, to take the angular separation of the confusion lines containing the chromaticity points as this measure; that is, if we have two chromaticities specified by chromaticity coordinates u_1, v_1, and u_2, v_2 on the UCS diagram, the perceived size ΔC_d of the chromaticity difference for a dichromat whose convergence point is at u_d, v_d is:

$$\Delta C_d = K_d \left\{ \tan^{-1}\left[\frac{v_1 - v_d}{u_1 - u_d}\right] - \tan^{-1}\left[\frac{v_2 - v_d}{u_2 - u_d}\right] \right\}. \qquad (9)$$

The small open circles connected by dot-dash lines on figure 2 show the wavelength difference just detectable in protanopic vision computed by this measure for $K_d = 0.81$ with the angles expressed in degrees, and for $u_d = 0.658$, $v_d = 0.334$. This choice of $K_d = 0.81$ is derived from the assumption that a change in the direction of the chromaticity confusion line by 1.23° is required for a protanope to detect the chromaticity difference [36]. Note that the wavelength-sensibility curve predicted by this measure for protanopic vision shows a pronounced minimum of about 1.2 nm at about 481 nm and rises to 10 nm both at 434 and 517 nm.

The double circles connected by dashed lines on figure 2 show analogous predictions of the wavelength difference just detectable in tritanopic vision computed from eq (9) also for $K_d = 0.81$. The tritanopic intersection point has been taken as required by the Müller theory at $x = 0.164$, $y = -0.004$ by setting $u_d = 0.249$, $v_d = -0.009$. Note that this predicted curve of tritanopic sensibility to wavelength difference among spectrum colors is much more complicated than that for protanopic sensibility. It has three

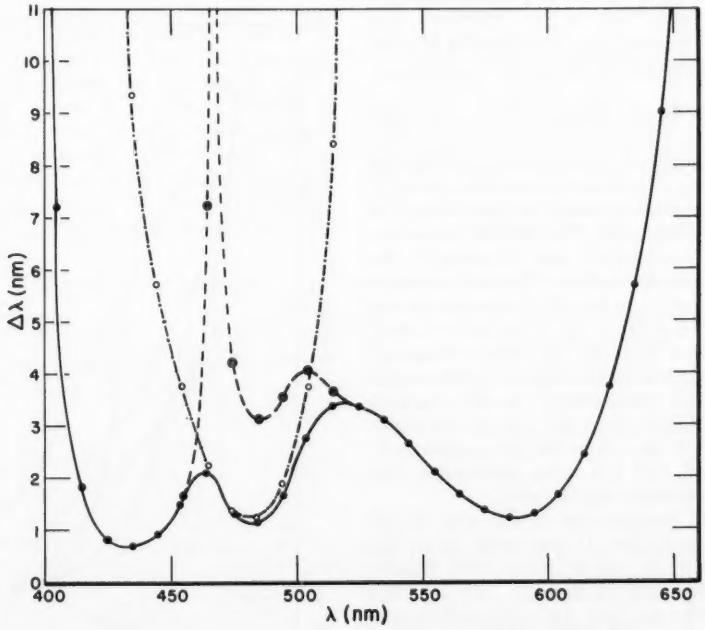

FIGURE 2. *Wavelength difference just detectable by chromaticity discrimination according to the Müller theory for protanopic (circles connected by dot-dash line), tritanopic (double circles connected by dashed line), and normal (solid circles connected by solid line) vision as a function of wavelength; see eqs (9) and (10),* $K_d = 0.81$.

Note that tritanopic wavelength discrimination by this theory differs significantly from normal wavelength discrimination only between 450 and 520 nm, the region where protanopic discrimination is relatively good.

minima (430, 487, and 585 nm), one sharp maximum (467 nm) and one relative maximum (504 nm) as well as two indefinitely high maxima at the spectrum extremes. We might say that the computations indicate "good discrimination in the yellow region of the spectrum, discontinuity in the blue-green wavelengths where wavelength discrimination virtually disappears, and, most striking of all, very keen wavelength discrimination in the far violet." These are, however, not our words, but those of Wright [37] describing wavelength discrimination found experimentally by him for four tritanopes. Detailed quantitative comparison will be shown presently.

5. Proposed General Measure of Perceived Size of Chromatic Differences

Three main types of dichromatic vision, all reduced forms of normal trichromatic vision, are generally recognized and dealt with theoretically both in the three-components theory, and in the Müller stage theory. These are protanopia, deuteranopia, and tritanopia. A fourth type of reduced color vision, tetartanopia, has mainly theoretical existence. It corresponds to failure of the yellow-blue process of the Hering opponent-colors theory which is the same as the third stage of the Müller theory. No uncomplicated case of tetartanopia has ever been reported.

In the Müller second stage, normal vision may be regarded as the result of combining the protanopic discriminative ability with that of the tritanope. The Müller second stage thus suggests the following general measure of perceived size of chromatic differences:

$$\Delta C = [(K_p \Delta\theta_p)^2 + (K_t \Delta\theta_t)^2]^{1/2} \qquad (10)$$

where $K_p\Delta\theta_p$ is eq (9) applied to protanopic vision, and $K_t\Delta\theta_t$ is eq (9) applied to tritanopic vision. The assumption on which this proposal is based is that whatever the protanope can discriminate, the normal observer, endowed with both protanopic and tritanopic discriminative ability, can see better. The solid circles connected by a solid curve on figure 2 correspond to a combination of the two dotted curves in accord with eq (10). It will be noted that, by this view, tritanopic vision accounts for nearly all of the ability of the normal observer to discriminate wavelength by chromaticity difference in the spectrum up to 430 nm at the short-wave end and from 520 nm on in the long-wave end; only between 430 and 520 nm does protanopic discriminative ability contribute appreciably.

The form of eq (10), square-root of the sum of two squares, is a usual assumption. It was made in eq (24) of the previous paper [32], and by Stiles [38], Sinden [20], Schrödinger [39], and Helmholtz [40] in their treatments of sensibility to color differences from the standpoint of the three-components theory. This assumption applied to angular measures becomes identical to that on which the UCS diagram is based for the special case of a projective transformation in which both protanopic and tritanopic convergence points are projected to infinity. Wyszecki [41] derived such a projective transformation, but the resulting chromaticity diagram proved to be spectacularly different from a UCS diagram.

The argument by which eq (10) is proposed may seem somewhat circular. The CIE 1960 UCS diagram is used to justify the measure for dichromatic discriminations given by eq (9); then a new measure, eq (10), based on eq (9) is proposed that implies that distance on the UCS diagram does not really accord precisely with the perceived size of chromaticity difference after all. The justification of this circular argument lies in whether a more successful model of chromatic discrimination is thereby discovered. The model need not necessarily be that suggested by the Müller second stage; it might be that suggested by the Müller third stage, a combination of deuteranopia and tetartanopia; it might be a combination of all three established forms of dichromatic vision as in the three-components theory; or it might be based on a view, suggested by Walraven [42] that normal color vision be considered a combination of tritanopia with deuteranopia.

6. Wavelength Discrimination by Theory and by Experiment

Figure 3 compares the wavelength difference just detectable in protanopic vision computed from eq (9) with wavelength discrimination curves of six protanopes studied by Pitt [43]. The same values of u_d, v_d used for

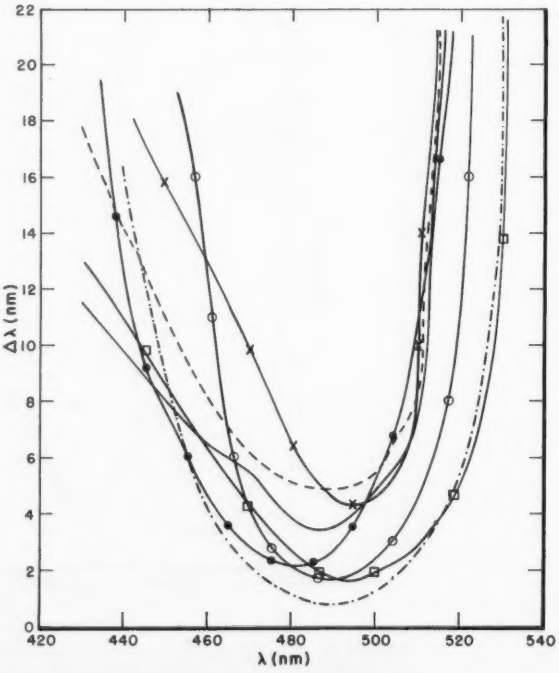

FIGURE 3. *Wavelength difference just detectable by chromaticity discrimination in protanopic vision.*

Solid dots connected by a solid line refer to values computed from eq (9) for K_d=0.47; all other curves refer to values found experimentally by Pitt [41] for six protanopes.

figure 2 were used again, but K_d was set at 0.47. This choice of K_d corresponds to detectability of an angular change of 2.13° for protanopic vision. The agreement is seen to be good in the sense that the predictions are generally within the spread among the six observers, but not perfect. The computed curve has a minimum at about 481 nm; the minima of the experimental curves range between 486 and 496 nm.

Figure 4 compares the wavelength difference just detectable in tritanopic vision computed from eq (9) with wavelength discrimination curves of four tritanopes studied by Wright [36]. K_d was set at 0.24 (corresponding to detectability of a 4.17° change for tritanopic vision), but the tritanopic convergence point implied by combining the Müller theory with the CIE standard observer ($x=0.164$, $y=-0.004$) was not used. Instead we have taken advantage of the fact that Wright [36] determined the color-matching functions of seven tritanopes including the four whose wavelength discrimination curves are shown in figure 4. By using the method previously used by Thomson and Wright [44] to evaluate the tritanopic convergence point within a colorimetric coordinate system tentatively proposed for the consideration of the CIE Committee on Colorimetry, we have found it in the standard CIE coordinate system [4] to be $x=0.171$, $y=-0.001_5$ with an uncertainty less than 0.002 at the 0.1 of 1% level of confidence. These values are rather close to those (0.164, −0.004) yielded by the Müller theory applied to that system, and are still closer to those (0.171, 0.000) given by Wyszecki and Stiles [45] without indicating the source. It will be noted by comparing figure 4 with figure 2 that the small change in tritanopic convergence point has caused the minimum in the violet region of the spectrum to be higher relative to that at 585 nm by about a factor of two and has changed the wavelength position from about 435 to 425 nm. The agreement with the experimentally determined wavelength differences detected by the four tritanopes (indicated by plotted points) is nearly perfect. The predicted curve falls outside the observer spread only for the spectral range 440 to 470 nm.

Figure 5 compares the wavelength difference just detectable in normal vision computed from eq (10) for $K_p=K_t=0.47$ with the wavelength discrimination curves found by Bedford and Wyszecki [46] for observing fields subtending 1° with luminance held constant throughout the spectrum. Note that the secondary minimum in the far violet, previously explained only by the Stiles [37] three-components theory, is more simply and precisely accounted for by eq (10), though it would seem that reasonable modifications of the Stiles theory would permit a similar accounting within the framework of the three-components theory. We think, however, that this degree of agreement, combined with the simplicity of the theory warrants comparison of the model formulated by eq (10) with other types of chromaticity discrimination data.

7. References

[1] König, A., Naturwissenschaftliche Rundschau, No. 50, p. 464 (1886); also Gesammelte Abhandlungen, Leipzig: Barth, 1903, p. 107.
[2] Judd, D. B., J. Opt. Soc. Am. **22**, 72 (1932).
[3] Judd, D. B., J. Opt. Soc. Am. **25**, 24 (1935); J. Res. Nat. Bur. Stand. (U.S.) **14**, 41–57 (Jan. 1935).
[4] Judd, D. B., J. Opt. Soc. Am. **23**, 359 (1933).
[5] MacAdam, D. L., J. Opt. Soc. Am. **27**, 294 (1937).
[6] Breckenridge, F. C., and Schaub, W. R., J. Opt. Soc. Am. **29**, 370 (1939).
[7] Breckenridge, F. C., Colors of Signal Lights, Nat. Bur Stand. (U.S.), Monogr. **75**, 59 pages (April 1967).
[8] Scofield, F., Judd, D. B., and Hunter, R. S., ASTM Bulletin No. 110, p. 19 (May 1941).
[9] Wright, W. D., J. Opt. Soc. Am. **33**, 642 (1943).
[10] Committee on Colorimetry, J. Opt. Soc. Am. **34**, 677 (1944).
[11] MacAdam, D. L., J. Opt. Soc. Am. **32**, 2 (1942).
[12] Committee on Colorimetry, Optical Society of America, The Science of Color, New York: Crowell, 1953, p. 301.
[13] Farnsworth, D., Memorandum Report 44–1, Med. Res. Lab., U.S. Submarine Base, New London, Conn., April, 1944.

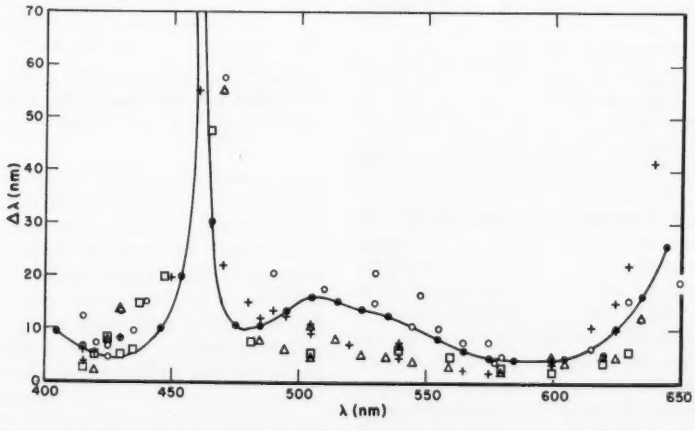

FIGURE 4. *Wavelength difference just detectable by chromaticity discrimination in tritanopic vision.*

Solid dots connected by a solid line refer to values computed from eq (9) for $K_d=0.24$; the plotted points refer to values found experimentally by Wright [36] for four tritanopes.

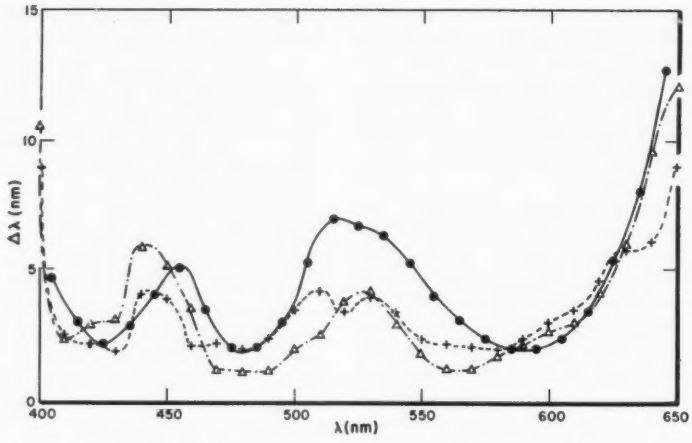

FIGURE 5. *Wavelength difference just detectable by chromaticity discrimination in normal vision.*

Solid dots connected by a solid line refer to values computed from eq (10) for $K_p = K_t = 0.47$; the other two curves refer to values obtained by Bedford and Wyszecki [44] for observation of a 1°-field by observers (themselves) having normal vision.

[14] Newhall, S. M., Nickerson, D., and Judd, D. B., J. Opt. Soc. Am. **33,** 385 (1943).
[15] Neugebauer, H. E. J., Z. Wiss. Photogr. **44,** 193 (1949).
[16] Sugiyama, Y., and Fukuda, T., J. Appl. Phys. Japan, **28,** 157 (1959); Bulletin Gov. Osaka Ind. Res. Inst. **11,** 307 (1960).
[17] MacAdam, D. L., J. Opt. Soc. Am. **32,** 247 (1942).
[18] CIE (Commission Internationale de l'Eclairage), Proc. 14th Session, Brussels, 1959, Vol. **A,** p. 36.
[19] Wyszecki, G., and Wright, H., J. Opt. Soc. Am. **55,** 1166 (1965).
[20] Sinden, R. H., J. Opt. Soc. Am. **27,** 124 (1937); **28,** 339 (1938).
[21] Adams, E. Q., J. Opt. Soc. Am. **32,** 168 (1942).
[22] Moon, P., and Spencer, D. E., J. Opt. Soc. Am. **33,** 260 (1943).
[23] Farnsworth, D., J. Opt. Soc. Am. **33,** 569 (1943); Visual Problems of Colour, Vol. **II,** Nat. Phys. Lab. Symp. No. 8 (London, Her Majesty's Stationery Office, 1958) p. 429.
[24] Glasser, L. G., McKinney, A. H., Reilly, C. D., and Schnell, P. D., J. Opt. Soc. Am. **48,** 736 (1958).
[25] Nickerson, D., Judd, D. B., and Wyszecki, G., Farbe, **4,** 285 (1955).
[26] Saunderson, J. L., and Milner, B. I., J. Opt. Soc. Am. **36,** 36 (1946).
[27] Godlove, I. H., Am. Dyestuff Reptr., **40,** No. 18 (3 September 1951).
[28] Nickerson, D., Textile Research **6,** 509 (1936).
[29] MacAdam, D. L., J. Opt. Soc. Am. **33,** 18 (1943); **54,** 249, 1161 (1946); **55,** 91 (1965); **56,** 1784 (1966).
[30] Friele, L. F. C., Farbe **10,** 193 (1961); J. Opt. Soc. Am. **55,** 1314 (1965); **56,** 259 (1966).
[31] Chickering, K. D., J. Opt. Soc. Am. **57,** 537 (1967).
[32] Judd, D. B., J. Res. Nat. Bur. Stand. (U.S.), **42,** 1–16. (Jan. 1949).
[33] Priest, I. G., and Brickwedde, F. G., J. Opt. Soc. Am. **13,** 306 (1926); **28,** 133 (1938).
[34] Purdy, D. McL., Brit. J. Psychol. Gen. Sec. **21,** 283 (1930–31).
[35] Condon, E. U., and Odishaw, Hugh, Handbook of Physics, 2nd ed.; pp. 6–70 (McGraw-Hill Book Co., New York).
[36] We choose to normalize the wavelength-discrimination curve at $\Delta\lambda = 1.23$ nm for $\lambda = 485$ nm; that is, we choose to take a value of K_d in eq (9) such that $\Delta C_d = 1$ for $\Delta\lambda = 1.23$. Equation (9) may be written: $\Delta C_d = K_d(\theta_1 - \theta_2)$. On the diagram formed by plotting $-0.32rB/S$ against $0.42yR/S$ (see fig. 1), $\theta_1 - \theta_2$ (the angle subtended at the protanopic convergence point P by the line connecting the point representing 480 nm to that representing 490 nm) for $\Delta\lambda = 10$ nm happens to be closely 10 degrees. The angle corresponding to $\Delta\lambda = 1.23$ nm is thus closely 1.23 degrees, and from eq (9) for $\Delta C_d = 1$, $K_d = 1/1.23 = 0.81$.
[37] Wright, W. D., J. Opt. Soc. Am. **42,** 509 (1952).
[38] Stiles, W. S., Proc. Phys. Soc. (London) **58,** 41 (1946).
[39] Schrödinger, E., Ann. Phys. (IV) **63,** 481 (1920).
[40] von Helmholtz, H., Z. Sinnesphysiol. **3,** 517 (1891).
[41] Wyszecki, G., J. Opt. Soc. Am. **44,** 524 (1954).
[42] Walraven, P. C., and Bouman, M. A., Vision Research **6,** 567 (1965).
[43] Pitt, F. G. H., Reports of the Committee upon the Physiology of Vision, XIV. Characteristics of dichromatic vision, Special Report Series No. 200, London, 1935.
[44] Thomson, L. C., and Wright, W. D., J. Opt. Soc. Am. **43,** 890 (1953).
[45] Wyszecki, G., and Stiles, W. S., Color Science, p. 405 (John Wiley & Sons, New York, N.Y., 1967).
[46] Bedford, R. E., and Wyszecki, G. W., J. Opt. Soc. Am. **48,** 129 (1958).

(Paper 74A1–580)

JOURNAL OF RESEARCH of the National Bureau of Standards—A. Physics and Chemistry
Vol. 74A, No. 1, January–February 1970

Blemish Formation in Processed Microfilm II

C. I. Pope

Institute for Basic Standards, National Bureau of Standards, Washington, D.C. 20234

(October 3, 1969)

Gaseous peroxides form blemishes on some processed microfilms. Two procedures are given for testing the blemish susceptibility of processed microfilm, one using peroxide paper and the other zinc powder as a source of peroxide. The susceptibility of microfilm to blemish formation decreased when conditioned at 86 percent relative humidity and 26 °C. Coarse-grain microfilms are less susceptible to blemish formation than fine-grain microfilm. Fine-grain microfilms fixed in ammonium thiosulfate were less susceptible to blemish formation than those fixed in sodium thiosulfate. Oven-aged microfilm storage cartons were found to generate peroxide when wetted. The microfilm base readily absorbed hydrogen peroxide.

Key words: Archival record film, microfilm, microfilm storage cartons, permanent record film, peroxides, redox blemishes, zinc powder.

1. Introduction

A previous study [1] [1] showed that blemishes were formed in processed microfilm by oxidizing and reducing agents, probably peroxides, emitted by paper cartons in which the microfilm was stored. Further study has led to the development of reproducible test procedures for determining the susceptibility of processed microfilm to such blemish formation. Other factors affecting the formation of blemishes were also investigated. In this paper the term "blemish" means the redox type of blemish.

2. Test Procedures for Determining the Susceptibility of Processed Microfilm to Blemish Formation

Procedures were developed using peroxide paper and zinc powder as peroxide sources for testing the susceptibility of processed microfilm to blemish formation. The test apparatus, methods of maintaining relative humidities, and the solutions used to process the films in this study are described in a previous publication [1]. A fine grain microfilm sample which is known to be susceptible to blemish formation should be used as a control with a microfilm sample being tested for blemish formation.

2.1. Peroxide Paper Test

a. Procedure for Making the Peroxide Paper

Whatman No. 3 MM filter paper [2] which is used in chromatography, was selected for this test method. The filter paper was immersed 30 min in a 5-percent solution of hydrogen peroxide at room temperature, with occasional stirring, and hung in a ventilating hood to dry. Eight samples of the paper, 5 cm by 10 cm, were used in each run. The hydrogen peroxide concentration in the filter paper was determined after drying 2 hr and at the end of each 30 min interval thereafter during the drying time. The hydrogen peroxide concentration was immediately plotted against the drying time and, by extrapolating the curve, it was possible to estimate when to terminate the drying to obtain a concentration of approximately 85 $\mu g/cm^2$. If the concentration is not over 150 $\mu g/cm^2$, the paper is usable since the area may be adjusted in the film test. After drying, the peroxide paper was immediately stored in a sealed glass bottle containing anhydrous calcium sulfate, in a refrigerator at −10 °C. Portions of the paper used in testing for blemish formation were removed rapidly and the bottle was immediately returned to the refrigerator. During storage, the concentration of hydrogen peroxide in the filter paper decreased a few percent after 30 days, about 20 percent after 100 days, and about 30 percent after 6 months.

[1] Figures in brackets indicate the literature references at the end of this paper.

[2] A commercial material is identified in this paper in order to adequately specify the experimental procedure. Such identification does not imply recommendation or endorsement by the National Bureau of Standards.

b. Peroxide Content of the Peroxide Paper

The procedure for measuring the residual hydrogen peroxide in the peroxide paper was as follows. A sample of the paper, 2 cm by 4 cm, was immersed in 30 ml of distilled water for 15 min, after which it was removed and washed with about 15 ml of distilled water. About 5 ml of 1-percent starch solution, 3 drops of a 3-percent ammonium molybdate solution, 20 ml 4*N* sulfuric acid solution and 1 g of potassium iodide were added to the above solution and the iodine liberated by the peroxide titrated with 0.01 *N* sodium thiosulfate. The hydrogen peroxide content of 1 cm^2 of the paper was calculated from the amount of sodium thiosulfate required.

A study was made to determine the effect of the concentration of the residual hydrogen peroxide in the peroxide paper used in the test for blemish formation in microfilm. The optimum concentration of residual hydrogen peroxide was found to be about 85 $\mu g/cm^2$. The microfilm samples were exposed in the desiccator to the peroxide paper for 24 hr at 86 percent relative humidity (maintained by a saturated solution of potassium chloride) and 26 °C. Three or four consecutive exposures of the microfilm to a fresh 1 cm^2 piece of paper containing about 85 μg of hydrogen peroxide were usually sufficient to develop well defined spots. The three or four exposures to 1 cm^2 of the paper developed spots more like the natural type than one exposure to a 3 or 4 cm^2 piece.

The first exposure formed very small white spots and occasionally a few small light yellow spots. With further exposures the spots began to enlarge, became more yellow and formed a ring structure. Most of the spots appeared to start with the first exposure. When the microfilm sample was desiccated over anhydrous calcium sulfate 24 hr at room temperature between each exposure to peroxide paper the spots developed a sharper ring structure, resembling more closely the natural spots. A $\frac{1}{2}$ cm^2 piece of paper containing approximately 85 μg of hydrogen peroxide was just about as effective as 1 cm^2 having 85 μg, but when the concentration was about 40 $\mu g/cm^2$, 2 cm^2 did not cause as much spot development as 1 cm^2 containing 85 μg. One exposure to 40 μg of hydrogen peroxide caused development of a few minute white spots in the high densities of the microfilm samples. The paper emitted about 80 percent of its peroxide during the first 4 hr of the test, when it initially contained about 85 $\mu g/cm^2$.

The test procedure was used on old rolls of microfilm processed several years ago and having spots on the leader and in the information near the leader. Samples from some of the rolls in blemish-free areas developed spots after one or two exposures to 1 cm^2 of paper at optimum concentration while samples from other rolls developed no spots.

2.2. Zinc Powder Test

Henn and Wiest [2] have shown that film may be tested for blemish formation by incubating the film in contact with zinc powder. Tests showed that zinc powder placed some distance from the microfilm sample generated sufficient peroxide to form spots in microfilm susceptible to blemish formation. The apparatus used in this test was the same as that described in the above paper peroxide test. A layer of zinc powder about 2 to 3 mm thick was placed in the glass dish which supported the peroxide paper.

Microfilm susceptible to blemish formation readily developed spots and image-edge attack after exposure to the zinc powder at 76 percent relative humidity (maintained by saturated sodium chloride) for 15 days at 26 °C. The spots began to form after 3 to 5 days exposure. The spots were more numerous than in the paper test and were light yellow in color as compared to the deeper yellow in the paper test. Tests were made on microfilms with varying degrees of spot susceptibility and the zinc test correlated well with the paper test. Microfilms that did not form spots with the paper test formed no spots with the zinc test. These results show that the zinc test may be used to determine the blemish susceptibility of processed microfilm, though the paper test forms spots more like the natural ones in color and appearance.

Microfilms exposed to the zinc powder at 76 percent relative humidity for 5 days at 40 °C developed spots very similar, in number and color, to those formed in the paper test. The test was not satisfactory when conducted at 76 percent relative humidity and 50 °C.

2.3. Processing the Control Microfilm Sample for Testing Blemishes in Microfilm

Microfilm susceptible to blemish formation should be used as a control in testing microfilm for blemish formation. The test for blemish susceptibility in a processed microfilm sample was the comparison of its blemish formation, if any, with that of the control sample. It has been shown [1] that fine-grain microfilm washed in chlorine-free tap water during processing formed spots readily when exposed to peroxide. About 50-cm lengths of a fine-grain microfilm were exposed to an image-pattern, developed, stopped, fixed in the acid hardening fixing bath and washed in 1-liter baths of chlorine-free tap water [1] in 1.5-liter beakers for 30 min. Eight baths were used, 2 min in the first two, 3 min in the next two, and 5 min in the remaining baths. The sample was transferred from beaker to beaker and agitated with a glass rod. The temperature of the processing solutions and wash water was 26 °C. The sample was dried 24 hr at room temperature and humidity and stored in a metal can about a week before exposing to peroxide. Microfilm washed in chlorine-free tap water from four sources suffered heavy spot formation. Microfilm washed in distilled water and in water from one well formed no spots. Microfilm washed in water drawn from the hot tap and cooled to room temperature formed none or only a few spots. The distilled water, well water, and hot tap water contained no residual chlorine. The effect of the type of wash water may be due to its influence on the residual thiosulfate concentration. Samples washed in chlorine-free tap water contained 0.0 to 0.6 $\mu g/cm^2$ of residual sodium thiosulfate for the image area while samples washed in the other wash

waters generally had a higher concentration. If the residual sodium thiosulfate in the microfilm was not reduced below 1 $\mu g/cm^2$ by the chlorine-free tap water wash, spots did not form.

3. Effect of Humidification on Blemish Formation in Fine-Grain Microfilm

The relative humidity was found to be a critical factor in testing processed microfilm for blemish formation. Tests were made with the peroxide paper on microfilms susceptible to blemish formation at 76, 86, and 97 percent relative humidity and 26 °C. Only minute spots and even yellowing occured at 76 percent relative humidity. Spots and edge attack similar to the natural types formed at 86 percent relative humidity. At 97 percent relative humidity (maintained with saturated potassium sulfate) no spots formed but a slight reddish even attack sometimes took place. The 76 percent relative humidity was too dry and the 97 percent relative humidity was too wet to form natural-looking spots. Natural-type spots formed in the zinc powder test at 76 percent relative humidity. Zinc powder at 86 percent relative humidity caused only even yellowing.

A study was made to determine the effect of conditioning processed fine-grain microfilm at 86 percent relative humidity and 26 °C before testing. The microfilm samples tested were highly susceptible to blemish formation when they had been conditioned after processing in metal cans at room humidity, which ranged between about 25 and 50 percent, and room temperature, which was 26 °C. In these tests a control sample stored at room humidity was exposed to the peroxide paper along with a sample which had been conditioned at 86 percent relative humidity. Numerous spots always formed on the control samples in the low and high silver density areas. The test samples were conditioned at 86 percent relative humidity and 26 °C (over a saturated solution of potassium chloride) in a desiccator jar on a porcelain plate with the emulsion side up, removed, stored at room humidity and exposed to the peroxide paper. The results of tests for four different conditioning periods at 86 percent relative humidity and briefer periods in room air are given in table 1. Blemish susceptibility was reduced to about 50 percent after conditioning at 86 percent relative humidity and 26 °C for 14 days, to about 10 percent after 41 days, and to almost nothing after 7 months. The reduction of spot susceptibility by aging at this high humidity was probably caused by formation of silver chloride on the image silver. Residual chloride ions, which are always present in the gelatin layer of the processed microfilm, probably reacted readily with the image silver in the moist gelatin to form silver chloride, which would inhibit spot formation if present in excessive amounts. Microfilm samples conditioned at 81 percent relative humidity at 50 °C for 1 day showed inhibition of spot formation comparable to conditioning the microfilm at 86 percent relative humidity and 26 °C for 41 days. No spots formed on microfilm samples conditioned at 97 percent relative humidity and 26 °C for 2 days.

TABLE 1. *Effect of storage at 86 percent relative humidity and 26 °C on blemish formation for one microfilm*

Storage conditions for microfilm samples before exposure to peroxide	Observations
7 days at 86 percent relative humidity, 24 hr at room humidity.	The number of spots on the samples was slightly less than on the control samples.
14 days at 86 percent relative humidity, 24 hr at room humidity.	The number of spots on the samples was about 50 percent of those on the control samples showing appreciable inhibition of spot formation. Most of the spots were in the high density areas and were larger than those on the control samples.
41 days at 86 percent relative humidity, 66 days at room humidity.	The number of spots on the samples was about 10 percent of that on the control samples. Spot formation was inhibited more in the low density areas than in the high and the edges of the spots were not as well defined as those in the control samples.
7 months at 86 percent relative humidity, 20 days at room humidity.	A few spots formed in the high density areas and none in the low. The edges of the spots were not as well defined as those in the controls.

Tests were made to determine the effect of desiccation on blemish formation in processed microfilm. Microfilm strips were dried over anhydrous calcium sultate for 5 months at 26 °C, stored 7 days at room humidity and 26 °C and with control samples exposed to the peroxide paper. The number of spots formed in the low densities were appreciably less than on the control samples and slightly less in the high densities. The spots on the desiccated samples showed a better defined ring structure than those on the control samples. Other samples from the desiccated microfilm strips were exposed to peroxide paper after storage for about 6 months at room humidity and 26 °C. The spot formation was similar to that of the control samples. The tests showed that desiccation reduced the spot forming susceptibility but it recovered after storage for about 6 months at room humidity.

4. Blemish Formation in Coarse-Grain Processed Microfilm

The tests described above in this and a previous paper [1] have been made on fine-grain microfilms. However, microfilms with a larger grain are also used for record purposes. This microfilm is designated as coarse-grain microfilm in this paper. A few blemishes, mostly spots, have been found in processed coarse-grain microfilms in actual storage. Observations made on all types of film in storage indicated that the susceptibility to blemish formation decreased as the grain size increased. The effect of processing variables was investigated for one coarse-grain microfilm.

367 -409 OL-70—3

The coarse-grain 16-mm microfilm was exposed, developed, stopped, fixed, washed, dried, and exposed to peroxide by the same procedures as described for fine-grain microfilm [1]. Some microfilm samples were fixed in a neutral bath and others in an acid hardening bath, and samples were washed 3, 15, and 30 min, respectively, at 26 °C in chlorine-free tap water. None of these samples formed spots on exposure to peroxide, although there was a light even yellowing of the silver image. Fine-grain microfilm was very susceptible to spot formation when processed by the same procedures. In another series of tests, mocrofilm samples were fixed in the nonhardening bath or the acid hardening bath and washed, 3, 7½, 15, 30, or 60 min in running tap water at 25 °C, containing 1.2 ppm of chlorine. There was a light even yellowing of the silver image for the 3 and 7½-min washes and a few spots without background yellowing for the 15, 30, and 60-min wash. Fine-grain microfilm processed by these same procedures formed many spots in samples washed 3 min but none in those washed 15, 30, and 60 min. The tests suggest that chlorine in the tap wash water formed a trace of residual silver chloride in the image silver, making it susceptible to some spot formation in the longer washes. It is evident from these tests that grain size is one of the factors in blemish formation.

5. Ammonium Thiosulfate Versus Sodium Thiosulfate for Fixing

Tests were made to determine the effect of fixation in an acid hardening bath containing 200 g of anhydrous ammonium thiosulfate, 15 g of sodium sulfite, 15 ml of glacial acetic acid, 7.5 g of boric acid, and 15 g of potassium aluminum sulfate per liter. A nonhardening bath, containing 150 g of anhydrous ammonium thiosulfate and 68 g of sodium bisulfite per liter, was also tried, as was a neutral bath containing 150 g of anhydrous ammonium thiosulfate per liter. A fine-grain 16-mm microfilm was exposed, developed, stopped, fixed, dried, and exposed to peroxide by the same procedure as previously described [1] except that ammonium thiosulfate fixing baths were used instead of the sodium thiosulfate baths.

Microfilm samples were fixed in the neutral bath and washed 3, 15, or 30 min in chlorine-free tap water at 26 °C. The samples formed large light yellow spots, light yellowing of the image silver and edge attack. The blemish attack was similar to that found on films fixed in neutral sodium thiosulfate.

Microfilm samples were fixed in the nonhardening bath and washed 3, 15, or 30 min in chlorine-free tap water at 26 °C. The samples developed several small light yellow spots, some yellowing of the image silver, and slight edge attack. Resistance to spot formation was greater than in samples fixed in a nonhardening sodium thiosulfate bath.

Microfilm samples were fixed in the acid hardening bath and washed 3, 15, or 30 min in chlorine-free tap water at 26 °C. Samples washed 3 min developed a few small spots and a trace of even yellowing, but no attack on the edge of the information. No blemishes formed on samples washed 15 or 30 min. Thus microfilm fixed in an ammonium thiosulfate acid hardening bath was more resistant to blemish formation than that fixed in a sodium thiosulfate acid hardening bath. The same microfilm fixed in a sodium thiosulfate acid hardening bath and washed 30 min in chlorine-free tap water readily formed spots [1].

Microfilm samples were fixed in the acid hardening bath and washed 3, 7½, 15, or 30 min in running tap water containing 1.2 ppm of chlorine, at 25 °C. Samples washed 3 min showed a few spots with irregular edges and some even yellowing, but no attack on the edge of the image characters. No blemishes formed on samples washed 7½, 15, or 30 min. The results in this last test approximate those obtained with films fixed in a sodium thiosulfate acid hardening bath and washed in tap water containing about 1 ppm of chlorine.

Ammonium thiosulfate fixing made the microfilm more resistant to spot formation than sodium thiosulfate fixing, when the microfilm was washed in chlorine-free tap water. The susceptibility was about the same if the film was washed in tap water containing about 1 ppm of chlorine.

6. Detection of Peroxide Evolved by Oven-Aged Storage Cartons

Three paper cartons, made by three manufacturers and designed for storing 16-mm microfilm, were tested for peroxide formation due to aging. Tests for peroxide on the three cartons before aging were negative. The cartons were aged at 100±3 °C in an oven without forced ventilation for 7 and 14 days or in a furnace oven at 175±5 °C for 2 hr.

Hydrogen peroxide forms a soluble yellow complex compound with titanium in a sulfuric acid solution. When sulfuric acid is exposed to the gases emitted by aged paper, the acid takes on a yellowish tint. A deeper yellow color in the presence of titanium ions was taken as a positive test for the presence of peroxide.

The following procedure was used in making qualitative tests for peroxide evolved by the paper cartons. About 10 g of the paper carton stock was cut into 1 cm^2 pieces and placed in a flat weighing bottle about 65 mm in diameter and 45 mm high, when closed, and having an enclosed volume of about 150 ml. The cover was a ground glass fit. One 5-ml beaker containing 3 ml of a solution of titanium ions in 9 molar sulfuric acid and a second 5-ml beaker containing 3 ml of 9 molar sulfuric acid, as a control solution, were placed in the weighing bottle with the paper carton stock. About 15 ml of distilled water was poured on the paper and the weighing bottle was closed and allowed to stand for 6 to 24 hr at 26 °C. The evolved gases were absorbed by the titanium-sulfuric acid solution and the sulfuric acid solution forming a yellow layer at the surface of each solution. The solutions were stirred and then viewed from the top of the beakers to determine the difference in the depth of the yellow color. The aqueous solution in contact with the paper was also tested for peroxide by adding

1 ml of that solution to 3 ml of the titanium-sulfuric acid solution and to 3 ml of the sulfuric acid solution in 5-ml beakers.

The titanium solution was prepared by treating about 10 g of titanium dioxide with about 150 ml of concentrated sulfuric acid in a glass stoppered bottle at 50 °C for one week with occasional stirring and filtering through a medium porosity glass filter without pressure. Filtration may require 1 to 3 days and the funnel should be kept covered. The filtrate was diluted with an equal volume of distilled water by slowly pouring the sulfuric acid solution down the side of the flask into the distilled water with frequent mixing to obtain a 9 molar solution containing titanium ions. A 9 molar solution of sulfuric acid was made up for the control solution.

The test for peroxide formation was positive in the evolved gases and the aqueous solutions for the three cartons. The yellow color in the test solution was light for cartons aged for 7 days at 100 °C, more yellow after aging 14 days at 100 °C, and a deep yellow after aging 2 hr at 175 °C. Cartons aged at 100° for 7 and 14 days showed some visual degradation. Cartons aged at 175 °C for 2 hr became brittle and sometimes slightly charred showing exteme degradation. One high grade filter paper, aged at 175° for 2 hr, gave a positive test for peroxides in the gases evolved. A sample of multigraph paper, brownish in color and about 20 years old, also evolved peroxide gases. One cellulose acetate microfilm base, with gelatin layer removed, aged at 175 °C for 2 hr gave a negative test for peroxides in the gases evolved and in the aqueous solution.

The paper cartons underwent degradation during aging, probably forming peroxide groups in the cellulose as indicated by Kleinert and Marraccini [3]. Resinous materials, usually present, may also form peroxides. These results lend considerable weight to the theory that paper cartons slowly degrade with time especially at high temperatures and high relative humidities to form peroxides which attack the image silver in the microfilm to form blemishes. Peroxide groups probably form in the paper carton over a period of time and are released as a gas by hydrolysis at high relative humidity. This reaction may be repeated several times as spots with several rings have been found on microfilm in storage. Spots with many rings were produced in the laboratory by exposing the microfilm several times to 1 cm^2 of the peroxide paper containing about 80 μg of hydrogen peroxide. Thus Liesegang reactions may not be required to account for the ring structure, as has been suggested.

7. Absorption of Peroxide by the Cellulose Acetate Base

Four microfilm bases or supports, made by four manufacturers, were permeable to gaseous hydrogen peroxide. Microfilm base samples, clear or dyed, used for tests were prepared by removing the gelatin layer and backing, if any, from unprocessed microfilm by scraping with a razor blade. Processed microfilm susceptible to blemish formation was stapled to the microfilm base samples with the emulsion side next to the microfilm base and the other side of the microfilm base was sealed with petroleum jelly to the top of a glass vial, 15 mm in diameter and 45 mm long, containing peroxide paper having about 40 μg of hydrogen peroxide per cm^2. The vial was then stored in a desiccator jar at 86 percent relative humidity at 26 °C for 24 hr. The hydrogen peroxide diffused through each of the four microfilm bases, forming a few light yellow spots and light even yellowing in the image silver of the attached processed microfilm. Processed microfilm susceptible to blemish formation sealed to the vial in the above test with the base exposed to the gas suffered the same blemish formation in the image silver by diffusion of the peroxide through the microfilm base.

The four above microfilm bases were tested for absorbed hydrogen peroxide. Samples were stapled between two sheets of peroxide paper containing about 170 μg of hydrogen peroxide per cm^2, stored in a glass bottle at room humidity and 26 °C for 24 hr, removed from the bottle, exposed to room atmosphere for 24 hr, and tested for peroxide by dissolving a 1 cm^2 sample in 3 ml of the titanium-sulfuric acid solution described in section 6. When the sample contained absorbed peroxide it turned yellow before complete solution and dissolved in about 2 hr with occasional stirring to form a yellow colloidal solution. If no peroxide was present the sample turned white before complete solution and the colloidal solution was white. The microfilm bases formed a yellow color in the titanium-sulfuric acid solution while dissolving and in the colloidal solution. An uncoated cellulose acetate strip also showed a yellow color in the titanium-sulfuric acid solution.

Microfilm base which absorbed and retained the peroxide was used to detect peroxide evolved by aged storage cartons. Two of the microfilm bases did not retain the absorbed peroxide during the tests on the aged storage cartons. It is not known what determines the retention of peroxide by film bases. The subbing, plasticizer or other compounds may be determining factors. Samples of clear microfilm base were stored at 86 or 100 percent relative humidity and 26 °C in a desiccator jar for 24 hr in closed microfilm storage cartons which had been aged for 14 days at 100 °C or 2 hr at 175 °C. The microfilm base was tested for absorbed peroxide immediately after removal from the carton by dissolving 1 cm^2 samples in 3 ml portions of each of the titanium-sulfuric acid solution and the sulfuric acid solution described in section 6. Gaseous compounds other than peroxide formed a yellow colloidal solution in both of the above solutions. The samples turned yellow in both solutions before dissolving but the one in the titanium-sulfuric acid solution was always a deeper yellow than the control solution. The color in the colloidal solution containing titanium ions was also always a deeper yellow than the control solution and this was taken as evidence that peroxide had been emitted by the aged cartons and absorbed by the microfilm base.

Absorption of peroxides by the microfilm was shown to precede blemish formation. Samples of a microfilm susceptible to blemish formation were exposed 4 hr to 1 cm^2 of peroxide paper, containing about 80 μg of hydrogen peroxide, in a desiccator at 86 percent relative humidity and 26 °C. The samples evidenced no blemishes when examined with a stereomicroscope at a magnification of 30. The samples were immediately stored in another desiccator containing no peroxide at 86 percent relative humidity and 26 °C. After 20 hr a few colorless minute spots formed in the high densities of the image silver, indicating that peroxide had been absorbed before spots developed.

8. Summary

Peroxide paper or zinc powder were used as peroxide sources for testing the susceptibility of processed microfilm to blemish formation. Microfilm samples having a high susceptibility to spot formation were used as controls in the test procedures.

Conditioning of processed microfilm at 86 percent relative humidity and 26 °C reduced blemish formation. Only a few spots formed in the high densities after conditioning for 7 months. About 10 percent as many spots formed after conditioning for 41 days, about 50 percent as many spots after 14 days and a slight reduction in spot formation after 7 days when compared to spot formation in the control samples. Samples desiccated for 5 months over anhydrous calcium sulfate showed a noticeable decrease in spot formation but after storage for about 6 months at room atmosphere, the spot formation was similar to that of the control samples.

Coarse-grain microfilm fixed in a neutral bath or an acid hardening bath and washed 3 to 30 min in chlorine-free tap water formed no spots but a light even yellowing of the image silver when exposed to peroxide. In comparison, fine-grain microfilm was very susceptible to spot formation when processed by the same procedures. The coarse-grain microfilm fixed in a nonhardening or acid-hardening bath and washed in tap water containing 1.2 ppm of chlorine showed a light even yellowing in samples washed 3 and 7½ min and a few spots in those washed 15 to 60 min. In comparison, fine-grain microfilm formed many spots if washed 3 min but none in those washed 15, 30, and 60 min when processed by the same procedures.

Fine-grain microfilm fixed in an ammonium thiosulfate nonhardening bath and washed in chlorine-free tap water showed more resistance to spot formation than film fixed in a sodium thiosulfate nonhardening bath. Fing-grain microfilm fixed in the ammonium thiosulfate acid hardening bath and washed in chlorine-free tap water formed a few small spots and a trace of even yellowing on samples washed 3 min and no spots on samples washed 15 or 30 min. In comparison, fine-grain microfilm fixed in the sodium thiosulfate acid hardening bath by the same procedure was very susceptible to spot formation. Fine-grain microfilm fixed in an ammonium thiosulfate acid hardening bath and washed in running tap water containing 1.2 ppm of residual chlorine formed blemishes about as readily as film fixed in a sodium thiosulfate acid hardening bath by the same procedure.

Paper cartons used for storage of microfilms aged for 7 and 14 days at 100 °C and for 2 hr at 175 °C gave a positive test for peroxide in both the gases evolved and the water solution in contact with the sample tested.

Microfilm base readily absorbed hydrogen peroxide when clamped between sheets of the peroxide paper. Microfilm base samples stored in aged paper cartons at 86 or 100 percent relative humidity and 26 °C gave a positive test for peroxide, evidencing absorption of peroxide emitted by the storage carton. Tests indicated that hydrogen peroxide diffused through the base of microfilm to form small spots and even yellowing in the image silver. Spots developed in microfilm when the exposure to peroxide was terminated before spot formation was visible.

9. References

[1] Pope, C. I., Blemish formation in processed microfilm, Nat. Bur. Stand. (U.S.), **72A** (Phys. and Chem.), No. 3, 251–259 (May–June 1968).

[2] Henn, R. W., and D. G., Wiest, Microscopic spots in processed microfilm; their nature and prevention, Photo. Sci. Eng. **7**, 253 (1963).

[3] Kleinert, T. N., and Marraccini, L. M., Aging and colour reversion of bleached pulps, Svensk Papperstidning **66**, 189–195 (Jan.–June 1963).

(Paper 74A1–581)

JOURNAL OF RESEARCH of the National Bureau of Standards—A. Physics and Chemistry
Vol. 74A, No. 1, January–February 1970

Positive and Negative Ion Sublimation from Transition Metal Surfaces: A Review of Some Recent Results

Milton D. Scheer

Institute for Materials Research, National Bureau of Standards, Washington, D.C. 20234

(September 8, 1969)

Singly charged, positive and negative, atomic ions have been observed to sublime freely from 4*d* and 5*d* transition metal surfaces in the 1800 to 2600 K temperature range. The rates of sublimation were found to be about equal to those which would be observed under conditions of thermal equilibrium. Ion sublimation energies were obtained from the temperature dependence of these sublimation rates. The energies were found to be consistent with currently accepted values for the atom sublimation energy, electron work function, and first ionization potentials of the elements investigated.

The electron affinities of these metal atoms were determined from an isothermal measurement of the ratio of positive to negative ion sublimation rates. The results were compared with some recent theoretical estimates of this quantity for those 3*d* transition metals whose valence electron configurations are analogous to the 4*d* and 5*d* elements considered here.

Key words: Mass spectrometry; positive and negative ions; sublimation; transition metals.

An atomically clean metal surface may be characterized by the energies associated with the sublimation processes:

(1) $e_s \rightarrow e_g$; ϕ, the electron work function

(2) $M_s \rightarrow M_g$; l_0, the atom sublimation energy

(3) $M_s - e_s \rightarrow M_g^+$; l_+, the positive ion sublimation energy

(4) $M_s + e_s \rightarrow M_g^-$; l_-, the negative ion sublimation energy.

At temperatures less than about $\frac{2}{3}$ of the melting point, the energies associated with these processes may be strongly influenced by the geometric arrangement of the surface atoms. The observed difference in work function between different crystalline faces is an example of such anisotropic behavior. At high temperatures the geometric structure and symmetry characteristics of the surface become less important as a result of rapid surface migration and large sublimation rates. In fact, in the neighborhood of the melting point the surface can be thought of as a two-dimensional liquid whose properties tend to be uniform in contrast to the considerable anisotropy exhibited at lower temperatures.

Process (3) has been observed for a number of refractory transition metals [1–8, 10].[1] Early attempts at a reliable measurement of l_+ were limited by primitive vacuum conditions and the presence of easily ionized alkali atom impurities. Process (4) can be observed when $A(M)$, the electron affinity of M, is positive (M_g^- is stable). It has been reported for graphite, tungsten, rhenium, molybdenum, and tantalum [7, 8, 9, 10].

1. A Generalized Saha-Langmuir Equation

Consider the thermodynamic equilibrium existing inside of an isothermal metal enclosure. In addition to blackbody photons, the stable gaseous species are electrons e_g, metal atoms M_g, singly charged positive ions M_g^+, and singly charged negative ions M_g^- when the electron affinity of the atom is positive. If the number density of charged particles is sufficiently small so that space-charge effects may be neglected, then the partial pressures (p_x) are governed by the following equilibria:

$$M_g \mp e_g \rightleftharpoons M_g^{\pm}; \quad \Delta E = +I \text{ upper sign for positive ionization} \quad = -A \text{ lower sign for negative ionization.}$$

The quantity ΔE is the energy (or free-energy) change for these ionization processes at absolute zero. The equilibrium constants are given by

$$(p_{\pm}/p_0)(p_e)^{\pm 1} = (Q_{\pm}/Q_0)(Q_e)^{\pm 1} \exp(-\Delta E/kT). \quad (1)$$

[1] Figures in brackets indicate the literature references at the end of this paper.

The Q's are the molar partition functions for these gaseous species which are assumed to be in thermal equilibrium with the walls of the enclosure. The partial pressure of electrons (p_e) is given by the well-known Richardson equation:

$$p_e = Q_e \exp(-\phi/kT) \tag{2}$$

The electronic work function ϕ is defined as the free-energy change at 0 K for electron sublimation. Substituting eq (2) into (1) yields the result that

$$(p_\pm/p_0) = (Q_\pm/Q_0) \exp[(-\Delta E \pm \phi)/kT]. \tag{3}$$

The flux (j) of particles evaporating from (or condensing upon) the walls of the enclosure is given by

$$j = \alpha p/(2\pi mkT)^{1/2} \tag{4}$$

where α is the evaporation (or condensation) coefficient and p is the equilibrium vapor pressure. Since the masses (m) of the atomic ions and atoms are very nearly equal and, *assuming* that the *evaporation coefficients* for *ions* and *atoms* are also *equal*, the ratio of sublimation rates obtained from eqs (3) and (4) is

$$j_\pm/j_0 = (Q_\pm/Q_0) \exp[(-\Delta E \pm \phi)/kT]. \tag{5}$$

For the atomic and ionic species under consideration, the ratio of molar partition functions is equal to the ratio of electronic partition functions:

$$(Q_\pm/Q_0) = (\omega_\pm/\omega_0),$$

since the translational factors cancel because of the equality of the particle masses. When Russel-Saunders spin-orbit coupling is obeyed, the electronic partition function can be written as

$$\omega = \sum_n g_n \exp(-\epsilon_n/kT) \tag{6}$$

where $\epsilon_0 = 0$ and $g_n = 2J_n + 1$. The quantity g_n is the statistical weight of the level of energy ϵ_n, and J_n the inner quantum number of the electronic state n. The summation need only be carried out for those states which are significantly populated at the temperature T. Under the condition of thermal equilibrium on the metal surface, eq (5) yields a result for the sublimation ratio of singly charged positive ions to neutral atoms which may be recognized as the familiar Saha-Langmuir equation [11]; namely,

$$j_+/j_0 = (\omega_+/\omega_0) \exp[(\phi - I)/kT]. \tag{7}$$

Similarly, when negative self-surface ionization is considered, eq (5) yields the ratio of subliming negative ions to atoms:

$$j_-/j_0 = (\omega_-/\omega_0) \exp[(A - \phi)/kT]. \tag{8}$$

The ratio of positive to negative self-surface ionization, obtained from eqs (7) and (8), is

$$j_+/j_- = (\omega_+/\omega_-) \exp[(2\phi - I - A)/kT]. \tag{9}$$

The atomic properties I and A can be shown to be related to the sublimation energies ϕ, l_0, l_+, and l_- from a consideration of the cycles given in figure 1; namely, that

$$\phi - I = l_0 - l_+, \tag{10}$$

$$A - \phi = l_0 - l_-, \tag{11}$$

and

$$2\phi - I - A = l_- - l_+ = l_0 + \phi - A - l_+. \tag{12}$$

The equilibrium vapor pressure of metal atoms (p_0) is given by

$$p_0 = \exp[(\Delta S/k) - (l_0/kT)], \tag{13}$$

where ΔS and l_0 are the atom sublimation entropy and energy at some temperature T. Substituting eq (13) into (3), one obtains for the sublimation pressure of positive and negative ions:

$$p_\pm \left[\frac{Q_0}{Q_\pm} \exp\left(\frac{-\Delta S}{k}\right)\right] = \exp\left(\frac{-\Delta E \pm \phi - l_0}{kT}\right). \tag{14}$$

Using eq (4) and collecting terms, the dependence of the rates of positive- and negative-ion sublimation upon temperature is given by

$$j_+\left[T^{1/2}\left(\frac{\omega_0}{\omega_+}\right) \exp\left(-\frac{\Delta S}{k}\right)\right] = \frac{\alpha_+}{(2\pi\, mk)^{1/2}} \exp\left(\frac{\phi - I - l_0}{kT}\right) \tag{15a}$$

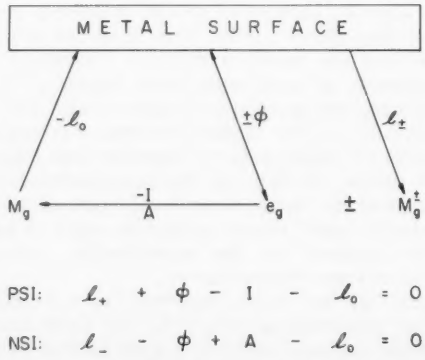

FIGURE 1. *Thermal cycles for positive and negative self-surface ionization.*

and

$$j_- \left[T^{1/2} \left(\frac{\omega_0}{\omega_-} \right) \exp \left(-\frac{\Delta S}{k} \right) \right]$$

$$= \frac{\alpha_-}{(2\pi mk)^{1/2}} \exp \left(\frac{A - \phi - l_0}{kT} \right), \qquad (15b)$$

where from eqs (10) and (11) it is seen that $\phi - I - l_0 = -l_+$ and $A - \phi - l_0 = -l_-$. The l's are sublimation energies at some mean temperature T in the middle of an experimental temperature range, and, like ϕ, I, and A, remain virtually unchanged from their values at absolute zero.

2. Apparatus

The apparatus used in these studies consisted of a direction-focusing mass spectrometer. The surface ionization source of the mass analyzer was designed to facilitate the collection of negative ions, which evaporate in observable quantities only at surface temperatures at which electron emission is intense. A cylindrical modification of a Pierce lens [12] was used to collect the charged particles evaporating from the experimental surfaces. When the apparatus was biased for the detection of negative charges, the large electron flux focused by the lens was deflected by a small magnetic field and collected on a molybdenum plate. Because of space limitations in the ion source, the lens design was limited to the efficient collection of only about 2 mA of electron emission. At surface temperatures in excess of that which yields this value of the saturation electron current, a negative space charge begins to accumulate and the collection efficiency for negative ions decreases. This problem is not encountered in the case of positive ion sublimation so that meaningful measurements at a constant ion collection efficiency can be made at higher surface temperatures and larger positive ion currents.

Both the positive and negative ions were accelerated by the components of the Pierce lens to an energy of 4 kV prior to their traversal through the entrance slit of the 15-cm radius, 60° sector, magnetic analyzer. The first dynode of a 16-stage Cu-Be electron multiplier detector was maintained at ground potential, so that both positive and negative mass analyzed ions were collected with 4 kV of energy. The multiplier was operated with 190 V between stages so that the sixteenth dynode was at +3040 V for both positive- and negative-ion detection. The output pulses were 20 to 30 ns. wide and were amplified with a voltage gain of 5000. The resultant pulse-height distribution was found to be about the same for both positive and negative ions. Thus, the secondary electron yields for 4 kV positive and negative ions impacting on the first dynode surface do not appear to exhibit any significant charge discrimination. This is of particular importance for the determination of the ratio of positive to negative ion sublimation rates. The amplified pulses were then processed to give uniform 1-V, 50-ns pulses which actuated a counter with a 10-MHz bandpass. The background count for this instrument was usually less than 10 pulses/minute with the magnetic analyzer detuned and the experimental surface temperature well below 1800 K.

3. Experimental Results

The temperature dependence of the rates of sublimation of singly charged positive and negative ions of tungsten, rhenium, molybdenum, and tantalum are shown in figures 2, 3, and 4. Figure 5 gives the results of some measurements of the rate of positive ion sublimation from a niobium surface. The quantity $j_\pm$ (corrected) is the experimental ion count corrected for the slightly temperature dependent factor

$$[T^{1/2}(\omega_0/\omega_\pm) \exp(-\Delta S/k)]$$

given on the lefthand side of eqs (15a) and (15b). The values obtained for this factor were normalized in the middle of each experimental temperature range. The values for ΔS were obtained from the compilation of Stull and Sinke [13]. The ω_0 and ω_+ were calculated from eq (6) using Moore's energy level compilation [14]. For the negative ion electronic partition function ω_-, only one bound state was assumed with a J_0 value equal to that of the ground state of the atom with the next highest atomic number. This assumption appears to be reasonable since virtually all of the negative ions which have been observed so far exhibit this property [15]. The evaporation coefficients ($\alpha_\pm$) were assumed to be temperature independent with values of unity.

Table 1 gives a summary of the sublimation energies, obtained in this laboratory, for the positive ions of a number of transition metals [5, 7, 8, 10] of rows 4 and 5 of the periodic table. The agreement between the l_+ calculated from eq (10) and the experimental values

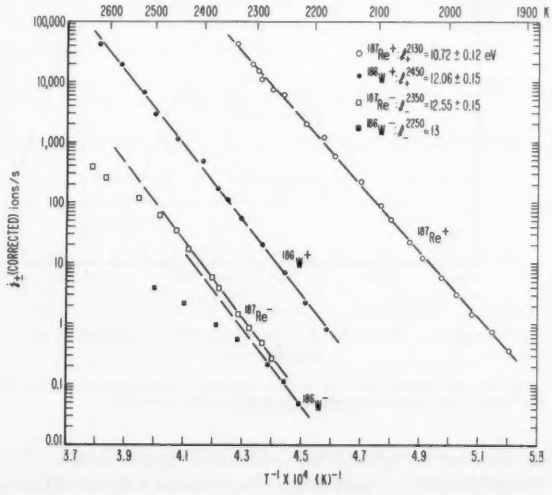

FIGURE 2. *Positive and negative self-surface ionization of tungsten and rhenium.*

The uncertainties in the sublimation energies are the standard errors in the slopes of the lines.

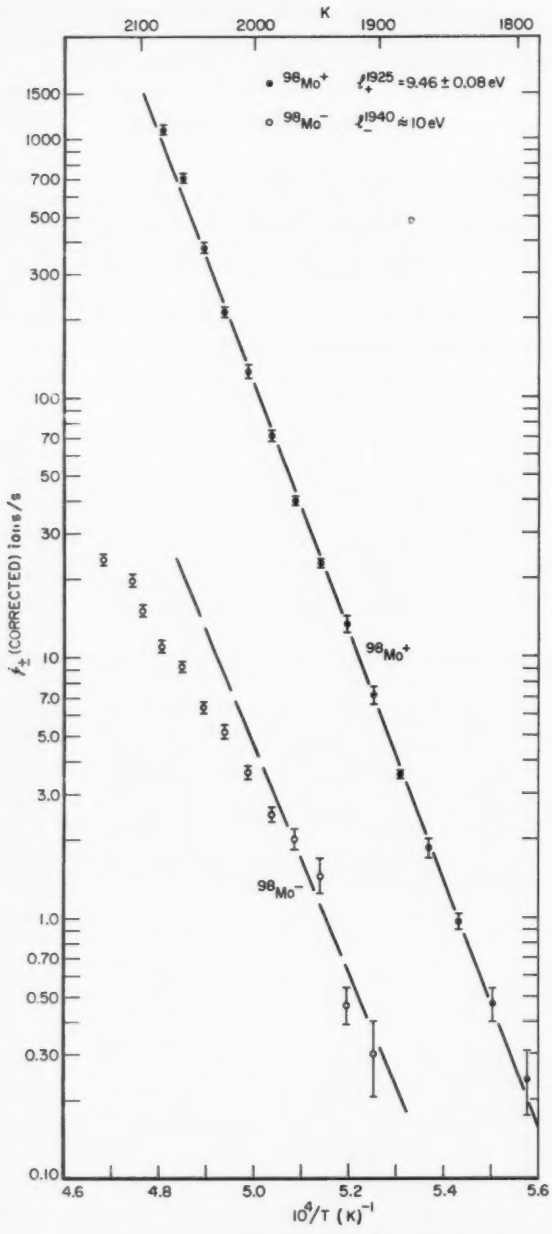

FIGURE 3. *Positive and negative self-surface ionization of molybdenum.*

The error bars represent the range of values obtained in at least ten determinations. The uncertainty in the sublimation energy is the standard error in the slope.

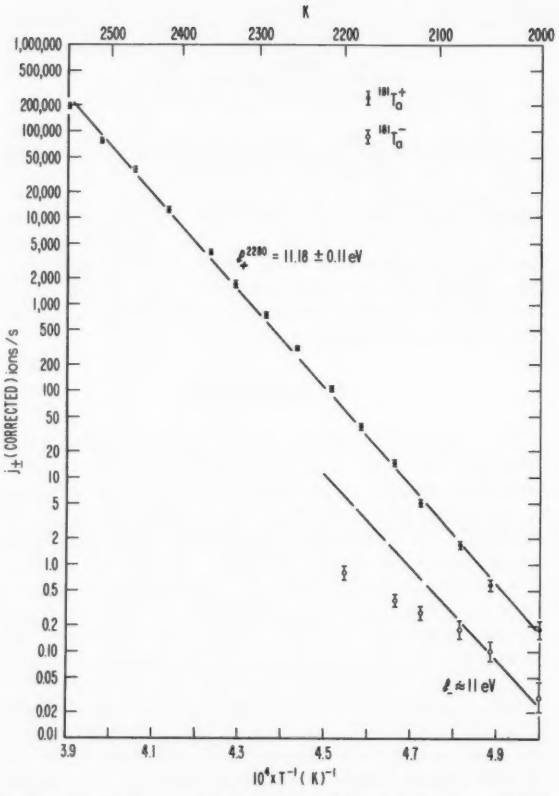

FIGURE 4. *Positive and negative ion sublimation from a tantalum surface.*

The error bars represent the range of values obtained in at least ten determinations. The uncertainty in the sublimation energy is the standard error in the slope.

is seen to be within the estimated uncertainties. The quantities l_0, I, and ϕ for these metals were obtained from recent compilations [10, 13, 14, 16]. The intercepts of all of the experimental lines given in figures 2 to 5, divided by the subliming surface areas, fall within a factor of three of a value 5×10^{28} cm^{-2} sec^{-1}. This is consistent with a maximum limiting sublimation rate of one monolayer ($\sim 10^{15}$ cm^{-2}) per lattice vibration time ($\sim 10^{-14}$ s). It can therefore be concluded that a relatively large fraction of the evaporating ions was focused by the Pierce lens into the mass analyzer and ultimately detected by the electron multiplier. This result, together with the demonstrated validity of the thermal cycle eq (10), supports the conclusion that the observed free sublimation rates are approximately equal to those which would be observed in a closed

TABLE 1. *Positive ion sublimation energies*

Ion	T	[a] $l_{+(\text{obs.})}$	[b] $(l_0+I-\phi)$
	(K)	(eV)	(eV)
$^{93}Nb^+$	2100	10.4	7.5+6.8−3.9=10.5
$^{98}Mo^+$	1925	9.5	6.7+7.1−4.3=9.5
$^{181}Ta^+$	2280	11.2	7.9+7.9−4.1=11.7
$^{186}W^+$	2450	12.1	8.9+8.0−4.5=12.4
$^{187}Re^+$	2130	10.7	7.8+7.9−5.0=10.7

[a] Typical standard errors in the least square determination of l_+ are between 0.1 and 0.2 eV.

[b] Uncertainties in l_0, I and ϕ are each about 0.1 eV.

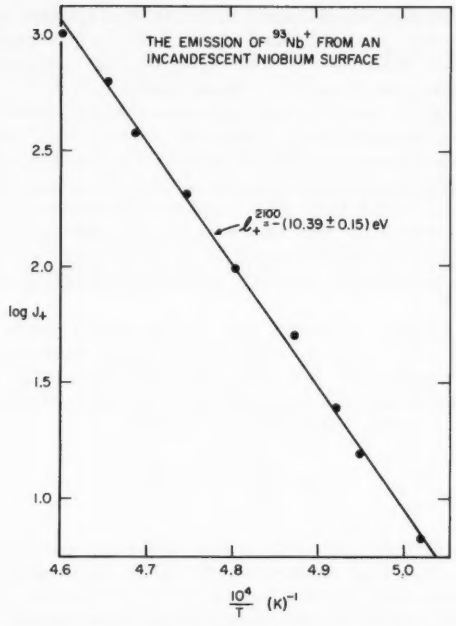

FIGURE 5. *The sublimation of* $^{93}Nb^+$ *from a heated niobium surface.*

The uncertainty in the sublimation energy is the standard error in the slope of the line.

system in thermal equilibrium with vaporization coefficients ($\alpha_\pm$) not very different from unity.

The ratio of positive to negative self-surface ionization could be reliably measured only over a rather limited temperature range. This is seen in figures 2 to 4, where the lowest temperature was determined by the smallest negative ion sublimation rate detectable with the present apparatus (5 to 20 ions/minute). The upper temperature was limited by an electron emission which was sufficient to saturate the Pierce lens. This resulted in a negative space charge buildup with a consequent lowering of the negative ion collection efficiency. It is seen that this limiting temperature was about 2100 K for the low work function metals, tantalum and molybdenum, while the higher work functions of tungsten and rhenium allowed efficient negative ion collection up to temperatures of 2300 and 2500 K, respectively.

The results obtained for these positive to negative ion ratios are given in table 2. The quantities j_+ and j_- are the actual ion count rates observed at each of the experimental temperatures. The partition function ratios (ω_-/ω_+) were calculated in the manner described above. The quantity $kT \ln [(\omega_-/\omega_+)(j_+/j_-)]$, given in the last column, is equal to $(2\phi - I - A)$ or $(\phi + l_0 - l_+ - A)$ according to eqs (9) and (12). Solving (9), (10), (11), and (12) for A, the electron affinity, yields

$$A = \phi + l_0 - l_- = \phi + l_0 - l_+ - kT \ln \left[\frac{\omega_- j_+}{\omega_+ j_-} \right]. \qquad (16)$$

TABLE 2. *Isothermal positive to negative ion ratios obtained for the self-surface ionization of molybdenum, tantalium, tungsten, and rhenium.*

The errors given for j_+ and j_- are average deviations from an arithmetic mean of at least six successive ion counts.

Ion	T	j_+	j_-	$kT \ln [\omega_- j_+/\omega_+ j_-]$
	(K)	(ions/sec)	(ions/sec)	(eV)
^{98}Mo	1903	7.4 ± 0.4	0.30 ± 0.12	0.53 ± 0.07
	1924	13.3 ± 0.6	0.45 ± 0.08	0.56 ± 0.03
	1945	22.3 ± 0.5	1.40 ± 0.20	0.46 ± 0.02
	1965	37.5 ± 0.4	1.87 ± 0.13	0.51 ± 0.01
	1985	66.8 ± 1.5	2.30 ± 0.15	0.58 ± 0.01
				0.53 ± 0.03 eV
^{181}Ta	2000	0.18 ± 0.04	0.03 ± 0.01	−0.04 ± 0.08
	2047	0.58 ± 0.10	0.10 ± 0.03	−0.06 ± 0.06
	2077	1.67 ± 0.13	0.18 ± 0.05	+0.02 ± 0.06
				−0.03 ± 0.07 eV
^{186}W	2225	3.0 ± 0.2	0.07 ± 0.03	0.76 ± 0.08
	2250	6.6 ± 0.2	0.18 ± 0.03	0.74 ± 0.04
	2280	12.6 ± 0.2	0.30 ± 0.06	0.77 ± 0.04
				0.76 ± 0.05 eV
^{187}Re	2272	7,210 ± 40	0.32 ± 0.05	2.01 ± 0.03
	2290	11,020 ± 60	0.49 ± 0.04	2.02 ± 0.02
	2314	18,650 ± 100	0.84 ± 0.08	2.04 ± 0.02
	2333	30,730 ± 120	1.40 ± 0.15	2.06 ± 0.02
				2.03 ± 0.02 eV

Table 3 gives the electron affinities for the four transition metals. They were calculated using eq (16). A reliable value for l_- could be obtained from eq (15b) only in the case of rhenium, as shown in figure 2. Consequently, it was possible to make two independent estimates of its electron affinity. It is seen that, despite the small absolute value of A(Re), the agreement between the two estimates is good and considerable confidence in the stability of Re^- is gained.

TABLE 3. *The electron affinities of* Mo, Ta, W, *and* Re *as calculated from eq (16).*

	$\phi + l_0 - l_+ - kT \ln [\omega_- j_+/\omega_+ j_-]$	$(\phi + l_0 - l_-)$
	eV	(eV)
A(Mo):	4.3 + 6.7 − 9.5 − 0.5 = 1.0	.....
A(Ta):	4.1 + 7.9 − 11.2 + 0.03 = 0.8	.....
A(W):	4.5 + 8.9 − 12.1 − 0.8 = 0.5	.....
A(Re):	5.0 + 7.8 − 10.7 − 2.0 = 0.1	5.0 + 7.8 − 12.6 = 0.2

4. Conclusions

It has been shown that at temperatures in excess of about 1800 K the sublimation of singly charged, positive and negative ions from refractory metal surfaces are in accordance with the thermal cycle eqs (10) and (11). The measured quantities l_+, l_-, and A are consistent with the currently accepted values for

l_0, ϕ, and I. Under the high-temperature conditions of these measurements, no evidence for surface anisotropy was observed.

A detailed review of atomic negative ions has been given recently by Smirnov [17]. He summarized both the experimental and theoretical electron affinity estimates that have been made for the elements of rows, 2, 3, and 4 and columns 1 and 6 of the periodic table. The experimental results given here are the first determinations of the electron affinities of the transition elements in rows 5 and 6. The method described should be applicable to all of those refractory metals whose atoms can form stable negative ions.

Clementi [18] has made a set of Hartree-Fock calculations for the 4th-row transition elements. From these calculations he was able to make correlation energy corrections to the 4th-row negative ion energies and hence obtained estimates of the electron affinities. Table 4 shows a comparison between these theoretical estimates and the self-surface ionization values determined in this laboratory for the 5th- and 6th-row transition metals. The value for niobium was estimated on the basis of approximate negative ion yields. Because of its low work function [5] (~ 3.9 eV), copious electron emission made it impossible to obtain accurate positive to negative ion ratios with the present instrument. Molybdenum and chromium as well as tantalum and vanadium have analogous valence electron configurations and there is remarkably good agreement between the theoretical and measured electron affinities. In the case of the manganese-rhenium pair, however, where there is a full s and half-filled d shell in their ground-state configurations, there is disagreement. Clementi predicts that such a valence electron structure should *not* yield a stable negative ion. In fact, his calculation gives a value of -1.1 eV for A(Mn). The negative self-surface ionization of rhenium has shown however, that the $5d^5 6s^2$ structure is indeed capable of producing a stable rhenium negative ion with a binding energy of about 0.15 eV.

TABLE 4. *Electron affinities*

(Comparison with theoretical estimates)

E. Clementi: Phys. Rev. **135**, A980 (1964). (correlation energy estimates)		V	Cr	Mn
	4th row valence electron configuration	$3d^3 4s^2$	$3d^5 4s$	$3d^5 4s^2$
	A(eV)	0.94 ± 0.25	0.98 ± 0.35	-1.07 ± 0.20
This work: (self-surface ionization)		Nb	Mo	Tc
	5th row valence electron configurtion	$4d^4 5s$	$4d^5 5s$	$4d^5 5s^2$
	A(eV)	~ 1.0 (est.)	1.0 ± 0.2	.....
		Ta	W	Re
	6th row valence electron configuration	$5d^3 6s^2$	$5d^4 6s^2$	$5d^5 6s^2$
	A(eV)	0.8 ± 0.3	0.5 ± 0.3	0.15 ± 0.10

A number of years ago, Gordy and Thomas [19] found that a linear relationship exists between the electronegativity and work function of metals. This empirical fact can be understood in terms of eqs (10) and (11), since elimination of l_0 yields

$$\phi = \frac{I+A}{2} + \frac{l_- - l_+}{2}. \tag{17}$$

The quantity $(I+A)/2$ is the absolute electronegativity (X_m) first defined by Mulliken [20]. Gordy and Thomas showed that for most of the metals in the periodic table the following relation was obeyed:

$$\phi = 2.3 X_p + 0.34, \tag{18}$$

where the quantity X_p is the electronegativity given by Pauling [21]. Skinner and Pritchard [22] have shown that $X_m = 3.1\ X_p$ so that (18) may be written in terms of X_m as follows:

$$\phi = 0.74\ X_m + 0.34. \tag{19}$$

Comparing this result with eq (17) shows that, while the linear dependence of ϕ on X_m is predicted, the empirically determined coefficient is not quite unity as required by eq (17). However, detailed examination of the Gordy-Thomas correlation shows that a 25 percent increase in the coefficient of X_m would not do much of an injustice to the data which they used. In any case, the results of the present work strongly suggests the general applicability of eq (17) rather than its empirical counterpart, eq (19). It should be pointed out that the "constant" term in eq (19) is really given by $(l_- - l_+)/2$, which from eq (16) is seen to be equal to $kT/2 \ln [\omega_- / j_+ / \omega_+ j_-]$. As shown in table 2 this quantity depends upon the metal to which it is applied. Consequently, the empirical validity of eq (19) can only be considered approximate at best.

5. References

[1] Smith, L. E., Phys. Rev. **35**, 381 (1929).
[2] Barnes, L. L., Phys. Rev. **42**, 492 (1932).
[3] Wahlin, H. B., and Sordahl, L. O., Phys. Rev. **45**, 886 (1934).
[4] Fiske, M. D., Phys. Rev. **61**, 513 (1942).
[5] Scheer, M. D. and Fine, J., J. Chem. Phys. **42**, 3645 (1965).
[6] Zandberg, E. Y., Ionov, N. I. and Tontegode, A. Ya., Zh. Tekn. Fiz. **35**, 1504 (1965).
[7] Scheer, M. D., and Fine, J., J. Chem. Phys. **46**, 3998 (1967).

[8] Scheer, M. D., and Fine, J., J. Chem. Phys. **47,** 4267 (1967).
[9] Honig, R. E., J. Chem. Phys. **22,** 128 (1954).
[10] Scheer, M. D., and Fine, J., Proc. 4th Intern. Material Symp. (Berkeley, California, 1968, in press).
[11] Langmuir, I., and Kingdon, K. H., Proc. Roy. Soc. (London) **A107,** 61 (1925).
[12] Pierce, J. R., Theory and Design of Electron Beams (D. Van Nostrand Co., Inc., New York, 1949).
[13] Stull, D. R., and Sinke, G. C., Advan. Chem. Ser. **18** (1956); Hultgren, R., Orr, R. L., Anderson, P. D., and Kelley, K. K., Selected Values of Thermodynamic Properties of Metals and Alloys (John Wiley & Sons, Inc., New York 1965); Szwarc, R., Plante, E. R., and Diamond, J. J., J. Res. Nat. Bur. Stand. (U.S.), **69A** (Phys. and Chem.), No. 5, 417–421 (Sept.–Oct. 1969); Plante, E. R., and Szwarc, R., J. Res. Nat. Bur. Stand. (U.S.), **70A** (Phys. and Chem.), No. 2, 175–179 (Mar.–Apr. 1966).
[14] Moore, C. E., Atomic Energy Levels, Nat. Bur. Stand. (U.S.), Circ. 467, Vol. III, 282 pages (1958).
[15] Branscomb, L. M., Advan. Electron. Phys. **9,** 65 (1957).
[16] Fomenko, V. S., Handbook of Thermionic Properties (Plenum Press, Inc., New York, 1966).
[17] Smirnov, B. M., Teplofiz. Vyz. Temp. **3,** 775 (1965).
[18] Clementi, E., Phys. Rev. **135,** A980 (1964).
[19] Gordy, W., and Thomas, W. J. O., J. Chem. Phys. **24,** 439 (1956).
[20] Mulliken, R. S., J. Chem. Phys. **2,** 782 (1934).
[21] Pauling, L., J. Am. Chem. Soc. **54,** 3570 (1932).
[22] Skinner, H. A., and Pritchard, H. O., Trans. Faraday Soc. **49,** 1254 (1953).

(Paper 74A1–582)

JOURNAL OF RESEARCH of the National Bureau of Standards—A. Physics and Chemistry
Vol. 74A, No. 1, January–February 1970

Generation of Controlled Low Pressures of Nitrogen by Means of Dissociation Equilibria

Ronald H. Orcutt

Institute for Basic Standards, National Bureau of Standards, Washington, D.C. 20234

(October 3, 1969)

It is shown that fixed low pressures of nitrogen in the vacuum region can be generated by chemical dissociation in a system at equilibrium at constant temperature. Dissociation pressures ranging from 2×10^{-5} to 0.7 torr (3×10^{-3} to 90 $N\cdot m^{-2}$), corresponding to temperatures of 740 to 1150 K, for the reaction

$$Ba_3N_2 \rightleftarrows \tfrac{3}{2}\,Ba_2N + \tfrac{1}{4}\,N_2$$

have been measured. The pressures, p, in $N\cdot m^{-2}$ are represented by the equation

$$\ln p = (22.02\pm0.14) - \frac{(20{,}080\pm140)}{T},$$

where T is the absolute temperature, and the uncertainties are least squares estimates of the standard deviations of the parameters.

Key words: Barium nitride; dissociation equilibria; nitrides; nitrogen; thermodynamic properties; vacuum; vacuum measurement.

1. Introduction

The calibration of a vacuum-measuring device at pressures less than 10^{-3} torr is difficult, owing to the lack of both absolute and relative standards. Furthermore, most devices normally used for pressure measurement at this level are sensitive to composition as well as to pressure. Thus, any useful standard should control both of these variables simultaneously. The present paper reports studies concerned with the development of a procedure for establishing "fixed pressure points" in the high-vacuum region which provide such control.

The procedure relies on the fact that, for a two-component system consisting of two solid phases in equilibrium with a gas phase, the pressure of the gas is a function only of temperature. Owing to its widespread use as a reference medium, nitrogen was chosen for the gas phase [1].[1] The systems, consisting of nitrogen, metal, and/or metallic nitride(s), of the following metals were investigated: magnesium, manganese, boron, chromium, and barium. For temperatures less than 1300 K and pressures below one torr, only the barium/nitrogen system attained an equilibrium state rapidly enough for consideration as a possibly useful standard.

2. Concept

Ariya et al. [2] have shown that barium nitride decomposes according to the reaction

$$Ba_3N_2(s) \rightleftarrows \tfrac{3}{2}Ba_2N(s) + \tfrac{1}{4}N_2(g). \qquad (1)$$

The application of the second law of thermodynamics to this system at equilibrium gives the approximate expression

$$\ln p_{N_2} = 4\left(\frac{\Delta S^\circ}{R} - \frac{\Delta H^\circ}{RT}\right), \qquad (2)$$

relating the pressure of nitrogen, p_{N_2}, to the absolute temperature T, in terms of the entropy and enthalpy changes, ΔS° and ΔH°, for the reaction. Assuming that ΔS° and ΔH° are nearly independent of temperature and are determined by measurements of p and T over a range of values in which p can be determined absolutely and accurately, values of p can be calculated for lower temperatures by use of eq (2), thus extrapolating the pressure into a region where it

[1] Figures in brackets indicate the literature references at the end of this paper.

cannot be absolutely determined, providing that the system reaches equilibrium.

Two series of measurements, one at relatively high pressures (0.05 to 0.7 torr)[2] and the other at low pressures (2×10^{-5} to 0.05 torr), are reported here. The consistency of these measurements supports the validity of such an extrapolation.

3. Apparatus

The vacuum system used for these measurements is shown schematically in figure 1 [3]. The fluid manometer was of the type described by Thomas and Cross [4], and used a silicone material of low vapor pressure as a working fluid. A commercial high-pressure ion gage [5] tube was used for the low-pressure measurements.

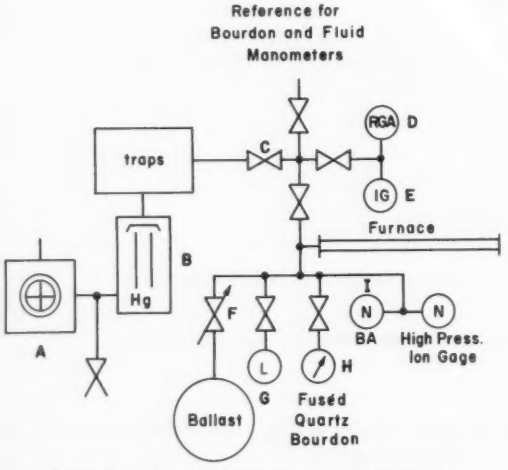

FIGURE 1. *Furnace/vacuum system (schematic).*

A: mechanical pump; B: mercury diffusion pump; C: valve; D: residual gas analyzer (omegatron); E: ionization gage; F: leak valve; G: fluid manometer; H: fused quartz bourdon gage; I: nude ionization gage (Bayard-Alpert type).

The system above the traps was constructed from stainless steel. All connections, save that to the furnace, were either by tungsten-inert gas penetration weld or by bolted aluminum foil or copper gasket.

The 99 percent alumina ceramic furnace tube was provided with tapered ends, which were waxed into matching stainless steel flanges with a low-vapor-pressure wax. During operation of the furnace, the waxed joints were kept cool by means of water jackets.

The furnace was a conventional clamshell-type combustion tube furnace. Temperature control above 900 °C was obtained from a proportional controller using a Pt/Pt-Rh thermocouple as sensing element; below this temperature a similar controller employing a platinum resistance thermometer as sensor was used.

Temperature on the IPTS scale of 1948 [14] was measured with a calibrated Pt/Pt-10 percent Rh thermocouple whose emf was determined potentiometrically with an accuracy of better than 1 μV. Separate measurements showed that the sample temperature did not differ from that indicated by more than 0.5 °C.

The pressure measurements reported in table 1 from 0.05 to 1 torr were made with the fused-quartz bourdon gage, whereas pressures below 0.05 torr were measured with the high-pressure ion gage, and are marked with the symbol #. The precision and calibration uncertainty of the bourdon gage was about 5×10^{-4} torr; the gage was periodically calibrated against the standard manometer [4] and showed no drift over the period of the measurements. The reference pressure for both the manometer and the bourdon gage was less than 5×10^{-8} torr. The high-pressure ion gage was operated with its emission current regulated to better than 0.1 percent by means of an emission regulator developed at the Bureau [6]. The ion currents were measured with a precision of at least 1 percent by means of a calibrated electrometer. The high-pressure ion gage was also periodically calibrated against the standard manometer and was free from drift over the time of the measurements. Its precision of calibration was 1 to 2 percent, the limitation being set by the current measurement. It is conservatively estimated that, for pressures greater than 0.05 torr, combined errors

TABLE 1. *Dissociation pressures for the reaction* $Ba_3N_2 \rightleftarrows \frac{3}{2}Ba_2N + \frac{1}{4}N_2$ *as a function of temperature*

T_{48}(K)	$p_{measured}$ (torr)	$p_{corrected}$ (torr)
738	2.11(−5)*#	3.18(−5)
748	4.80(−5)#	7.28(−5)
764	5.95(−5)#	9.11(−5)
770	9.20(−5)#	1.42(−4)
792	2.06(−4)#	3.20(−4)
795	1.64(−4)#	2.55(−4)
815	3.78(−4)#	5.93(−4)
844	7.87(−4)#	1.24(−3)
845	8.30(−4)#	1.31(−3)
874	1.90(−3)#	2.95(−3)
894	4.26(−3)#	6.30(−3)
927	8.00(−3)#	1.11(−2)
934	1.10(−2)#	1.47(−2)
958	1.68(−2)#	2.12(−2)
989	3.34(−2)#	3.84(−2)
1000	4.9 (−2)	5.4 (−2)
1023	6.8 (−2)	7.3 (−2)
1025	7.10(−2)#	7.56(−2)
1029	8.9 (−2)	9.3 (−2)
1030	1.04(−1)	1.08(−1)
1042	9.5 (−2)	9.9 (−2)
1048	1.23(−1)	1.27(−1)
1067	1.78(−1)	1.82(−1)
1082	2.36(−1)	2.36(−1)
1084	2.90(−1)	2.90(−1)
1112	3.98(−1)	3.98(−1)
1132	5.55(−1)	5.55(−1)
1133	5.23(−1)	5.23(−1)
1134	5.57(−1)	5.57(−1)
1135	5.81(−1)	5.81(−1)
1135	6.22(−1)	6.22(−1)
1150	7.24(−1)	7.24(−1)

*The notation $a(n)$ means $a \cdot 10^n$; thus, for example, 2.11(−5) means 2.11×10^{-5}.
#Measurements were made with ion gage.

[2] 1 torr = 1.33322×10^2 N·m^{-2}.

of temperature and pressure measurement do not exceed 5 percent of the pressure on an absolute basis. At lower pressures the absolute error is thought to be less than 20 percent, the larger value being due to the uncertainty of extrapolation.

Samples of Ba_3N_2 in alumina ceramic trays were enclosed in a nickel shield whose function was to insure that there should be a negligible temperature gradient across the sample. The container and its relation to the furnace tube are shown in figure 2.

4. Experimental Procedures

Commercial samples of Ba_3N_2 in powder form were used for the measurements. Two samples from different lots gave identical results; in addition, a sample prepared in situ from Ba and N_2 gave the same results. Since the material decomposes in the presence of water, samples were handled under an atmosphere of dry nitrogen.

Samples were transferred to the furnace in the nickel sample shield and the furnace evacuated. The samples were found to contain large quantities of absorbed nitrogen, the bulk of which was removed by pumping on the samples for several hours at 700 to 750 °C under a nitrogen pressure of about 0.1 torr. The temperature for which the dissociation pressure was to be measured was selected and the furnace allowed to stabilize. The pressure in the system was then reduced to a value below the anticipated decomposition pressure for the set temperature, and the sample was isolated from the pump. The increase of pressure was then observed as a function of time: If the sample had been completely degassed, the pressure reached a constant value after a period of from one to three hours; otherwise the pressure would continue to rise, nearly linearly with time.

In the event that a constant pressure was not attained, the sample was further degassed and the procedure repeated until a constant value was obtained. The rate of approach to a stable value was found to be a linear function of the logarithm of time, and was apparently nearly independent of temperature.

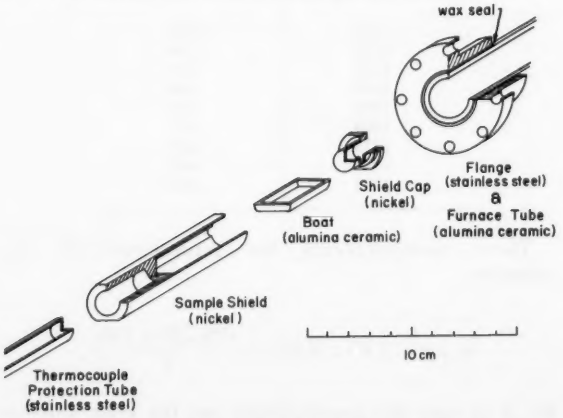

FIGURE 2. *Sample holder detail (oblique drawing).*

5. Results

Measurements of the dissociation pressure of Ba_3N_2 made at 32 temperatures ranging from 740 to 1150 K with corresponding pressures of from 2×10^{-5} to 0.7 torr are given in table 1. The data were fitted by ordinary least squares [7] to the equation

$$(\ln p)=A+B\left(\frac{1}{T}\right). \tag{3}$$

The values of A and B resulting from the fit were 18.17 ± 0.14 and $-21{,}250\pm130$, respectively, for p in torr. The uncertainties given are the estimates of the standard deviations of the parameters: The estimate of the standard deviation of the fit was 0.12 in the logarithm of pressure. The data and the least squares line are plotted in figure 3.

In addition to the results on dissociation, some results for recombination at pressures from 0.05 to 0.7 torr were obtained. These results, which are given in the appendix, were on the average 15 percent higher than the results obtained by decomposition; it was at first thought that the system exhibited hysteresis as has been observed in some other systems [8]. It seems more likely, however, that equilibrium was not attained because of a very slow rate [9].

Since the gages used for determining the dissociation pressures were operated at temperatures different from that of the sample, the results must be corrected for thermomolecular pressure gradients (thermal transpiration). The data span the transition region from viscous to molecular flow; thus, the correction factor can range from unity for viscous flow to $(T_2/T_1)^{1/2}$ for molecular flow, where T_2 is the furnace temperature and T_1 that of the gage.

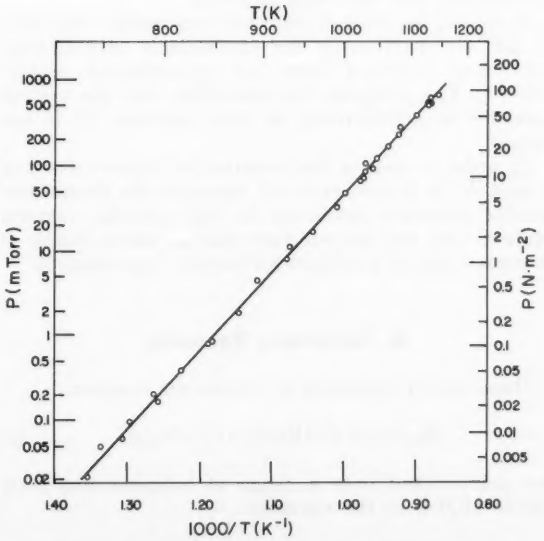

FIGURE 3. *Dissociation pressure of* Ba_3N_2 *as a function of temperature.*

There exists no exact theory for calculating the correction factor in the transition region. In order to estimate the correction the empirical equation of Liang [10] was used, although its accuracy is not known. This equation for the correction factor R can be written in the form

$$R=\frac{p_1}{p_2}=\frac{\alpha(\varphi_g x)^2+\beta(\varphi_g x)+(T_1/T_2)^{1/2}}{\alpha(\varphi_g x)^2+\beta(\varphi_g x)+1}, \qquad (4)$$

where $x=p_2 d$, with p_2 in torr and d, in millimeters, the diameter of the tubing joining the regions at temperatures T_1 and T_2 with $T_1 \leq T_2$.

Using values of the parameters, $\alpha=2.13$ and $\beta=4.82[1-(T_1/T_2)^{1/2}]$ [10] and $\varphi_g=3.53$ [11] taken from the literature, together with $d=5$ mm and $T_1=325$ K, values of p_2 corresponding to the measured values of p_1 were calculated; these values along with the measured values of p_1 and the temperatures are given in table 1. The resulting values of p_2 yielded a linear relationship within experimental error between the logarithm of pressure and the reciprocal temperature. Fitting the corrected dissociation pressures to eq (3) yielded the results: $A=17.13\pm0.14$, $B=-20{,}080\pm140$, and $s=0.12$, where the uncertainties are the estimates of the standard deviations of the parameters, s is the estimate of the standard deviation of the fit, and the pressures are given in torr.

These values correspond to values of 21.8 $J\cdot K^{-1}\cdot mol^{-1}$ and 41.7 $kJ\cdot mol^{-1}$, respectively, for $\Delta S°$ and $\Delta H°$ for the reaction represented by eq (1). Ariya et al. [2] report a value of 8.8 $kcal\cdot mol^{-1}$ (36.8 $kJ\cdot mol^{-1}$) for the enthalpy change of this reaction at 298 K. Since the heat capacities of Ba_3N_2 and Ba_2N have not been determined as a function of temperature, the present value (which corresponds to $\Delta H°$ at about 950 K) cannot be corrected so as to make a valid comparison with the value at 298 K.

It should be pointed out that reasonable estimates of $\Delta S°$ for reaction (1) are significantly greater than the value obtained from the experimental results [12, 13]. This suggests the possibility that the system was not at equilibrium, or that reaction (1) is not correct.

In order to assess the accuracy of these values of A and B, it is necessary to measure the thermomolecular pressure gradients for the specific vacuum system over the temperature and pressure region of interest. This is a subject for further investigation.

6. Summary Remarks

Dissociation pressures in torr for the reaction

$$Ba_3N_2(s) \rightleftarrows \tfrac{3}{2}Ba_2N(s)+\tfrac{1}{4}N_2(g) \qquad (1)$$

are represented over a range of temperatures from 740 to 1150 K by the equation

$$\ln p=(17.13\pm0.14)-\frac{(20{,}080\pm140)}{T}$$

and the pressures in $N\cdot m^{-2}$ are represented by the equation

$$\ln p=(22.02\pm0.14)-\frac{(20{,}080\pm140)}{T} \qquad (6)$$

where the uncertainties are least squares estimates of the standard deviations of the parameters.

The reaction goes to equilibrium in times of a few hours and the rate of approach to equilibrium is independent of temperature. This reaction can be used to generate stable and reproducible pressures of nitrogen in the range 10^{-5} to 1 torr, and is thus useful in checking the variation in response of pressure measuring devices.

In order to use this means of checking, it is necessary only to append a chamber with suitable valving containing a sample of Ba_3N_2 to one's vacuum system. Means of controlling and measuring the sample temperature must also be provided.

Once the corrections for thermomolecular pressure gradients are known and the true values of $\Delta H°$ and $\Delta S°$ are derived, the technique becomes absolute.

The possible role of hysteresis in this system and the feasibility of extending the measurements to lower pressures are subjects for further investigation.

The author is grateful to Stanley Ruthberg for many helpful discussions concerning this work and to William Cullins for help in the design and construction of the equipment used.

7. Appendix

Tabulated below are the pressures obtained at various temperatures upon approaching the equilibrium pressure from above.

T_{48}(K)	p(torr)
1023	0.087
1043	.124
1070	.225
1078	.238
1083	.300
1084	.315
1113	.492
1136	.657
1151	.803

These measurements are represented by the equation

$$\ln p=(17.85\pm0.67)-\frac{(20{,}720\pm730)}{T},$$

for p in torr; the uncertainties are the least squares estimates of the standard deviations of the parameters

and the standard deviation of the fit is 0.07 in the logarithm of the pressure.

8. References

[1] Recently the use of H_2 in an analogous manner was reported; cf. Lundin, C. E., "The Use of Thermodynamic Properties of Metal-Gas Systems as Reduced-Pressure Standards" NASA Report CR-1271.

[2] Ariya, S. M., et al., J. Gen. Chem. USSR **25,** 609 (1955).

[3] The symbols used in figure 1 are those adopted as standard by the AVS; see J. Vac. Sci. and Tech. **4,** 139 (1967).

[4] Thomas, A. M., and Cross, J. L., J. Vac. Sci. and Tech. **4,** 1 (1967).

[5] The high pressure ion gage used a Millitorr™ gage tube manufactured by Varian Associates, Vacuum Division, Palo Alto, California. This statement is for the purpose of information and does not constitute an endorsement or recommendation on the part of NBS.

[6] Yee, K. W., and Carpenter, R. J., Rev. Sci. Instr. **34,** 1101 (1963).

[7] Natrella, M. G., Experimental Statistics, chapter 5, p. 10.

[8] cf. for example, Spedding, F. H., et al., Nucleonics **4,** 4 (1949).

[9] Extremely slow rates of recombination have been noted in, for example, the Si/N_2 system; see Hincke, W. B., and Brantley, L. R., J. Am. Chem. Soc. **52,** 48 (1930).

[10] Edmonds, T., and Hobson, J. P., J. Vac. Sci. and Tech. **2,** 182 (1965).

[11] Bennett, M. J., and Tompkins, F. C., Trans. Faraday Soc. **53,** 185 (1957).

[12] Lewis, G. N., and Randall, M., Thermodynamics as revised by Pitzer, K. S., and Brewer, L. (McGraw-Hill Book Co., New York, 1961).

[13] Latimer, W. M., J. Am. Chem. Soc. **73,** 1480 (1951).

[14] Temperature: Its Measurement and Control in Science and Industry, Vol. **3,** Ed. Herzfeld, C. M. (Reinhold, New York, 1962).

(Paper 74A1-583)

367-409 OL-70—4

JOURNAL OF RESEARCH of the National Bureau of Standards—A. Physics and Chemistry
Vol. 74A, No. 1, January–February 1970

Temperature Coefficient of the Bismuth I–II Transition Pressure

James C. Houck

**Institute for Basic Standards, National Bureau of Standards,
Washington, D.C. 20234**

(September 24, 1969)

A rotatable piston in a supported cylinder was used to determine the temperature coefficient of the bismuth I–II transition pressure for the temperature range of 20 to 50 °C. The temperature coefficient of the transition pressure is −40.6 bar/°C.

Key words: Bismuth transition; calibration point; high pressure; pressure measurement; temperature coefficient.

1. Introduction

The importance of the Bi I–II transition, also called the α, β transition, as a fixed point on the pressure scale is well established and warrants continuing efforts to improve the determination of the pressure at which it occurs. P. W. Bridgman [1, 2][1] reported the pressures for the Bi I–II transition over the temperature range −50 to 183 °C. His values show a constant temperature coefficient of −50 bar/°C for the Bi I–II transition over the range of −50 to 150 °C. A later determination by Bridgman [3] for use in calibration of a manganin gage gave a temperature coefficient of −45 bar/°C between 30 and 75 °C. V. P. Butuzov and Ye. G. Ponyatovsky [4, 5] give a temperature coefficient of −38 bar/°C from 65.5 to 125 °C, −56 bar/°C from 125 to 163.5 °C, and −96 bar/°C from 163.5 to 184 °C.

P. L. M. Heydemann [6, 7] ascribes a best value for the bismuth I–II transition pressure of 25499 bar[2] with an uncertainty of 60 bar at 25 °C. In his work a value of the temperature coefficient of the transition pressure of −54.5 bar/°C, chosen as an average of various values computed from the literature, was used but not presented as a correction for use of the transition at other temperatures.

It was desired to obtain a value of the temperature coefficient of the transition pressure both to present as an aid in the use of the transition as a reference value in pressure calibrations and for our use in the future redetermination of the bismuth transition pressure in a planned improved version of the dead-weight piston gage. Because of the difficulties and expense encountered in operation of a dead-weight piston gage to these pressures a rotatable piston and supported cylinder device which is readily operated at these pressures was used for these measurements.

2. Rotatable Piston and Supported Cylinder Apparatus

The rotatable piston and supported cylinder device used for these measurements has been described previously [8]. It had been used several years ago for the determination of transition pressures of solid to solid transitions in bismuth and thallium similarly to the method of Kennedy and LaMori [9]. The pressure then obtained for the bismuth I–II transition at 25 °C from a mean value of transition in both directions was 25212 bar with a standard deviation of 18 bar, a half-friction of 15 bar, and an estimated systematic uncertainty of 100 bar. These results agree with the value of 25154 bar extrapolated from Bridgman [3], but they disagree with the value of 25405 bar reported by Kennedy and LaMori [9] and with the value of 25499 bar established by Heydemann [6, 7] in the dead-weight piston gage by more than the combined uncertainties. However for the purpose of determining the temperature coefficient of the transition pressure the uncertainties due to the ratio of the area of the ram to that of the piston, the ratio of the effective area of the piston and cylinder at elevated pressure to the measured area of the cylinder, the location of the transition within the half-friction band, and corrections to the bourdon tube gage are greatly reduced by performing as nearly identical experiments as possible at the different temperatures.

[1] Figures in brackets indicate the literature references at the end of this paper.
[2] 1 bar = 10^5 N/m^2

3. Determination of the Temperature Coefficient

Bismuth with a purity of 99.999 percent was obtained from the American Smelting and Refining Company. It was cast in vacuum and machined. The finished sample was 0.882 cm long, the edges were bevelled at 45° to receive steel anti-extrusion rings, and the diameter was a close fit to the cylinder which was 1.263 cm I.D. The short 1 cm cylinders were used for these experiments.

The transition was detected by observing the volume change accompanying the transition. The volume of the sample was indirectly observed by following the piston advance with dial indicators mounted to bear on arms fixed to one of the intermediate pieces between the 15.25 cm diameter low pressure ram and the 1.263 cm high pressure piston. The motion of the dial gage indicators is due to the sum of the compression of the bismuth sample, the compression of the parts of the piston stack between the arms and the sample end of the high pressure piston, the cylinder expansion, and the distortion of a bridge plate. The method of determining the transition pressures is shown in figure 1. One psi oil pressure on the ram causes approximately 10 bar pressure on the sample. With all of the bismuth in phase I the pressure was increased to point A approximately 500 bar below the transition pressure. After a 10 min interval the piston stack was rotated approximately 2° and then rotated back 2° to its original position. This reduced the friction and permitted the piston to advance causing the pressure on the ram to decrease to point B. The ram pressure was then increased to 20 psi above the pressure at A. This was followed by a similar interval, rotation and pressure increase routine. Then the pressure increments were reduced to 10 psi. These routines were continued until at point D it was observed that the pressure decrease due to the piston advance on rotation was greater than the preceding ones. The pressure was then increased to E, equaling that at C rather than exceeding it. This was followed by a series of five 10-min intervals and piston rotations which ended at point F. The pressure was increased to point G and six more 10-min intervals and piston rotations established point H. The average of the pressure at points F and H, suitably corrected, was taken as one determination of the bismuth I to II transition pressure. At this point approximately 2 percent of the bismuth had been transformed to phase II. It is important that the phase conversion occurs in the immediate vicinity of the piston so that friction can be effectively reduced. An additional 2 percent (point J) was transformed by increasing the pressure to point I and then relieving friction by waiting and rotating the piston twice. Pressure was then released by valving to point K. A series of 10-min intervals, rotations and pressure releases then led to point L. From previous experience and from the details of the trace shown in figure 1 we expected that at this point the piston had retracted enough, so that after further relief of friction by rotation bismuth would convert from II to I. As the bismuth sample converted, the piston was pushed out and the ram pressure was further increased. A series of five 10-min intervals and rotations led to point M. A repetition through point N to point O verified point M. The average of the pressure at points M and O, suitably corrected, was taken as one determination of the bismuth II to I transition.

The equilibrium transition pressure is taken as the mean of the two pressures obtained for different directions of the transition. For a discussion of the characterization of the bismuth I–II transition see R. J. Zeto et al. [10].

The temperatures 24.8 °C and above were obtained by use of an air bath. All the equipment including the

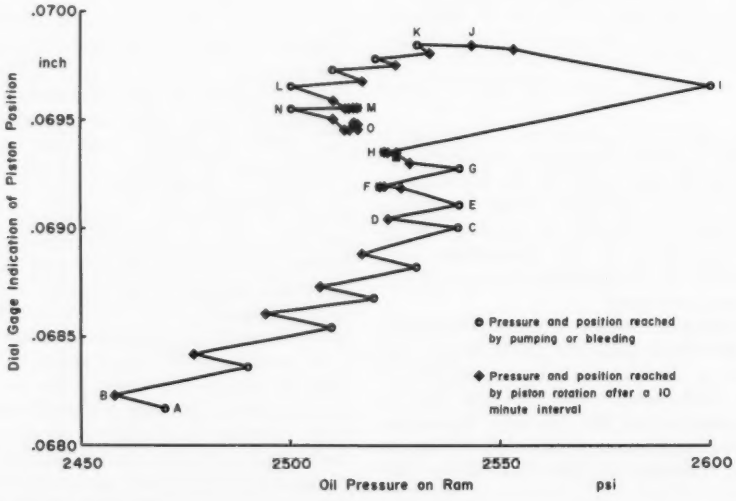

FIGURE 1. *Bismuth I to II and II to I Transition Pressures as shown by Dial Gage Indication of Piston Position.*

clamping press which held the low pressure piston and cylinder assembly with bridge plates and the high pressure piston and cylinder was in the bath. A long lever for the rotation of the piston stack was brought out through a cloth covered slit. Thermometers and the dial gage were read through a plastic window. Two to four days were required for the equipment to reach equilibrium. The temperatures 22.5 °C and below were obtained through control of the room temperature.

Table 1 shows the transition pressures for both directions, the temperatures, the average pressures, the difference between the pressures, and the average temperature. The transition pressures were calculated from the observed ram pressures with corrections for ram weight, difference in height, gage correction, ratio of area of low pressure cylinder to high pressure cylinder, and cylinder expansions due to pressure and temperature. Figure 2 shows the transition pressures for both directions of the transition plotted versus temperature. The straight line is drawn to a least squares fit of the average pressures.

Omnitab POLYFIT least squares solutions for first degree equations were obtained for the set of pressures and temperatures for Bi I to II, for the set of pressures for Bi II to I, and for the set of average pressures of each pair of determinations. The fits were obtained from data taken over the temperature range 20 to 50 °C. For convenient use of the statistics available from the POLYFIT program the straight line was fitted to:

$$P_T = P_{25°} + (T - 25\ °C)dP/dT$$

TABLE 1. *Temperature dependence of the transition pressure of the bismuth I–II transition*

P_{I-II}	T	P_{II-I}	T	P_{av}	$P_{I-II} - P_{II-I}$	T
Bar	°C	*Bar*	°C	*Bar*	*Bar*	°C
25366.	20.8	25276.	20.8	25321.	90	20.8
25356.	20.9	25256.	21.0	25306.	100	20.95
25336.	21.0	25216.	21.1	25276.	120	21.05
25256.	21.9	25187.	22.0	25222.	69	21.95
25267.	22.1	25217.	22.0	25242.	50	22.05
25306.	22.1	25187.	22.1	25247.	119	22.1
25237.	22.4	25177.	22.4	25207.	60	22.4
25267.	22.5	25177.	22.4	25222.	90	22.45
25138.	24.8	25098.	24.8	25118.	40	24.8
25148.	24.8	25093.	24.8	25120.	55	24.8
25143.	25.0	25088.	25.0	25115.	55	25.0
24731.	34.0	24711.	34.0	24721.	20	34.0
24751.	34.0	24701.	34.0	24726.	50	34.0
24771.	34.1	24716.	34.1	24744.	55	34.1
24424.	42.7	24374.	42.7	24399.	50	42.7
24444.	42.7	24394.	42.7	24419.	50	42.7
24419.	42.7	24384.	42.7	24402.	35	42.7
24117.	49.9	24067.	49.9	24092.	50	49.9
24102.	50.1	24057.	50.1	24080.	45	50.1
24092.	50.1	24057.	50.1	24075.	35	50.1
25202.	22.5	25147.	22.6	25174.	55	22.55
25157.	23.1	25107.	23.1	25132.	50	23.1
25157.	23.0	25077.	23.0	25117.	80	23.0

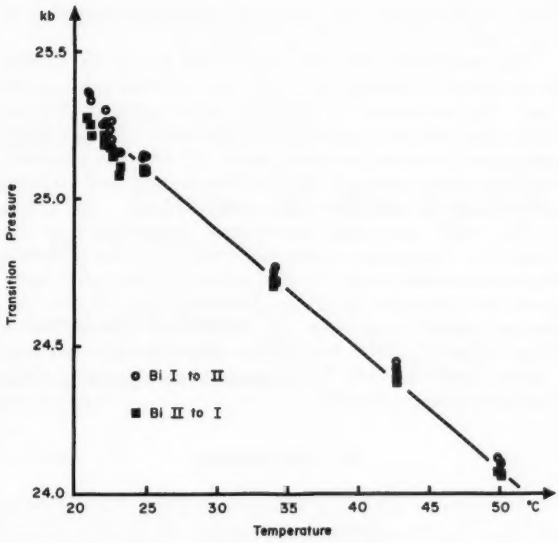

FIGURE 2. *Temperature Dependence of the Bismuth I–II Transition Pressure.*

where

T = temperature in degrees celsius (IPTS 1948)
P_T = transition pressure in bar at temperature T
$P_{25°C}$ = transition pressure in bar at 25 °C
$\frac{dP}{dT}$ = derivative of transition pressure with respect to temperature in bar per °C.

Table 2 shows the results of the three POLYFITs. The temperature coefficient of the transition pressure from the averaged points is −40.6 bar/°C with a standard deviation of 0.5 bar/°C. The systematic uncertainties due to the area of the pistons and cylinders, the effective area at elevated pressure, and the gage calibration do not influence this temperature coefficient. The uncertainty in thermal expansions of the tungsten carbide high pressure cylinder and of the steel ram cylinder are systematic in this measurement but are less than 0.1 bar/°C. The estimated systematic uncertainty of the temperature is 0.2° at 20 °C and 0.4 °C at 50 °C resulting in an estimated systematic uncertainty of 0.8 bar/°C. The maximum uncertainty due to friction is the difference between the tempera-

TABLE 2

Omnitab POLYFIT least squares fit of $P = P_{25} + (T - 25\ °C)\ dP/dT$

Transition	Standard deviation of the fit	Transition pressure at 25 °C	Standard deviation of transition pressure	dP/dT	Standard deviation of dP/dT
	Bar	*Bar*	*Bar*	*Bar/°C*	*Bar/°C*
I to II	33	25140	8	−41.3	0.6
II to I	25	25072	6	−39.9	.5
Average	27	25106	6	−40.6	.5

ture coefficient of the averaged pressures and that of the I to II or II to I which is 0.7 bar/°C.

The transition pressure was 25106 bar at 25 °C with a standard deviation of 6 bar and a half-friction of 34 bar. The estimated systematic uncertainty is 200 bar (150 bar cylinder expansion correction, 20 bar high-pressure cylinder measurement, 10 bar low-pressure cylinder measurement, 10 bar ram weight and oil head correction, 10 bar gage calibration).

The high estimated systematic uncertainty in the cylinder expansion correction arises from bismuth having extruded past the anti-extrusion ring and therefore the effective area lies between that of the corrected piston area and the corrected cylinder area. The value of 25106 bar differs from the present best value 25499 bar [6, 7] by more than the sum of the estimated uncertainties.

4. Conclusion

A value of −40.6 bar/°C with a standard deviation of 0.5 bar/°C, an estimated systematic uncertainty due to temperature of 0.8 bar/°C, and an estimated uncertainty due to friction of 0.7 bar/°C was found for the temperature coefficient of the bismuth I–II transition over the range of 20 to 50 °C. This value may be used for temperature correction within the range 20 to 50 °C of the present best value of 25499 bar at 25 °C for the pressure of the bismuth I–II transition.

5. References

[1] Bridgman, P. W., Phys. Rev. **47,** 427 (1935).
[2] Bridgman, P. W., Phys. Rev. **48,** 893 (1935).
[3] Bridgman, P. W., Proc. Am. Acad. Arts. Sci. **74,** No. 1, 1–10 (1940).
[4] Butuzov, V. P., and Ponyatovsky, Ye. G., Crystallography **1,** No. 5, 572–576 (1956).
[5] Butuzov, V. P., Soviet Physics-Crystallography **2,** 533, (1957).
[6] Heydemann, P. L. M., J. Appl. Phys. **38,** No. 6, 2640–2644 (1967).
[7] Heydemann, P. L. M., J. Appl. Phys. **38,** No. 8, 3424 (1967).
[8] Heydemann, P. L. M., and Houck, J. C., J. Res. Nat. Bur. Stand. (U.S.), **71C** (Eng. and Instr.) No. 1, 11–17 (Jan-Feb. 1967).
[9] Kennedy, G. C., and LaMori, P. N., Geophysical Research **67,** No. 2, 851–856 (1962).
[10] Zeto, R. J., and others, Characterization of the Bismuth I–II and Barium I–II Points under Hydrostatic Pressure, to be published in proceedings of the Symposium on the Accurate Characterization of the High-Pressure Environment, Oct. 14–18, 1968 at National Bureau of Standards.

(Paper 74A1–584)

JOURNAL OF RESEARCH of the National Bureau of Standards—A. Physics and Chemistry
Vol. 74A, No. 1, January–February 1970

Isothermal Diffusion in the Dilute Range of the System $Ca(OH)_2 - H_3PO_4 - H_2O$: Theory

E. C. Moreno,* P. R. Patel,** and W. E. Brown**

Institute for Materials Research, National Bureau of Standards,
Washington D.C. 20234

(September 8, 1969)

The equations describing isothermal diffusion in the dilute range of the ternary system $Ca(OH)_2-H_3PO_4-H_2O$ are derived in two ways, first, assuming that the components are electroneutral species and, second, considering the actual ionic species present in solution. It is shown that the two models are thermodynamically equivalent. The theory permits the calculation of the four fundamental diffusion coefficients (phenomenological coefficients) in the concentration range where the Debye-Hückel theory suffices for the calculation of ionic activity coefficients. The equations can be used to test the Onsager reciprocal relations for the diffusion process in the above system. The ionic model was used to calculate practical diffusion coefficients for the electroneutral components from the limiting equivalent conductances of the ions in solutions saturated with respect to hydroxyapatite, $Ca_{10}(OH)_2(PO_4)_6$. Large diffusion interferences, as revealed by relatively large values for the cross-terms in D_{ij}, are predicted even for solutions with total molarity in the order of 10^{-5}. Therefore, diffusion models based on independent fluxes of the components appear to be invalid.

Key words: Diffusion; phenomenological coefficients; polycomponent systems; reciprocal relations.

1. Introduction

Diffusion processes in dilute solutions of the ternary system $Ca(OH)_2-H_3PO_4-H_2O$ have biological and theoretical importance. Mechanisms for calcification and for formation of caries in teeth based upon diffusion of calcium and phosphate species have been advanced [1, 2, 3].[1] Ternary systems are the simplest systems in which the validity of the Onsager's reciprocal relations [4, 5, 6] can be tested for a diffusion process. The theoretical and experimental treatments of the present system have, besides the difficulties inherent to any multicomponent system, the complications originating from the presence of a weak electrolyte (phosphoric acid) and the impossibility of using optical methods to monitor the diffusion process such as has been done at higher concentrations [7, 8, 9]. In order to test Onsager's reciprocal relations, it is necessary to calculate the partial derivatives of activity coefficients with respect to the concentration of the components. Previous treatments of this problem in ternary systems have either assumed invariance of activity coefficients with concentration [10] or have used assumptions applicable to symmetric electrolytes [11]. The present treatment applies to the ternary system $Ca(OH)_2-H_3PO_4-H_2O$ in the concentration range where the Debye-Hückel theory has been shown [12, 13] to describe adequately ionic activity coefficients. Derivations will be given for two models in which electroneutral components and ionic constituents are considered, respectively. It will be shown that these two models are thermodynamically equivalent.

The mathematical treatment is applied here to the calculation of "fundamental" and "practical" diffusion coefficients for electroneutral components in solutions saturated with respect to hydroxyapatite; such systems were selected because of their biological relevance. In a subsequent publication, the present derivations will be applied to results obtained in diffusion experiments using diaphragm cells.

2. Procedure

2.1. Selection of Model

All the equilibrium properties of the ternary system referred to in this paper can be defined in terms of the components $Ca(OH)_2$, H_3PO_4, and H_2O. For diffusion purposes, the number of components, C', may be obtained from the expression $C'=n-r$, in which n is the total number of chemical species, ionic and electroneutral, present in the system and r is the number of restrictions operating on those species. Usually, for the case of strong electrolytes the only restriction is electroneutrality. If $Ca(OH)_2$, H_3PO_4, and

*Present address: Sunnyside Lane, RFD No. 2, Lincoln, Mass. 01773.
**Research Associates from the American Dental Association at the National Bureau of Standards.
[1] Figures in brackets indicate the literature references at the end of this paper.

H_2O are selected as components, in general, n would comprise eight constituents: H_2O, H_3PO_4, $H_2PO_4^-$, $HPO_4^=$, $PO_4^{\equiv}$, H^+, Ca^{++}, and OH^-. The system would have five restrictions: the three expressions for the three ionization constants of H_3PO_4, the expression for the ionization constant of H_2O, and the condition of electroneutrality. Therefore, the system is ternary.[2]

It is neither fruitful nor realistic to consider all the foregoing consitutents and restrictions. The derivations would become unnecessarily complicated; besides, because of the magnitudes of the ionization constants of H_3PO_4, in any given system only two phosphate species can be present in significant concentrations. Furthermore, as done by other investigators [10, 14], it will be assumed that the solvent, H_2O, is undissociated. If now, neutral components that do not contain the ion OH^- are selected, n will be equal to five (H_2O, two phosphate-containing species, Ca^{++}, and H^+), and r will be two (equilibrium between the two phosphate-containing species and electroneutrality); hence the simplified model is ternary for diffusion purposes. The two phosphate species considered here are $H_2PO_4^-$ and $HPO_4^=$ which are the only species present in significant concentrations in dilute solutions and in the pH range 4.5 to 7.5. The other two components, besides H_2O, correspond to electroneutral combinations of the ions considered and their selection is arbitrary. For convenience, $CaHPO_4$ and H_3PO_4 are selected here, but the treatment would apply equally well to, for example, $CaHPO_4$ and $Ca(H_2PO_4)_2$.

2.2 Derivations

For the range of dilute solutions considered here, total molarity in the order of 10^{-4} to 10^{-2}, it is reasonable to assume that the partial molar volumes of the components are independent of concentration. Under these conditions, the practical diffusion coefficients, $(D_{ij})_c$, obtained in a cell-fixed frame of reference (a porous diaphragm cell), become identical with those referred to a constant-volume frame of reference, $(D_{ij})_v$ [10, 15]. Furthermore, the solvent-fixed diffusion coefficients, $(D_{ij})_0$, are related to the volume-fixed frame of reference [10, 14] by

$$(D_{ij})_0 = (D_{ij})_v + \frac{C_i}{C_0 \bar{v}_0} \sum_{k=1}^{q} \bar{v}_k (D_{kj})_v$$

$$i = 1, \ldots, q \qquad k = 1, \ldots, q$$

in which C_i and C_0 are the concentrations of the ith components and the solvent, respectively; $\bar{v}_0$ and $\bar{v}_k$, the partial molar volumes of the solvent and the component K, respectively; the summation is taken over q components, excluding the solvent. It is apparent that at infinite dilution, $(D_{ij})_0 = (D_{ij})_v$; even for concentrations about $1M$, the two sets of coefficients do not differ by more than 1 to 5 percent [16].

[2] In this paper, the presence of calcium-phosphate ion pairs is ignored; in the concentration and pH ranges for which the present derivations are intended, the concentration of these ion pairs is small. Introduction of these species, however, does not alter the ternary nature of the system since for each one there is a corresponding dissociation expression (restriction).

For the foregoing reasons, it is assumed that the derivations shown here, although strictly applicable only to a solvent-fixed frame of reference, are valid for the systems under consideration, since their highest concentration is in the order of $10^{-2}M$.

a. Electroneutral Model

According to the principles of nonequilibrium thermodynamics [17, 18], the diffusion flow for the component i, J_i, in a ternary system may be described by

$$J_i = -\sum_{j=0}^{2} \tilde{L}_{ij} (\partial \mu_j / \partial x) \qquad i = 0, 1, 2 \tag{1}$$

in which $\tilde{L}_{ij}$ are phenomenological coefficients and the quantity within parenthesis is the gradient of the chemical potential μ_j for component j along x; the summation in (1) includes the solvent designated by the subscript zero.

From the Gibbs-Duhem equation, at constant temperature and pressure, it is obtained

$$\sum_{j=0}^{2} C_j \partial \mu_j / \partial x = 0. \tag{2}$$

Solution of eq (2) for $\partial \mu_0 / \partial x$ and substitution into eqs (1) gives

$$J_i = -\sum_{j=1}^{2} L_{ij} (\partial \mu_j / \partial x) \qquad i = 1, 2 \tag{3}$$

in which $L_{ij} = \tilde{L}_{ij} - C_j / C_0 \tilde{L}_{i0}$. In eqs (3), the flow of the component i is given in terms of the chemical potential gradients of the solutes; therefore, the phenomenological coefficients, usually called "fundamental diffusion coefficients" L_{ij}, display Onsager's reciprocal relations [14].

The flow J_i in eqs (3) may now be given in terms of practical diffusion coefficients, D_{ij}. In a ternary system, only the concentrations, C_1 and C_2, of two of the components are independent variables. Therefore,

$$\frac{\partial \mu_j}{\partial x} = \sum_{k=1}^{2} \frac{\partial \mu_j}{\partial C_k} \frac{\partial C_k}{\partial x} \qquad j = 1, 2. \tag{4}$$

Substitution of eq (4) into eq (3) gives

$$J_i = -\sum_{j=1}^{2} L_{ij} \sum_{k=1}^{2} \frac{\partial \mu_j}{\partial C_k} \frac{\partial C_k}{\partial x} \tag{5}$$

or

$$J_i = -\sum_{k=1}^{2} D_{ik} \frac{\partial C_k}{\partial x} \qquad i = 1, 2 \tag{6}$$

in which the practical diffusion coefficients, D_{ik} are given by

$$D_{ik} = \sum_{j=1}^{2} L_{ij} \frac{\partial \mu_j}{\partial C_k} \qquad \begin{matrix} i = 1, 2 \\ k = 1, 2. \end{matrix} \tag{7}$$

The four practical diffusion coefficients D_{ik} can be obtained through a minimum of two diffusion experiments by the use of eqs (6) with the appropriate boundary conditions. For the case of diaphragm cell experiments, however, the integrated form [19] of eq (6) does not permit an analytical solution for the D_{ik}; the calculation of these coefficients in ternary systems has been effected by either imposing restrictions in the experimental conditions [20, 21] or approximations in the flux equations [22]. Recently, statistical procedures that obviate these limitations have been reported [23, 24].

From eqs (7), the following relations may be obtained by solving for the L_{ij}:

$$\begin{aligned} L_{11} &= (D_{11}\mu_{22} - D_{12}\mu_{21})/s \\ L_{12} &= (D_{12}\mu_{11} - D_{11}\mu_{12})/s \\ L_{21} &= (D_{21}\mu_{22} - D_{22}\mu_{21})/s \\ L_{22} &= (D_{22}\mu_{11} - D_{21}\mu_{12})/s \end{aligned} \tag{8}$$

in which μ_{ij} stand for the partial derivatives $\partial\mu_i/\partial C_j$ and the denominator s is given by

$$s = \mu_{11}\mu_{22} - \mu_{12}\mu_{21}.$$

Equation (8), previously used by other investigators [14, 25] permit the calculation of the fundamental diffusion coefficients, L_{ij}, from practical diffusion coefficients that are determined experimentally, provided that the values of the various partial derivatives are known. The method for evaluation of these derivatives is given next.

The chemical potential of the ith component, μ_i, is defined in terms of its activity a_i, by

$$\mu_i = \mu_i^\circ + RT \ln a_i$$

in which μ_i° is a constant under fixed temperature and pressure, and R is the gas constant. The partial derivatives, μ_{ij}, are given by

$$\mu_{ij} = \frac{RT}{a_j} a_{ij} \qquad \begin{matrix} i = 1, 2 \\ j = 1, 2 \end{matrix} \tag{9}$$

in which a_{ij} represents the partial derivatives $\partial a_i/\partial C_j$. Thus, the evaluation of μ_{ij} is accomplished if appropriate expressions of a_{ij} are available.

As shown in eqs (46) and (47) in appendix 1, the activities, a_1 and a_2, for components 1 and 2 ($CaHPO_4$ and H_3PO_4, respectively) are functions of their concentrations C_1 and C_2. Other quantities in those expressions (hydrogen activity and ionic activity coefficients) are also functions of C_1 and C_2. Therefore

$$a_{ij} = \left(\frac{\partial a_i}{\partial C_j}\right)_{c_k} = \left(\frac{\partial a_i}{\partial C_j}\right)_{c_k, H, \gamma_l} + \left(\frac{\partial a_i}{\partial H}\right)_{c_j, c_k, \gamma_l} \left(\frac{\partial H}{\partial C_j}\right)_{c_k} + \sum_l \left(\frac{\partial a_i}{\partial \gamma_l}\right)_{c_j, c_k, H} \left(\frac{\partial \gamma_l}{\partial C_j}\right)_{c_k} \qquad \begin{cases} i = 1, 2 \\ j = 1, 2 \\ k = 1, 2 \\ j \neq k \end{cases} \tag{10}$$

in which H represents the ionic activity of hydrogen, and γ_l represents the activity coefficient of each of the l ions assumed to be present in the system (i.e., Ca^{++}, H^+, $H_2PO_4^-$, and $HPO_4^=$).

The electroneutrality function E, eq (42) in appendix 1, which will be used later, is defined on the basis that only these ions are present. In the subsequent equations through eq (19), indexes i, j, and k, assume the same values as in eq (10).

In the dilute range of the ternary system under consideration, where the Debye-Hückel theory provides an adequate expression for the calculation of ionic activity coefficients [12, 13], γ_l are explicit functions of the ionic strength I. Therefore, the second factor in the summation term of eq (10) becomes

$$\left(\frac{\partial \gamma_l}{\partial C_j}\right)_{c_k} = \frac{d\gamma_l}{dI}\left(\frac{\partial I}{\partial C_j}\right)_{c_k}. \tag{11}$$

By substitution of eq (11) into eq (10) and making

$$\sum_l \left(\frac{\partial a_i}{\partial \gamma_l}\right)_{c_j, c_k, H} \frac{d\gamma_l}{dI} = a_i^*$$

eq (10) becomes

$$a_{ij} = \left(\frac{\partial a_i}{\partial C_j}\right)_{c_k, H, \gamma_l} + \left(\frac{\partial a_i}{\partial H}\right)_{c_j, c_k, \gamma_l} \left(\frac{\partial H}{\partial C_j}\right)_{c_k} + a_i^* \left(\frac{\partial I}{\partial C_j}\right)_{c_k}. \tag{12}$$

By differentiation of eq (43) in appendix 1, it follows that

$$\left(\frac{\partial I}{\partial C_j}\right)_{c_k} = \left(\frac{\partial I}{\partial C_j}\right)_{c_k, H, \gamma_l} + \left(\frac{\partial I}{\partial H}\right)_{c_j, c_k, \gamma_l} \left(\frac{\partial H}{\partial C_j}\right)_{c_k} + \sum_l \left(\frac{\partial I}{\partial \gamma_l}\right)_{c_j, c_k, H} \left(\frac{\partial \gamma_l}{\partial C_j}\right)_{c_k}. \tag{13}$$

By substitution of eq (11) into (13) and making

$$\sum_l \left(\frac{\partial I}{\partial \gamma_l}\right)_{c_j, c_k, H} \frac{d\gamma_l}{dI} = I^*$$

eq (13) becomes

$$\left(\frac{\partial I}{\partial C_j}\right)_{c_k} = \left(\frac{\partial I}{\partial C_j}\right)_{c_k, H, \gamma_l} + \left(\frac{\partial I}{\partial H}\right)_{c_j, c_k, \gamma_l} \left(\frac{\partial H}{\partial C_j}\right)_{c_k} + I^* \left(\frac{\partial I}{\partial C_j}\right)_{c_k}. \tag{14}$$

Solving eq (14) for $(\partial I/\partial C_j)_{c_k}$

$$\left(\frac{\partial I}{\partial C_j}\right)_{c_k} = \left[\left(\frac{\partial I}{\partial C_j}\right)_{c_k, H, \gamma_l} + \left(\frac{\partial I}{\partial H}\right)_{c_j, c_k, \gamma_l} \left(\frac{\partial H}{\partial C_j}\right)_{c_k}\right] (1 - I^*)^{-1}. \tag{15}$$

Substitution of eq (15) into eq (12) gives an expression for a_{ij} in terms of partial derivatives that can be readily calculated from experimental measurements, except for the derivative $(\partial H/\partial C_j)_{c_k}$. The derivation for $(\partial H/\partial C_j)_{c_k}$ is given next.

Differentiation of the electroneutrality function E, eq (42) in appendix 1, gives

$$\left(\frac{\partial E}{\partial C_j}\right)_{c_k} = 0 = \left(\frac{\partial E}{\partial C_j}\right)_{c_k, H, \gamma_l} + \left(\frac{\partial E}{\partial H}\right)_{c_j, c_k, \gamma_l}\left(\frac{\partial H}{\partial C_j}\right)_{c_k} + \sum_l \left(\frac{\partial E}{\partial \gamma_l}\right)_{c_j, c_k, H}\left(\frac{\partial \gamma_l}{\partial C_j}\right)_{c_k}. \quad (16)$$

By substitution of eq (11) into eq (16) and making

$$\sum_l \left(\frac{\partial E}{\partial \gamma_l}\right)_{c_j, c_k, H} \frac{d\gamma_l}{dI} = E^*$$

eq (16) becomes

$$\left(\frac{\partial E}{\partial C_j}\right) = 0 = \left(\frac{\partial E}{\partial C_j}\right)_{c_k, H, \gamma_l} + \left(\frac{\partial E}{\partial H}\right)_{c_j, c_k, \gamma_l}\left(\frac{\partial H}{\partial C_j}\right)_{c_k} + E^*\left(\frac{\partial I}{\partial C_j}\right)_{c_k}. \quad (17)$$

Substitution of eq (15) into eq (17) gives the solution for $(\partial H/\partial C_j)_{c_k}$.

$$\left(\frac{\partial H}{\partial C_j}\right)_{c_k} = -\frac{(1-I^*)\left(\frac{\partial E}{\partial C_j}\right)_{c_k, H, \gamma_l} + E^*\left(\frac{\partial I}{\partial C_j}\right)_{c_k, H, \gamma_l}}{(1-I^*)\left(\frac{\partial E}{\partial H}\right)_{c_j, c_k, \gamma_l} + E^*\left(\frac{\partial I}{\partial H}\right)_{c_j, c_k, \gamma_l}}. \quad (18)$$

Substitution of eq (18) into eq (15) gives

$$\left(\frac{\partial I}{\partial C_j}\right)_{c_k} = \frac{\left(\frac{\partial I}{\partial C_j}\right)_{c_k, H, \gamma_l}\left(\frac{\partial E}{\partial H}\right)_{c_j, c_k, \gamma_l} - \left(\frac{\partial I}{\partial H}\right)_{c_j, c_k, \gamma_l}\left(\frac{\partial E}{\partial C_j}\right)_{c_k, H, \gamma_l}}{(1-I^*)\left(\frac{\partial E}{\partial H}\right)_{c_j, c_k, \gamma_l} + E^*\left(\frac{\partial I}{\partial H}\right)_{c_j, c_k, \gamma_l}}. \quad (19)$$

The right-hand terms in eqs (18) and (19) involve quantities that can be readily calculated from experimental measurements. The actual expressions used for such calculations are given in appendix 2. Substitution of eqs (11), (18), and (19) into eq (10) gives the needed expression for the evaluation of a_{ij}; then, by the use of eq (9), evaluation of μ_{ij} is accomplished, and substitution of the μ_{ij} into eqs (8) permits the calculation of the fundamental diffusion coefficients, L_{ij}, and, therefore, the testing of the Onsager's reciprocal relations.

b. Ionic Model

In the foregoing treatment, the components have been considered as neutral species, although in defining their activities, their ionic nature was taken into account. Consideration of an ionic model for the present system is advantageous in that practical diffusion coefficients can be calculated for the electroneutral components on the basis of ionic conductances [10]. It is then possible to compare the practical diffusion coefficients derived here with those obtained experimentally.

The ionic model selected here is given in eqs (20) to (22)

$$CaHPO_4 \rightarrow Ca^{++} + HPO_4^{=} \quad (20)$$

$$H_3PO_4 \rightarrow 2H^+ + HPO_4^{=} \quad (21)$$

$$H_2PO_4^- \rightleftarrows H^+ + HPO_4^{=} \quad (22)$$

This ionic model implies that there is no undissociated H_3PO_4, an assumption which is justifiable for the pH range considered here. It will be shown now that this system is thermodynamically equivalent to the one in which $CaHPO_4$ and H_3PO_4 are considered as the neutral components. In the following derivations, the numerals 1 and 2 are used for the constituents $CaHPO_4$ and H_3PO_4; the numerals 3, 4, 5, and 6 represent the ions $H_2PO_4^-$, Ca^{++}, $HPO_4^{=}$ and H^+, respectively.

The stoichiometric coefficients in the right-hand terms of eqs (20) to (22) are represented by ν_{ij}. For example, ν_{14} is the stoichiometric coefficient for the Ca^{++} that comes from $CaHPO_4$ and ν_{15} is for the $HPO_4^{=}$ that comes from the $CaHPO_4$. The numerical values for the ν_{ij}'s are: $\nu_{14} = \nu_{15} = \nu_{25} = \nu_{35} = \nu_{36} = 1$; $\nu_{16} = \nu_{24} = \nu_{34} = 0$; $\nu_{26} = 2$.

On the basis of the ionic model, the entropy production, σT, in the diffusion system is given by [18, 26]

$$\sigma T = \sum_{j=3}^{6} J_j \bar{X}_j = \sum_{j=4}^{6} J_j \bar{X}_j + J_3 \bar{X}_3 \quad (23)$$

in which J_j represents the diffusion flow of the jth ion and $\bar{X}_j$ its generalized driving force (in this case, its electrochemical potential gradient); σ is the rate of entropy production at temperature T.

We consider now as new generalized forces the chemical potential gradients, $\bar{X}_i$, of the neutral com-

ponents 1 and 2 and the electrochemical potential $\bar{X}_3$. The transformation equations for the new forces are

$$X_i = \sum_{j=4}^{6} \nu_{ij}\bar{X}_j \qquad (i=1, 2) \qquad (24)$$
$$\bar{X}_3 = \sum_{j=4}^{6} \nu_{3j}\bar{X}_j$$

which are linear combinations of the old forces $\bar{X}_j$. The transformation equations for the new flows, derived from the mass balance condition in eqs (20) to (22), are

$$J_j = \sum_{i=1}^{2} \nu_{ij}J_i - \nu_{3j}J_3 \qquad (j=4 \text{ to } 6). \qquad (25)$$

Substitution of eq (25) into (23) gives

$$\sigma T = \sum_{i=1}^{2}\sum_{j=4}^{6} \nu_{ij}\bar{X}_j J_i - J_3\left(\sum_{j=4}^{6} \nu_{3j}\bar{X}_j - \bar{X}_3\right). \qquad (26)$$

But, according to eq (24) the summation term within parenthesis equals $\bar{X}_3$, therefore, the quantity within parenthesis vanishes and

$$\sigma T = \sum_{i=1}^{2} J_i X_i \qquad (27)$$

hence, the ionic model is thermodynamically equivalent to the diffusion system in which the neutral compounds $CaHPO_4$ and H_3PO_4 are considered as components.

The procedure to calculate fundamental diffusion coefficients for neutral components from ionic conductances has been given in detail by Wendt [10] and it was tested by the same author with diffusion data [27] for the system H_2SO_4—Na_2SO_4—H_2O. For this reason, only a summary of our derivation is given next in which we apply Wendt's treatment to the present system. We use the same terminology except that his L_{ij} (for ions) corresponds to our Γ_{ij} and his a_{ij} correspond to our α_{ij}.

The diffusion flows J_j of the j ions are related to the chemical potential gradients, X_n, of the two neutral components by

$$J_j = -\nu^{-1}\sum_{n=1}^{2}\sum_{k=3}^{6} \alpha_{kn}X_n\Omega_{jk} \qquad (j=3 \text{ to } 6) \qquad (28)$$

in which ν is the value of the determinant of the ν_{ij} matrix (equal to -1 in the present case); α_{kn}, the elements of the matrix $[\alpha_{kn}]$, have the numerical values $\alpha_{31}=\alpha_{32}=\alpha_{51}=\alpha_{61}=0$, $\alpha_{33}=\alpha_{41}=\alpha_{42}=\alpha_{62}=-1$, $\alpha_{52}=\alpha_{63}=1$, $\alpha_{43}=2$, $\alpha_{53}=-2$; the coefficients Ω_{jk} are given by

$$\Omega_{jk} = \delta_{jk}\Gamma_{jk} - \frac{\Gamma_{jj}\alpha_{j3}\Gamma_{kk}\alpha_{k3}}{\sum_{q=3}^{6}\Gamma_{qq}\alpha_{q3}^2} \qquad \begin{matrix} j=3 \text{ to } 6 \\ k=3 \text{ to } 6. \end{matrix} \qquad (29)$$

In eq (29), δ_{jk} is the Kronecker delta (it has the value 1 for $j=k$, and zero for $j \neq k$), and the Γ's are the main terms of the fundamental diffusion coefficients for the subscripted ions, 3 to 6. Equation (29) is consistent with Wendt's assumption [10] that the coefficients Γ_{jk} are zero for $j \neq k$. These ionic coefficients can be calculated from

$$\Gamma_{jj} = (\lambda_j^\circ C_j)/|Z_j|F^2 \times 10^7 \qquad j=3 \text{ to } 6 \qquad (30)$$

in which λ_j° is the limiting equivalent conductance of the ion j, C_j its molarity, $|Z_j|$ the absolute value of its valence and F is the Faraday constant (96,493 coulombs per equivalent of charge). Values used for λ_j° in this investigation are given in appendix 1.

Expanding eq (25) and solving for J_1 and J_2 (using the numerical values for the corresponding ν_{ij}) we get

$$J_1 = J_4$$
$$J_2 = \tfrac{1}{2}(J_3 + J_6). \qquad (31)$$

The expressions for the ionic flows J_3, J_4, and J_6 given by eq (28) can now be substituted into eqs (31) to obtain

$$J_1 = \sum_{n=1}^{2}\sum_{k=3}^{6} \alpha_{kn}X_n\Omega_{4k} \qquad (32)$$

$$J_2 = \frac{1}{2}\sum_{n=1}^{2}\sum_{k=3}^{6} \alpha_{kn}X_n\Omega_{6k} + \frac{1}{2}\sum_{n=1}^{2}\sum_{k=3}^{6} \alpha_{kn}X_n\Omega_{3k} \qquad (33)$$

But from eq (3) we can also write

$$J_1 = -\sum_{n=1}^{2} L_{1n}X_n \qquad (34)$$

$$J_2 = -\sum_{n=1}^{2} L_{2n}X_n. \qquad (35)$$

Through a comparison of the coefficients of X_n in eqs (34) and (35) with those in eqs (32) and (33), respectively, it is obtained

$$L_{1n} = -\sum_{k=3}^{6} \alpha_{kn}\Omega_{4k}$$
$$L_{2n} = -\frac{1}{2}\sum_{k=3}^{6} \alpha_{kn}(\Omega_{6k} + \Omega_{3k}) \qquad n=1, 2 \qquad (36)$$

Equations (36) together with (29) and (30), permit the calculation of theoretical fundamental diffusion coefficients, L_{ij}, from a knowledge of the limiting conductance of the ions involved.

3. Calculation of Diffusion Coefficients

The values for L_{ij} and D_{ij}, calculated from eqs (36) and (7), respectively, are shown in table 1, together with the composition of the 13 solutions used for

this purpose. The concentrations C_1 and C_2 were taken from the solubility isotherm for hydroxyapatite [13]. Since, in the present derivations, ion pairs are ignored, the values for pH in table 1 were calculated solving eq (42) for (H^+). The calculated pH values do not depart appreciably from the corresponding values for the isotherm [13].

The data in table 1 suggest that, while the interference represented by D_{12} is important in all the systems considered, the effect of D_{21} becomes important only in the systems having pH's lower than about 6. Study of system number 4 showed this to be the case. Calculations of the D_{ii} were made keeping the concentration of one of the components constant and decreasing the concentration of the other component. The results of these calculations are shown in figures 1a and 1b. It is apparent that, as the concentration of $CaHPO_4$, C_1, approaches zero, figure 1a, D_{22} approaches a value very close to 1.575×10^{-5}; this is the Nernst limiting diffusion coefficient calculated with the values for the limiting equivalent conductances given in appendix 1 for the ions H^+ and $H_2PO_4^-$; in other words, the diffusion of $4.888 \times 10^{-5} M$ H_3PO_4 in the binary system $H_3PO_4-H_2O$ essentially fulfills the expectations for infinite dilution.

The calculated Nernst limiting diffusion coefficient for $CaHPO_4$ is 1.342×10^{-5}. Examination of figure 1b indicates that this limiting value is not approached even at the lowest concentration of H_3PO_4. It must be concluded, therefore, that, according to the model adopted here, the interference of H_3PO_4 on the diffusion of $CaHPO_4$ persists even at very low concentrations of both components. This conclusion was also verified by similar calculations on systems more dilute than system 4.

The values in table 1 and the curve in figures 1a and 1b clearly show that in diffusion processes occurring in dilute solutions of the system $CaHPO_4-H_3PO_4-H_2O$, the magnitude of the interferences, as given by the cross terms in D_{ij}, will affect the fluxes appreciably and therefore cannot be ignored. Also, for a test of the Onsager reciprocal relations, experimental conditions should be selected such that the interferences are

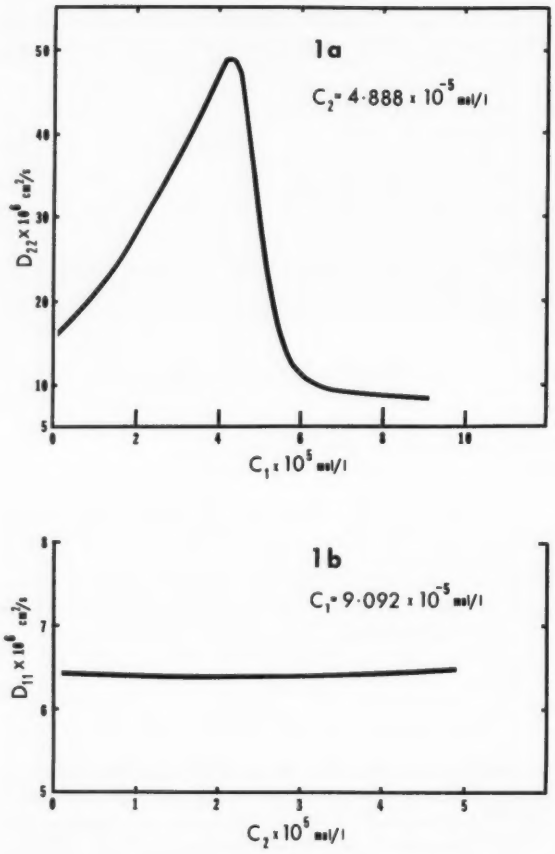

FIGURE 1a. *Plot of the main diffusion coefficient of* H_3PO_4 *against concentration of* $CaHPO_4$.

The concentration of H_3PO_4 is fixed at 4.888×10^{-5} mol/l.

FIGURE 1b. *Plot of the main diffusion coefficient of* $CaHPO_4$ *against concentration of* H_3PO_4.

The concentration of $CaHPO_4$ is fixed at 9.092×10^{-5} mol/l.

TABLE 1. *Calculated* L_{ij} *and* D_{ij} *for the Ternary System* $CaHPO_4$ *(1)—*H_3PO_4 *(2)—*H_2O *at 25°*

Systems	C_1, mol/l $\times 10^4$	C_2, mol/l $\times 10^4$	pH	$L_{11} \times 10^{13}$	$L_{12} \times 10^{13}$	$L_{21} \times 10^{13}$	$L_{22} \times 10^{13}$	$D_{11} \times 10^6$	$D_{12} \times 10^6$	$D_{21} \times 10^6$	$D_{22} \times 10^6$
1	0.319	0.0596	7.521	0.4201	0.05890	0.05890	0.1002	6.552	1.509	0.05540	8.724
2	0.420	0.114	7.311	0.5468	0.1139	0.1139	0.1851	6.533	1.536	0.08048	8.644
3	0.658	0.280	7.008	0.8343	0.2863	0.2863	0.4288	6.506	1.564	0.1085	8.533
4	0.909	0.489	6.808	1.131	0.5079	0.5079	0.7160	6.493	1.568	0.09988	8.483
5	1.54	1.07	6.512	1.857	1.129	1.129	1.458	6.500	1.536	−0.008148	8.497
6	2.71	2.20	6.220	3.198	2.370	2.370	2.846	6.568	1.423	−0.3150	8.704
7	4.03	3.51	6.027	4.703	3.796	3.796	4.401	6.674	1.275	−0.6894	9.008
8	6.74	6.20	5.785	7.790	6.752	6.753	7.585	6.920	0.959	−1.448	9.670
9	10.3	9.75	5.598	11.85	10.65	10.65	11.76	7.217	0.5940	−2.303	10.44
10	19.9	19.3	5.312	22.79	21.19	21.19	23.01	7.982	−0.2990	−4.300	12.28
11	31.4	30.8	5.113	35.86	33.81	33.81	36.46	8.851	−1.270	−6.385	14.26
12	64.0	63.5	4.787	72.96	69.62	69.62	74.83	11.23	−3.822	−11.64	19.32
13	105.	105.	4.485	120.2	114.6	114.6	124.6	15.78	−8.510	−20.87	28.42

Units of L_{ij}: $Mol^2/(J \cdot cm \cdot s)$
Units of D_{ij}: cm^2/s

detectable with the measurements used within reasonable errors. For example, with system 1 of table 1 it would be practically impossible to arrive at a reliable value for L_{21}. On the other hand, it is predicted that diffusion experiments with systems 12 or 13 will yield the required information for calculation of L_{ij}.

4. Appendix 1

C_1 = molar concentration of $CaHPO_4$
C_2 = molar concentration of H_3PO_4 used in preparation of solution
P_1 = molar concentration of $H_2PO_4^-$
P_2 = molar concentration of $HPO_4^=$
γ_1 = molar activity coefficient for $H_2PO_4^-$
γ_2 = molar activity coefficient for $HPO_4^=$
γ_3 = molar activity coefficient for Ca^{++}
γ_4 = molar activity coefficient for H^+
[H] = molar concentration of H^+
H = activity of H^+
K_1 = first ionization constant of H_3PO_4, $7.10_8 \times 10^{-3}$ [28]
K_2 = second ionization constant of H_3PO_4, $6.33_8 \times 10^{-8}$ [29]
(P_2) = activity of $HPO_4^=$
λ_3° = limiting equivalent conductance of $H_2PO_4^-$, 32.3 [30]
λ_4° = limiting equivalent conductance of Ca^{++}, 59.50 [31]
λ_5° = limiting equivalent conductance of $HPO_4^=$, 43.7 [32]
λ_6° = limiting equivalent conductance of H^+, 349.8_1 [31].

The total molar concentration of phosphorus in the solutions of $CaHPO_4$ in dilute H_3PO_4 is given by (C_1+C_2). The balance equation for phosphorus, for solutions with pH values below 7.5, may be written

$$(C_1+C_2)=P_1+P_2. \tag{37}$$

The quantity P_1 may be written in terms of P_2 by the use of the expression for the second ionization of H_3PO_4; then, solving eq (37) for P_2 gives

$$P_2=(C_1+C_2)/\gamma_2\left(\frac{1}{\gamma_2}+\frac{H}{K_2\gamma_1}\right). \tag{38}$$

Calling f_2 the quantity within parenthesis in the denominator of eq (38)

$$P_2=(C_1+C_2)/\gamma_2 f_2 \tag{39}$$

and by substitution of eq (39) into the expression for the second ionization of H_3PO_4,

$$P_1=(C_1+C_2)H/f_2\gamma_1K_2. \tag{40}$$

The function E, that defines electroneutrality, is

$$E=0=2C_1+\frac{H}{\gamma_4}-2P_2-P_1. \tag{41}$$

Substitution of eqs (39) and (40) into (41) gives

$$E=0=2C_1+\frac{H}{\gamma_4}-\frac{(C_1+C_2)}{f_2}\left[\frac{H}{\gamma_1K_2}+\frac{2}{\gamma_2}\right]. \tag{42}$$

The ionic strength, I, is given by

$$I=2C_1+\frac{H}{2\gamma_4}+\frac{C_1+C_2}{2f_2}\left[\frac{H}{\gamma_1K_2}+\frac{4}{\gamma_2}\right]. \tag{43}$$

For brevity in the expressions given in appendix 2, we define the quantities within square brackets in eqs (42) and (43) as

$$Q=\frac{H}{K_2\gamma_1}+\frac{2}{\gamma_2} \tag{44}$$

$$G=\frac{H}{K_2\gamma_1}+\frac{4}{\gamma_2}. \tag{45}$$

The activities of $CaHPO_4$ and H_3PO_4 in solution are given by eqs (46) and (47), respectively.

$$a_1=\frac{(C_1^2+C_2C_1)\gamma_3}{f_2} \tag{46}$$

$$a_2=\frac{(C_1+C_2)H}{f_1K_1}. \tag{47}$$

The function f_1 in eq (47) is defined by

$$f_1=\frac{K_2}{H\gamma_2}+\frac{1}{\gamma_1}. \tag{48}$$

The ionic activity coefficients, γ_l, are calculated from the Debye-Hückel theory

$$\ln \gamma_l=-\frac{AZ_l^2\sqrt{I}}{1+B\alpha_l\sqrt{I}} \tag{49}$$

in which the constants A and B, dependent on temperature and the dielectric constant of water, have numerical values of 0.5092 and 0.3286×10^8, respectively [33] at 25 °C; Z_l is the valence of the lth ion, and α_l its distance of closest approach. Numerical values for α_l [34] are: Ca^{++}, 6×10^{-8} cm; H^+, 9×10^{-8} cm; $HPO_4^=$ and $H_2PO_4^-$, 4×10^{-8} cm.

5. Appendix 2

In this appendix are given the expressions for the calculation of the partial derivatives used in the text; these expressions are based on the equations in appendix 1.

$$\frac{d\gamma_l}{dI}=\gamma_l\frac{\Phi(I)}{2I(1+B\alpha_l\sqrt{I})}$$

in which

$$\Phi(I) = -\frac{AZ_i^2\sqrt{I}}{1+B\alpha_i\sqrt{I}}$$

$$\left(\frac{\partial I}{\partial C_1}\right)_{c_2,H,\gamma_l} = 2+\frac{G}{2f_2}$$

$$\left(\frac{\partial I}{\partial C_2}\right)_{c_1,H,\gamma_l} = \frac{G}{2f_2}$$

$$\left(\frac{\partial I}{\partial H}\right)_{c_1,c_2,\gamma_l} = \frac{1}{2\gamma_4}+\frac{(C_1+C_2)}{2f_2K_2}\left[\frac{1}{\gamma_1}-\frac{G}{f_2\gamma_1}\right]$$

$$\left(\frac{\partial I}{\partial \gamma_2}\right)_{c_1,c_2,H,\gamma_{l\neq 2}} = \frac{C_1+C_2}{2f_2\gamma_2^2}\left[\frac{G}{f_2}-4\right]$$

$$\left(\frac{\partial I}{\partial \gamma_1}\right)_{c_1,c_2,H,\gamma_{l\neq 1}} = \frac{(C_1+C_2)}{2f_2K_2\gamma_1^2}\left[\frac{G}{f_2}-1\right]$$

$$\left(\frac{\partial I}{\partial \gamma_4}\right)_{c_1,c_2,H,\gamma_{l\neq 4}} = -\frac{H}{2\gamma_4^2}$$

$$\left(\frac{\partial a_1}{\partial C_1}\right)_{c_2,H,\gamma_l} = \frac{(2C_1+C_2)\gamma_3}{f_2}$$

$$\left(\frac{\partial a_1}{\partial C_2}\right)_{c_1,H,\gamma_l} = \frac{C_1\gamma_3}{f_2}$$

$$\left(\frac{\partial a_1}{\partial H}\right)_{c_1,c_2,\gamma_l} = -\frac{(C_1^2+C_1C_2)\gamma_3}{f_2^2K_2}\left(\frac{2H}{K_1}+\frac{1}{\gamma_1}\right)$$

$$\left(\frac{\partial a_1}{\partial \gamma_1}\right)_{c_1,c_2,H,\gamma_{l+1}} = \frac{(C_1^2+C_1C_2)\gamma_3 H}{f_2^2K_2\gamma_1^2}$$

$$\left(\frac{\partial a_1}{\partial \gamma_2}\right)_{c_1,c_2,H,\gamma_{l+2}} = \frac{(C_1^2+C_1C_2)\gamma_3}{f_2^2\gamma_2^2}$$

$$\left(\frac{\partial a_1}{\partial \gamma_3}\right)_{c_1,c_2,H,\gamma_{l+3}} = \frac{(C_1^2+C_1C_2)}{f_2}$$

$$\left(\frac{\partial a_2}{\partial C_2}\right)_{c_1,H,\gamma_l} = \left(\frac{\partial a_2}{\partial C_1}\right)_{c_2,H,\gamma_l} = \frac{H}{f_1K_1}$$

$$\left(\frac{\partial a_2}{\partial H}\right)_{c_1,c_2,\gamma_l} = \frac{(C_1+C_2)}{f_1^2K_1}\left(f_1+\frac{K_2}{H\gamma_2}-\frac{H}{K_1}\right)$$

$$\left(\frac{\partial a_2}{\partial \gamma_1}\right)_{c_1,c_2,\gamma_{l+1}} = \frac{(C_1+C_2)H}{f_1^2K_1\gamma_1^2}$$

$$\left(\frac{\partial a_2}{\partial \gamma_2}\right)_{c_1,c_2,\gamma_{l+2}} = \frac{(C_1+C_2)K_2}{f_1^2K_1\gamma_2^2}$$

$$\left(\frac{\partial E}{\partial C_1}\right)_{c_2,H,\gamma_l} = 2-\frac{Q}{f_2}$$

$$\left(\frac{\partial E}{\partial C_2}\right)_{c_1,H,\gamma_l} = -\frac{Q}{f_2}$$

$$\left(\frac{\partial E}{\partial H}\right)_{c_1,c_2,\gamma_l} = \frac{1}{\gamma_4}-\frac{(C_1+C_2)}{f_2K_2\gamma_1}\left(1-\frac{Q}{f_2}\right)$$

$$\left(\frac{\partial E}{\partial \gamma_1}\right)_{c_1,c_2,H,\gamma_{l+1}} = \frac{(C_1+C_2)H}{f_2K_2\gamma_1^2}\left(1-\frac{Q}{f_2}\right)$$

$$\left(\frac{\partial E}{\partial \gamma_2}\right)_{c_1,c_2,H,\gamma_{l+2}} = \frac{(C_1+C_2)}{f_2\gamma_2^2}\left(2-\frac{Q}{f_2}\right)$$

$$\left(\frac{\partial E}{\partial \gamma_4}\right)_{c_1,c_2,H,\gamma_{l+4}} = -\frac{H}{\gamma_4^2}.$$

This investigation was supported in part by research grant DE02659 to the American Dental Association from the National Institute of Dental Research and is part of the dental research program conducted by the National Bureau of Standards, in cooperation with the Council on Dental Research of the American Dental Association; the U.S. Army Medical Research and Development Command; the Dental Sciences Division of the School of Aerospace Medicine, USAF; the National Institute of Dental Research; and the Veterans Administration.

6. References

[1] Higuchi, W. I., Gray, J. A., Hefferren, J. J., and Patel, P. R., J. Dent. Res. **44**, 330 (1965).
[2] Gray, J. A., and Francis, M. D., in Mechanisms of hard tissue destruction, AAAS, Washington, D.C., 1963.
[3] Holly, F. J., and Gray, J. A., Arch. Oral Biol. **13**, 319 (1968).
[4] Onsager, L., Phys. Rev. **37**, 405 (1931).
[5] Onsager, L., Phys. Rev. **38**, 2265 (1931).
[6] Onsager, L., Ann. N.Y. Acad. Sci. 46, 241 (1945).
[7] Dunn, R. L., and Hatfield, J. D., J. Phys. Chem. **69**, 4361 (1965).
[8] Edwards, O. W., Dunn, R. L., Hatfield, J. D., Huffman, E. O., and Elmore, K. L., J. Phys. Chem. **70**, 217 (1966).
[9] Edwards, O. W., and Huffman, E. O., J. Phys. Chem. **63**, 1830 (1959).
[10] Wendt, R. P., J. Phys. Chem. **69**, 1227 (1965).
[11] Miller, D. G., J. Phys. Chem. **63**, 570 (1959).
[12] Moreno, E. C., Gregory, T. M., and Brown, W. E., J. Res. Nat. Bur. Stand. (U.S.), **70A** (Phys. and Chem.) No. 6. 545–552 (Nov.–Dec. 1966).
[13] Moreno, E. C., Gregory, T. M., and Brown, W. E., J. Res. Nat. Bur. Stand. (U.S.), **72A**, (Phys. and Chem.) No. 6, 773–782 (Nov.–Dec. 1968).
[14] Kirkwood, J. G., Baldwin, R. L., Dunlop, P. J., Gosting, L. G., and Kegeles, G., J. Chem. Phys. **33**, 1505 (1960).
[15] Hooyman, G. J., Holtan, H. R., Mazur, P., and de Groot, S. R., Physica **19**, 1095 (1953).
[16] Dunlop, P. J., and Gosting, L. G., J. Phys. Chem. **63**, 86 (1959).
[17] Prigogine, I., Bull. Classe Sci. Acad. roy. Belg. **34**, 930 (1948).
[18] de Groot, S. R., and Mazur, P., Non-Equilibrium Thermodynamics (Interscience Publishers, Inc., New York, N.Y., 1962).
[19] Gilliland, E. R., Baddour, R. F., and Goldstein, D. J., Can. J. Chem. Eng. **35**, 10 (1957).

[20] Kelly, F. J., Ph.D. Thesis, University of New England, Armidale, N.S.W., Australia (1961).
[21] Kelly, F. J., and Stokes, R. H., Electrolytes, pp. 96–100, B. Pesce, Ed. (Pergamon Press Ltd., Oxford, 1962).
[22] Burchard, J. K., and Toor, H. L., J. Phys. Chem. **66,** 2015 (1962).
[23] Cussler, E. L., Jr., and Dunlop, P. J., J. Phys. Chem. **70,** 1880 (1966).
[24] Patel, P. R., E. C. Moreno, and T. M. Gregory, J. Res. Nat. Bur. Stand. (U.S.), **73A** (Phys. and Chem.) No. 1, 43–49 (1969).
[25] Gosting, L. G., in Advances in Protein Chemistry, Vol. XI, Academic Press, Inc., New York, N.Y. (1956).
[26] Prigogine, I., Introduction to Thermodynamics of Irreversible Processes (Interscience Publishers, Inc., New York, N.Y., 1961).
[27] Wendt, R. P., J. Phys. Chem. **66,** 1279 (1962).
[28] Bates, R. G., J. Res. NBS **47,** 127 (1951), RP 2236.
[29] Bates, R. G., and Acree, S. F., J. Res. NBS **34,** 373 (1945) RP 1648.
[30] Selvaratnam, M., and Spiro, M., Trans. Faraday Soc. **61,** 360 (1965).
[31] Robinson, R. A., and Stokes, R. H., Electrolyte Solutions, p. 463 (Academic Press, Inc., New York, N.Y., 1959).
[32] Tatarinov, B. P., and Fursenko, V. F., Russian J. Phys. Chem. **34,** 62 (1960).
[33] Manov, G. G., Bates, R. G., Hamer, W. J., and Acree, S. F., J. Am. Chem. Soc. **65,** 1765 (1943).
[34] Kielland, J. J., J. Am. Chem. Soc. **59,** 1675 (1937).

(Paper 74A1–585)

JOURNAL OF RESEARCH of the National Bureau of Standards—A. Physics and Chemistry
Vol. 74A, No. 1, January–February 1970

High-Speed (Subsecond) Measurement of Heat Capacity, Electrical Resistivity, and Thermal Radiation Properties of Molybdenum in the Range 1900 to 2800 K*

A. Cezairliyan, M. S. Morse, H. A. Berman, and C. W. Beckett

Institute for Materials Research, National Bureau of Standards, Washington, D.C. 20234

(October 16, 1969)

A technique is described for the high-speed measurement of heat capacity, electrical resistivity, hemispherical total and normal spectral emittances of electrical conductors at high temperatures (above 1900 K) with millisecond resolution. Duration of an individual experiment, in which the specimen is heated from room temperature to close to its melting point, is less than one second. Temperature measurements are made with a high-speed photoelectric pyrometer. Quantities are recorded by a high-speed digital data acquisition system which has a resolution of approximately one part in 8000. Time resolution of the entire system is 0.4 ms. Results on the above properties of molybdenum in the temperature range 1900 to 2800 K are reported and are compared with those in the literature. Estimated inaccuracy of measured properties in the above temperature range is: 2 to 3 percent for heat capacity, 0.5 percent for electrical resistivity, 3 percent for hemispherical total emittance and 2 percent for normal spectral emittance.

Key words: Electrical resistivity; emittance; heat capacity; high-speed measurements; high temperature; molybdenum; thermal radiation properties; thermodynamics.

1. Introduction

Most measurements of heat capacity, electrical resistivity, and various other thermophysical properties at high temperatures employ "drop", steady-state, and quasi steady-state experiments. In all these techniques, the specimen is exposed to high temperatures for relatively long periods of time (minutes-to-hours).

When these techniques are extended to very high temperatures (above 2000 K), many problems are created as the result of increased heat transfer, chemical reactions, evaporation, diffusion, loss of mechanical strength, etc., and these limit their application. Consequently, it has become necessary to develop a dynamic method which permits the heating of the specimen and the measurement of the pertinent quantities in a very short time. With this method the contributions of most of the phenomena which limit the application of conventional techniques at very high temperatures become negligible.

In recent years, considerable progress has been made in high-speed thermodynamic measurement methods and related instrumentation techniques. A general review of these is given in [10][1].

Over the past 50 years several investigators [6, 8, 21, 37, 40, 41, 47, 49–55, 65, 69, 70, 72] have developed dynamic and quasi-dynamic techniques for the measurement of heat capacity of electrical conductors. They differ considerably depending on the pulse power source and the method of measurement of specific quantities. In general, either batteries or capacitors have been used as the pulse power source. In most cases, power imparted to the specimen was obtained from pulse current and voltage measurements. The temperature of the heating specimen was either measured by thermocouples or was determined from dynamic electrical resistivity measurements. Use of thermocouples has several limitations and is not applicable to very high-speed work. The electrical resistivity method requires a separate steady-state determination of the electrical resistivity of the specimen as a function of temperature. A dynamic experiment of preliminary nature where a photomultiplier was used for the measurement of specimen temperature was described in [12]. In all of the recent investigations, with one exception [37], oscilloscopic techniques have been employed for the high-speed recording of quantities. Most of the experiments reported in the literature which utilized dynamic techniques were exploratory and were confined to temperatures below 1500 K.

In the present study, a technique is described for

*This work was supported in part by the Propulsion Division of the U.S. Air Force Office of Scientific Research under contract ISSA–69–0001.

[1] Figures in brackets indicate the literature references at the end of this paper.

367–409 OL–70—5

the dynamic measurement of heat capacity, electrical resistivity, hemispherical total emittance, and normal spectral emittance of electrical conductors at high temperatures (above 1900 K). Duration of an individual experiment, in which the specimen is heated from room temperature to close to its melting point, is less than 1 s. A millisecond resolution photoelectric pyrometry technique was employed for the temperature measurements. The dynamic recording of quantities was made with a high-speed, multichannel, digital data acquisition system which has a capability of recording data with 0.4 ms resolution. A distinct advantage of the present system is that it provides the capability of measuring several properties simultaneously. Experiments were conducted on molybdenum to measure the properties enumerated above over the temperature range 1900 to 2800 K.

2. Description of the Method

2.1. General Description

The dynamic method employed in this study is based upon rapid resistive heating of the specimen by a single pulse (subsecond duration) of direct current and measuring the pertinent quantities with millisecond resolution. Heat capacity and electrical resistivity are calculated from data obtained during the pulse heating period. Because of the short duration of the experiment, the only significant heat loss is that due to thermal radiation. Data taken during the initial free cooling period following the heating period enables one to compute hemispherical total emittance and thus apply a correction to heat capacity for the radiation heat loss. From separate dynamic experiments, in which radiation from the surface of the specimen is measured in addition to its temperature, normal spectral emittance is obtained. In the following paragraphs the formulation of the relationships between various variables is presented.

2.2. Formulation of Equations

a. Heating Period

The power balance for the specimen during the heating period can be expressed as

$$\text{Power Imparted} = \text{Power Stored} + \text{Power Losses.}$$

In high temperature dynamic experiments of millisecond resolution the major source of power loss is that due to thermal radiation. Using the proper quantities, the above relation becomes

$$ei = c_p n (dT/dt)_h + \epsilon\sigma A_s (T^4 - T_e^4) \tag{1}$$

where

e = potential difference across the effective specimen in V

i = current through the specimen in A

c_p = heat capacity in J mol^{-1} K^{-1}

n = effective amount of specimen in mol

ϵ = hemispherical total emittance

σ = Stephan-Boltzmann constant (5.6697×10^{-8} W m^{-2} K^{-4})

A_s = effective surface area in m^2

T = specimen temperature in K

T_e = room temperature in K

$(dT/dt)_h$ = heating rate in K s^{-1}.

Solving eq (1) for c_p one obtains

$$c_p = \frac{ei - \epsilon\sigma A_s (T^4 - T_e^4)}{n (dT/dt)_h}. \tag{2}$$

b. Cooling Period

The power balance for the specimen during the initial cooling period can be written as

$$\text{Power Loss} = \text{Power Radiated}$$

which can be expressed as

$$-c_p n (dT/dt)_c = \epsilon\sigma A_s (T^4 - T_e^4) \tag{3}$$

where

$(dT/dt)_c$ = cooling rate in K s^{-1}.

Solving eq (3) for c_p one obtains

$$c_p = \frac{\epsilon\sigma A_s (T^4 - T_e^4)}{-n (dT/dt)_c}. \tag{4}$$

c. Relations for Properties

Combination of eqs (2) and (4) yields

$$ei = \epsilon\sigma A_s (T^4 - T_e^4) - \epsilon\sigma A_s (T^4 - T_e^4) \left[\frac{(dT/dt)_h}{(dT/dt)_c}\right]. \tag{5}$$

Defining,

$$M = -\frac{(dT/dt)_h}{(dT/dt)_c} \tag{6}$$

and substituting eq (6) in eq (5) and solving for ϵ one obtains

$$\epsilon = \frac{ei}{\sigma A_s (T^4 - T_e^4)(1 + M)}. \tag{7}$$

Equation (7) is used to compute values for hemispherical total emittance, ϵ, at selected temperatures which are used to obtain a function for ϵ in terms of temperature. Then ϵ values from this function are substituted in eq (2) to obtain heat capacity over the entire temperature range.

Electrical resistivity is calculated with the aid of the equation

$$\rho = \frac{RA_c}{l} \tag{8}$$

where

ρ = electrical resistivity in Ω m

R = resistance of effective specimen in Ω

A_c = effective cross-sectional area in m^2

l = effective length in m.

Normal spectral emittance is calculated by the relation

$$\epsilon_{N,\lambda} = \frac{L_s}{L_b} \tag{9}$$

where

L_b = blackbody radiance from sighting hole in specimen as observed by the pyrometer,

L_s = radiance from surface of specimen as observed by the pyrometer.

In all the above equations geometrical quantities are corrected for the fact that a sighting hole is present; quantities related to radiation from the sighting hole are corrected for scattered light and departure from blackbody conditions.

3. Description of the System

The system used in this study consists of an electric power pulsing circuit and associated high-speed measuring circuits. The pulsing circuit includes the specimen in series with a battery bank, a variable resistance, a shunt (standard resistance), and a fast-acting switch. The high-speed measuring circuits include detectors, an analog-to-digital converter, a core memory, and other related equipment and circuitry necessary for the dynamic measurement and recording of the pertinent quantities. A functional diagram of the complete system is presented in figure 1. A photograph of the experiment chamber and the high-speed pyrometer is given in figure 2.

3.1. Specimen and Experiment Chamber

The specimen upon which the pulse experiments were made is a tube of the following nominal dimensions: length = 4 in (101.6 mm), outside diameter = 0.25 in (6.35 mm), wall thickness = 0.02 in (0.51 mm). A small rectangular hole (1.09 mm long, 0.56 mm wide) was fabricated in the wall at the middle of the specimen to approximate blackbody conditions. Potential probes were molybdenum knife edges each at a distance of 12.7 mm from the end clamps. The knife edges defined an "effective" portion of the specimen which should be free of axial temperature gradients for the duration of the experiment. A schematic diagram showing the arrangement of the specimen, clamps, and potential probes is presented in figure 3. Thermocouples are connected (electrically insulated) to the two end clamps to measure the specimen temperature before each pulse experiment. The chamber is designed for conducting experiments with the specimen either in vacuum or in a controlled atmosphere.

3.2. Pulsing Circuit

The power supply for the pulse heating of the specimen is a 28 V heavy-duty battery bank. A series-connected, water-cooled, variable resistance enables one to adjust the main current and thus to control the heating rate. The fast-acting switch is operated by a series of pulse control units which control the pulse length in addition to providing timing pulses to other electronic measuring and recording instruments. A standard resistor (0.001 Ω) placed in the main circuit is used to measure the heavy pulse current flowing through the specimen.

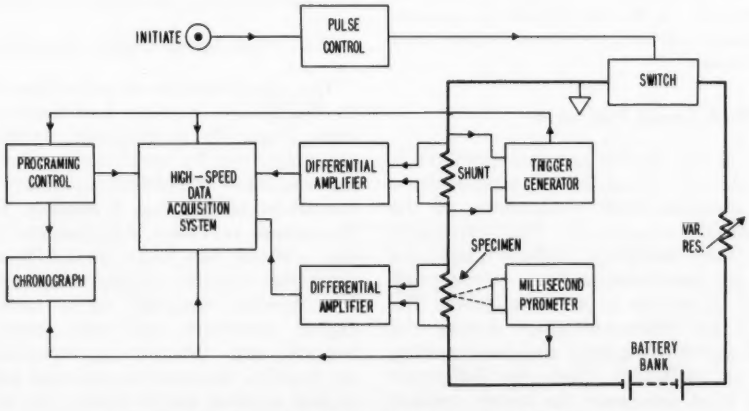

FIGURE 1. *Functional diagram of the complete high-speed measurement system.*

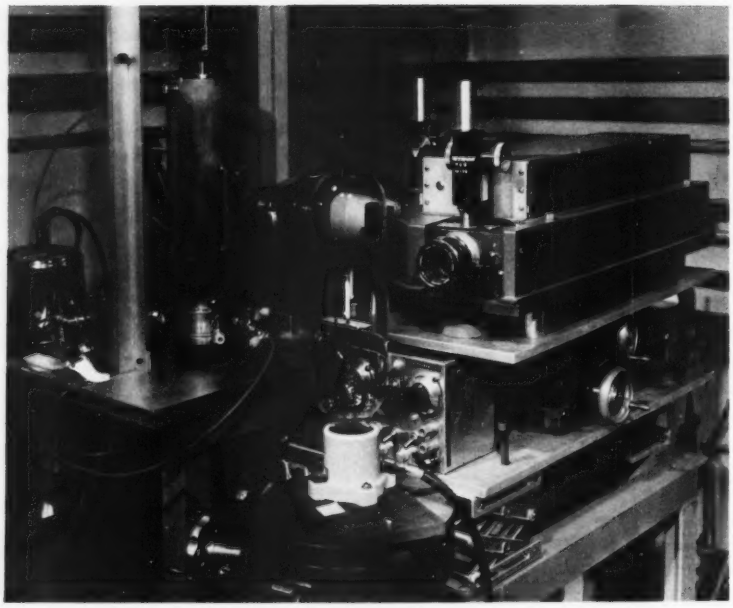

FIGURE 2. *Experiment chamber and high-speed pyrometer.*

3.3 Measuring and Control Circuits

Timing of various events, such as opening and closing of the switch, triggering of various electronic equipment, etc., during a dynamic experiment is achieved by a series of time-delay units. A 400 Hz synchronous motor used in the high-speed pyrometer provides the time base for the data acquisition system. Voltage signals from both the standard resistor and the specimen are sent to the recording system via differential amplifiers. Triaxial cables are used for the signals to be recorded and coaxial cables for all the controls. A potentiometric system is used to calibrate pulse voltage and pulse current measuring circuits including the differential amplifiers and the digital recording system. A Kelvin bridge is used to measure the resistance of the specimen before and after a pulse experiment.

3.4. High-Speed Pyrometer

The temperature of the rapidly heating specimen is measured by means of a high-speed photoelectric pyrometer, which permits 1200 evaluations of the specimen temperature per second. The pyrometer passes a precisely timed sample of radiation from the specimen through an interference filter (wavelength 650 nm, bandwidth 10 nm) to a photomultiplier. The anode current of the photomultiplier during the exposure time (208 μs) is integrated and the resulting integrator voltage is recorded. Then the integrator is reset to permit it to integrate the anode current due to a similar sample of radiation, which is provided by a calibrated, gas-filled tungsten filament lamp and suitably attenuated by an optical attenuator. Thus, the pyrometer collects the results of an interlaced sequence of exposures to specimen and reference source. Successive exposures to the reference lamp are taken through a sequence of three different optical attenuators mounted on a rotating disc, resulting in a staircase of reference exposures with approximately 50 percent attenuation for each step. This scheme is used for temperature measurements up to 2500 K, the limit of reliable operation of gas-filled lamps. For the measurement of higher temperatures, calibrated optical attenuators are placed in the path of the radiation from the specimen. A manuscript regarding constructional and operational details of the high-speed pyrometer is in preparation [20].

3.5. High-Speed Digital Data Acquisition System

The signals at the output of detectors corresponding to the voltage, current, and temperature are in analog form. Normally, in dynamic experiments such signals are measured by oscilloscopic techniques. However, the expected recording accuracy of such methods cannot be better than 1 percent. In order to improve the overall accuracy, a high-speed digital data acquisition system has been designed and constructed to meet the special requirements of the experiments. The system consists of a multiplexer, analog-to-digital converter and core memory together with control and interfacing equipment. Oscilloscopes are used to monitor the general pattern of the experimental results, and to detect any anomalies.

All signals are brought to the multiplexer through differential amplifiers in order to avoid the inaccuracies

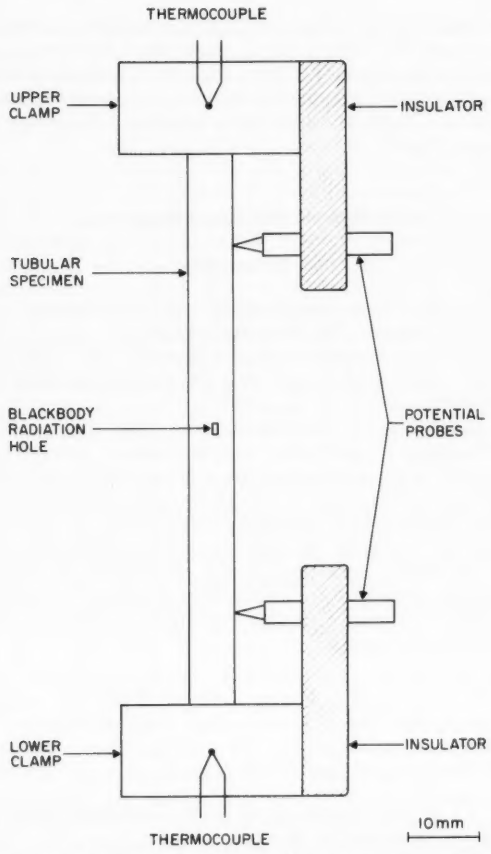

FIGURE 3. *Schematic diagram showing the arrangement of the specimen, clamps and potential probes.*

Potential probes are spring loaded knife edges which are free to move in vertical direction to allow for thermal expansion of the specimen.

arising from common ground points. The multiplexed signals go to the analog-to-digital converter, which has a full-scale reading of ± 10 V and a full-scale resolution of one part in 8192 ($8192 = 2^{13}$). Digital output from the converter consists of 13 binary bits plus a sign bit. This output is stored in a core memory having a capacity of 2048 words of sixteen bits each.

All the above takes place during a dynamic experiment of sub-second duration. After the experiment is over, information stored in the core memory, which is in parallel binary coded form, is converted to serial binary coded decimal form and retrieved in the form of numeric printing and punched paper tape using a teletypewriter. Since the laboratory has access to a remote-control, time-sharing computer, it is possible to unload the memory directly to the computer. This allows one to process the data immediately after an experiment, bypassing the intermediate stage of punching paper tape. A functional diagram of the high-speed data acquisition system is presented in figure 4. A manuscript regarding constructional and operational details of the high-speed digital data acquisition system is in preparation [46].

4. Measurements on Molybdenum

4.1. Procedure in Experimentation

The temperature interval 1900 to 2800 K was covered in four ranges with several experiments in each range. This entire set of experiments is referred to as a series. Temperature ranges were as follows:

Low:	1900 − 2100 K
Medium:	2000 − 2280 K
High:	2200 − 2520 K
Very High:	2400 − 2800 K

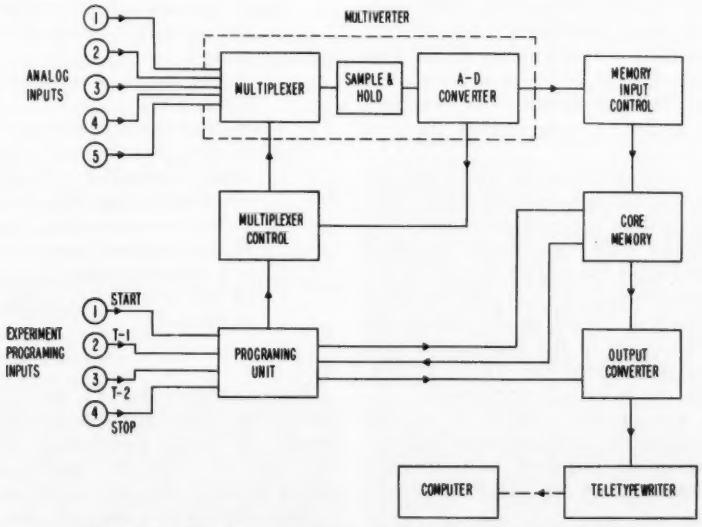

FIGURE 4. *Functional diagram of the high-speed data acquisition system.*

The selection of the above temperature ranges was based upon the criterion of optimizing the operation of the pyrometer. In all the experiments the specimen was heated rapidly from room temperature to its respective maximum temperature with a single pulse. The instruments are set at the beginning of an experiment to give information covering the desired temperature range. Two complete series of experiments were conducted on one of the specimens (Mo-1); that is, after the initial series covering the interval 1900 to 2800 K in four ranges, new experiments were started from 1900 K and were carried up to 2800 K in four ranges. To study possible effects arising from different heating rates, two different heating rates, designated as "fast" and "slow", were used in the experiments during the second series. The durations of heating current pulses for "fast" experiments were in the range 270 to 380 ms, depending on temperature level. Heating current pulse durations for "slow" experiments ranged from 540 to 750 ms.

During the first series, six "fast" experiments were conducted for each temperature range. During the second series, two "fast" and four "slow" experiments were made for each range. Two additional experiments were performed in each range for the determination of normal spectral emittance. All of the above experiments (a total of 56) were conducted with the specimen in a low vacuum environment. An experiment, in the medium temperature range, was performed with the specimen in argon environment under atmospheric pressure.

Experiments on the second specimen (Mo-2) were made in the medium temperature range (3 "slow" experiments).

Fourteen separate experiments were performed to determine the magnitude of the scattered light effect in temperature measurements.

Nine pulse experiments around room temperature were made on a calibrated resistance to compare its value measured under dynamic conditions with that measured under steady-state conditions.

The specimen resistance at room temperature was measured with a Kelvin bridge before and after each dynamic experiment. The specimen was weighed before and after the series of experiments in each range.

The pyrometer was calibrated before and after the series of experiments in each temperature range. The standard lamp, used for the pyrometer calibrations, was calibrated against the NBS temperature standard (IPTS 1948) before and after the entire set of experiments. The calibration of amplifiers (for pulse voltage and current measurements), including the entire system of electronic components in the high-speed data acquisition system, was performed three times: before, midway, and after the entire set of experiments.

Other calibrations and checks related to conventional measurement equipment, such as potentiometer, bridge, standard resistance, standard cell, thermocouples, etc., were made before and after the entire set of experiments.

In a dynamic experiment, quantities such as temperature, voltage, current, which are needed for the computation of properties, are obtained at equal time intervals. Then these data are used to obtain quadratic functions for each quantity in terms of time. Properties are computed using the pertinent equations given in section 2.2 with these quadratic functions for the quantities.

4.2. Directly Measured Quantities

a. Temperature

The specimen temperature was determined with the high-speed photoelectric pyrometer, which was used as a comparison device between the radiation from a standard lamp and the radiation from the specimen.

Calibration. A calibration was first made under steady-state conditions to determine parameters inherent to the pyrometer, by comparing the radiation of the standard lamp to that of an equivalent reference lamp. These parameters were then used in the determination to compare the reference lamp radiation with the specimen radiation under conditions of rapidly changing temperature. The Wien radiation equation, modified for use with this pyrometer, served as the transfer mechanism:

$$\frac{1}{T_X}=\frac{1}{T_R}+A_R-A_X+\frac{\lambda}{c_2}\ln\left(\frac{R+C_4}{X+C_4}\right) \qquad (10)$$

where

T_X is the temperature of the standard lamp (or specimen) in K.
T_R is the temperature of the reference lamp in K.
A_R is the optical attenuation of the channel through which the reference lamp radiation is received by the pyrometer, in K^{-1}.
A_X is the optical attenuation of the channel for the standard lamp (or specimen) radiation, in K^{-1}.
λ is the mean wavelength of the interference filter in m.
c_2 is the second radiation constant, in mK.
R is the arbitrary scale number furnished by the data acquisition system for the radiance received in the reference lamp channel.
X is the corresponding number for the radiance in the standard lamp (or specimen) channel.
C_4 is a constant inherent in the electronic circuit of the pyrometer, in the same arbitrary scale as R and X.

The quantities A_R, A_X, and C_4 are properties of the pyrometer. They are determined in calibration experiments, in which a standard lamp is substituted for the specimen with the window of the chamber interposed between the lamp and the pyrometer.

The attenuator disk of the pyrometer produces three levels of radiance in the reference channel for each half-revolution of the attenuator, and each un-

known or standard radiance is sandwiched between two reference radiances. There are, therefore, twelve radiances per revolution, six reference and six unknown. By making three exposures per calibration, one with the standard lamp adjusted to produce a response in the unknown channel nearly equal to that obtained in the reference channel with the largest attenuator opening (smallest attenuation), one with the standard lamp adjusted to a response near that of the smallest attenuator opening, and one near that of the medium attenuator opening, it was possible to calculate all six A_X values and all six A_R values, and the C_4 value for each exposure. The redundancy of three separate exposures (36 equations for 15 parameters to be determined) makes it possible to choose those ratios of R and X which give the most accurate values of A and C_4. Because of the random variation of the radiances in any one exposure, the data from a large number of revolutions (usually 30) were averaged before calculating the A values. The standard deviation of an individual radiance from its mean was normally about 0.2 percent, and the standard deviation of the mean was normally about 0.04 percent.

Specimen Temperature. The A_R and A_X values obtained from the calibration make it possible to calculate the temperature of an unknown specimen placed in the same position that the standard lamp occupied in the calibration, the reference lamp remaining in the reference channel. Equation (10) is now used to obtain T_X directly. The quantity C_4 is calculated separately for each half-revolution by comparing the high-reference radiance (largest attenuation opening) with the low-reference radiance and inserting the corresponding A_R values; the temperature terms drop out because "T_X" $= T_R$. Because of possible pyrometer drift, calculations of a given T_X were confined within a half-revolution (2.5 ms); it was also found that within this time period temperature determinations were most accurate if unknown radiances were calculated against reference radiances nearest in level rather than closest in time. Each unknown temperature was calculated separately from each of the bracketing reference radiances, and the two T_X values thus obtained were weighted linearly for their nearness to the respective references and averaged, thus:

$$T_X = \frac{T_{X_1}(X - R_2) + T_{X_2}(R_1 - X)}{R_1 - R_2} \tag{11}$$

where

T_{X_1} is the temperature calculated by eq (10) from reference radiance R_1.
T_{X_2} is similarly obtained from R_2.
X is the unknown radiance.
R_1, R_2, and X are corrected for C_4.

In calculating all unknown (specimen) temperatures, corrections were made for (1) scattered light and (2) departure from blackbody conditions (geometrical). The expressions for the correction of both the scattered light effect and departure from ideal blackbody conditions, which are discussed in detail in sections 4.3a and 4.3b below, have essentially the same form; thus, one may combine them from eqs (13) and (16), and obtain the relation

$$\frac{1}{T_c} = \frac{1}{T_0} - \frac{\lambda}{c_2} \ln\left(\frac{1}{F}\right) \tag{12}$$

where T_0 and T_c are observed and corrected (both for scattered light and blackbody departure) temperatures, respectively, and the quantity $F = SQ$, the product of the scattered light correction factor and the blackbody quality. Equation (12) was used to correct all observed temperatures.

During a pulse experiment some of the material which evaporated from the specimen deposited on the window of the specimen chamber, causing additional radiance attenuation in the specimen channel of the pyrometer. Thus a calibration made through the window at the end of a series of experiments resulted in higher A_X values than before the series. Therefore, two calibrations were made, one before and one after a series of dynamic experiments for a given temperature range, and all A values used for specimen temperature calculation were estimated by linear interpolation between the two sets. Inasmuch as most of the deposited material is evaporated during the relatively long cooling period, the first determination was based directly on the first calibration; the last was interpolated one step short of the final calibration. The window was cleaned after the second calibration.

Temperature determinations beyond the upper limit of the standard lamps were made by inserting an attenuator in the optical path of the specimen radiation, and performing two calibrations, one without and one with the external attenuator. From the A values of the first calibration without the external attenuator and the apparent temperature of the standard lamp through the external attenuator in the second calibration, the attenuation of the external attenuator was determined and added to all the A_X values, so that specimen temperatures higher than the standard lamp range could be calculated.

b. Voltage and Current

Voltages across and currents through the specimen were determined by multiplying the arbitrary scale numbers furnished by the data acquisition system by calibration factors in volts and amperes per recording scale unit. The calibration factors were determined by supplying known voltages to the system in a steady-state condition and averaging 40 such readings for each of 10 different levels between 0 and 10 V. The slope of the linear plot of voltage or current versus unit reading is the calibration factor. The standard deviation of a typical individual voltage reading from the mean at a given level was 0.02 percent, the standard deviation of the mean 0.005 percent, and the standard deviation of the function representing applied voltage vs. reading was 0.01 percent. For current, the corresponding standard deviations were 0.02 percent, 0.005 percent, and 0.03 percent. Three such voltage and current calibrations made during the course of

the determinations (two months) indicated a small linear drift of each of these calibration factors with time. The calibration factors used for each day were interpolated from the three sets of calibrations. The drift corresponding to each day was 0.0001 percent for voltage and 0.0004 percent for current.

c. Mass

The mass of the specimen was determined before and after a series of experiments in a given temperature range. The mass to be used for each experiment was calculated by linear interpolation, with the assumption (as in the temperature calibrations) that no mass was evaporated during the heating period of the first experiment in the series. The rate of loss of mass varied from 0.05 mg (0.001 percent) per experiment to 0.36 mg (0.008 percent), depending on the temperature range of the experiment.

The effective mass of the specimen was calculated from the total mass by ratio of the surface area between voltage probes to total surface area. Loss of mass during an experiment took place only on the exposed portion of the specimen (between the clamps). A correction to account for this was included in the determination of the effective mass.

d. Dimensions and Density

The total length, length between clamps, length between probes, outer diameter, and slit and hole lengths were measured at 298 K with a micrometer microscope to the nearest 0.03 mm. The thickness of cylinder wall was calculated from the mass, surface areas, and density.

Density of molybdenum at 298 K was obtained by the water displacement method in a pycnometer. The results of four determinations gave a value of 10.21×10^3 kg m^{-3} with a standard deviation of the mean of 0.02 percent. This compares favorably with the reported values of 10.2×10^3 kg m^{-3} [33], and 10.22×10^3 kg m^{-3} [67].

4.3. Corrections

Several corrections were made on both observed and derived quantities at different stages of the computations. The small corrections are described in the appropriate places in the text. The most significant corrections are those due to the scattered light effect and departure from blackbody conditions in the computations of temperature, and thermal radiation loss in the computations of heat capacity. The mathematical correction due to thermal radiation loss is presented in section 2.2. In the following paragraphs corrections due to scattered light and departure from blackbody conditions are described.

a. Scattered Light Effect

The optics of the pyrometer scatter light from regions immediately surrounding the target area into the pyrometer. Since the radiance distribution around the target on the tubular specimen differs from that around the target area on the calibrating lamp, a correction is required.

Temperature correction due to the scattered light effect may be expressed by

$$\frac{1}{T_c}=\frac{1}{T_0}-\frac{\lambda}{c_2}\ln\left(\frac{1}{S}\right) \tag{13}$$

where T_0 and T_c are observed and corrected temperatures, respectively, and S is the scattered light correction factor, which is given by

$$S=\frac{1+\epsilon_{N,\lambda}K}{1+K} \tag{14}$$

where $\epsilon_{N,\lambda}$ is normal spectral emittance, and K is the scattering ratio.

The scattering ratio, K, is the fraction of radiation that the pyrometer senses which comes from an area outside the defined target. The parameter K may be expressed by

$$K=K_1-K_2 \tag{15}$$

where

K_1 = total scattered radiation from outside of target
K_2 = scattered radiation from background.

The quantity K_1 can be obtained experimentally by employing a specimen similar to the one used in dynamic experiments with the exception that the portion of the tube behind the sighting hole is removed. Then, K_1 is the ratio of radiation from hole to that from surface. The required values were obtained by conducting two experiments, one with the pyrometer aimed at the hole, and another with the pyrometer aimed at the surface.

In the above case, radiation from the hole includes scattered radiation from adjacent surfaces, as well as scattered radiation from the background (chamber wall) as seen through the hole. In order to determine the magnitude of the background radiation, separate experiments were conducted on a specimen composed of two strips (3.2 mm wide) placed parallel to each other with a separation of approximately 4 mm. Since in this arrangement the opening between the strips was large, the contribution of surface scattering was negligible and thus one was able to obtain the scattered radiation from the background. This quantity was then used to correct K_1 according to eq (15). All of the above described experiments were performed under dynamic heating conditions, and the pyrometer outputs for each pair of experiments were related to each other on the basis of times corresponding to equal resistance values of the specimen.

The results for scattering ratios for two different sighting hole geometries are given in figure 5. It may be seen that they are not dependent on radiation level. Therefore, a constant value for K (0.0738) was assumed for all temperatures for a given specimen. The scatter-

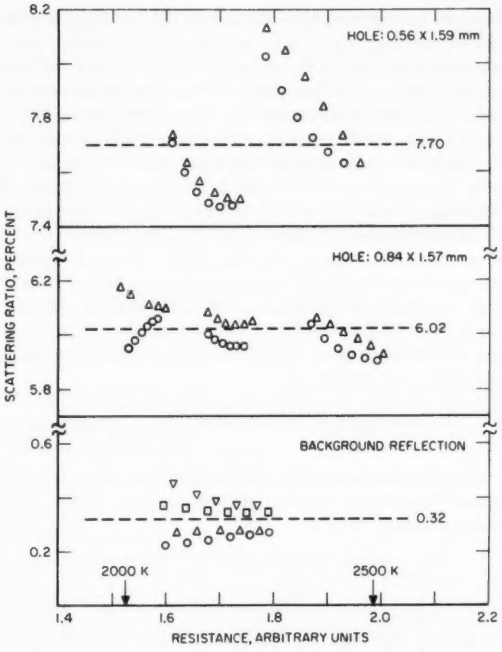

FIGURE 5. *Scattering ratio for different size sighting holes.*

ing light correction factor, S, was obtained as a function of temperature using the measured values of normal spectral emittance as a function of temperature together with the value of K, eq (14).

b. Blackbody Quality

Temperature correction due to departure of the specimen from blackbody conditions may be expressed by

$$\frac{1}{T_c}=\frac{1}{T_0}-\frac{\lambda}{c_2}\ln\left(\frac{1}{Q}\right) \tag{16}$$

where T_0 and T_c are observed and corrected temperatures, respectively, and Q is the blackbody quality.

Departure from ideal blackbody conditions (geometrical factor) for the specimen was estimated using DeVos' [15] method. Computations were made assuming perfectly diffuse, perfectly specular, and two intermediate conditions for the internal surface of the tubular specimen. The sighting hole (0.56×1.09 mm) was 0.79 mm off-center to improve blackbody conditions. Because of the uncertainty in temperature gradients in the specimen close to the clamps, two sets of calculations were made using two different effective specimen lengths (50 and 76 mm). Since the variation of the dependence of blackbody quality on internal surface conditions and length of the effective specimen was small (0.994 to 0.997), a value of 0.995 was used for Q in all the computations related to the temperature of the specimen with the sighting hole geometry given above.

4.4. The Molybdenum Specimen

Molybdenum specimens used were in tubular form with dimensions given in section 3.1. The outer surface of each specimen was polished to reduce heat loss due to thermal radiation.

Specimen characterization was made by the following methods: (1) photomicrographic, (2) chemical analysis, (3) residual resistivity ratio.

Photomicrographs of the specimen before and after the entire set of experiments were prepared. The results on Mo-1 are shown in figure 6. It may be seen that considerable grain growth had taken place as the result of pulse heating of the specimen to high temperatures.

Chemical analyses were made of the specimen before and after the entire set of experiments. Comparison of results does not indicate any detectable change in impurity concentrations. A list of the nature and concentration of impurities in the molybdenum specimen is given in table 1.

The residual resistivity ratio of the specimen (ratio of electrical resistance at 273 K to that at 4 K) was measured before and after the entire set of experiments. The resistivity ratio before and after are 3.4 and 5.4, respectively, with an uncertainty of ±0.05.

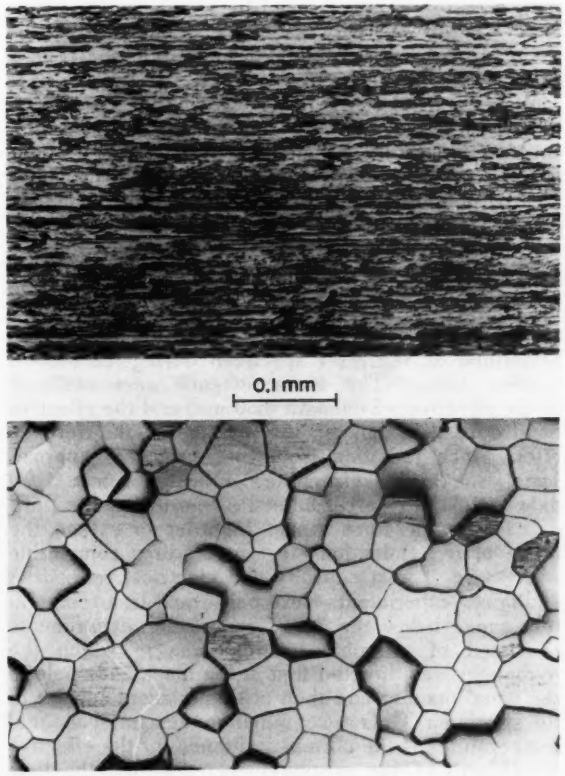

FIGURE 6. *Photomicrographs of the molybdenum specimen corresponding to the conditions before (upper photograph) and after (lower photograph) the entire set of experiments.*

TABLE 1. *Impurities in molybdenum specimen*

Impurity	Composition ppm (by weight)
Ag	<10
Al	<10
C	20
Ca	<10
Co	<10
Cr	10
Cu	100
Fe	<10
Mg	<10
Mn	<10
Ni	100
N	10
O	40
Si	<10
Sn	<10
Ti	<10
W	80
Zr	<100

$360 < \text{Total} < 560$

In addition, the electrical resistance of the specimen was measured at 293 K under steady-state conditions before and after the entire set of experiments. After correcting for weight losses, the results indicate that the electrical resistivity of the specimen at 293 K had changed from 5.681×10^{-8} Ω m to 5.674×10^{-8} Ω m, a decrease of 0.12 percent.

Measurements of the length of the specimen which were made after each set of experiments over the entire temperature range 1900 to 2800 K do not indicate any permanent elongation (within the measurement resolution of approximately 0.04 percent).

4.5. Experimental Results on Molybdenum

a. Normal Spectral Emittance

Normal spectral emittance measurements were performed on the Mo-1 specimen during the second heating series. The measurements were confined to the effective wavelength (650 nm) and the effective bandwidth (10 nm) of the pyrometer interference filter. Since radiation from the surface is approximately one third that from the sighting hole, meaningful data in this case are confined to the upper one third of each temperature range. In order to extend the range of determinations to temperatures compatible with those of heat capacity and electrical resistivity, additional experiments were performed in a temperature range below the "low" range. The experiments consisted of alternate heating runs in which the pyrometer was directed first at the black-body hole in the usual manner and then at the adjacent surface of the specimen. The ratio of radiances measured at equal temperatures is the normal emittance for the effective wavelength of the measurement, provided the hole measurement is corrected for departure from black-body conditions and any scattered radiation originating from the adjacent surface. Times of equal temperature in the two experiments were found by locating times of equal resistance since the temperatures could not be measured directly in the surface experiment. In order to eliminate partially some of the systematic errors caused by the difference in the time sequence of surface and hole experiments, the following order was adopted: hole-surface-surface-hole. The average of the two sets of normal spectral emittances for each range, which were computed from hole-surface and surface-hole combinations, were used in the final results. A linear function for normal spectral emittance was obtained by least squares approximation of the individual results, with a standard deviation of 6.5×10^{-4} (0.2 percent). The results are presented in figure 7. The function, which is valid in the temperature range 1850 to 2800 K, is

$$\epsilon_{N,\lambda} = 0.3540 - 1.173 \times 10^{-5} T \text{ (second series)}. \quad (17)$$

The experimental results (individual points) on normal spectral emittance of molybdenum are given in the appendix (table A–3).

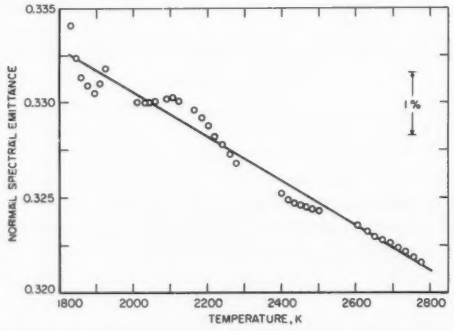

FIGURE 7. *Normal spectral emittance of molybdenum at λ=650 nm (second series).*

b. Hemispherical Total Emittance

Hemispherical total emittance of the Mo–1 specimen was measured during the first and second heating series. Since emittance was determined from data taken during the initial free cooling period, only the upper portion of each temperature range was used. In order to extend the range of determinations to temperatures compatible to those in heat capacity and electrical resistivity, an additional determination for a range below the "low" range was also made.

Temperatures were taken at equal time intervals along the initial cooling curve (approximately the initial 20–40 K) and the corresponding instants of time for each temperature were calculated for both the cooling and heating curves. The voltage and current were computed for each instant on the heating curve, and heating and cooling rates from both curves. Emittance could then be computed for each temperature taken by using eq (7). The emittances thus obtained were averaged in each experiment and related to an average temperature. During the first heating series two to three experiments for each temperature range

were made to yield emittance, while during the second heating series only one experiment for each range was performed. A linear function for hemispherical total emittance for each heating series was obtained by least squares approximation of individual results. Standard deviation of the points from the function for the first and second heating series were 2.5×10^{-3} (0.8 percent) and 2.8×10^{-3} (1 percent), respectively. The results are presented in figure 8. The functions which are valid in the temperature range 1900 to 2800 K, are

$$\epsilon = 0.1424 + 6.749 \times 10^{-5} T \text{ (first series)} \quad (18)$$

$$\epsilon = 0.1210 + 7.061 \times 10^{-5} T \text{ (second series)} \quad (19)$$

The experimental results (individual points) on hemispherical total emittance of molybdenum are given in the appendix (table A–4).

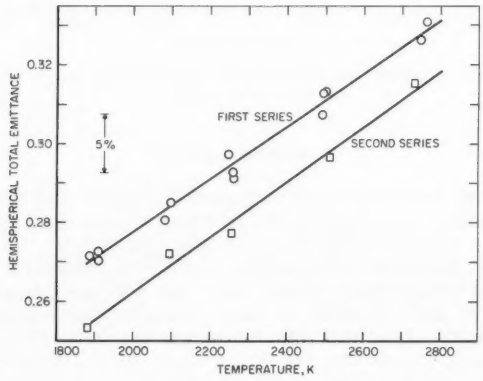

FIGURE 8. *Hemispherical total emittance of molybdenum*

c. Heat Capacity

The experiments which contributed to the determination of heat capacity of Mo-1 were performed as follows:

First heating series: fast (270–380 ms pulse length), six experiments in each temperature range.

Second heating series: fast (270–380 ms pulse length), two experiments in each temperature range.

Second heating series: slow (540–750 ms pulse length), four experiments in each temperature range.

A quadratic function for heat capacity for each temperature range and also for each heating series was obtained by least squares approximation of results from individual experiments. Results corresponding to the very high range in the first series showed a systematic drift with time. Because of this, fits involving data of the very high range gave high standard deviations. Since this range was the only exception, the results in the very high range were not considered in the overall fits for the first series. The following equations were obtained:

First series (1900 – 2520 K)

$$c_p = 45.19 - 2.090 \times 10^{-2} T + 8.037 \times 10^{-6} T^2 \quad (20)$$

Second series (1900 – 2800 K) – fast

$$c_p = 45.80 - 2.098 \times 10^{-2} T + 7.796 \times 10^{-6} T^2 \quad (21)$$

Second series (1900 – 2800 K) – slow

$$c_p = 43.81 - 1.937 \times 10^{-2} T + 7.494 \times 10^{-6} T^2 \quad (22)$$

where T is in K and c_p is in J mol^{-1} K^{-1}.

Standard deviations of individual points from these functions are 0.5 percent for eq (20), and 0.3 percent for eqs (21) and (22). The differences between the results of "slow" and "fast" experiments in the second series are given in table 2. Since in the second series the number of "slow" experiments was twice that of the "fast" experiments and since the average difference between them was within the standard deviation of each set, the results of "slow" experiments were considered as the basis of comparison with the results of the first series. The differences between the results of the first and second heating series are tabulated in table 3. Deviations of individual results from smooth functions for the first and second (slow) heating are presented in figures 9 and 10, respectively. The experimental results (individual points) on heat capacity of molybdenum for the first and second (slow) series are given in the appendix (tables A–1 and A–2).

All the experiments described above were conducted with the Mo-1 specimen in a low vacuum environment. An additional experiment (second series – slow, medium temperature range) was performed with the specimen

TABLE 2. *Differences in measured values for heat capacity and electrical resistivity between "slow" and "fast" experiments*

Temperature K	Heat Capacity		Resistivity	
	Δ J mol^{-1}K^{-1}	Δ %	Δ 10^{-8} Ωm	Δ %
2000	0.02	0.05	0.10	0.19
2200	.09	.23	.12	.20
2400	.13	.32	.11	.18
2600	.15	.34	.09	.13
2800	.14	.30	.04	.05

Δ = Slow – Fast

TABLE 3. *Differences in measured values of heat capacity and electrical resistivity between first and second series*

Temperature K	Heat Capacity		Resistivity	
	Δ J mol^{-1}K^{-1}	Δ %	Δ 10^{-8} Ωm	Δ %
1900	0.43	1.26	0.24	0.48
2000	.49	1.39	.29	.55
2100	.56	1.54	.36	.64
2200	.64	1.70	.44	.74
2300	.73	1.87	.53	.86
2400	.83	2.05	.64	.98
2500	.94	2.23	.76	1.12

Δ = First – Second

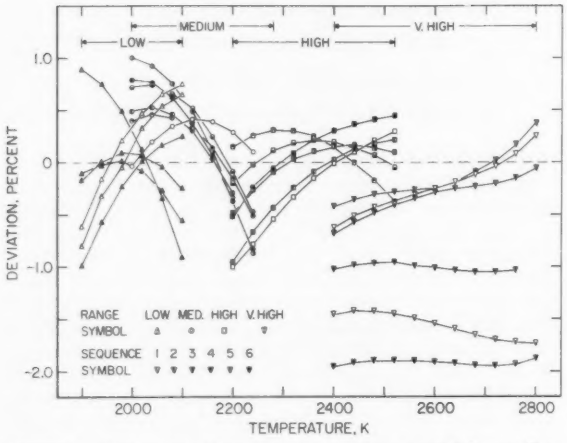

FIGURE 9. *Deviation of heat capacity results on molybdenum (first series) from equation* (20).

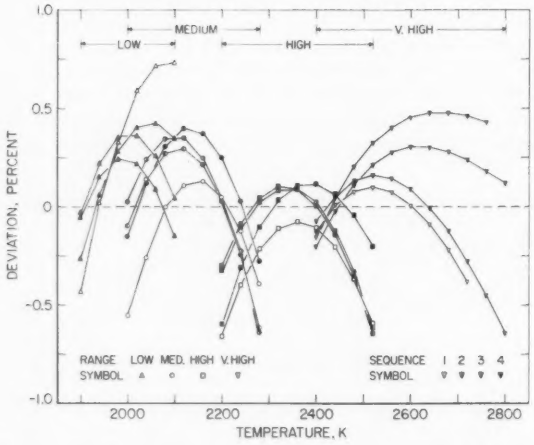

FIGURE 10. *Deviation of heat capacity results on molybdenum (second series) from equation* (22).

in an argon environment. Comparison of the results (vacuum versus argon environment) yielded an average difference of 0.11 J mol^{-1} K^{-1} (0.31 percent) in heat capacity, which is approximately equal to the standard deviation of the measurements.

A limited number of experiments was conducted (in vacuum) on another molybdenum specimen, designated as Mo-2. A quadratic fit of the results of three experiments in the medium temperature range yielded a standard deviation of 0.03 J mol^{-1} K^{-1} (0.08 percent) in heat capacity. Comparison of the results on Mo-2 with those on Mo-1 (first series) showed an average difference of 0.04 J mol^{-1} K^{-1} (0.12 percent). The smoothed heat capacity results on Mo-1 and Mo-2 are presented graphically in figure 11. In the computations of heat capacity the atomic weight of molybdenum was taken as 95.94 [13].

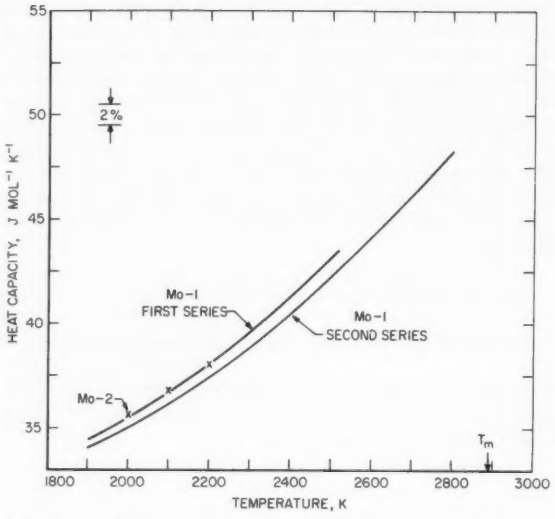

FIGURE 11. *Heat capacity results on molybdenum (smooth) for first and second series.*

d. Electrical Resistivity

The experiments which contributed to the determination of electrical resistivity of Mo-1 and Mo-2 were identical with those for heat capacity.

A quadratic function for electrical resistivity for each temperature range and also for each heating series was obtained by least squares approximation of results from individual experiments. As in the heat capacity case, the results of tests in the very high range in the first series showed a systematic drift with time. Because of this, fits involving data of the very high range gave high standard deviations. Since this range was the only exception, the results in the very high range were not considered in the overall fits for the first series. The following equations were obtained:

First series (1900–2520 K)

$$\rho = -11.39 + 3.219 \times 10^{-2} T - 3.172 \times 10^{-8} T^2 \qquad (23)$$

Second series (1900–2800 K)—fast

$$\rho = -12.04 + 3.320 \times 10^{-2} T - 4.667 \times 10^{-7} T^2 \qquad (24)$$

Second series (1900–2800 K)—slow

$$\rho = -13.34 + 3.445 \times 10^{-2} T - 7.417 \times 10^{-7} T^2 \qquad (25)$$

where T is in K, and ρ is in 10^{-8} Ωm.

Standard deviations (individual point) of the above functions are 0.09 percent for eq (23), 0.07 percent for eq (24), and 0.08 percent for eq (25). The differences between the results of "slow" and "fast" experiments in the second series are given in table 2. For reasons explained in the previous section, the results of "slow" experiments were considered as the basis of comparison with the results of the first series. Differences between the results of first and second heating series are tabulated in table 3. Deviations of individual results

from the smooth functions for first and second (slow) heating are presented in figures 12 and 13, respectively. The experimental results (individual points) on electrical resistivity of molybdenum for the first and second (slow) series are given in the appendix (tables A–1 and A–2).

Comparison of the results (vacuum versus argon environment) yielded an average difference of $0.03 \times 10^{-8}\Omega$m (0.06 percent) in electrical resistivity, which is approximately equal to the standard deviation of the measurements.

Quadratic fit of the results for Mo-2 in the medium temperature range gave a standard deviation of $0.02 \times 10^{-8}\Omega$m (0.03 percent) in electrical resistivity. Comparison of the results for Mo-2 with those for Mo-1 (first series) showed an average difference of $0.31 \times 10^{-8}\Omega$m (0.54 percent). The smoothed electrical resistivity results on Mo-1 and Mo-2 are presented graphically in figure 14. Results on electrical resistivity at 293 K are given in section 4.4.

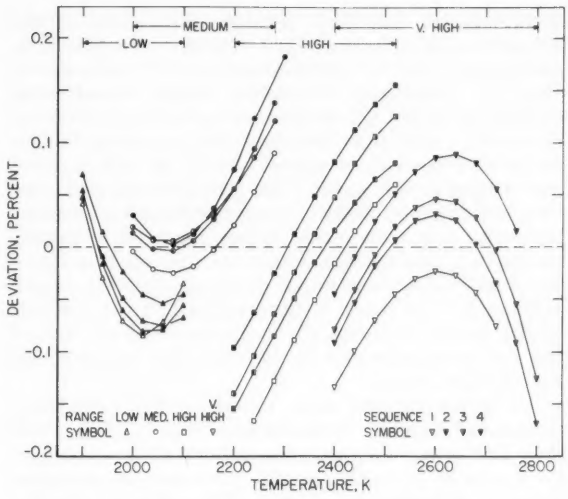

FIGURE 13. *Deviation of electrical resistivity results on molybdenum (second series) from equation (25).*

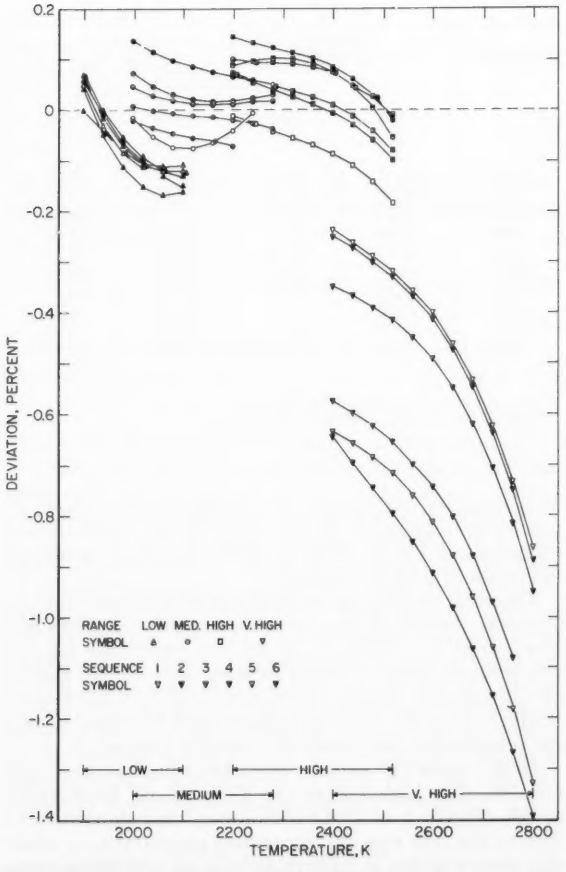

FIGURE 12. *Deviation of electrical resistivity results on molybdenum (first series) from equation (23).*

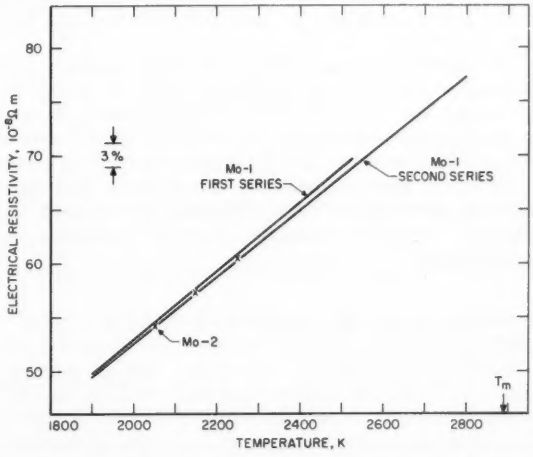

FIGURE 14. *Electrical resistivity results on molybdenum (smooth) for first and second series.*

5. Interpretation of Results

Measurements on all three properties (heat capacity, electrical resistivity, hemispherical total emittance) indicate a difference in the results between the first and second heating series. This difference is approximately one order of magnitude greater than the precision of the measurements. This may be attributed to a change in the physical and chemical state of the specimen which might have taken place during its exposure to high temperatures (above 2500 K, in the very high range) in the first heating series. Since the results on all three properties in the second series are lower than those in the first series, and since no further changes are observed in the very high range of the

second series, one may consider the results of the second series to be more representative of equilibrium conditions. This is substantiated by: (1) decrease in electrical resistivity (measured under steady-state conditions at 293 K), (2) increase in residual electrical resistivity ratio; both between the beginning of first series and the end of second series. An indication of the change in the state of the specimen may be seen by observing the results of weight and resistance measurements that were made before each set of experiments in a given range. These are presented in figure 15. A sudden change in the trend of weight vs. resistance of the specimen is observed which corresponds to the period between the beginning and the end of the set of experiments in the very high range of the first heating series.

All measurements were based on the 1948 International Practical Temperature Scale (IPTS 1948) [64]. This scale was used throughout all the computations as well as in the results expressed by equations given in the previous section. This offered computational convenience and also facilitated the comparison of present results with those in the literature. The final results are corrected to IPTS 1968 [29] by applying proper transformations to both temperature and heat capacity [16].

The results (second series) for heat capacity and electrical resistivity are given in tables 4 and 5, respectively, both in IPTS 1948 and 1968 scales. Results for electrical resistivity are expressed: (1) in terms of ambient temperature (298 K) dimensions, (2) in terms of corrected high temperature dimensions. High temperature dimensions were obtained by utilizing the following equation for the thermal expansion of molybdenum.

$$\frac{l_T - l_{298}}{l_{298}} = -6.33 \times 10^{-2} + 2.94 \times 10^{-4} T + 1.57 \times 10^{-7} T^2. \quad (26)$$

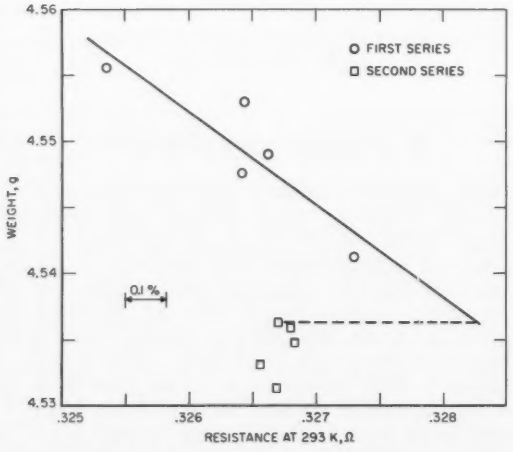

FIGURE 15. *Weight of molybdenum specimen as a function of resistance at 293 K.*

TABLE 4. *Heat capacity of molybdenum (second series) corresponding to IPTS 1948 and IPTS 1968*

Temperature K	c_p J mol^{-1} K^{-1}	
	1948	1968
1900	34.06	33.97
2000	35.05	34.95
2100	36.18	36.07
2200	37.47	37.35
2300	38.90	38.77
2400	40.49	40.34
2500	42.22	42.06
2600	44.11	43.92
2700	46.14	45.94
2800	48.33	48.10

TABLE 5. *Electrical resistivity of molybdenum (second series) corresponding to IPTS 1948 and IPTS 1968*

Temperature K	ρ (amb.)[a] 10^{-8} Ωm		ρ (corr.)[b] 10^{-8} Ωm	
	1948	1968	1948	1968
1900	49.44	49.37	49.96	49.89
2000	52.59	52.52	53.20	53.12
2100	55.73	55.66	56.43	56.34
2200	58.86	58.78	59.65	59.56
2300	61.97	61.88	62.87	62.77
2400	65.07	64.97	66.07	65.97
2500	68.15	68.05	69.28	69.17
2600	71.22	71.11	72.47	72.35
2700	74.27	74.15	75.66	75.53
2800	77.31	77.19	78.84	78.71

[a] Based on ambient temperature (298 K) dimensions.
[b] Corrected for dimensions at the specimen temperature.

This equation represents the average of the results of four investigators [3, 18, 55, 73] over the approximate temperature range 1500 to 2800 K with a standard deviation of 0.04 (3 percent).

The final results on hemispherical total and normal spectral emittances are presented in table 6. They are given in IPTS 1948 only, since any correction for the temperature scale is much smaller than the resolution of the reported values. Hemispherical total emittance is given both for ambient temperature dimensions and for dimensions corrected for thermal expansion.

Heat capacity results at high temperatures are considerably higher than the Dulong and Petit value of $3R$ (24.943 J mol^{-1}K^{-1}). Some of this departure is due to the fact that the measured property is c_p while the theory is for c_v. There is also an additional term which arises from the electronic contribution to heat capacity.

TABLE 6. *Hemispherical total and normal spectral (at λ=650 nm) emittances of molybdenum, (second series)*

Temperature K	ϵ		$\epsilon_{N,\lambda}$
	(amb.)[a]	(corr.)[b]	
1900	0.255	0.250	0.332
2000	.262	.256	.331
2100	.269	.263	.329
2200	.276	.269	.328
2300	.283	.275	.327
2400	.290	.281	.326
2500	.298	.288	.325
2600	.305	.294	.324
2700	.312	.300	.322
2800	.319	.307	.321

[a] Based on ambient temperature (298 K) dimensions.
[b] Corrected for dimensions at the specimen temperature.

Based on thermodynamic principles, the difference between c_p and c_v is expressed by

$$c_p - c_v = \frac{TV\alpha_v^2}{\beta} \tag{27}$$

where V is volume, α_v coefficient of volume thermal expansion, and β is compressibility. Considering the Gruneisen relation

$$G = \frac{3V\alpha_l}{\beta c_v} \tag{28}$$

where α_l is coefficient of linear thermal expansion, and assuming that G is temperature independent, eq (27) becomes

$$\frac{c_p}{c_v} = 1 + 3G\alpha_l T. \tag{29}$$

Electronic heat capacity may be expressed by

$$c_e = \gamma T \tag{30}$$

where γ is the coefficient of electronic heat capacity.

It may be seen that, to a first approximation, relations representing $c_p - c_v$ and c_e are linear in temperature. This implies that above the Debye temperature, θ, the measured heat capacity departs from $3R$ approximately linearly with temperature. In the case of molybdenum, this is found to be true up to approximately 1000 K. Above this temperature present results as well as those in literature are found to increase more rapidly than allowed by a linear function.

The linear term was evaluated with the aid of the recommended values given in JANAF [31] in the temperature interval 200 to 1000 K. Then from the results of the present investigation, a fourth-degree temperature term was added. The relation for heat capacity resulting from this approach (in IPTS 1948) is

$$c_p = 24.943 - \frac{1.70\times 10^5}{T^2} + 3.27\times 10^{-3}T + 2.315\times 10^{-13}T^4 \tag{31}$$

where the T^{-2} term is the first term in the expansion of the Debye function needed to correlate approximately the temperature region around θ. The average departure of results computed by eq (31) from the quadratic relation representing the present results, eq (22), in the temperature range 1900 to 2800 K is 0.068 J mol^{-1}K^{-1} (0.17 percent). This departure is less than the standard deviation of the present measurements. Equation (31) is presented graphically in figure 16.

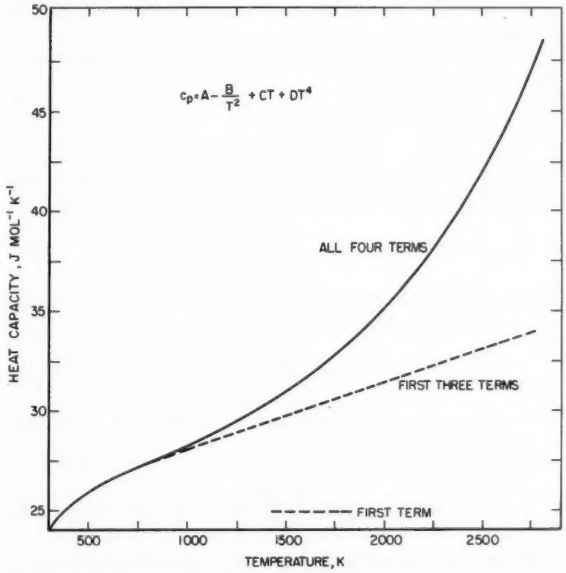

FIGURE 16. *Heat capacity of molybdenum according to equation (31).*

The T^{-2} term corresponds to a Debye θ of 370 K for molybdenum. This value is somewhat lower than those reported in the literature; θ=445 K according to Horowitz [27], θ=440 K according to JANAF [31], and θ=459 K according to Gshneidner [23]. Such a deviation may be expected since in the above analysis only data above 200 K were considered while other determinations were based on more elaborate treatment of lower temperature data. Argent and Milne [4] reported that θ for molybdenum based on low temperature data is 445 K, while based on high temperature data it becomes 380 K. The latter value is very close to that of the present study.

The reported values for the coefficient of the electronic heat capacity for molybdenum are: $\gamma = 2.13\times 10^{-3}$ J mol^{-1}K^{-2} according to Horowitz [27], and $\gamma = 1.97\times 10^{-3}$ J mol^{-1}K^{-2} from JANAF [31]. If one assumes a value of 1.5 for the Gruneisen constant and one considers the values of 6.1×10^{-6} K^{-1} for the coefficient of linear thermal expansion at 1000 K given by Kirby [34], the coefficient for the $c_p - c_v$ term becomes 0.68×10^{-3} J mol^{-1}K^{-2}. If one considers the higher of the two γ values and adds to it the coefficient of $c_p - c_v$ term, the sum becomes 2.81×10^{-3} J mol^{-1}K^{-2}, which is somewhat lower than the coefficient of the linear term (3.27×10^{-3}) in eq (31). The result of the

sum of the first three terms on the right-hand side of eq (31) is represented by the dashed curve in figure 16. It may be seen that this curve is much lower than that representing measured heat capacity at high temperatures.

No satisfactory explanation has been found as to the nature of the increase of heat capacity above the combined value of $3R$ and the linear term at high temperatures. Although the mechanisms of vacancy generation become important at high temperatures, it is not possible to attribute the high values entirely to vacancies.

Vacancy concentration n, in fractional form, may be expressed by

$$n = Ae^{-\frac{E_f}{kT}} \tag{32}$$

where E_f is vacancy formation energy. Energy per mole of a substance required to form vacancies is given by

$$U = nN_A E_f \tag{33}$$

where N_A is Avogadro's number. Substituting eq (32) in eq (33), one obtains

$$U = N_A A E_f e^{-\frac{E_f}{kT}} . \tag{34}$$

Then, the expression for the contribution of vacancies to heat capacity becomes

$$c_{vac} = \frac{N_A A E_f^2}{kT^2} e^{-\frac{E_f}{kT}} \tag{35}$$

If one assumes that vacancy formation energy is approximately proportional to the melting point and considers the value 0.97 eV given by DeSorbo [14] for gold, one obtains 2.10 eV for the vacancy formation energy of molybdenum. This is in reasonable agreement with the values 2.4 eV, 2.24 eV, and 1.86 eV given by Meakin et al. [45], Kraftmacher [38] and Kirillin et al. [36], respectively. If one considers the vacancy formation energy of 3.30 eV for tungsten reported by Schultz [59], the estimated value for the vacancy formation energy for molybdenum becomes 2.59 eV. There are no accurate measurements on molybdenum related to vacancy concentration at high temperatures. Dilatometric measurements made by Simmons and Balluffi [61, 62] on gold and copper by combined direct optical and x-ray techniques indicate vacancy concentrations of approximately 0.07 and 0.09 percent at their respective melting points. The results of quenching experiments on tungsten reported by Schultz [59] give a vacancy concentration of 0.011 percent at its melting point. Quenching experiments on molybdenum described by Meakin et al. [45] indicate a vacancy concentration of 0.005 percent at its melting point.

The contribution of vacancy formation to the heat capacity of molybdenum is estimated with the assumption of a somewhat high vacancy concentration of 0.1 percent at the melting point (2889 K) and a vacancy formation energy of 2.1 eV. The results are presented in table 7 together with the quartic term in eq (31)

TABLE 7. *Estimated vacancy contribution to heat capacity of molybdenum and* DT^4 *in eq (31)*

T	c_{vac}	DT^4
K	J mol^{-1} K^{-1}	J mol^{-1} K^{-1}
2000	0.03	3.70
2200	.07	5.42
2400	.15	7.68
2600	.29	10.58
2800	.48	14.23

which represents the magnitude to which the measured heat capacity departs from the sum of $3R$ and the linear term at high temperatures. Vacancy contribution is evidently small, less than 0.5 J mol^{-1} K^{-1} (upper limit) at 2800 K, and does not account for high heat capacity values. The fact that electrical resistivity does not show any sharp increase at high temperatures is also an indication that the effect of vacancies is small. A recent discussion on thermodynamic properties of solids containing vacancies is given by Holder and Granato [26]. Energy associated with grain growth during heating is also negligible compared to the total energy absorbed by the specimen [44]. A possible contribution of higher order terms in the electronic heat capacity may partially account for high values of heat capacity at high temperatures.

If the entire deviation of measured heat capacity from the sum of $3R$ and the linear term at high temperatures is represented by an expression similar to eq (35), one could obtain, after rearrangement

$$\ln (T^2 \Delta c_p) = \ln B - \frac{M}{T} . \tag{36}$$

This equation indicates that a plot of the left side versus $1/T$ should yield a straight line with slope equal to $-M$. From the data on molybdenum in the range 1900 to 2800 K, a straight line with a standard deviation of 0.3 percent was obtained. However, the parameters obtained through this fit do not seem to have any physical significance. As a crude analogy to vacancy concentration, the computations yielded a value of 1.21 eV for energy and 7.5 percent for concentration at the melting point. Both of these values seem to be unrealistic for molybdenum.

Unlike heat capacity and electrical resistivity, thermal radiation properties are very sensitive to surface conditions (mechanical, chemical, etc.). Therefore, it is difficult to correlate measured quantities in terms of the fundamental properties of the substance. In this investigation the main motivation in the measurement of both hemispherical total and normal spectral emittances was to apply corrections to heat capacity and temperature, respectively. However, as seen in the next section, the results are in good agreement with those in the literature.

6. Comparison With Results in Literature

6.1. Heat Capacity

Above approximately 1000 K, heat capacity reported in the literature was measured both by drop and pulse calorimetry. The quantity measured in drop calorimetry is enthalpy. Therefore, in order to obtain heat capacity, one has to fit enthalpy data to a smooth function and differentiate that function with respect to temperature. In pulse calorimetry, heat capacity is obtained directly through the measurement of the quantity dT/dt, the rate of change of temperature with time.

The results reported in the literature for the heat capacity of molybdenum are presented in figure 17. A comparison of selected literature results with those of the present study is given in table 8. All values are based on IPTS 1948. Estimates of errors in papers cited lead to an estimate of inaccuracy in previously reported heat capacity of approximately 4 to 7 percent in the temperature range considered. The agreement is within the combined estimated errors in all cases. However, if equal weight is given to literature values, the present results from the second series are systematically low by about 1.5 percent. Although the results from the first series are in good agreement with the average of previous measurements, it is believed that they are less accurate than those from the second series.

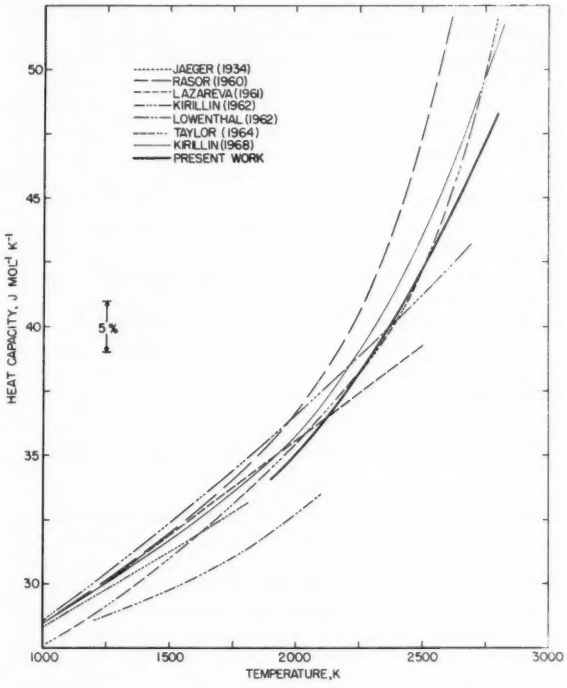

FIGURE 17. *Heat capacity of molybdenum reported in the literature.*

TABLE 8. *Heat capacity difference (previous literature values minus present work, second series, values) in percent*

Investigator	Ref.	Year	Method	Temperature, K				
				2000	2200	2400	2600	2800
Jaeger and Veenstra	30	1934	drop	[a]−2.1				
Lazareva et al.	42	1961	drop	+1.5	−1.2	−4.9		
Kirillin et al.	35	1962	drop	+4.3	+2.4	−0.6	−4.3	
Taylor and Finch	65	1964	pulse	+1.0	+0.4	−0.8	+1.6	+7.6
Kirillin et al.	36	1968	drop	+2.1	+2.2	+2.6	+3.8	+5.7

[a] Extrapolated from 1873 K.

6.2. Electrical Resistivity

The electrical resistivity of molybdenum reported in the literature was measured by steady-state techniques. Since transport properties are sensitive to the history of the specimen, one would expect to see differences in the results of various investigators. The literature results for the electrical resistivity of molybdenum are presented in figure 18. A comparison of selected literature results with those of the present study is given in table 9. All values are based on IPTS 1948. Estimates of errors in papers cited lead to an estimate of inaccuracy in previously reported electrical resistivity of approximately 1 to 2 percent in temperature range considered. Measurements of the electrical resistivity of molybdenum corresponding to 293 K, as well as values reported in the literature, are given in table 10.

TABLE 9. *Electrical resistivity difference (previous literature values minus present work, second series, values) in percent*

Investigator	Ref.	Year	Temperature, K				
			2000	2200	2400	2600	2800
Worthing	73	1926	+1.1	+0.9	+0.9	+1.2	+1.6
Osborn	48	1941	+0.1				
Taylor	66	1964 (p.c.)	+1.0	+0.2	−0.3	−0.5	−0.5

367-409 OL-70—6

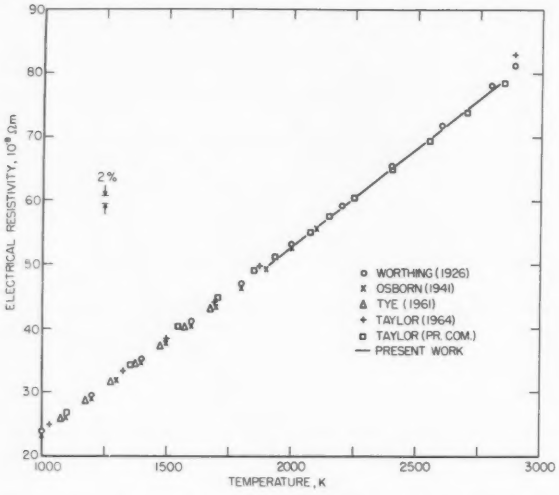

FIGURE 18. *Electrical resistivity of molybdenum reported in the literature.*

TABLE 10. *Electrical resistivity of molybdenum at 293 K (literature)*

Investigator	Ref.	Year	Resistivity 10^{-8} Ωm
Worthing	73	1926	5.62
White and Woods	71	1959	[a] 5.27
Tye	68	1961	5.65
Feith	19	1965	5.86
Present work			5.67

[a] Ideal resistivity.

6.3. Hemispherical Total and Normal Spectral Emittances

Because of the strong dependence of emittance on surface conditions, large deviations are to be expected between the results of various investigators.

Results for hemispherical total and normal spectral emittances of molybdenum reported in the literature are presented in figures 19 and 20, respectively.

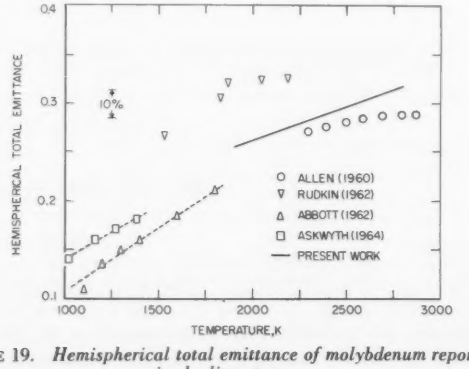

FIGURE 19. *Hemispherical total emittance of molybdenum reported in the literature.*

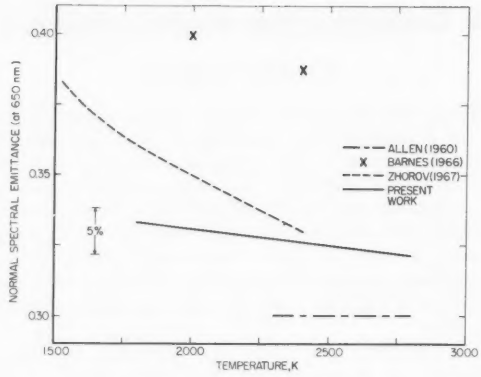

FIGURE 20. *Normal spectral emittance of molybdenum at λ=650 nm reported in the literature.*

7. Estimate of Errors

Uncertainty in properties depends upon: (1) errors in directly measured quantities, and (2) departure from assumed operational conditions. These are discussed in the following sections.

In this paper the term "imprecision", unless otherwise stated, refers to the standard deviation of the individual measurement; computed from the differences of single data points from a polynomial function fitted by the method of least squares. The term "inaccuracy", unless otherwise stated, refers to the estimated maximum total error (random and systematic) approximately equivalent to two standard deviations.

7.1. Errors in Directly Measured Quantities

Estimated total error (which includes random as well as systematic errors) in directly measured quantities such as temperature, voltage, current, dimensions, weight, etc., is obtained from auxiliary tests, analyses of experimental results or computations of several minor sources of error. The details are given below.

a. Errors in Temperature Measurements

Total error in temperature measurements results from several contributions. Their estimates are summarized in the following paragraphs.

Standard Lamp. The National Bureau of Standards report of calibration for the tungsten filament standard lamp states "The maximum uncertainties of the values reported correspond to about ±1 degree at 1500 °C and increase to about ±2.5 degrees at 2200 °C". In the measurements above 2500 K an attenuator was used in the unknown channel. The uncertainty due to the attenuator's calibration brings the total uncertainty at 2800 K to 3.5 K.

Stability of Standard Lamp. Calibrations of the standard lamp before and after the entire set of experiments show a change of approximately 0.9 K at 2000 K and 1.4 K at 2500 K. In the computations of

the properties an average of the initial and final calibrations was used which reduced the temperature inaccuracy due to lamp instability to 0.5 K at 2000 K and 1 K at 2800 K.

Radiation Source Alinement. Since the pyrometer had to be moved between a calibration and a pulse experiment and again for a calibration during each set of experiments in a given temperature range, an additional uncertainty in the calibration of the pyrometer develops as a result of the uncertainties in the visual alinement of the lamps. Based on an analysis of experimental results on approximately 20 tests with steady-state radiation sources, it is estimated that the error arising from this uncertainty is approximately 1 K at 2000 K and 2 K at 2800 K.

Pyrometer Reproducibility. Based on calibration results, the short time reproducibility of the pyrometer (between two calibrations in one day) is estimated to be approximately 1 K at 2000 K and 2 K at 2800 K. This includes changes in the optical attenuations in the pyrometer that result from the collection of dust, etc.

Scattered Light Correction. Although a correction was made to temperature to allow for the scattering effect in the optics of the pyrometer, an uncertainty still exists as to the actual magnitude of this correction. The uncertainty in the scattering factor S given by eq (14) is obtained by considering the uncertainties in scattering ratio and normal spectral emittance. The results indicate an uncertainty of 0.5 percent in radiance which corresponds to approximately 0.4 K at 2000 K and 1 K at 2800 K.

Blackbody Quality (Geometrical). The computed blackbody quality (0.995), which was based on geometrical considerations only, is estimated to have a maximum uncertainty of 0.5 percent (in radiance) which corresponds to approximately 1 K at 2000 K and 2 K at 2800 K.

Specimen Temperature Nonuniformity. Heat transfer from specimen to clamps causes the establishment of temperature gradients in the specimen. However, since the "effective" portion of the specimen (between potential probes) is 12.7 mm away from the clamps, the sharp temperature gradients near them do not affect the measurements. The magnitude of the axial temperature gradient in the "effective" specimen is estimated by solving the transient heat conduction equation assuming constant properties [11]. Computations indicate that the average temperature in the "effective" specimen in the "slow" experiments due to axial heat conduction is approximately 1 K below midpoint value at 2000 K and 2 K below at 2800 K, and the difference, of course, is less in the "fast" experiments.

Radial temperature difference across the thin wall specimen is calculated for the "slow" experiments to be less than 0.1 K at 2000 K and 0.5 K at 2800 K. No corrections were made for the small axial and radial temperature gradients. Effect of the sighting hole on temperature distribution in the specimen is considered negligible for good conductors [28].

From potentiometric measurements of the resistance of the specimen along its length at room temperature, random variations in the thickness of the tube averaged over lengths of approximately 3 mm were estimated. Temperature nonuniformity corresponding to the variations in the thickness of the specimen is approximately 2 K at 2000 K and 4 K at 2800 K.

The total temperature inaccuracy resulting from the above items is estimated to be approximately 3 K at 2000 K and 4 K at 2800 K.

Error in Window Attenuation. The interpolations which were made before and after each set of experiments in a given range introduce a small additional error of approximately 0.5 K at 2000 K and 1 K at 2800 K. The magnitude of this effect is estimated from the drift of the electrical resistivity results in a given set of experiments.

Magnetic Fields. The effect on the pyrometer of varying electric and magnetic fields associated with the pulse currents was tested and was found to be negligible (less than 0.5 K, the resolution of temperature measurements).

Use of Wien's Law. For the computations of temperature, Wien's instead of Planck's Law was used. The difference in temperature obtained by these two functions for the mean wavelength of 650 nm is approximately 0.003 K at 2000 K and 0.13 K at 2800 K. Since the same procedure was used for both calibration and pulse experiments, the error introduced as the result of the use of Wien's Law is completely negligible.

Resultant Error in Temperature. From a consideration of various errors and their magnitudes listed above, it may be concluded that the inaccuracy in temperature measurements is approximately 4 K at 2000 K and 7 K at 2800 K. A summary of estimated errors in temperature is given in table 11.

b. Errors in Electrical Measurements

Identifiable sources of errors that affect the measurement of electrical quantities, such as voltage and current, are given below.

Skin Effect. Since molybdenum is nonmagnetic and the specimen was of tubular shape and the current was a single trapezoidal pulse of several hundred milli-

TABLE 11. *Estimated inaccuracies in temperature measurements*

	Source	Inaccuracy, K	
		at 2000 K	at 2800 K
1	Standard Lamp	1.5	3.5
2	Instability of Standard Lamp	0.5	1
3	Radiation Source Alinement	1	2
4	Pyrometer Reproducibility	1	2
5	Scattered Light Correction	0.5	1
6	Blackbody Quality	1	2
7	Specimen Temperature Non-Uniformity.	3	4
8	Window Attenuation	0.5	1
	Total Inaccuracy in Temperature. [a]	4	7

[a] Root sum square of items 1 to 8.

seconds duration, the contribution of skin effect is negligible. Computations indicate that in the present experiments the skin effect (which manifests itself as a change in effective resistance of the conductor) was much less than 0.01 percent.

Inductive Effects. Consideration of self- and mutual-inductances [22] of pertinent components indicate that their contribution to the electrical signals is less than 1 mV, which is the resolution of the digital data acquisition system. This is due to the fact that the current changes slowly during the period of the measurements.

Thermoelectric Effects. Both experimental checks and computations indicate that the contribution of the thermoelectric effects in the present system is less than 1 mV, which is the resolution of the digital data acquisition system.

Errors Due to Calibrations. A precision voltage source (0.001 percent stability) and potentiometric method were used for the calibration of the electrical measuring circuits. Moreover, the stability of the components (amplifiers, analog-to-digital converter, etc.) was better than 0.01 percent over the actual period of measurements. This implies that the limiting factor in the electrical calibrations was the resolution of the digital data acquisition system.

Resultant Error in Electrical Measurements. The estimated error in electrical measurements arising from items listed above is only a few parts in 10^4. In order to have a more direct check on the accuracy of electrical measurements, experiments were conducted to determine the value of a test resistance by measuring the current flowing through it and the voltage drop across its terminals under transient conditions and comparing this measurement with its resistance under steady-state conditions as determined by the potentiometric method. The average of the results of nine experiments indicates that resistance measurements by pulse and steady-state techniques are in agreement within 0.02 percent.

Based on the foregoing, the estimated inaccuracies in voltage and current measurements are 0.05 and 0.06 percent, respectively, introducing an inaccuracy of 0.08 percent in power and resistance.

c. Errors in Other Measurements

Length. The inaccuracy in an individual length measurement is 0.03 mm. When related to the specimen dimensions, it yields an inaccuracy of approximately 0.04 percent. Based on this, the inaccuracy in establishing the length of the "effective" specimen becomes approximately 0.08 percent.

Weight. The inaccuracy in an individual weight measurement is 0.5 mg, producing an inaccuracy of less than 0.01 percent for the specimen. However, the uncertainty in determining the weight of the "effective" specimen is greater than this. Based on the combined uncertainties of weight and length measurements, the inaccuracy in the weight of the "effective" specimen is estimated to be not more than 0.1 percent.

Density. The inaccuracy in density measurements is approximately 0.1 percent. This uncertainty enters into the computation of the thickness of the specimen.

Time. The time base of the experiments was a synchronous motor which derived its power from a 400 Hz regulated power supply. Measurements have indicated that the inaccuracy in time due to frequency instability was less than 0.005 percent.

7.2. Errors Due to Departure from Assumed Conditions

a. Errors in Heat Loss Correction

Since the dynamic experiments were made with the specimen in vacuum, heat loss from the specimen took place by thermal radiation and by axial conduction to the end clamps. In the previous section it was reported that axial temperature gradients in the "effective" specimen were very small; thus heat loss by conduction in the axial direction is negligible. Heat conduction to the voltage probes is also negligible since the cross-sectional area of the knife-edges is small and the conduction path is long. Thus, thermal radiation is the only major source of heat loss. To correct for this, a term representing thermal radiation is included in the relation for heat capacity, eq (2). However, any uncertainty in this term affects heat capacity. Radiation heat loss, which was obtained from data during the cooling period, has an uncertainty of approximately 1 percent. Then, uncertainty in heat capacity is obtained by multiplying the uncertainty in heat loss by thermal radiation by the ratio of radiated power to input power. Results of "slow" experiments indicate that the contribution of this uncertainty to heat capacity is approximately 0.03 percent at 2000 K and 0.14 percent at 2800 K. This uncertainty, of course, is less in "fast" experiments.

b. Evaporation

Evaporation at high temperatures introduces effects due to: (1) the heat of vaporization of the material lost, and (2) reduction in the mass of the specimen. Using evaporation data given by Jones et al. [32] and vapor pressures tabulated by JANAF [31], the total weight loss corresponding to present experimental conditions was computed. The resulting total weight loss is 3×10^{-5} mg and 0.35 mg per experiment in dynamic experiments where temperature maxima were at approximately 2000 K and 2800 K, respectively. The measured weight loss was 0.1 mg and 0.36 mg for approximately the same temperatures. This shows that evaporation accounts for most of the weight loss at high temperatures. The relatively large measured weight loss at lower temperatures which cannot be attributed to evaporation may be due to oxidation and subsequent evaporation of the oxide. At the highest temperature weight loss is less than 0.01 percent of the weight of the effective specimen, thus the effect of evaporation on the results is negligible. The heat loss effect computed was much smaller than radiation loss. It is included in the radiation heat loss correction to the heat capacity and hence does not contribute any additional error to heat capacity, but may introduce a small error in the hemispherical total emittance.

c. Thermionic Emission

Considering the values 55×10^4 A m^{-2} K^{-2} for the thermionic emission constant and 4.15 eV for the thermionic work function of molybdenum [17, 63], thermionic emission current is computed to be approximately 7×10^{-5} A mm^{-2} at 2000 K and 0.15 A mm^{-2} at 2800 K. It may be noted that computed values are for the case where electrons are continuously removed from the surface which requires a collector plate at positive potential. In the present system, the chamber wall is electrically neutral and the only electrical potential gradient that exists is that across the specimen, which is less than 10 V. Thus, in the present experiments thermionic emission is most probably space charge limited, as a result of which its contribution is much less than the values computed above and therefore negligible. Since the positive ion work function for molybdenum is 8.6 eV [74], the contribution of positive ion emission can also be neglected.

7.3. Statistical Error Analysis of Experimental Results

Possible sources and estimates of combined systematic and random errors were discussed in the previous sections. In this section, an analysis of heat capacity and electrical resistivity results is presented from the viewpoint of the random errors in the experimental data.

The imprecision in the determination of properties may be calculated both in terms of the imprecision of a set of data in a single experiment and in terms of the imprecision of the results of many experiments.

a. Imprecision of Heat Capacity in a Single Experiment

The variables which contribute random uncertainty to the heat capacity in a single experiment are: voltage, current, temperature, and heating rate. Each of these variables enters the heat capacity calculation as a function of time. The uncertainty of an individual voltage, current, or temperature has been obtained as a percent standard deviation in the course of the computer calculation of a variable-time equation according to the following equation:

$$s = \left[\frac{\sum \left(\frac{T_{\text{obs}} - T_{\text{cal}}}{T_{\text{obs}}} \right)^2}{n-3} \right]^{1/2} \tag{37}$$

where n is the number of measurements in an experiment. From experimental results the average standard deviation is found to be 0.02 percent for temperature, 0.02 percent for voltage and 0.03 percent for current. The uncertainty of a heating rate has been calculated from the standard deviation of the coefficients of the temperature-time equation differentiated to obtain the heating rate. Although temperature and heating rate are interdependent functions, the variances in heat capacity derived from these two variables are so different in magnitude that they are treated here as independent functions.

The total variance in heat capacity, s_c^2, resulting from uncertainties in the four variables is given by

$$s_c^2 = s_{ce}^2 + s_{ci}^2 + s_{cT}^2 + s_{cr}^2 \tag{38}$$

which may be expressed as

$$s_c^2 = s_e^2 \left(\frac{\partial C}{\partial e} \right)^2 + s_i^2 \left(\frac{\partial C}{\partial i} \right)^2 + s_T^2 \left(\frac{\partial C}{\partial T} \right)^2 + s_r^2 \left(\frac{\partial C}{\partial r} \right)^2 \tag{39}$$

where s_{ce}^2 is the heat capacity variance contributed by voltage, s_{ci}^2 by current, s_{cT}^2 by temperature, s_{cr}^2 by heating rate; and s_e^2, s_i^2, s_T^2, s_r^2 are the variances of the variables voltage, current, temperature, and heating rate, respectively. The result of computations of above quantities yields an average random uncertainty of 0.55 percent for heat capacity.

b. Imprecision of Heat Capacity from a Series of Experiments

A large number of experiments was conducted in several temperature ranges. Each experiment consisted of approximately 50 sets of measurements of temperature, voltage, and current, which have standard deviations discussed above. When heat capacity was computed from these quantities and the results of the many experiments were combined to obtain a polynomial function, the resultant standard deviation was 0.32 percent. However, since individual experimental results had been smoothed in the initial data reduction, the 0.32 percent standard deviation does not include all of the random variations that would have been observed without this prior processing. If the sum of the variances for the two processes are taken into consideration, one obtains an estimate of the variance of an individual determination which gives approximately 0.6 percent for this standard deviation of an individual point. This is an indication of the imprecision of the measurement. However, the imprecision of a single determination has relatively little effect on the inaccuracy of the results because (1) imprecision is already much smaller than estimated total error, (2) properties are obtained from several thousand measurements of temperature and electrical quantities.

c. Imprecision of Electrical Resistivity in a Single Experiment

The variables affecting the imprecision of resistivity based on room-temperature dimensions are voltage and current. The uncertainty in the dimensions of the electrical path represent a systematic error only. Total variance in electrical resistivity, s_ρ^2, resulting from uncertainties in the two variables may be expressed by the following equation.

$$s_\rho^2 = s_e^2 \left(\frac{\partial \rho}{\partial e} \right)^2 + s_i^2 \left(\frac{\partial \rho}{\partial i} \right)^2. \tag{40}$$

The result of above computations gives an average imprecision of 0.032 percent for electrical resistivity.

d. Imprecision of Electrical Resistivity from a Series of Experiments

The function combining all the resistivity experiments shows a standard deviation of 0.076 percent for the second series. As in the case of heat capacity, this represents the variability of different groups of smoothed values and its variance must therefore be combined with that of the individual experiments (0.032 percent). The results indicate that the total imprecision in resistivity is approximately 0.08 percent.

7.4. Summary of Error Estimates

Based on detailed analysis of identifiable random and systematic errors of each variable given in the previous sections, errors in properties are estimated. A summary of the imprecision and inaccuracy of measured and computed quantities is presented in table 12.

TABLE 12. *Imprecision and inaccuracy of measured and computed quantities*

Quantity	Imprecision %	Inaccuracy %
Temperature	0.02 (0.5K)	0.2 (4 K) at 2000 K 0.25 (7 K) at 2800 K
Voltage	0.02	0.05
Current	.03	.06
Power	.04	.08
Resistance	.04	.08
Length	.04	.08
Weight	.01	.1
Density	.02	.1
Heat Capacity	.6	2 at 2000 K 3 at 2800 K
Resistivity	.08	0.5
Hem. Total Emittance	1	3
Norm. Spectral Emittance	0.2	2

Uncertainty in the heating rate is the major contribution to the total error in heat capacity. The uncertainty in heating rate is related primarily to the temperature errors. The electrical resistivity is dependent primarily on uncertainties in temperature and dimensions and, to a lesser extent, on uncertainties in voltage and current measurements. The major source of error in total hemispherical emittance is due to the uncertainty in the ratio of heating rate to cooling rate, while in the case of normal spectral emittance, uncertainty in temperature (through uncertainties in blackbody quality and scattered light correction) plays the most important role.

8. General Discussion and Conclusions

Since the interpretation of results for measured properties is given in detail in section 5, and since comparison of results of the present work with those in the literature is presented in section 6, this section will be confined to discussion of other subjects directly or indirectly related to the high-speed measurement of properties at high temperatures.

Whether a specimen is under thermodynamic equilibrium while measurements are taken during dynamic heating and cooling periods may be determined by considering the relaxation times of various rate processes. In pure electrical conductors the main relaxation process is due to electron-phonon interactions. For metals at room temperature the relaxation time of this process is estimated to be less than 10^{-12}s. Since relaxation time is directly proportional to electrical conductivity and since the latter decreases with increasing temperature, it takes a longer time to establish thermal equilibrium at high temperatures. The variation of electrical conductivity in metallic elements between room temperature and the melting point is within a factor of 100; therefore, relaxation time in metals at high temperatures is of the order of 10^{-10}s. Thus, in experiments of millisecond and even microsecond resolution the electronic and vibrational states of the specimen can be considered to be in thermodynamic equilibrium during the time of measurements.

The equilibrium concentration of vacancies in the lattice has been discussed in section 5, and its estimated contribution to heat capacity is given in table 7. These estimates may be considered to be an indication of the upper limit of the change in the heat capacity if the concentration departs from equilibrium values during a rapid heating or cooling process. From this, one may conclude that departures of heat capacity from equilibrium values are less than the imprecision of the measurements throughout most of the temperature range.

Information concerning relaxation times for vacancy equilibrium is not readily obtainable; but since the mechanism is related to that of diffusion, the relaxation time is an exponential function of temperature. The magnitude of vacancy relaxation time as observed in quenching experiments at lower temperatures and extrapolated up to the melting point may be of the order of a millisecond for molybdenum in the temperature range 2500 to 2800 K. The vacancy kinetics of molybdenum has not been investigated sufficiently to permit reliable estimates.

The difference between the measured weight loss of the specimen and the computed weight loss due to evaporation, which in all cases was less than 0.01 percent per experiment, is attributed to oxidation followed by evaporation of the oxide. It can be noted that at very high temperatures actual weight loss was very close to that computed for evaporation, while at low and medium temperatures the weight loss was probably primarily due to oxidation.

Molybdenum forms primarily two oxides, MoO_2 and MoO_3. Studies reported in the literature [39, 60] indicate that the oxidation rate of molybdenum may be represented by a parabolic function in time at moderately high temperatures and by a linear function at temperatures above 1000 K because of the volatility

of MoO_3. Thus, above about 1000 K oxidation is accompanied by a loss in specimen weight.

The results for electrical resistivity (high and ambient temperature) and residual electrical resistivity ratio indicate a reduction in impurity content or in other imperfections at the end of the experiments. Chemical analysis did not show any detectable change in the impurity content between the initial and final states of the specimen. This fact may be partly attributed to the low sensitivity of the analysis.

It has been reported [25, 56] that at high temperatures certain impurities in a solid can diffuse to the surface and evaporate thus causing partial purification of the specimen and the generation of clean surfaces. Several investigators [9, 24, 58, 75] have observed that small amounts of oxygen present in the system may react with the carbon impurities in the specimen (refractory metals) and produce CO and CO_2.

In conclusion, changes in impurity content, grain growth, or departures of vacancy concentrations from equilibrium, discussed above or earlier in the text, all together may conceivably account for the observed changes of 1.3 to 2.2 percent in heat capacity between the first and second series of measurements. No other satisfactory explanation has been found. The results of the second series are recommended to represent the properties of molybdenum.

Experimental results reported in this study have shown the feasibility of accurate measurement of heat capacity and electrical resistivity of electrical conductors at high temperatures (above 2000 K) by a pulse method of millisecond resolution. The results also indicate that under proper surface and environmental conditions the technique allows the measurement of total hemispherical and normal spectral emittances. At 2000 K the accuracy of measured properties by this method is estimated to be about the same as that obtained by conventional methods. At temperatures above 2500 K it surpasses any other method now known. In fact, high-speed measurements play a unique role in research at very high temperatures where conventional techniques cannot be used because of excessive heat losses, evaporation, chemical reactions, mechanical instability, etc. Thus, dynamic measurement techniques become an important and very attractive tool in the study of refractory metals and their alloys, as well as other high melting electrically conducting substances. Another distinct advantage of this technique is that it permits the measurement of several properties simultaneously.

The authors extend their appreciation to G. M. Foley of Leeds and Northrup Co. (also guest worker at NBS) for his research on the millisecond pyrometer and for his advice and assistance in connection with the operation of the pyrometer.

9. Appendix

TABLE A–1. *Experimental results on heat capacity and electrical resistivity of molybdenum (first series)*

Range and Exp. No.	T K	c_p J mol^{-1} K^{-1}	ρ 10^{-8} Ωm
Low			
246	1900	34.28	49.68
246	1940	34.83	50.92
246	1980	35.38	52.18
246	2020	35.93	53.45
246	2060	36.47	54.73
246	2100	37.01	56.02
247	1900	34.43	49.68
247	1940	34.89	50.93
247	1980	35.34	52.19
247	2020	35.79	53.45
247	2060	36.22	54.72
247	2100	36.65	55.99
248	1900	34.15	49.67
248	1940	34.69	50.91
248	1980	35.23	52.16
248	2020	35.77	53.43
248	2060	36.30	54.70
248	2100	36.83	55.98
251	1900	34.21	49.69
251	1940	34.77	50.93
251	1980	35.33	52.19
251	2020	35.88	53.45
251	2060	36.43	54.73
251	2100	36.98	56.02
252	1900	34.45	49.69
252	1940	34.89	50.94
252	1980	35.32	52.19
252	2020	35.73	53.46
252	2060	36.14	54.73
252	2100	36.53	56.00
253	1900	34.80	49.65
253	1940	35.15	50.91
253	1980	35.48	52.18
253	2020	35.80	53.45
253	2060	36.11	54.72
253	2100	36.40	56.01
Medium			
223	2000	35.52	52.86
223	2040	36.07	54.12
223	2080	36.61	55.39
223	2120	37.15	56.67
223	2160	37.68	57.96
223	2200	38.21	59.26
223	2240	38.73	60.57
224	2000	35.71	52.86
224	2040	36.19	54.13
224	2080	36.65	55.41
224	2120	37.11	56.69
224	2160	37.56	57.96
224	2200	37.99	59.24
225	2000	35.89	52.87
225	2040	36.33	54.15
225	2080	36.76	55.43
225	2120	37.18	56.71
225	2160	37.58	57.99
225	2200	37.97	59.27
225	2240	38.36	60.55

TABLE A–1. *Experimental results on heat capacity and electrical resistivity of molybdenum (first series) – Con.*

Range and Exp. No.	T K	c_p J mol^{-1} K^{-1}	ρ 10^{-8} Ωm
Medium			
229	2000	35.67	52.90
229	2040	36.16	54.17
229	2080	36.65	55.45
229	2120	37.12	56.73
229	2160	37.59	58.01
229	2200	38.04	59.30
229	2240	38.49	60.58
230	2000	35.79	52.89
230	2040	36.26	54.16
230	2080	36.73	55.44
230	2120	37.18	56.73
230	2160	37.63	58.01
230	2200	38.07	59.29
230	2240	38.50	60.58
232	2000	35.81	52.94
232	2040	36.27	54.21
232	2080	36.71	55.49
232	2120	37.14	56.77
232	2160	37.56	58.05
232	2200	37.97	59.32
232	2240	38.37	60.60
High			
235	2200	37.69	59.28
235	2240	38.39	60.55
235	2280	39.10	61.83
235	2320	39.82	63.10
235	2360	40.56	64.37
235	2400	41.31	65.64
235	2440	42.09	66.91
235	2480	42.87	68.17
235	2520	43.69	69.42
236	2200	37.74	59.33
236	2240	38.44	60.60
236	2280	39.14	61.88
236	2320	39.86	63.15
236	2360	40.59	64.42
236	2400	41.33	65.70
236	2440	42.09	66.96
236	2480	42.86	68.22
236	2520	43.66	69.48
237	2200	37.92	59.33
237	2240	38.59	60.60
237	2280	39.28	61.88
237	2320	39.97	63.16
237	2360	40.67	64.43
237	2400	41.38	65.71
237	2440	42.10	66.97
237	2480	42.84	68.24
237	2520	43.60	69.49
240	2200	38.16	59.34
240	2240	38.80	60.63
240	2280	39.43	61.91
240	2320	40.08	63.20
240	2360	40.72	64.48
240	2400	41.38	65.75
240	2440	42.04	67.01
240	2480	42.71	68.27
240	2520	43.39	69.51
241	2200	38.04	59.34
241	2240	38.70	60.63
241	2280	39.36	61.91
241	2320	40.03	63.19
241	2360	40.71	64.47

TABLE A–1. *Experimental results on heat capacity and electrical resistivity of molybdenum (first series) – Con.*

Range and Exp. No.	T K	c_p J mol^{-1} K^{-1}	ρ 10^{-8} Ωm
High			
241	2400	41.40	65.75
241	2440	42.10	67.02
241	2480	42.81	68.28
241	2520	43.54	69.54
242	2200	37.91	59.37
242	2240	38.59	60.65
242	2280	39.29	61.93
242	2320	39.99	63.21
242	2360	40.71	64.48
242	2400	41.45	65.76
242	2440	42.19	67.02
242	2480	42.96	68.28
242	2520	43.75	69.53
Very High			
268	2400	41.06	65.54
268	2440	41.82	66.80
268	2480	42.60	68.06
268	2520	43.39	69.32
268	2560	44.21	70.57
268	2600	45.06	71.81
268	2640	45.93	73.04
268	2680	46.84	74.26
268	2720	47.78	75.47
268	2760	48.77	76.66
268	2800	49.80	77.83
269	2400	41.14	65.53
269	2440	41.89	66.79
269	2480	42.65	68.05
269	2520	43.43	69.31
269	2560	44.23	70.56
269	2600	45.05	71.80
269	2640	45.90	73.03
269	2680	46.79	74.25
269	2720	47.70	75.46
269	2760	48.65	76.65
269	2800	49.65	77.81
270	2400	41.04	65.47
270	2440	41.80	66.73
270	2480	42.58	67.99
270	2520	43.38	69.25
270	2560	44.20	70.50
270	2600	45.05	71.74
270	2640	45.93	72.98
270	2680	46.85	74.20
270	2720	47.81	75.41
270	2760	48.81	76.59
270	2800	49.86	77.76
273	2400	40.90	65.32
273	2440	41.62	66.57
273	2480	42.37	67.83
273	2520	43.13	69.08
273	2560	43.91	70.33
273	2600	44.71	71.56
273	2640	45.54	72.79
273	2680	46.40	74.01
273	2720	47.29	75.21
273	2760	48.22	76.39
274	2400	40.72	65.28
274	2440	41.44	66.53
274	2480	42.17	67.79
274	2520	42.92	69.04
274	2560	43.69	70.28
274	2600	44.48	71.51
274	2640	45.29	72.74

TABLE A–1. *Experimental results on heat capacity and electrical resistivity of molybdenum (first series)* – Con.

Range and Exp. No.	T K	c_p J mol^{-1} K^{-1}	ρ 10^{-8} Ωm
Very High			
274	2680	46.12	73.95
274	2720	46.98	75.14
274	2760	47.88	76.31
274	2800	48.81	77.46
275	2400	40.51	65.27
275	2440	41.23	66.51
275	2480	41.97	67.75
275	2520	42.73	68.98
275	2560	43.51	70.22
275	2600	44.31	71.44
275	2640	45.13	72.66
275	2680	45.98	73.87
275	2720	46.86	75.06
275	2760	47.78	76.25
275	2800	48.74	77.41

TABLE A–2. *Experimental results on heat capacity and electrical resistivity of molybdenum (second series)*

Range and Exp. No.	T K	c_p J mol^{-1} K^{-1}	ρ 10^{-8} Ωm
Low			
293	1900	33.91	49.45
293	1940	34.44	50.68
293	1980	34.96	51.91
293	2020	35.47	53.17
293	2060	35.96	54.43
293	2100	36.44	55.70
294	1900	33.97	49.45
294	1940	34.46	50.68
294	1980	34.94	51.92
294	2020	35.40	53.17
294	2060	35.86	54.43
294	2100	36.31	55.69
295	1900	34.05	49.45
295	1940	34.51	50.69
295	1980	34.96	51.93
295	2020	35.39	53.17
295	2060	35.80	54.43
295	2100	36.20	55.68
296	1900	34.04	49.46
296	1940	34.49	50.70
296	1980	34.92	51.94
296	2020	35.34	53.19
296	2060	35.74	54.44
296	2100	36.13	55.70
Medium			
303	2000	34.85	52.58
303	2040	35.40	53.83
303	2080	35.94	55.08
303	2120	36.47	56.34
303	2160	36.98	57.60
303	2200	37.49	58.86
303	2240	37.98	60.13
303	2280	38.45	61.39

TABLE A–2. *Experimental results on heat capacity and electrical resistivity of molybdenum (second series)* – Continued

Range and Exp. No.	T K	c_p J mol^{-1} K^{-1}	ρ 10^{-8} Ωm
Medium			
304	2000	35.01	52.59
304	2040	35.53	53.84
304	2080	36.04	55.09
304	2120	36.53	56.35
304	2160	37.01	57.61
304	2200	37.48	58.88
304	2240	37.93	60.15
304	2280	38.36	61.42
305	2000	35.05	52.59
305	2040	35.57	53.84
305	2080	36.07	55.10
305	2120	36.55	56.36
305	2160	37.03	57.62
305	2200	37.48	58.88
305	2240	37.93	60.15
305	2280	38.35	61.41
306	2000	34.99	52.60
306	2040	35.53	53.84
306	2080	36.06	55.10
306	2120	36.57	56.36
306	2160	37.07	57.62
306	2200	37.56	58.89
306	2240	38.04	60.17
306	2280	38.50	61.45
High			
315	2200	37.22	58.73
315	2240	37.87	59.99
315	2280	38.52	61.26
315	2320	39.16	62.52
315	2360	39.81	63.79
315	2400	40.44	65.04
315	2440	41.08	66.30
315	2480	41.71	67.55
315	2520	42.34	68.79
316	2200	37.35	58.76
316	2240	37.99	60.02
316	2280	38.62	61.29
316	2320	39.25	62.55
316	2360	39.87	63.81
316	2400	40.49	65.07
316	2440	41.10	66.32
316	2480	41.71	67.57
316	2520	42.31	68.81
317	2200	37.34	58.77
317	2240	37.98	60.03
317	2280	38.62	61.30
317	2320	39.25	62.56
317	2360	39.87	63.83
317	2400	40.49	65.09
317	2440	41.11	66.34
317	2480	41.72	67.59
317	2520	42.32	68.84
318	2200	37.24	58.79
318	2240	37.90	60.06
318	2280	38.56	61.32
318	2320	39.22	62.59
318	2360	39.88	63.85
318	2400	40.54	65.11
318	2440	41.19	66.36
318	2480	41.85	67.61
318	2520	42.50	68.86

TABLE A–2. *Experimental results on heat capacity and electrical resistivity of molybdenum (second series)*—Continued

Range and Exp. No.	T K	c_p J mol^{-1} K^{-1}	ρ 10^{-8} Ωm
Very High			
324	2400	40.44	64.97
324	2440	41.17	66.22
324	2480	41.90	67.47
324	2520	42.63	68.72
324	2560	43.37	69.96
324	2600	44.11	71.19
324	2640	44.86	72.41
324	2680	45.62	73.61
324	2720	46.39	74.81
325	2400	40.46	64.99
325	2440	41.19	66.25
325	2480	41.92	67.51
325	2520	42.66	68.76
325	2560	43.40	69.99
325	2600	44.15	71.22
325	2640	44.90	72.44
325	2680	45.67	73.65
325	2720	46.44	74.84
325	2760	47.22	76.01
325	2800	48.02	77.16
326	2400	40.40	65.00
326	2440	41.15	66.26
326	2480	41.91	67.52
326	2520	42.68	68.76
326	2560	43.46	70.00
326	2600	44.24	71.24
326	2640	45.04	72.46
326	2680	45.85	73.67
326	2720	46.68	74.86
326	2760	47.52	76.04
326	2800	48.39	77.19
327	2400	40.42	65.02
327	2440	41.18	66.28
327	2480	41.95	67.54
327	2520	42.73	68.79
327	2560	43.51	70.03
327	2600	44.31	71.26
327	2640	45.12	72.49
327	2680	45.94	73.70
327	2720	46.78	74.90
327	2760	47.64	76.09

TABLE A–3. *Experimental results on normal spectral emittance of molybdenum at $\lambda = 650$ nm (second series)*

Exp. No.	T K	$\epsilon_{N,\lambda}$
288	1833	0.3341
288	1847	.3324
288	1862	.3314
288	1876	.3309
288	1896	.3305
288	1910	.3310
288	1924	.3318
297	2011	.3300
297	2030	.3301
297	2041	.3300
297	2057	.3300
297	2090	.3302
297	2104	.3303
297	2123	.3302
307	2165	.3296
307	2184	.3292
307	2203	.3288
307	2222	.3283
307	2240	.3278
307	2259	.3273
307	2277	.3268
319	2401	.3252
319	2418	.3250
319	2434	.3248
319	2451	.3246
319	2467	.3245
319	2483	.3244
319	2500	.3243
328	2606	.3235
328	2628	.3232
328	2650	.3230
328	2672	.3228
328	2694	.3226
328	2715	.3224
328	2736	.3222
328	2757	.3219
328	2777	.3216

TABLE A–4. *Experimental results on hemispherical total emittance of molybdenum (first and second series)*

Series and Exp. No.	T K	ϵ
First Series		
264	1887	0.2718
258	1910	.2726
259	1911	.2702
248	2082	.2807
252	2099	.2851
224	2247	.2976
223	2261	.2931
229	2263	.2913
237	2493	.3075
236	2494	.3130
241	2501	.3132
269	2747	.3263
270	2763	.3310
Second Series		
284	1881	.2534
294	2094	.2720
304	2255	.2773
317	2510	.2967
325	2731	.3154

10. References

[1] Abbott, G. L., N. J. Alvares, and W. J. Parker, WADD–TR–61–94, II (1962).
[2] Allen, R. D., L. F. Glasier, Jr., and P. L. Jordan, J. Appl. Phys., **31,** 1382 (1960).
[3] Amonenko, V. M., P. N. V'yugov, and V. S. Gumenyuk, High Temperature **2,** 22 (1964).
[4] Argent, B. B., and J. G. C. Milne, The physical properties of niobium, Tantalum, Molybdenum, and Tungsten, in Niobium, Tantalum, Molybdenum and Tungsten, p. 162, A. G. Quarrell, Ed. (Elsevier, Amsterdam, 1961).
[5] Askwyth, W. H., R. J. Yahes, R. D. House, and G. Mikk, NASA–CR–56496 (1964).
[6] Avramescu, A., Z. Tech. Physik **20,** 213 (1939).
[7] Barnes, B. T., J. Opt. Soc. Am. **56,** 1546 (1966).
[8] Baxter, H. W., Nature **153,** 316 (1944).
[9] Becker, J. A., E. J. Becker, and R. G. Brandes, J. Appl. Phys. **32,** 411 (1961).
[10] Beckett, C. W., and A. Cezairliyan, High-Speed Thermodynamic Measurements and Related Techniques , in Experimental Thermodynamics, Vol. I, Calorimetry of Non-Reacting Systems, p. 551 J. P. McCullough and D. W. Scott, Eds. (Butterworths, London, 1968).
[11] Carslaw, H. S., and J. C. Jaeger, Conduction of Heat in Solids (Oxford University Press, Oxford, 1959).
[12] Cezairliyan, A., A High-Speed (Millisecond) Method for the simultaneous measurement of enthalpy, specific heat, and resistivity of electrical conductors at high temperatures, in Advances in Thermophysical Properties at Extreme Temperatures and Pressures, p. 253 ASME, New York, (1965).
[13] Compt. Rend. of the 21st Conference of the International Union of Pure and Applied Chemistry, Montreal (1961), Report of the Committee on Atomic Weights, pp. 284–327.
[14] DeSorbo, W., Phys. Rev. **117,** 444 (1960).
[15] DeVos, J. C., Physica **20,** 669 (1954).
[16] Douglas, T. B., J. Res. Nat. Bur. Stand. (U.S.), **73A** (Phys. and Chem), No. 5, 451 (Sept.–Oct. 1969).
[17] DuBridge, L. A., and W. W. Roehr, Phys. Rev. **42,** 52 (1932).
[18] Edwards, J. W., R. Speiser, and H. L. Johnston, J. Appl. Phys. **22,** 424 (1951).
[19] Feith, A. D., Measurement of the Thermal Conductivity and Electrical Resistivity of Molybdenum, General Electric Report (GE–TM 65–10–1), (1965).
[20] Foley, G. M., High-Speed Optical Pyrometer, in preparation.
[21] Grew, K. E., Proc. Roy. Soc. (London) **145,** 509 (1934).
[22] Grover, F. W., Inductance Calculations (Van Nostrand, New York, 1946).
[23] Gshneidner, K. A., Physical Properties and Interrelationships of Metallic and Semimetallic Elements, in Solid State Physics, Vol. **16,** p. 275 F. Seitz and D. Turnbull, Eds. (Academic Press, New York, 1965).
[24] Haas, T. W., Res. Rev. (Off. of Aerospace Research–USAF) **5,** 3 (Apr. 1966).
[25] Hagstrum, H. D., and C. D'Amico, J. Appl. Phys. **31,** 715 (1960).
[26] Holder, J., and A. V. Granato, Phys. Rev. **182,** 729 (1969).
[27] Horowitz, M., and J. G. Daunt, Phys. Rev., **91,** 1099 (1953).
[28] House, R. D., G. J. Lyons, and W. H. Askwyth, Measurement of Spectral Normal Emittance of Materials Under Simulated Spacecraft Powerplant Operating Conditions, in Measurement of Thermal Radiation Properties of Solids, J. C. Richmond, Ed., NASA, Washington, p. 343 (1963).
[29] International Practical Temperature Scale of 1968, Metrologia **5,** 35 (1969).
[30] Jaeger, F. M., and W. A. Veenstra, Rec. Trav. Chim. **53,** 677 (1934).
[31] JANAF Thermochemical Tables (Second Addendum), Clearinghouse for Federal Scientific and Technical Information, U.S. Department of Commerce, PB 168 370–2 (1967).
[32] Jones, H. A., I. Langmuir, and G. M. J. MacKay, Phys. Rev. **30,** 201 (1927).
[33] Killeffer, D. H., and A. Linz, Molybdenum Compounds, p. 14 (Interscience Publishers, New York, 1952).
[34] Kirby, R. K., Thermal Expansion, in American Institute of Physics Handbook, sect. 4, p. 64 (McGraw-Hill, Book Co., New York, 1963).
[35] Kirillin, V. A., A. E. Sheindlin, and V. Y. Chekhovskoi, Int. J. Heat Mass Transfer **5,** 1 (1962).
[36] Kirillin, V. A., A. E. Sheindlin, V. Y. Chekhovskoi, and V. A. Petrov, Enthalpy and Heat Capacity of Molybdenum at Extremely High Temperatures, in Proc. of Fourth Symposium on Thermophysical Properties, J. R. Moszynski, Ed., ASME, New York, p. 54 (1968).
[37] Kollie, T. G., Rev. Sci. Instr. **38,** 1452 (1967).
[38] Kraftmacher, Y. A., Physica Status Solidi **5,** K48 (1964).
[39] Kubaschewski, O., and B. E. Hopkins, Oxidation Mechanisms of Niobium, Tantalum, Molybdenum and Tungsten, in Niobium, Tantalum, Molybdenum, and Tungsten, p. 181 A. G. Quarrell, Ed. (Elsevier, Amsterdam, 1961).
[40] Kurrelmeyer, B., W. H. Mais, and E. H. Green, Rev. Sci. Instr. **14,** 349 (1943).
[41] Lapp, E., Ann. Chimie et Physique **12,** 442 (1929).
[42] Lazareva, L. S., P. B. Kantor, and V. V. Kandyba, Phys. Metals and Metallog. (USSR), **11,** 133 (1961).
[43] Lowenthal, G. C., Aust. J. Phys. **16,** 47 (1963).
[44] McLean, D., Grain Boundaries in Metals (Oxford University Press, Oxford, 1957).
[45] Meakin, J. D., A. Lawley, and R. C. Koo, Vacancy Loops in Quenched Molybdenum, in Lattice Defects in Quenched Metals, p. 767 R. M. J. Cotterill, M. Doyama, J. J. Jackson, and M. Meshi, Eds. (Academic Press, New York, 1965).
[46] Morse, M. S., and A. Cezairliyan, High-Speed Digital Data Acquisition System for Thermodynamic Measurements, in preparation.
[47] Nathan, A. M., J. Appl. Phys. **22,** 234 (1951).
[48] Osborn, R. H., J. Opt. Soc. Am. **31,** 428 (1941).
[49] Pallister, P. R., J. Iron Steel Inst. **161,** 87 (1949).
[50] Parker, R., Trans. Met. Soc. AIME **233,** 1545 (1965).
[51] Pasternak, R. A., E. C. Fraser, B. B. Hansen, and H. U. D. Wiesendanger, Rev. Sci. Instr. **33,** 1320 (1962).
[52] Pasternak, R. A., H. U. D. Wiesendanger, and B. B. Hansen, J. Appl. Phys. **34,** 3416 (1963).
[53] Pochapsky, T. E., Acta Met. **1,** 747 (1953).
[54] Pochapsky, T. E., Rev. Sci. Instr. **25,** 238 (1954).
[55] Rasor, N. S., and J. D. McClelland, J. Phys. Chem. Solids **15,** 17 (1960).
[56] Roberts, R. W., Brit. J. Appl. Phys. **14,** 537 (1963).
[57] Rudkin, R. L., W. J. Parker, and R. J. Jenkins, Measurement of Thermal Properties of Metals at Elevated Temperatures, in Temperature, Its Measurement and Control in Science and Industry, Vol. **III,** C. M. Herzfeld, ed., Reinhold, New York, Part 2, p. 523 (1962).

[58] Schlier, R. E., J. Appl. Phys. **29,** 1162 (1958).
[59] Schultz, H., Quenching of Vacancies in Tungsten, in Lattice Defects in Quenched Metals, R. M. J. Cotterill, M. Doyama, J. J. Jackson, and M. Meshi, Eds., p. 761 (Academic Press, New York, 1965).
[60] Seybolt, A. U., Adv. in Phys. **12,** 1 (1963).
[61] Simmons, R. O., and R. W. Balluffi, Phys. Rev. **125,** 862 (1962).
[62] Simmons, R. O., and R. W. Balluffi, Phys. Rev. **129,** 1533 (1963).
[63] Stanley, J. K., Electrical and Magnetic Properties of Metals, American Society for Metals, Metals Park, Ohio (1963).
[64] Stimson, H. F., J. Res. Nat. Bur. Stand. (U.S.), **65A** (Phys. and Chem.) No. 3, 139 (May–June 1961).
[65] Taylor, R. E., and R. A. Finch, J. Less-Common Metals **6,** 283 (1964).
[66] Taylor, R. E., private Communication (1964).
[67] Tietz, T. E., and J. W. Wilson, Behavior and Properties of Refractory Metals, p. 28 (Stanford University Press, California, 1965).
[68] Tye, R. P., J. Less-Common Metals **3,** 13 (1961).
[69] Wallace, D. C., Phys. Rev. **120,** 84 (1960).
[70] Wallace, D. C., P. H. Sidles, and G. C. Danielson, J. Appl. Phys. **31,** 168 (1960).
[71] White, G. K., and S. B. Woods, Phil. Trans. Royal Soc. (London), **251,** 273 (1959).
[72] Worthing, A. G., Phys. Rev. **12,** 199 (1918).
[73] Worthing, A. G., Phys. Rev. **28,** 190 (1926).
[74] Wright, R. W., Phys. Rev. **60,** 465 (1941).
[75] Young, J. R., J. Appl. Phys. **30,** 1671 (1959).
[76] Zhorov, G. A., High Temperature **5,** 881 (1967).

(Paper 74A1–586)

JOURNAL OF RESEARCH of the National Bureau of Standards—A. Physics and Chemistry
Vol. 74A, No. 1, January–February 1970

P–V–T, Thermodynamic and Related Properties of Oxygen from the Triple Point to 300 K at Pressures to 33 MN/m²*

L. A. Weber**

**Institute for Basic Standards, National Bureau of Standards,
Boulder, Colorado 80302**

(October 14, 1969)

The results of new experimental pressure-volume-temperature measurements on oxygen are presented. The data range in temperature from 54 to 300 K and in pressure from 0.1 to about 33 MN/m². The following properties are tabulated for selected isobars: molar volume, $(\partial P/\partial \rho)_T$, $(\partial P/\partial T)_\rho$, internal energy, enthalpy, entropy, specific heats at constant volume and at constant pressure, and the velocity of sound. Additional tables present the above properties for saturated liquid and vapor, the freezing liquid P–V–T relationship, and the derived Joule-Thomson inversion curve. New values for the critical density and triple point density are presented, and the second and third virial coefficients are tabulated.

Key words: Density; enthalpy; entropy; equation of state; fixed points (PVT); Joule-Thomson; latent heat; melting curve; oxygen; properties of fluids; saturated liquid and vapor; specific heat; vapor pressure; velocity of sound.

List of Symbols and Units

The symbols and units used here are listed below. Values of fixed points and other quantities used here are given where applicable.

R = gas constant; 8.3147 N-m/mol-K (Note: this value differs by less than 1/20000 from the currently accepted best value.)
P = pressure, MN/m².
P_{sat} = vapor pressure.
P_{melt} = melting pressure.
P_c = critical pressure, 5.043 ± .002 MN/m².
P_t = triple point pressure, 152 ± 6 N/m².
V = molar volume, cm³/mol.
T = absolute temperature, Kelvins International Practical Temperature Scale of 1948 where the triple point of water is 273.16 K; below the oxygen boiling point the NBS 1955 temperature scale is used.
T_c = critical temperature, 154.576 ± .010 K.
T_t = triple point temperature, 54.3507 ± .0010K.
T_b = boiling point temperature, 90.18 K (90.188 K on the IPTS 1968 scale).
ρ = density, mol/cm³ = 1/V.
ρ_c = critical density, 0.01363 ± .00002 mol/cm³.
ρ_t = liquid triple point density, 0.04083 ± .00004 mol/cm³.
$\rho_{sat\,L}$ = saturated liquid density.
$\rho_{sat\,G}$ = saturated vapor density.
$\rho_{melt\,L}$ = density of the liquid along the liquid-solid boundary.
ρ_1 = a selected density in the compressed liquid, 0.028687 mol/cm³.
A_J = generalized coefficients in approximating equations; numerical values given in tables.
$B(T)$ = second virial coefficient, cm³/mol.
$C(T)$ = third virial coefficient, (cm³/mol)².
$C_v(T, \rho)$ = heat capacity at constant volume, J/mol K $C_v^\circ(T)$ heat capacity of the ideal gas.
$C_p(T, \rho)$ = heat capacity at constant pressure, J/mol K.
C_{sat} = heat capacity of the saturated liquid, J/mol K.
$S(T, \rho)$ = entropy, J/mol K.
$H(T, \rho)$ = enthalpy, J/mol.
$U(T, \rho)$ = internal energy, J/mol.
W = velocity of sound, m/s.
Molecular Weight = 31.9988 g.

*This work was carried out at NBS under the sponsorship of the National Aeronautics and Space Administration Headquarters Fund Transfer No. R-06-006-046.
**Cryogenics Division, National Bureau of Standards, Boulder, Colo. 80302.

1. Introduction

The importance of oxygen in the U.S. space program and the lack of comprehensive and accurate data for many of its physical properties have led to an extensive research program at the NBS Institute for Basic Standards. The results of part of that program are presented here in the form of extensive tables of P–V–T data and derived thermodynamic properties.

Prior to 1960 there were relatively few measurements of the P–V–T properties of oxygen at low temperatures. This condition was especially true for the compressed liquid. In 1960 and 1961 Timrot and Borisoglebskii [1, 2][1] and Van Itterbeek and Verbeke [3, 4] published new P–V–T results for the liquid. However, these results were limited in scope and there was disagreement in the region in which they overlapped.

The results of the present investigation consist of approximately 1500 P–V–T points at 111 different densities varying from 0.0047 to 3 times the critical density. This constitutes approximately two-thirds of all the P–V–T data published for oxygen.

The data range from the triple point temperature to 300 K for the high densities and from 85 K to 300 K for the low (subcritical) density points. The data range in pressure up to about 33 MN/m².

The highest and lowest density data were represented by two analytic surfaces while the intermediate densities were fitted to a large number of isotherm polynomials. Second and third virial coefficients were extracted from the low density data.

This representation of the P–V–T surface together with the specific heat of the ideal gas [5] allowed the calculation of thermodynamic properties of the gas at temperatures below critical and of all densities at temperatures above critical. Thermodynamic calculations for the compressed liquid at subcritical temperatures made use of additional data in the form of new experimental determinations of the heat capacity at constant volume [6] and heat capacity of the saturated liquid [7] from this laboratory.

The properties calculated using this smoothed surface are compared with some of the P–V–T and thermodynamic property data from the literature.

Due to limitations of space only skeleton tables of thermodynamic properties are presented here. A more complete set of tables will be issued as NBS Tech. Note 384.

2. Experimental P–V–T Measurements

2.1. Apparatus

The cryostat designed and described by Goodwin [8] was used with minor modifications. These modifications are listed below in terms of the nomenclature used in reference [8]. Early vapor pressure measurements yielded results which were lower than published values by 4000 to 6000 N/m², indicating the presence of a cold spot in the stainless steel transition capillary which connects the sample holder to the top of the cryostat. Jacketing the capillary with $\frac{1}{8}$ in OD copper tubing removed this difficulty. For the high temperature ($T > 150$ K) portion of the measurements the shield, shown in figure 2 of reference [8], was replaced with one that completely surrounded the sample holder thereby reducing heat losses to the cold wall. For measurements above 200 K the only refrigerant used was the liquid nitrogen in the open dewar surrounding the cryostat. The oil operated dead-weight gage pressure measuring system was modified, as shown in figure 1 here, for safety. Two null pressure detectors were used. The first separated the oil in the gage from an intermediate nitrogen gas system. The second separated the nitrogen from the oxygen sample. Thus in the event of a diaphragm failure there was no chance of high pressure oxygen coming in contact with the oil.

With practice the two-diaphragm system could be operated with as much sensitivity as the one diaphragm system in reference [8]. All external capillary lines, valves, and gages were cleaned by flushing with liquid Freon. Repairs to several of the glass flasks in the gasometer system necessitated recalibration of these volumes. The 1-liter flask, which was the primary standard of volume, was calibrated by weighing with water and agreed with the original calibration by Goodwin [8] to within 0.02 percent. The 2- and 6-liter flasks were calibrated by both water weighing and by gas expansion from the 1-liter flask. These two independent determinations agreed to better than one part in ten thousand in each case. The 21-liter flask was calibrated by gas expansion only, with an estimated uncertainty of 0.04 percent. The volume of the sample holder was recalibrated by gas expansion into the 1- and 2-liter flasks. The volume obtained was 25.852 ± 0.015 cm³ in good agreement with the earlier measurements, by weighing with water, of reference [8].

The relationship used to calculate the elastic stretching of the sample holder due to pressure was modified to correspond more closely to experimental results on similar thick walled vessels [9]. Thus, eq (5.2–7) of reference [8] was modified to become

$$V/V_o = 1 + a\,[1 + 4.35 \cdot 10^{-4}\,T] \cdot P, \qquad (1)$$

with $a = 2.3 \times 10^{-5}$ m²/MN. This modification changed the calculated densities by 0.04 percent at 30 MN/m². A quartz bourdon gage with a sensitivity of 7 N/m² was used to measure the pressure in the gasometer flasks for the density determinations.

The estimated relative error in the measured pressures is 0.01 percent, increasing somewhat at the lower pressures. Corrections were made for the hydrostatic pressure of the oxygen in the capillaries, which often amounted to several thousandths of a MN/m². Temperature readings may deviate from the thermometer calibration by 2 millidegrees at 50 K, increasing to 28 millidegrees at 300 K, due to the specifications of the potentiometer used. The uncertainty of the calibration itself is probably less than 0.002 K. To this must be added the deviations of the International Practical

[1] Figures in brackets indicate the literature references at the end of this paper.

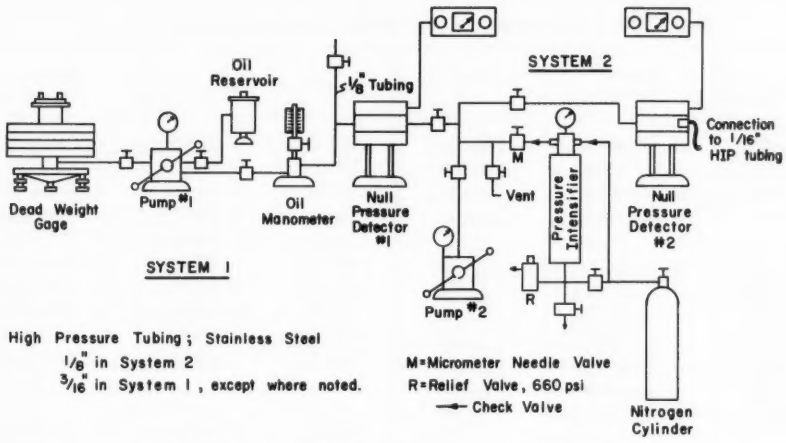

FIGURE 1. *Dead weight gage pressure measuring system.*

Temperature Scale (1948) from the thermodynamic temperature scale, perhaps as much as 0.04 K. With this apparatus, however, temperatures are reproducible to within 1 millidegree. Uncertainty in the density determinations is estimated at 0.1 percent for low pressures, increasing to 0.14 percent at the highest pressures. A precision of the order of 0.025 percent in density has been realized.

The samples used came from commercially available cylinders of ultra pure oxygen with a nominal purity of 99.99 percent and were passed through a molecular sieve trap at 76 K to remove water.

2.2 The Data

The measuring technique used here is the modified Reichsanstalt method described by Goodwin [8]. The data were taken along experimental pseudo-isochores, hereafter referred to as runs. Due to the precisely reproducible nature of the temperature control system, data on the various runs were measured at the same temperatures and therefore, could be rearranged into isotherms at the conclusion of the experimental work. Data were taken at integral temperatures with 2 K spacing from 56 K to 160 K, 5 K spacing from 160 K to 200 K, and 10 K spacing from 200 K to 300 K. In the low density gas phase a 5 K spacing was used between 85 K and 150 K.

For convenience the data may be divided chronologically into four series. Table 1 shows the distribution of the data between the series. Between Series I and II certain changes were made in the apparatus which necessitated recalibration of some of the volumes external to the cryostat. Between Series II and III the apparatus was moved to a new building and most of the external volumes were rebuilt. Series IV differed from the others by the way in which the density and pressure were determined.

The data were checked for systematic deviations between Series I, II, and III in the following way. Isotherm polynomials were fitted to the data in the regions where the data of different series overlapped. The deviations of all points in a series, expressed as percent

TABLE 1. *Four series of experimental runs*

Series	No. of data points	Run No.
I	239	33–51
II	922	53–108
III	275	109–137
IV	67	138–145

error in density, were averaged. The results showed that the internal precision within each series was good (0.015 to 0.025 percent). However, while Series I and III were in agreement, the data of Series II differed systematically by an average of 0.066 percent in density. The origin of this difference is not clear. However, since the smoothness of the P–V–T surface is of utmost importance in the calculation of thermodynamic properties, the densities of the data of Series II were arbitrarily multiplied by 1.00066. This difference falls within the estimated overall uncertainty of the data.

Series IV consisted of data in the very low density ($0.0047 \leq \rho/\rho_c \leq 0.14$) gas phase between 85 K and 150 K. Pressures were measured with a quartz bourdon gage. Densities were too low for the use of the gasometer and were extracted from the measured pressure at 160 K, using virial coefficients obtained from the data of Series II and III.

The single-phase experimental P–V–T data are presented in table 2. The column labeled "IDENT" contains the identification number of each point. The first two or three digits are the number of the run or experimental isochore and the last two are the number of the point. The entries in runs 132 and 133 which contain no value for the density are pressures measured on the melting curve. In addition some pressures were measured along the vapor pressure curve. They are given in table 3 and were used mainly as a check on the vapor pressure curve taken from the literature. Because of the rather large vertical dimensions of the apparatus no attempt was made to take data in close proximity to the critical point.

TABLE 2. *Temperature-pressure-density observations on oxygen.*

T K	P MN/m²	Density mol/cm³	Ident
85.0	0.0444	0.0000644	14501
90.0	0.0472	0.0000644	14502
95.0	0.0500	0.0000643	14503
100.0	0.0527	0.0000643	14504
85.0	0.0506	0.0000739	14401
90.0	0.0540	0.0000739	14402
95.0	0.0572	0.0000738	14403
100.0	0.0603	0.0000738	14404
105.0	0.0634	0.0000737	14405
110.0	0.0665	0.0000737	14406
115.0	0.0696	0.0000736	14407
85.0	0.0566	0.0000895	14301
90.0	0.0652	0.0000894	14302
95.0	0.0691	0.0000893	14303
100.0	0.0729	0.0000893	14304
105.0	0.0766	0.0000892	14305
110.0	0.0804	0.0000892	14306
115.0	0.0840	0.0000891	14307
120.0	0.0877	0.0000891	14308
125.0	0.0914	0.0000890	14309
95.0	0.1353	0.0001787	14201
100.0	0.1431	0.0001786	14202
105.0	0.1507	0.0001785	14203
110.0	0.1583	0.0001784	14204
115.0	0.1658	0.0001783	14205
120.0	0.1733	0.0001782	14206
125.0	0.1807	0.0001781	14207
130.0	0.1882	0.0001780	14208
135.0	0.1956	0.0001778	14209
140.0	0.2030	0.0001777	14210
145.0	0.2104	0.0001776	14211
154.0	0.2236	0.0001774	14212
100.0	0.2112	0.0002684	14101
105.0	0.2229	0.0002683	14102
110.0	0.2344	0.0002681	14103
115.0	0.2458	0.0002679	14104
120.0	0.2572	0.0002678	14105
125.0	0.2685	0.0002676	14106
130.0	0.2799	0.0002675	14107
135.0	0.2911	0.0002673	14108
140.0	0.3024	0.0002672	14109
145.0	0.3135	0.0002670	14110
105.0	0.3435	0.0004259	14001
110.0	0.3623	0.0004256	14002
115.0	0.3811	0.0004254	14003
120.0	0.3996	0.0004251	14004
125.0	0.4179	0.0004249	14005
130.0	0.4363	0.0004246	14006
135.0	0.4543	0.0004243	14007
140.0	0.4723	0.0004241	14008
145.0	0.4904	0.0004238	14009
120.0	0.8598	0.0009979	13901
125.0	0.9060	0.0009972	13902
130.0	0.9515	0.0009966	13903
135.0	0.9970	0.0009959	13904
140.0	1.0417	0.0009953	13905
145.0	1.0865	0.0009947	13906
150.0	1.1308	0.0009940	13907
152.0	1.1484	0.0009938	13908
156.0	1.1837	0.0009933	13910
158.0	1.2011	0.0009930	13911
130.0	1.4564	0.0016669	13801
135.0	1.5375	0.0016657	13802
140.0	1.6176	0.0016646	13803
145.0	1.6966	0.0016635	13804
150.0	1.7748	0.0016624	13805
152.0	1.8059	0.0016619	13806
160.0	2.2294	0.0019671	12201
165.0	2.3220	0.0019658	12202
170.0	2.4140	0.0019644	12203
175.0	2.5054	0.0019630	12204
180.0	2.5964	0.0019617	12205
185.0	2.6867	0.0019603	12206
190.0	2.7767	0.0019589	12207
195.0	2.8663	0.0019576	12208
200.0	2.9554	0.0019562	12209
210.0	3.1328	0.0019534	12210
220.0	3.3086	0.0019507	12211
230.0	3.4832	0.0019479	12212
240.0	3.6571	0.0019452	12213
250.0	3.8298	0.0019423	12214
260.0	4.0014	0.0019395	12215
270.0	4.1723	0.0019366	12216
280.0	4.3423	0.0019337	12217
290.0	4.5115	0.0019308	12218
300.0	4.6800	0.0019279	12219
160.0	3.1728	0.0030701	10701
165.0	3.3268	0.0030660	10702
170.0	3.4788	0.0030619	10703
175.0	3.6296	0.0030579	10704
180.0	3.7787	0.0030538	10705
185.0	3.9267	0.0030498	10706
190.0	4.0735	0.0030457	10707
195.0	4.2193	0.0030417	10708
200.0	4.3642	0.0030377	10709
210.0	4.6508	0.0030298	10710
220.0	4.9342	0.0030219	10711
230.0	5.2143	0.0030140	10712
240.0	5.4914	0.0030061	10713
250.0	5.7663	0.0029982	10714
260.0	6.0384	0.0029903	10715
270.0	6.3082	0.0029824	10716
280.0	6.5757	0.0029745	10717

TABLE 2. *Temperature-pressure-density observations on oxygen.*—Continued

T K	P MN/m²	Density mol/cm³	Ident	T K	P MN/m²	Density mol/cm³	Ident
290.0	6.8411	0.0029667	10718	280.0	8.5202	0.0038995	10626
300.0	7.1046	0.0029590	10719	290.0	8.8839	0.0038880	10627
				300.0	9.2427	0.0038783	10628
140.0	2.6702	0.0033734	12101				
142.0	2.7450	0.0033723	12102	146.0	3.4249	0.0046103	10502
144.0	2.8190	0.0033713	12103	148.0	3.5322	0.0046058	10503
146.0	2.8924	0.0033703	12104	150.0	3.6353	0.0045729	10504
148.0	2.9652	0.0033692	12105	152.0	3.7403	0.0045701	10505
150.0	3.0373	0.0033681	12106	154.0	3.8443	0.0045674	10506
152.0	3.1087	0.0033672	12107	156.0	3.9471	0.0045647	10507
154.0	3.1799	0.0033661	12108	158.0	4.0491	0.0045623	10508
156.0	3.2505	0.0033651	12109	160.0	4.1507	0.0045596	10509
158.0	3.3208	0.0033641	12110	165.0	4.4004	0.0045529	10510
160.0	3.3908	0.0033631	12111	170.0	4.6470	0.0045463	10511
165.0	3.5635	0.0033606	12112	175.0	4.8898	0.0045397	10512
170.0	3.7358	0.0033581	12113	180.0	5.1302	0.0045333	10513
175.0	3.9057	0.0033556	12114	185.0	5.3678	0.0045269	10514
180.0	4.0742	0.0033530	12115	190.0	5.6034	0.0045204	10515
185.0	4.2415	0.0033505	12116	195.0	5.8366	0.0045140	10516
190.0	4.4076	0.0033481	12117	200.0	6.0683	0.0045077	10517
195.0	4.5727	0.0033454	12118	210.0	6.5252	0.0044948	10518
200.0	4.7368	0.0033430	12119	220.0	6.9767	0.0044822	10519
210.0	5.0624	0.0033378	12120	230.0	7.4220	0.0044695	10520
220.0	5.3852	0.0033329	12121	240.0	7.8623	0.0044571	10521
230.0	5.7048	0.0033278	12122	250.0	8.2968	0.0044445	10522
240.0	6.0220	0.0033227	12123	260.0	8.7279	0.0044321	10523
250.0	6.3369	0.0033176	12124	270.0	9.1541	0.0044196	10524
260.0	6.6496	0.0033123	12125	280.0	9.5772	0.0044073	10525
270.0	6.9606	0.0033072	12126	290.0	9.9958	0.0043949	10526
280.0	7.2697	0.0033019	12127	300.0	10.4111	0.0043827	10527
290.0	7.5765	0.0032967	12128				
300.0	7.8823	0.0032914	12129	148.0	3.7532	0.0052554	10402
				150.0	3.8810	0.0052520	10403
142.0	3.0360	0.0040880	10601	152.0	4.0068	0.0052487	10404
144.0	3.1304	0.0040841	10602	154.0	4.1312	0.0052454	10405
146.0	3.2226	0.0040803	10603	156.0	4.2543	0.0052423	10406
148.0	3.3134	0.0040765	10604	158.0	4.3761	0.0052392	10407
150.0	3.4031	0.0040728	10605	160.0	4.4971	0.0052361	10408
152.0	3.4918	0.0040691	10606	165.0	4.7947	0.0052282	10409
154.0	3.5765	0.0040376	10607	170.0	5.0875	0.0052204	10410
156.0	3.6646	0.0040353	10608	175.0	5.3761	0.0052126	10411
158.0	3.7519	0.0040329	10609	180.0	5.6612	0.0052049	10412
160.0	3.8385	0.0040306	10610	185.0	5.9432	0.0051971	10413
165.0	4.0528	0.0040248	10611	190.0	6.2223	0.0051896	10414
170.0	4.2643	0.0040192	10612	195.0	6.4989	0.0051822	10415
175.0	4.4730	0.0040134	10613	200.0	6.7727	0.0051745	10416
180.0	4.6796	0.0040079	10614	210.0	7.3142	0.0051597	10417
185.0	4.8842	0.0040022	10615	220.0	7.8480	0.0051448	10418
190.0	5.0869	0.0039967	10616	230.0	8.3747	0.0051300	10419
195.0	5.2879	0.0039911	10617	240.0	8.8948	0.0051153	10420
200.0	5.4875	0.0039857	10618	250.0	9.4093	0.0051008	10421
210.0	5.8823	0.0039748	10619	260.0	9.9184	0.0050864	10422
220.0	6.2716	0.0039639	10620	270.0	10.4217	0.0050719	10423
230.0	6.6563	0.0039531	10621	280.0	10.9169	0.0050571	10424
240.0	7.0367	0.0039424	10622	290.0	11.4114	0.0050426	10425
250.0	7.4130	0.0039316	10623	300.0	11.9005	0.0050281	10426
260.0	7.7856	0.0039209	10624				
270.0	8.1550	0.0039103	10625	150.0	3.9962	0.0056510	10301

367-409 OL-70—7

TABLE 2. *Temperature-pressure-density observations on oxygen.*—Continued

T K	P MN/m²	Density mol/cm³	Ident	T K	P MN/m²	Density mol/cm³	Ident
152.0	4.1356	0.0056473	10302	190.0	7.5556	0.0067993	10110
154.0	4.2729	0.0056436	10303	195.0	7.9437	0.0067883	10111
156.0	4.4080	0.0056401	10304	200.0	8.3285	0.0067782	10112
158.0	4.5419	0.0056367	10305	210.0	9.0876	0.0067571	10113
160.0	4.6747	0.0056330	10306	220.0	9.8356	0.0067362	10114
165.0	5.0014	0.0056242	10307	230.0	10.5727	0.0067158	10115
170.0	5.3224	0.0056156	10308	240.0	11.3005	0.0066948	10116
175.0	5.6383	0.0056070	10309	250.0	12.0189	0.0066750	10117
180.0	5.9505	0.0055985	10310	260.0	12.7291	0.0066550	10118
185.0	6.2594	0.0055901	10311	270.0	13.4311	0.0066350	10119
190.0	6.5649	0.0055817	10312	280.0	14.1273	0.0066158	10120
195.0	6.8673	0.0055734	10313	290.0	14.8133	0.0065950	10121
200.0	7.1671	0.0055651	10314	300.0	15.4953	0.0065748	10122
210.0	7.7596	0.0055486	10315				
220.0	8.3425	0.0055323	10316	160.0	5.1253	0.0068611	12301
230.0	8.9185	0.0055163	10317	165.0	5.5484	0.0068550	12302
240.0	9.4859	0.0054999	10318	170.0	5.9640	0.0068490	12303
250.0	10.0481	0.0054840	10319	175.0	6.3735	0.0068430	12304
260.0	10.6040	0.0054681	10320	180.0	6.7784	0.0068371	12305
270.0	11.1528	0.0054529	10321	185.0	7.1794	0.0068312	12306
280.0	11.6973	0.0054364	10322	190.0	7.5768	0.0068253	12307
290.0	12.2359	0.0054208	10323	195.0	7.9707	0.0068194	12308
300.0	12.7691	0.0054051	10324	200.0	8.3621	0.0068135	12309
				210.0	9.1370	0.0068018	12310
150.0	4.1753	0.0064527	10201	220.0	9.9022	0.0067901	12311
152.0	4.3425	0.0064484	10202	230.0	10.6600	0.0067784	12312
154.0	4.5061	0.0064441	10203	240.0	11.4094	0.0067667	12313
156.0	4.6673	0.0064399	10204	250.0	12.1533	0.0067550	12314
158.0	4.8266	0.0064357	10205	260.0	12.8904	0.0067433	12315
160.0	4.9842	0.0064316	10206	270.0	13.6219	0.0067316	12316
165.0	5.3714	0.0064212	10207	280.0	14.3480	0.0067199	12317
170.0	5.7514	0.0064109	10208	290.0	15.0693	0.0067082	12318
175.0	6.1252	0.0064010	10209	300.0	15.7857	0.0066965	12319
180.0	6.4955	0.0063909	10210				
185.0	6.8595	0.0063810	10211	154.0	4.8414	0.0084740	10001
190.0	7.2201	0.0063710	10212	156.0	5.0735	0.0084681	10002
195.0	7.5777	0.0063605	10213	158.0	5.3014	0.0084620	10003
200.0	7.9320	0.0063516	10214	160.0	5.5259	0.0084560	10004
210.0	8.6317	0.0063324	10215	165.0	6.0777	0.0084410	10005
220.0	9.3205	0.0063132	10216	170.0	6.6172	0.0084263	10006
230.0	9.9994	0.0062939	10217	175.0	7.1487	0.0084119	10007
240.0	10.6695	0.0062755	10218	180.0	7.6740	0.0083977	10008
250.0	11.3322	0.0062568	10219	185.0	8.1922	0.0083834	10009
260.0	11.9871	0.0062380	10220	190.0	8.7060	0.0083693	10010
270.0	12.6345	0.0062194	10221	195.0	9.2140	0.0083555	10011
280.0	13.2754	0.0062009	10222	200.0	9.7185	0.0083415	10012
290.0	13.9096	0.0061825	10223	210.0	10.7147	0.0083141	10013
300.0	14.5392	0.0061644	10224	220.0	11.6953	0.0082872	10014
				230.0	12.6624	0.0082605	10015
154.0	4.6059	0.0068794	10101	240.0	13.6170	0.0082344	10016
156.0	4.7815	0.0068747	10102	250.0	14.5610	0.0082088	10017
158.0	4.9549	0.0068702	10103	260.0	15.4914	0.0081834	10018
160.0	5.1265	0.0068653	10104	270.0	16.4137	0.0081580	10019
165.0	5.5472	0.0068540	10105	280.0	17.3251	0.0081334	10020
170.0	5.9599	0.0068428	10106	290.0	18.2257	0.0081089	10021
175.0	6.3664	0.0068319	10107	300.0	19.1188	0.0080843	10022
180.0	6.7682	0.0068210	10108				
185.0	7.1637	0.0068100	10109	154.0	4.9185	0.0097086	9901
				156.0	5.1960	0.0097003	9902

TABLE 2. *Temperature-pressure-density observations on oxygen.*—Continued

T K	P MN/m²	Density mol/cm³	Ident	T K	P MN/m²	Density mol/cm³	Ident
158.0	5.4669	0.0096936	9903	250.0	19.9644	0.0113263	9716
160.0	5.7333	0.0096862	9904	260.0	21.4189	0.0112897	9717
165.0	6.3882	0.0096689	9905	270.0	22.8569	0.0112531	9718
170.0	7.0310	0.0096510	9906	280.0	24.2784	0.0112171	9719
175.0	7.6648	0.0096342	9907	290.0	25.6871	0.0111835	9720
180.0	8.2922	0.0096172	9908	300.0	27.0831	0.0111495	9721
185.0	8.9127	0.0096003	9909				
190.0	9.5269	0.0095835	9910	156.0	5.2986	0.0121578	9601
195.0	10.1359	0.0095668	9911	158.0	5.6505	0.0121487	9602
200.0	10.7398	0.0095504	9912	160.0	6.0001	0.0121393	9603
210.0	11.9332	0.0095175	9913	165.0	6.8698	0.0121155	9604
220.0	13.1084	0.0094853	9914	170.0	7.7308	0.0120922	9605
230.0	14.2678	0.0094534	9915	175.0	8.5873	0.0120690	9606
240.0	15.4065	0.0094199	9916	180.0	9.4375	0.0120455	9607
250.0	16.5349	0.0093888	9917	185.0	10.2825	0.0120225	9608
260.0	17.6497	0.0093582	9918	190.0	11.1205	0.0119999	9609
270.0	18.7530	0.0093291	9919	195.0	11.9535	0.0119773	9610
280.0	19.8415	0.0092984	9920	200.0	12.7799	0.0119549	9611
290.0	20.9230	0.0092706	9921	210.0	14.4167	0.0119107	9612
300.0	21.9884	0.0092422	9922	220.0	16.0293	0.0118674	9613
				230.0	17.6212	0.0118240	9614
156.0	5.2598	0.0108709	9801	240.0	19.1929	0.0117824	9615
158.0	5.5700	0.0108625	9802	250.0	20.7463	0.0117418	9616
160.0	5.8766	0.0108537	9803	260.0	22.2789	0.0117037	9617
165.0	6.6321	0.0108333	9804	270.0	23.7979	0.0116668	9618
170.0	7.3766	0.0108131	9805	280.0	25.2927	0.0116298	9619
175.0	8.1125	0.0107927	9806	290.0	26.7829	0.0115936	9620
180.0	8.8432	0.0107729	9807	300.0	28.2536	0.0115602	9621
185.0	9.5654	0.0107538	9808				
190.0	10.2823	0.0107343	9809	156.0	5.3093	0.0127557	10802
195.0	10.9936	0.0107149	9810	158.0	5.6813	0.0127459	10803
200.0	11.6997	0.0106963	9811	160.0	6.0514	0.0127360	10804
210.0	13.0945	0.0106578	9812	165.0	6.9743	0.0127115	10805
220.0	14.4703	0.0106220	9813	170.0	7.8956	0.0126866	10806
230.0	15.8269	0.0105837	9814	175.0	8.8084	0.0126620	10807
240.0	17.1698	0.0105373	9815	180.0	9.7181	0.0126374	10808
250.0	18.4871	0.0105121	9816	185.0	10.6227	0.0126131	10809
260.0	19.7940	0.0104786	9817	190.0	11.5216	0.0125891	10810
270.0	21.0829	0.0104432	9818	195.0	12.4146	0.0125652	10811
280.0	22.3607	0.0104101	9819	200.0	13.3026	0.0125416	10812
290.0	23.6247	0.0103788	9820	210.0	15.0596	0.0124949	10813
300.0	24.8740	0.0103471	9821	220.0	16.7936	0.0124496	10814
				230.0	18.5030	0.0124050	10815
156.0	5.2876	0.0117217	9701	240.0	20.1940	0.0123615	10816
158.0	5.6258	0.0117126	9702	250.0	21.8609	0.0123194	10817
160.0	5.9613	0.0117035	9703	260.0	23.5072	0.0122786	10818
165.0	6.7902	0.0116814	9704	270.0	25.1341	0.0122388	10819
170.0	7.6122	0.0116591	9705	280.0	26.7459	0.0122002	10820
175.0	8.4263	0.0116365	9706	290.0	28.3407	0.0121635	10821
180.0	9.2345	0.0116151	9707	300.0	29.9184	0.0121274	10822
185.0	10.0364	0.0115927	9708				
190.0	10.8326	0.0115723	9709	156.0	5.3268	0.0136248	9301
195.0	11.6231	0.0115504	9710	158.0	5.7260	0.0136142	9302
200.0	12.4078	0.0115292	9711	160.0	6.1269	0.0136036	9303
210.0	13.9600	0.0114876	9712	165.0	7.1321	0.0135765	9304
220.0	15.4907	0.0114454	9713	170.0	8.1371	0.0135494	9305
230.0	17.0017	0.0114047	9714	175.0	9.1405	0.0135222	9306
240.0	18.4909	0.0113652	9715	180.0	10.1405	0.0134950	9307

TABLE 2. *Temperature-pressure-density observations on oxygen.*—Continued

T K	P MN/m²	Density mol/cm³	Ident	T K	P MN/m²	Density mol/cm³	Ident
185.0	11.1353	0.0134680	9308	175.0	10.6217	0.0165974	9207
190.0	12.1252	0.0134417	9309	180.0	12.0026	0.0165600	9208
195.0	13.1093	0.0134148	9310	185.0	13.3800	0.0165235	9209
200.0	14.0870	0.0133885	9311	190.0	14.7508	0.0164880	9210
210.0	16.0226	0.0133369	9312	195.0	16.1152	0.0164514	9211
220.0	17.9342	0.0132865	9313	200.0	17.4706	0.0164161	9212
230.0	19.8171	0.0132386	9314	210.0	20.1560	0.0163477	9213
240.0	21.6805	0.0131899	9315	220.0	22.8057	0.0162839	9214
250.0	23.5231	0.0131476	9316	230.0	25.4257	0.0162217	9215
260.0	25.3416	0.0131025	9317	240.0	28.0091	0.0161638	9216
270.0	27.1349	0.0130590	9318	250.0	30.5648	0.0161100	9217
280.0	28.9124	0.0130177	9319				
290.0	30.6783	0.0129802	9320	156.0	5.5827	0.0180496	6304
				158.0	6.1910	0.0180333	6305
156.0	5.3444	0.0145565	9501	160.0	6.8069	0.0180167	6306
158.0	5.7755	0.0145455	9502	165.0	8.3678	0.0179745	6307
160.0	6.2112	0.0145337	9503	170.0	9.9452	0.0179319	6308
165.0	7.3110	0.0145036	9504	175.0	11.5215	0.0178896	6309
170.0	8.4162	0.0144737	9505	180.0	13.0983	0.0178475	6310
175.0	9.5206	0.0144438	9506	185.0	14.6689	0.0178061	6311
180.0	10.6244	0.0144140	9507	190.0	16.2316	0.0177653	6312
185.0	11.7237	0.0143843	9508	195.0	17.7871	0.0177252	6313
190.0	12.8167	0.0143549	9509	200.0	19.3307	0.0176860	6314
195.0	13.9051	0.0143257	9510	210.0	22.3876	0.0176104	6315
200.0	14.9866	0.0142970	9511	220.0	25.4037	0.0175391	6316
210.0	17.1296	0.0142405	9512	230.0	28.3808	0.0174726	6317
220.0	19.2423	0.0141857	9513				
230.0	21.3305	0.0141316	9514	154.0	5.1333	0.0190870	9101
240.0	23.3915	0.0140813	9515	156.0	5.8032	0.0190691	9102
250.0	25.4265	0.0140321	9516	158.0	6.4840	0.0190507	9103
260.0	27.4425	0.0139864	9517	160.0	7.1717	0.0190325	9104
270.0	29.4323	0.0139423	9518	165.0	8.9088	0.0189849	9105
280.0	31.4036	0.0138997	9519	170.0	10.6555	0.0189387	9106
				175.0	12.4031	0.0188922	9107
156.0	5.3779	0.0156909	9401	180.0	14.1455	0.0188457	9108
158.0	5.8544	0.0156782	9402	185.0	15.8814	0.0188001	9109
160.0	6.3383	0.0156648	9403	190.0	17.6046	0.0187559	9110
165.0	7.5656	0.0156315	9404	195.0	19.3175	0.0187133	9111
170.0	8.8044	0.0155983	9405	200.0	21.0180	0.0186698	9112
175.0	10.0455	0.0155649	9406	210.0	24.3878	0.0185888	9113
180.0	11.2866	0.0155316	9407	220.0	27.7085	0.0185138	9114
185.0	12.5248	0.0154978	9408	230.0	30.9821	0.0184442	9115
190.0	13.7562	0.0154657	9409	240.0	34.2235	0.0183832	9116
195.0	14.9816	0.0154330	9410	154.0	5.3612	0.0199362	9001
200.0	16.2004	0.0154011	9411	156.0	6.1026	0.0199167	9002
210.0	18.6148	0.0153388	9412	158.0	6.8525	0.0198965	9003
220.0	21.0010	0.0152805	9413	160.0	7.6077	0.0198760	9004
230.0	23.3507	0.0152212	9414	165.0	9.5075	0.0198249	9005
240.0	25.6751	0.0151658	9415	170.0	11.4133	0.0197742	9006
250.0	27.9759	0.0151156	9416	175.0	13.3163	0.0197246	9007
260.0	30.2501	0.0150694	9417	180.0	15.2115	0.0196751	9008
270.0	32.4981	0.0150249	9418	185.0	17.0956	0.0196266	9009
				190.0	18.9669	0.0195792	9010
156.0	5.4346	0.0167364	9202	195.0	20.8269	0.0195317	9011
158.0	5.9624	0.0167225	9203	200.0	22.6685	0.0194883	9012
160.0	6.4993	0.0167081	9204	210.0	26.3129	0.0194036	9013
165.0	7.8629	0.0166713	9205	220.0	29.9058	0.0193259	9014
170.0	9.2396	0.0166348	9206	230.0	33.4607	0.0192574	9015

TABLE 2. *Temperature-pressure-density observations on oxygen.*—Continued

T K	P MN/m²	Density mol/cm³	Ident	T K	P MN/m²	Density mol/cm³	Ident
152.0	4.8922	0.0207491	8901	170.0	16.2685	0.0229021	8610
154.0	5.6977	0.0207282	8902	175.0	18.8486	0.0228383	8611
156.0	6.5111	0.0207064	8903	180.0	21.4030	0.0227773	8612
158.0	7.3309	0.0206843	8904	185.0	23.9358	0.0227180	8613
160.0	8.1540	0.0206626	8905	190.0	26.4455	0.0226621	8614
165.0	10.2182	0.0206074	8906	195.0	28.9325	0.0226094	8615
170.0	12.2836	0.0205531	8907	200.0	31.4012	0.0225604	8616
175.0	14.3415	0.0204994	8908				
180.0	16.3874	0.0204470	8909	144.0	3.4424	0.0241115	5901
185.0	18.4256	0.0203979	8910	146.0	4.6016	0.0240796	5902
190.0	20.4446	0.0203481	8911	148.0	5.7616	0.0240495	5903
195.0	22.4490	0.0203003	8912	150.0	6.9230	0.0240173	5904
200.0	24.4409	0.0202543	8913	152.0	8.0797	0.0239864	5905
210.0	28.3778	0.0201695	8914	154.0	9.2364	0.0239558	5906
220.0	32.2607	0.0200932	8915	156.0	10.3883	0.0239253	5907
				158.0	11.5364	0.0238951	5908
150.0	4.4935	0.0216871	8801	160.0	12.6804	0.0238651	5909
152.0	5.3844	0.0216635	8802	165.0	15.5240	0.0237922	5910
154.0	6.2821	0.0216398	8803	170.0	18.3300	0.0237212	5911
156.0	7.1852	0.0216154	8804	175.0	21.1062	0.0236531	5912
158.0	8.0910	0.0215911	8805	180.0	23.8578	0.0235882	5913
160.0	8.9981	0.0215670	8806	185.0	26.5823	0.0235273	5914
165.0	11.2654	0.0215073	8807	190.0	29.2880	0.0234701	5915
170.0	13.5244	0.0214480	8808	195.0	31.9645	0.0234173	5916
175.0	15.7711	0.0213901	8809				
180.0	18.0013	0.0213343	8010	144.0	4.0468	0.0245557	8502
185.0	20.2159	0.0212800	8811	146.0	5.2654	0.0245240	8503
190.0	22.4139	0.0212267	8812	148.0	6.4826	0.0244899	8504
195.0	24.5897	0.0211771	8813	150.0	7.6966	0.0244579	8505
200.0	26.7526	0.0211299	8814	152.0	8.9074	0.0244256	8506
210.0	31.0295	0.0210424	8815	154.0	10.1149	0.0243937	8507
				156.0	11.3177	0.0243627	8508
148.0	4.0774	0.0225087	8701	158.0	12.5132	0.0243309	8509
150.0	5.0499	0.0224821	8702	160.0	13.7050	0.0242999	8510
152.0	6.0286	0.0224568	8703	165.0	16.6622	0.0242242	8511
154.0	7.0117	0.0224301	8704	170.0	19.5864	0.0241525	8512
156.0	7.9954	0.0224035	8705	175.0	22.4752	0.0240836	8513
158.0	8.9804	0.0223775	8706	180.0	25.3386	0.0240185	8514
160.0	9.9644	0.0223511	8707	185.0	28.1758	0.0239570	8515
165.0	12.4179	0.0222870	8708	190.0	30.9888	0.0239022	8516
170.0	14.8570	0.0222231	8709	195.0	33.7711	0.0238486	8517
175.0	17.2765	0.0221614	8710				
180.0	19.6783	0.0221040	8711	142.0	3.6026	0.0250985	8201
185.0	22.0531	0.0220468	8712	144.0	4.8902	0.0250632	8202
190.0	24.4119	0.0219923	8713	146.0	6.1763	0.0250283	8203
195.0	26.7541	0.0219405	8714	148.0	7.4576	0.0249944	8204
200.0	29.0778	0.0218914	8715	150.0	8.7342	0.0249604	8205
210.0	33.6683	0.0218061	8716	152.0	10.0046	0.0249267	8206
				154.0	11.2713	0.0248936	8207
146.0	3.6426	0.0232356	8601	156.0	12.5293	0.0248604	8208
148.0	4.6947	0.0232067	8602	158.0	13.7817	0.0248277	8209
150.0	5.7514	0.0231796	8603	160.0	15.0311	0.0247958	8210
152.0	6.8101	0.0231506	8604	165.0	18.1219	0.0247183	8211
154.0	7.8704	0.0231220	8605	170.0	21.1793	0.0246445	8212
156.0	8.9296	0.0230937	8606	175.0	24.1977	0.0245747	8213
158.0	9.9869	0.0230657	8607	180.0	27.1899	0.0245091	8214
160.0	11.0426	0.0230377	8608	185.0	30.1612	0.0244499	8215
165.0	13.6660	0.0229691	8609	190.0	33.1017	0.0243940	8216

TABLE 2. *Temperature-pressure-density observations on oxygen.*—Continued

T K	P MN/m²	Density mol/cm³	Ident	T K	P MN/m²	Density mol/cm³	Ident
140.0	2.9844	0.0255208	6401	152.0	15.3345	0.0266345	6209
142.0	4.3289	0.0254839	6402	154.0	16.8057	0.0265973	6210
144.0	5.6699	0.0254472	6403	156.0	18.2678	0.0265608	6211
146.0	7.0069	0.0254118	6404	158.0	19.7213	0.0265251	6212
148.0	8.3375	0.0253768	6405	160.0	21.1703	0.0264904	6213
150.0	9.6613	0.0253417	6406	165.0	24.7576	0.0264076	6214
152.0	10.9798	0.0253070	6407	170.0	28.3036	0.0263312	6215
154.0	12.2914	0.0252727	6408	175.0	31.8143	0.0262620	6216
156.0	13.5268	0.0252405	6409				
158.0	14.8935	0.0252054	6410	134.0	2.4353	0.0272899	6501
160.0	16.1822	0.0251726	6411	136.0	4.0412	0.0272455	6502
165.0	19.3802	0.0250928	6412	138.0	5.6349	0.0272020	6503
170.0	22.5416	0.0250173	6413	140.0	7.2192	0.0271604	6504
175.0	25.6668	0.0249463	6414	142.0	8.7920	0.0271189	6505
180.0	28.7565	0.0248806	6415	144.0	10.3512	0.0270777	6506
185.0	31.8246	0.0248202	6416	146.0	11.9004	0.0270372	6507
				148.0	13.4382	0.0269972	6508
140.0	3.5318	0.0258049	8401	150.0	14.9657	0.0269580	6509
142.0	4.9176	0.0257671	8402	152.0	16.4808	0.0269236	6510
144.0	6.2966	0.0257298	8403	154.0	17.9937	0.0268821	6511
146.0	7.6697	0.0256933	8404	156.0	19.4930	0.0268456	6512
148.0	9.0394	0.0256518	8405	158.0	20.9821	0.0268099	6513
150.0	10.3966	0.0256218	8406	160.0	22.4666	0.0267753	6514
152.0	11.7472	0.0255864	8407	165.0	26.1395	0.0266927	6515
154.0	13.0917	0.0255515	8408	170.0	29.7724	0.0266173	6516
156.0	14.4295	0.0255170	8409	175.0	33.3743	0.0265493	6517
158.0	15.7605	0.0254835	8410				
165.0	20.3576	0.0253692	8412	134.0	3.6213	0.0276729	8101
170.0	23.5952	0.0252943	8413	136.0	5.2856	0.0276273	8102
175.0	26.7970	0.0252237	8414	138.0	6.9337	0.0275841	8103
180.0	29.9705	0.0251597	8415	140.0	8.5697	0.0275414	8104
185.0	33.1131	0.0251002	8416	142.0	10.1897	0.0274986	8105
				144.0	11.8000	0.0274564	8106
138.0	3.2401	0.0263501	8301	146.0	13.3971	0.0274152	8107
140.0	4.7034	0.0263104	8302	148.0	14.9791	0.0273744	8108
142.0	6.1593	0.0262711	8303	150.0	16.5533	0.0273338	8109
144.0	7.6076	0.0262331	8304	152.0	18.1184	0.0272988	8110
146.0	9.0479	0.0261951	8305	154.0	19.6721	0.0272580	8111
148.0	10.4778	0.0261578	8306	156.0	21.2147	0.0272206	8112
150.0	11.8976	0.0261198	8307	158.0	22.7532	0.0271849	8113
152.0	13.3104	0.0260824	8308	160.0	24.2849	0.0271500	8114
154.0	14.7130	0.0260463	8309	165.0	28.0785	0.0270686	8115
156.0	16.1089	0.0260120	8310	170.0	31.8365	0.0269965	8116
158.0	17.4975	0.0259772	8311				
160.0	18.8815	0.0259431	8312	132.0	2.7155	0.0279362	6101
165.0	22.3006	0.0258609	8313	134.0	4.4246	0.0278891	6102
170.0	25.6842	0.0257848	8314	136.0	6.1187	0.0278436	6103
175.0	29.0322	0.0257147	8315	138.0	7.7995	0.0277991	6104
180.0	32.3448	0.0256520	8316	140.0	9.4641	0.0277550	6105
				142.0	11.1144	0.0277114	6106
136.0	3.1979	0.0269549	6201	144.0	12.7511	0.0276687	6107
138.0	4.7513	0.0269125	6202	146.0	14.3767	0.0276270	6108
140.0	6.2944	0.0268710	6203	148.0	15.9898	0.0275859	6109
142.0	7.8278	0.0268306	6204	150.0	17.5914	0.0275456	6110
144.0	9.3501	0.0267903	6205	152.0	19.1801	0.0275097	6111
146.0	10.8599	0.0267504	6206	154.0	20.7647	0.0274681	6112
148.0	12.3609	0.0267111	6207	156.0	22.3354	0.0274309	6113
150.0	13.8523	0.0266724	6208	158.0	23.9003	0.0273929	6114

TABLE 2. *Temperature-pressure-density observations on oxygen.*—Continued

T K	P MN/m²	Density mol/cm³	Ident	T K	P MN/m²	Density mol/cm³	Ident
160.0	25.4595	0.0273601	6115	124.0	2.1104	0.0297581	3401
165.0	29.3210	0.0272787	6116	126.0	4.1084	0.0297011	3402
170.0	33.1481	0.0272056	6117	128.0	6.0901	0.0296468	3403
				130.0	8.0454	0.0295931	3404
130.0	1.9644	0.0282691	8001	132.0	9.9760	0.0295401	3405
132.0	3.7305	0.0282200	8002	134.0	11.8876	0.0294884	3406
134.0	5.4786	0.0281728	8003	136.0	13.7784	0.0294378	3407
136.0	7.2122	0.0281273	8004	138.0	15.6572	0.0293882	3408
138.0	8.9282	0.0280815	8005	140.0	17.5120	0.0293401	3409
140.0	10.6303	0.0280366	8006	142.0	19.3736	0.0292935	3410
142.0	12.3164	0.0279926	8007	144.0	21.2096	0.0292481	3411
144.0	13.9897	0.0279501	8008	146.0	23.0408	0.0292039	3412
146.0	15.6477	0.0279070	8009	148.0	24.8835	0.0291617	3413
148.0	17.2999	0.0278657	8010	150.0	26.7045	0.0291210	3414
150.0	18.9348	0.0278252	8011	152.0	28.5164	0.0290824	3415
152.0	20.5621	0.0277892	8012	154.0	30.3258	0.0290454	3416
154.0	22.1841	0.0277479	8013	156.0	32.1204	0.0290107	3417
156.0	23.7927	0.0277109	8014	158.0	33.9185	0.0289777	3418
158.0	25.4000	0.0276764	8015				
160.0	26.9994	0.0276436	8016	124.0	2.4906	0.0298327	3902
165.0	30.9550	0.0275640	8017	126.0	4.5012	0.0297757	3903
				128.0	6.4903	0.0297215	3904
128.0	2.3713	0.0288775	6702	130.0	8.4523	0.0296674	3905
130.0	4.2335	0.0288261	6703	132.0	10.3898	0.0296143	3906
132.0	6.0769	0.0287770	6704	134.0	12.3076	0.0295626	3907
134.0	7.8983	0.0287287	6705	136.0	14.2138	0.0295122	3908
136.0	9.7048	0.0286808	6706	138.0	16.1014	0.0294627	3909
138.0	11.4930	0.0286337	6707				
140.0	13.2662	0.0285875	6708	140.0	17.9733	0.0294142	3910
142.0	15.0161	0.0285426	6709	142.0	19.8321	0.0293674	3911
144.0	16.7645	0.0284985	6710	144.0	21.6795	0.0293219	3912
146.0	18.4948	0.0284554	6711	146.0	23.5223	0.0292780	3913
148.0	20.2117	0.0284137	6712	148.0	25.3593	0.0292355	3914
150.0	21.9178	0.0283731	6713	150.0	27.1780	0.0291949	3915
152.0	23.6195	0.0283339	6714	152.0	28.9939	0.0291564	3916
154.0	25.3119	0.0282959	6715	154.0	30.8030	0.0291195	3917
156.0	26.9952	0.0282594	6716	156.0	32.5978	0.0290848	3918
158.0	28.6739	0.0282246	6717				
160.0	30.3434	0.0281913	6718	122.0	1.5045	0.0300885	5801
165.0	34.4943	0.0281153	6719	124.0	3.5853	0.0300301	5802
				126.0	5.6416	0.0299753	5803
126.0	2.8771	0.0294561	7501	128.0	7.6720	0.0299216	5804
128.0	4.8428	0.0294031	7502	130.0	9.6778	0.0298684	5805
130.0	6.7841	0.0293525	7503	132.0	11.6604	0.0298166	5806
132.0	8.7049	0.0293020	7504	134.0	13.6259	0.0297660	5807
134.0	10.6061	0.0292524	7505	136.0	15.5763	0.0297171	5808
136.0	12.4883	0.0292043	7506	138.0	17.5050	0.0296696	5809
138.0	14.3534	0.0291570	7507	140.0	19.4202	0.0296221	5810
140.0	16.2006	0.0291100	7508	142.0	21.3249	0.0295768	5811
142.0	18.0375	0.0290651	7509	144.0	23.2160	0.0295330	5812
144.0	19.8600	0.0290217	7510	146.0	25.1035	0.0294909	5813
146.0	21.6706	0.0289789	7511	148.0	26.9727	0.0294508	5814
148.0	23.4713	0.0289381	7512	150.0	28.8442	0.0294124	5815
150.0	25.2612	0.0288996	7513	152.0	30.7008	0.0293759	5816
152.0	27.0409	0.0288613	7514	154.0	32.5574	0.0293415	5817
154.0	28.8206	0.0288239	7515				
156.0	30.5910	0.0287899	7516	122.0	3.0971	0.0303754	7601
158.0	32.3536	0.0287579	7517	124.0	5.2176	0.0303187	7602

TABLE 2. *Temperature-pressure-density observations on oxygen.*—Continued

T K	P MN/m²	Density mol/cm³	Ident	T K	P MN/m²	Density mol/cm³	Ident
126.0	7.3153	0.0302640	7603	136.0	24.2720	0.0308888	4312
128.0	9.3831	0.0302089	7604	138.0	26.3720	0.0308414	4313
130.0	11.4278	0.0301557	7605	140.0	28.4675	0.0307964	4314
132.0	13.4542	0.0301041	7606	142.0	30.5548	0.0307539	4315
134.0	15.4565	0.0300530	7607	144.0	32.6389	0.0307139	4316
136.0	17.4427	0.0300036	7608				
138.0	19.4169	0.0299566	7609	114.0	1.1925	0.0316910	7801
140.0	21.3819	0.0299100	7610	116.0	3.5782	0.0316243	7802
142.0	23.3248	0.0298649	7611	118.0	5.9272	0.0315631	7803
144.0	25.1294	0.0298245	7612	120.0	8.2441	0.0315011	7804
146.0	27.2006	0.0297814	7613	122.0	10.5249	0.0314415	7805
148.0	29.1284	0.0297431	7614	124.0	12.7809	0.0313840	7806
150.0	31.0539	0.0297066	7615	126.0	15.0139	0.0313277	7807
152.0	32.9587	0.0296710	7616	128.0	17.2189	0.0312723	7808
				130.0	19.4118	0.0312187	7809
120.0	1.8317	0.0305760	3503	132.0	21.5882	0.0311671	7810
122.0	3.9817	0.0305144	3504	134.0	23.7537	0.0311175	7811
124.0	6.1040	0.0304567	3505	136.0	25.9088	0.0310703	7812
126.0	8.1901	0.0303990	3506	138.0	28.0581	0.0310268	7813
128.0	10.2555	0.0303427	3507	140.0	30.1939	0.0309830	7814
130.0	12.2974	0.0302881	3508	142.0	32.3228	0.0309431	7815
132.0	14.3198	0.0302342	3509				
134.0	16.3141	0.0301819	3510	114.0	1.6723	0.0317542	3601
136.0	18.2971	0.0301309	3511	116.0	4.0458	0.0316862	3602
138.0	20.2666	0.0300820	3512	118.0	6.3776	0.0316230	3603
140.0	22.2342	0.0300334	3513	120.0	8.6721	0.0315592	3604
142.0	24.1917	0.0299871	3514	122.0	10.9361	0.0314980	3605
144.0	26.1323	0.0299431	3515	124.0	13.1733	0.0314380	3606
146.0	28.0750	0.0299007	3516	126.0	15.3804	0.0313799	3607
148.0	29.9939	0.0298608	3517	128.0	17.5761	0.0313231	3608
150.0	31.9298	0.0298226	3518	130.0	19.7850	0.0312682	3609
152.0	33.8303	0.0297873	3519	132.0	21.9571	0.0312151	3610
				134.0	24.1236	0.0311642	3611
120.0	4.6411	0.0310159	5601	136.0	26.2706	0.0311158	3612
122.0	6.8570	0.0309577	5602	138.0	28.4258	0.0310694	3613
124.0	9.0357	0.0308992	5603	140.0	30.5788	0.0310259	3614
126.0	11.1895	0.0308427	5604	142.0	32.7111	0.0309851	3615
128.0	13.3215	0.0307876	5605				
130.0	15.4214	0.0307340	5606	114.0	3.1928	0.0319426	6001
132.0	17.5178	0.0306813	5607	116.0	5.6146	0.0318793	6002
134.0	19.5936	0.0306304	5608	118.0	7.9924	0.0318148	6003
136.0	21.6614	0.0305812	5609	120.0	10.3328	0.0317539	6004
138.0	23.7302	0.0305343	5610	122.0	12.6486	0.0316940	6005
140.0	25.7819	0.0304892	5611	124.0	14.9309	0.0316357	6006
142.0	27.8251	0.0304458	5612	126.0	17.1917	0.0315791	6007
144.0	29.8568	0.0304050	5613	128.0	19.4386	0.0315240	6008
146.0	31.8845	0.0303665	5614	130.0	21.6625	0.0314713	6009
116.0	2.4087	0.0314615	4302	114.0	3.4335	0.0319827	4401
118.0	4.7189	0.0313964	4303	116.0	5.8265	0.0319178	4402
120.0	6.9894	0.0313346	4304	118.0	8.1737	0.0318519	4403
122.0	9.2248	0.0312732	4305	120.0	10.4832	0.0317892	4404
124.0	11.4280	0.0312137	4306	122.0	12.7639	0.0317278	4405
126.0	13.6026	0.0311555	4307	124.0	15.0271	0.0316680	4406
128.0	15.7621	0.0310987	4308	126.0	17.2542	0.0316097	4407
130.0	17.9023	0.0310434	4309	128.0	19.4810	0.0315532	4408
132.0	20.0292	0.0309899	4310	130.0	21.6969	0.0314984	4409
134.0	22.1447	0.0309381	4311	132.0	23.9049	0.0314459	4410

TABLE 2. *Temperature-pressure-density observations on oxygen.*—Continued

T K	P MN/m²	Density mol/cm³	Ident	T K	P MN/m²	Density mol/cm³	Ident
134.0	26.1218	0.0313961	4411	118.0	19.0577	0.0329835	7908
136.0	28.3244	0.0313487	4412	120.0	21.5622	0.0329196	7909
138.0	30.5134	0.0313039	4413	122.0	24.0594	0.0328629	7910
140.0	32.7007	0.0312620	4414	124.0	26.5419	0.0328092	7911
				126.0	29.0289	0.0327583	7912
110.0	1.3810	0.0324614	3301	128.0	31.5034	0.0327109	7913
112.0	3.8894	0.0323894	3302				
114.0	6.3591	0.0323218	3303	104.0	2.7447	0.0336423	4001
116.0	8.7833	0.0322556	3304	106.0	5.4804	0.0335653	4002
118.0	11.1786	0.0321914	3305	108.0	8.1584	0.0334933	4003
120.0	13.5419	0.0321287	3306	110.0	10.7880	0.0334226	4004
122.0	15.8805	0.0320677	3307	112.0	13.3821	0.0333534	4005
124.0	18.2001	0.0320083	3308	114.0	15.9470	0.0332863	4006
126.0	20.5350	0.0319516	3309	116.0	18.4948	0.0332212	4007
128.0	22.8186	0.0318968	3310	118.0	21.0292	0.0331584	4008
130.0	25.1045	0.0318442	3311	120.0	23.6101	0.0331000	4009
132.0	27.3950	0.0317940	3312	122.0	26.1304	0.0330430	4010
134.0	29.6685	0.0317468	3313	124.0	28.6680	0.0329889	4011
136.0	31.9258	0.0317028	3314	126.0	31.1985	0.0329387	4012
138.0	34.1856	0.0316615	3315				
				102.0	2.4536	0.0339664	5301
				104.0	5.2772	0.0338885	5302
108.0	1.7919	0.0328693	7701	106.0	8.0304	0.0338166	5303
110.0	4.4111	0.0327978	7702	108.0	10.7372	0.0337455	5304
112.0	6.9761	0.0327302	7703	110.0	13.4307	0.0336756	5305
114.0	9.5060	0.0326645	7704	112.0	16.0496	0.0336088	5306
116.0	12.0031	0.0326001	7705	112.0	16.0483	0.0336092	5306
118.0	14.4653	0.0325375	7706	114.0	18.6581	0.0335444	5307
120.0	16.9084	0.0324767	7707	116.0	21.2724	0.0334816	5308
122.0	19.3194	0.0324183	7708	118.0	23.8799	0.0334216	5309
124.0	21.7076	0.0323618	7709	120.0	26.4646	0.0333652	5310
126.0	24.1061	0.0323079	7710	122.0	29.0434	0.0333119	5311
128.0	26.4967	0.0322573	7711	124.0	31.6233	0.0332627	5312
130.0	28.8700	0.0322077	7712				
132.0	31.2479	0.0321626	7713	100.0	0.7417	0.0341475	5401
134.0	33.6213	0.0321216	7714	102.0	3.6253	0.0340649	5402
				104.0	6.4406	0.0339892	5403
108.0	3.1007	0.0330134	4101	106.0	9.1978	0.0339171	5404
110.0	5.7025	0.0329415	4102	108.0	11.9114	0.0338463	5405
112.0	8.2546	0.0328722	4103	110.0	14.5967	0.0337775	5406
114.0	10.7654	0.0328050	4104	112.0	17.2500	0.0337109	5407
116.0	13.2418	0.0327392	4105	114.0	19.8976	0.0336463	5408
118.0	15.7200	0.0326761	4106	114.0	19.9333	0.0336478	5408
120.0	18.1513	0.0326184	4107	116.0	22.5629	0.0335864	5409
122.0	20.5679	0.0325543	4108	118.0	25.1980	0.0335279	5410
124.0	22.9783	0.0324967	4109	120.0	27.8054	0.0334726	5411
126.0	25.3676	0.0324421	4110	122.0	30.4268	0.0334209	5412
128.0	27.7500	0.0323901	4111	124.0	33.0483	0.0333729	5413
130.0	30.1463	0.0323410	4112				
132.0	32.5168	0.0322954	4113	99.0	1.6534	0.0343798	5500
				100.0	3.1209	0.0343387	5501
104.0	0.6819	0.0334558	7901	102.0	6.0143	0.0342606	5502
106.0	3.4351	0.0333777	7902	104.0	8.8357	0.0341871	5503
108.0	6.1367	0.0333056	7903	106.0	11.6386	0.0341151	5504
110.0	8.7923	0.0332370	7904	108.0	14.3917	0.0340449	5505
112.0	11.4019	0.0331694	7905	110.0	17.1172	0.0339769	5506
114.0	13.9827	0.0331042	7906	112.0	19.8187	0.0339113	5507
116.0	16.5276	0.0330397	7907	114.0	22.5087	0.0338491	5508

TABLE 2. *Temperature-pressure-density observations on oxygen.*—Continued

T K	P MN/m²	Density mol/cm³	Ident	T K	P MN/m²	Density mol/cm³	Ident
116.0	25.2057	0.0337891	5509	112.0	28.6413	0.0345593	6910
118.0	27.8901	0.0337326	5510	114.0	31.5159	0.0345044	6911
98.0	1.8866	0.0345541	7001	94.0	3.6749	0.0353210	4201
100.0	4.8696	0.0344737	7002	96.0	6.7597	0.0352370	4202
102.0	7.7887	0.0343977	7003	98.0	9.7756	0.0351563	4203
104.0	10.6519	0.0343240	7004	100.0	12.7369	0.0350779	4204
106.0	13.4715	0.0342521	7005	102.0	15.6649	0.0350015	4205
108.0	16.2612	0.0341824	7006	104.0	18.5748	0.0349277	4206
110.0	19.0241	0.0341152	7007	106.0	21.4663	0.0348569	4207
112.0	21.7870	0.0340507	7008	108.0	24.3527	0.0347893	4208
114.0	24.5320	0.0339893	7009	110.0	27.2442	0.0347258	4209
116.0	27.2792	0.0339315	7010	112.0	30.1416	0.0346662	4210
118.0	30.0073	0.0338777	7011	114.0	33.0409	0.0346116	4211
120.0	32.7273	0.0338276	7012				
				90.0	0.5790	0.0357295	4601
98.0	2.3008	0.0345829	11001	92.0	3.7985	0.0356349	4602
100.0	5.6357	0.0345341	11002	94.0	6.9363	0.0355490	4603
102.0	8.9409	0.0344906	11003	96.0	9.9960	0.0354662	4604
104.0	12.2000	0.0344479	11004	98.0	13.0042	0.0353856	4605
106.0	15.3871	0.0344073	11005	100.0	15.9823	0.0353080	4606
108.0	18.5961	0.0343677	11006	102.0	18.9273	0.0352328	4607
110.0	21.7798	0.0343303	11007	104.0	21.8793	0.0351603	4608
				106.0	24.8244	0.0350914	4609
98.0	4.6684	0.0347714	6801	108.0	27.7800	0.0350264	4610
100.0	7.6506	0.0346931	6802	110.0	30.7253	0.0349663	4611
102.0	10.5760	0.0346172	6803				
104.0	13.4535	0.0345432	6804	90.0	2.1354	0.0358257	7101
106.0	16.2991	0.0344715	6805	92.0	5.4112	0.0357379	7102
108.0	19.1240	0.0344024	6806	94.0	8.6090	0.0356560	7103
110.0	21.9346	0.0343363	6807	96.0	11.7449	0.0355756	7104
112.0	24.7305	0.0342735	6808	98.0	14.8297	0.0354978	7105
114.0	27.5177	0.0342143	6809	100.0	17.8893	0.0354226	7106
116.0	30.3147	0.0341590	6810	102.0	20.9328	0.0353505	7107
118.0	33.1174	0.0341080	6811	104.0	23.9672	0.0352820	7108
				106.0	27.0073	0.0352176	7109
96.0	3.5267	0.0350023	7201	108.0	30.0554	0.0351578	7110
98.0	6.5819	0.0349220	7202	110.0	33.0707	0.0351031	7111
100.0	9.5691	0.0348452	7203				
102.0	12.4989	0.0347704	7204	88.0	1.1986	0.0360762	4801
104.0	15.3955	0.0346975	7205	90.0	4.4953	0.0359820	4802
106.0	18.2560	0.0346272	7206	92.0	7.6900	0.0358952	4803
108.0	21.0983	0.0345598	7207	94.0	10.8170	0.0358109	4804
110.0	23.9336	0.0344954	7208	96.0	13.8938	0.0357292	4805
112.0	26.7622	0.0344345	7209	98.0	16.9363	0.0356499	4806
114.0	29.5901	0.0343775	7210	100.0	19.9936	0.0355740	4807
116.0	32.4298	0.0343246	7211	102.0	23.0452	0.0355010	4808
				104.0	26.0566	0.0354331	4809
94.0	2.0325	0.0352031	6901	106.0	29.0753	0.0353689	4810
96.0	5.1647	0.0351187	6902	108.0	32.1434	0.0353088	4811
98.0	8.2265	0.0350409	6903				
100.0	11.2273	0.0349642	6904	88.0	3.7829	0.0362485	3801
102.0	14.1864	0.0348896	6905	90.0	7.0649	0.0361587	3802
104.0	17.1083	0.0348172	6906	92.0	10.2597	0.0360721	3803
106.0	20.0017	0.0347479	6907	94.0	13.3723	0.0359887	3804
108.0	22.8816	0.0346816	6908	96.0	16.4770	0.0359072	3805
110.0	25.7600	0.0346187	6909	98.0	19.5564	0.0358288	3806
				100.0	22.6519	0.0357533	3807

TABLE 2. *Temperature-pressure-density observations on oxygen.*—Continued

T K	P MN/m²	Density mol/cm³	Ident	T K	P MN/m²	Density mol/cm³	Ident
102.0	25.7577	0.0356832	3808	84.0	3.5900	0.0368114	5701
104.0	28.8557	0.0356166	3809	86.0	7.0633	0.0367205	5702
106.0	31.9572	0.0355554	3810	88.0	10.4638	0.0366324	5703
				90.0	13.7910	0.0365473	5704
86.0	2.5495	0.0364373	5101	92.0	17.0873	0.0364644	5705
88.0	5.9034	0.0363448	5102	94.0	20.3732	0.0363856	5706
90.0	9.1630	0.0362568	5103	96.0	23.6500	0.0363098	5707
92.0	12.3548	0.0361711	5104	98.0	26.9280	0.0362393	5708
94.0	15.5098	0.0360881	5105	100.0	30.2151	0.0361737	5709
96.0	18.6580	0.0360082	5106	102.0	33.5198	0.0361140	5710
98.0	21.7512	0.0359313	5107				
98.0	21.7694	0.0359315	5107	84.0	3.8384	0.0368285	4901
100.0	24.9373	0.0358575	5108	86.0	7.2501	0.0367359	4902
102.0	28.0181	0.0357899	5109	88.0	10.5740	0.0366462	4903
104.0	31.2240	0.0357250	5110	90.0	13.8416	0.0365592	4904
				92.0	17.0941	0.0364749	4905
86.0	2.1952	0.0364340	7401	94.0	20.3134	0.0363949	4906
88.0	5.6350	0.0363425	7402	96.0	23.5705	0.0363178	4907
90.0	8.9713	0.0362567	7403	98.0	26.8186	0.0362451	4908
92.0	12.2324	0.0361731	7404	100.0	30.0772	0.0361775	4909
94.0	15.4555	0.0360921	7405	102.0	33.3393	0.0361160	4910
96.0	18.6461	0.0360142	7406				
98.0	21.8211	0.0359398	7407	84.0	3.8882	0.0368308	7301
100.0	24.9894	0.0358695	7408	86.0	7.3692	0.0367405	7302
102.0	28.1582	0.0358035	7409	88.0	10.7646	0.0366530	7303
104.0	31.3296	0.0357426	7410	90.0	14.1014	0.0365684	7304
				92.0	17.3952	0.0364875	7305
86.0	2.4864	0.0364717	4501	94.0	20.6605	0.0364088	7306
88.0	5.8392	0.0363791	4502	96.0	23.9280	0.0363345	7307
90.0	9.0913	0.0362913	4503	98.0	27.1992	0.0362646	7308
92.0	12.2843	0.0362055	4504	100.0	30.4830	0.0361999	7309
94.0	15.4423	0.0361222	4505	102.0	33.7693	0.0361410	7310
96.0	18.5601	0.0360428	4506				
98.0	21.6686	0.0359648	4507	82.0	2.8589	0.0370683	3701
100.0	24.7791	0.0358919	4508	84.0	6.3331	0.0369734	3702
102.0	27.8932	0.0358232	4509	86.0	9.7564	0.0368824	3703
				88.0	13.0916	0.0367940	3704
86.0	4.0717	0.0365538	11601	90.0	16.4016	0.0367082	3705
86.0	4.0742	0.0365538	11601	92.0	19.6937	0.0366255	3706
88.0	8.0270	0.0365007	11602	94.0	22.9780	0.0365468	3707
90.0	11.9176	0.0364498	11603	96.0	26.2652	0.0364725	3708
92.0	15.7524	0.0364013	11604	98.0	29.5698	0.0364032	3709
94.0	19.5665	0.0363550	11605	100.0	32.8893	0.0363398	3710
96.0	23.3657	0.0363112	11606				
98.0	27.1523	0.0362700	11607				
100.0	30.9404	0.0362326	11608	84.0	7.7004	0.0370189	5001
102.0	34.7284	0.0361989	11609	86.0	11.0964	0.0369277	5002
				88.0	14.4374	0.0368397	5003
84.0	1.1839	0.0366764	6601	90.0	17.7589	0.0367543	5004
86.0	4.6859	0.0365818	6602	92.0	21.0792	0.0366723	5005
88.0	8.1053	0.0364940	6603	94.0	24.3975	0.0365946	5006
90.0	11.4530	0.0364085	6604	96.0	27.7112	0.0365219	5007
92.0	14.7392	0.0363259	6605	98.0	31.0432	0.0364546	5008
94.0	17.9906	0.0362463	6606	100.0	34.3986	0.0363933	5009
96.0	21.2208	0.0361700	6607				
98.0	24.4510	0.0360977	6608	80.0	2.9120	0.0373729	4701
100.0	27.6686	0.0360301	6609	82.0	6.4557	0.0372762	4702
102.0	30.9163	0.0359673	6610	84.0	9.9139	0.0371829	4703
104.0	34.1576	0.0359101	6611	86.0	13.3193	0.0370923	4704

TABLE 2. *Temperature-pressure-density observations on oxygen.*—Continued

T K	P MN/m²	Density mol/cm³	Ident	T K	P MN/m²	Density mol/cm³	Ident
88.0	16.6838	0.0370047	4705	86.0	20.0777	0.0374369	12005
90.0	20.0421	0.0369203	4706	88.0	24.2731	0.0373892	12006
90.0	20.0658	0.0369214	4706	90.0	28.4721	0.0373447	12007
92.0	23.4213	0.0368414	4707	92.0	32.6712	0.0373049	12008
94.0	26.8034	0.0367658	4708				
96.0	30.1975	0.0366956	4709	76.0	2.4072	0.0379133	12501
98.0	33.6100	0.0366321	4710	78.0	6.8711	0.0378520	12502
				80.0	11.2315	0.0377948	12503
82.0	3.6237	0.0371162	11101	82.0	15.5493	0.0377403	12504
84.0	7.8486	0.0370596	11102	84.0	19.8582	0.0376882	12505
86.0	11.9380	0.0370062	11103	86.0	24.1591	0.0376391	12506
88.0	15.9849	0.0369553	11104	88.0	28.4717	0.0375940	12507
90.0	20.0043	0.0369079	11105	90.0	32.7823	0.0375534	12508
92.0	24.0034	0.0368617	11106				
94.0	28.0024	0.0368196	11107	76.0	4.0138	0.0379820	11801
96.0	31.9946	0.0367814	11108	78.0	8.4856	0.0379228	11802
				80.0	12.8759	0.0378659	11803
80.0	2.5494	0.0373439	11301	82.0	17.2191	0.0378119	11804
82.0	6.8412	0.0372846	11302	84.0	21.5454	0.0377607	11805
84.0	11.0122	0.0372297	11303	86.0	25.8751	0.0377125	11806
86.0	15.1259	0.0371773	11304	88.0	30.2153	0.0376688	11807
88.0	19.2156	0.0371273	11305	90.0	34.5593	0.0376299	11808
90.0	23.3042	0.0370801	11306				
92.0	27.3871	0.0370368	11307	74.0	3.3886	0.0382372	11201
94.0	31.4658	0.0369970	11308	76.0	7.9765	0.0381756	11202
				78.0	12.4678	0.0381172	11203
80.0	4.7682	0.0374570	11401	80.0	16.9121	0.0380619	11204
82.0	9.0390	0.0374008	11402	82.0	21.3359	0.0380093	11205
84.0	13.2375	0.0373466	11403	84.0	25.7713	0.0379602	11206
86.0	17.4016	0.0372953	11404	86.0	30.2058	0.0379156	11207
88.0	21.5532	0.0372464	11405	88.0	34.6623	0.0378759	11208
90.0	25.6953	0.0372011	11406				
92.0	29.8415	0.0371593	11407	74.0	3.9031	0.0382532	11901
94.0	33.9782	0.0371218	11408	76.0	8.5252	0.0381918	11902
				78.0	13.0201	0.0381335	11903
79.0	3.0352	0.0375170	10901	80.0	17.4597	0.0380783	11904
80.0	5.2592	0.0374867	10902	82.0	21.8961	0.0380259	11905
82.0	9.5525	0.0374315	10903	84.0	26.3326	0.0379773	11906
84.0	13.7847	0.0373783	10904	86.0	30.7832	0.0379331	11907
86.0	17.9590	0.0373281	10905	88.0	35.2581	0.0378937	11908
88.0	22.1268	0.0372804	10906				
90.0	26.2913	0.0372360	10907	72.0	2.5060	0.0384810	12401
92.0	30.4444	0.0371957	10908	74.0	7.1914	0.0384173	12402
94.0	34.6000	0.0371595	10909	76.0	11.7895	0.0383572	12403
				78.0	16.3164	0.0383004	12404
78.0	1.6179	0.0375849	11701	80.0	20.8216	0.0382466	12405
80.0	6.0004	0.0375223	11702	82.0	25.3408	0.0381963	12406
82.0	10.2597	0.0374663	11703	84.0	29.8739	0.0381504	12407
84.0	14.4605	0.0374126	11704	86.0	34.4176	0.0381095	12408
86.0	18.6351	0.0373613	11705				
88.0	22.8052	0.0373124	11706	70.0	1.9433	0.0387405	12601
90.0	26.9628	0.0372679	11707	72.0	6.7402	0.0386743	12602
92.0	31.1310	0.0372269	11708	74.0	11.4313	0.0386129	12603
				76.0	16.0558	0.0385548	12604
78.0	3.0283	0.0376563	12001	78.0	20.6678	0.0384996	12605
80.0	7.3749	0.0375973	12002	80.0	25.2822	0.0384482	12606
82.0	11.6562	0.0375411	12003	82.0	29.9312	0.0384011	12607
84.0	15.8755	0.0374877	12004	84.0	34.5863	0.0383594	12608

TABLE 2. *Temperature-pressure-density observations on oxygen.*—Continued

T K	P MN/m²	Density mol/cm³	Ident	T K	P MN/m²	Density mol/cm³	Ident
68.0	2.0696	0.0390250	12701	60.0	13.7153	0.0405578	13503
70.0	6.9852	0.0389576	12702	62.0	19.2048	0.0404909	13504
72.0	11.7921	0.0388945	12703	64.0	24.7113	0.0404287	13505
74.0	16.5223	0.0388352	12704	66.0	30.2676	0.0403725	13506
76.0	21.2456	0.0387790	12705	68.0	35.8689	0.0403239	13507
78.0	25.9818	0.0387267	12706				
80.0	30.7343	0.0386793	12707	56.0	7.9532	0.0408851	13601
82.0	35.5145	0.0386375	12708	58.0	13.5708	0.0408129	13602
				60.0	19.1563	0.0407448	13603
66.0	1.8168	0.0392920	12801	62.0	24.7914	0.0406812	13604
68.0	6.8449	0.0392227	12802	64.0	30.4853	0.0406240	13605
70.0	11.7582	0.0391582	12803	66.0	36.2267	0.0405746	13606
72.0	16.6110	0.0390975	12804				
74.0	21.4597	0.0390399	12805	56.0	10.4922	0.0409650	13701
76.0	26.3164	0.0389866	12806	58.0	16.1270	0.0408944	13702
78.0	31.1907	0.0389391	12807	60.0	21.8078	0.0408273	13703
80.0	36.0790	0.0388971	12808	62.0	27.5211	0.0407659	13704
				64.0	33.2989	0.0407117	13705
64.0	2.2554	0.0395872	12901				
66.0	7.4132	0.0395174	12902				
68.0	12.4516	0.0394518	12903	54.5	1.3028		13201
70.0	17.4275	0.0393900	12904	55.0	5.6750		13202
72.0	22.4034	0.0393318	12905	55.5	10.0802		13203
74.0	27.3975	0.0392782	12906	56.0	14.3361	0.0410947	13204
76.0	32.4068	0.0392303	12907	58.0	20.0847	0.0410255	13205
				60.0	25.8750	0.0409613	13206
62.0	1.4944	0.0398369	13001	62.0	31.7297	0.0409040	13207
64.0	6.7815	0.0397637	13002				
66.0	11.9273	0.0396963	13003	54.5	1.2974		13302
68.0	17.0229	0.0396332	13004	54.6	2.1701		13303
70.0	22.0984	0.0395735	13005	54.7	3.0519		13304
72.0	27.1927	0.0395188	13006	54.8	3.9222		13305
74.0	32.3081	0.0394700	13007	54.9	4.7926		13306
				55.0	5.6718		13307
60.0	2.2489	0.0401416	13101	55.1	6.5512		13308
62.0	7.6364	0.0400686	13102	55.2	7.4260		13309
64.0	12.8871	0.0400007	13103	55.3	8.3066		13310
66.0	18.1156	0.0399367	13104	55.4	9.1872		13311
68.0	23.3568	0.0398767	13105	55.5	10.0759		13312
70.0	28.6098	0.0398218	13106	55.6	10.9541		13313
72.0	33.9010	0.0397732	13107	55.7	11.8427		13314
				55.8	12.7347		13315
58.0	3.3328	0.0404544	13401	55.9	13.6302		13316
60.0	8.8263	0.0403815	13402	56.0	14.5154		13317
62.0	14.2016	0.0403132	13403	56.1	15.4029		13318
64.0	19.5644	0.0402476	13404	56.2	16.2890		13319
66.0	24.9459	0.0401870	13405	56.3	16.5715	0.0411341	13320
68.0	30.3712	0.0401322	13406	56.4	16.8619	0.0411309	13321
70.0	35.8335	0.0400846	13407	57.0	18.5956	0.0411097	13322
				58.0	21.4877	0.0410759	13323
56.0	2.6086	0.0407032	13501	60.0	27.3250	0.0410127	13324
58.0	8.2297	0.0406280	13502	62.0	33.2259	0.0409570	13325

TABLE 3. *Comparison of vapor pressure data with equation (7)*

Temp	P_{exp}	$P_{exp}-P_{eq(7)}$
K	*MN/m²*	*MN/m²*
114.0	0.7088	0.0000
116.0	.8039	.0000
118.0	.9082	.0001
122.0	1.1451	.0001
126.0	1.4234	−.0002
138.0	2.5500	−.0003
139.0	2.6669	.0003
139.1	2.6787	.0003
139.2	2.6906	.0003
139.3	2.7026	.0004
139.4	2.7146	.0005
140.0	2.7863	−.0002
142.0	3.0380	−.0003
142.0	3.0386	.0003
146.0	3.5910	−.0008
154.0	4.9321	.0001
154.0	4.9320	.0000
154.1	4.9504	−.0006
154.2	4.9697	−.0005
154.3	4.9885	−.0008

2.3. Representation of the Data

a. Representation of Experimental Data

The purpose of the present calculations is the determination of the derived properties in the best possible way. Therefore no attempt was made to fit all the data with one wide-range equation of state. Instead the data were divided into three regions and the data in each region were smoothed and interpolated by the means which seemed most appropriate. These regions are illustrated in figure 2 and are considered separately below.

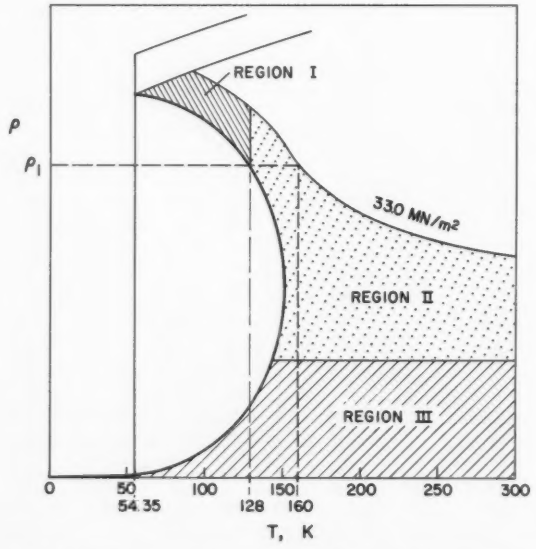

FIGURE 2. *Temperature–density phase diagram showing regions for thermodynamic computations.*

In all of the curve fitting the data were weighted in a manner appropriate to the expected uncertainties in the variables involved. In some cases curves were constrained to pass through a given point or to have a particular value of a derivative at a given point. For details of this technique see Hust and McCarty [12].

Low Density Gas.—At densities of 0.006709 mol/cm³ and less (Region III in fig. 2) the data were represented with a virial surface,

$$P=RT[\rho+B(T)\rho^2+C(T)\rho^3]. \tag{2}$$

The second and third virial coefficients were expressed as a function of temperature of the form

$$B(T)=\sum_{J=1}^{5}A_J T^{(1-J)/4} \tag{3a}$$

$$C(T)=\sum_{J=1}^{6}A_J T^{(1-J)/2}. \tag{3b}$$

The parameters used in eqs (3a) and (3b) are given in table 4. In addition to 296 P–V–T data points, 14 experimental C_v data points [6] between 150 K and 300 K, were included as data in fitting the surface. The average deviation of the calculated heat capacities is 1.36 percent, approximately equivalent to the uncertainties in the experimental points. Between 150 K and 300 K the standard deviation of the P–V–T points is 0.048 percent in density. At temperatures below 150 K the data of Series IV show an average deviation of 0.12 percent in density which is systematic and which becomes worse with decreasing temperature. These data carried relatively low weighting, and it is expected that eqs (2, 3a, 3b) represent the best approximation to the P–V–T surface at low temperatures. One possible explanation for this discrepancy would be physical adsorption on the walls of the sample holder. It is more likely, however, that we are seeing small systematic errors in the pressure measurements. The virial coefficients, calculated by means of eqs (3a) and (3b) are tabulated in table 5. The columns labeled "ISOTHERM" contain the results obtained by fitting equation (2) to the data along individual isotherms.

High Density Liquid.—The high density compressed liquid, (Region I, fig. 2), bounded by the melting curve, vapor pressure curve, 33 MN/m² isobar, and the 128 K isotherm, was represented by a 12 parameter empirical surface given by eq (4):

$$P=RT\rho+(A_1+A_2T+A_3T^2)+(A_4+A_5T+A_6T^2+A_7T^3)\rho+(A_8+A_9T+A_{10}T^2)\rho^2+(A_{11}+A_{12}T)\rho^3. \tag{4}$$

The values of the parameters are given in table 4. The surface was constrained to a value of 0.02869 mol/cm³ for the density of the saturated liquid at 128 K. The 557 experimental points in this region exhibited a standard deviation from the surface of 0.024 percent in density.

TABLE 4. *Parameter values for the various equations*

	Eq (3a)	Eq (3b)	Eq (4)	Eq (7)	Eq (13)	Eq (14)	Eq (9)	Eq (11)
A_1	$-1.5226420059 \times 10^3$	3.3711154314×10^5	-1.641561252×10^3	-64.8861406	2.105614214×10^2	$-3.222372953 \times 10^{-1}$	0.01363	1.81187
A_2	2.7768311172×10^4	$-2.5369852041 \times 10^7$	1.147287363×10^1	2.47450429	3.741590387×10^1	1.727532883×10^2	$6.02582799 \times 10^{-5}$	2.77986×10^{-1}
A_3	$-1.8606884996 \times 10^5$	7.6407469222×10^8	$-1.893991658 \times 10^{-2}$	$-4.68973315 \times 10^{-2}$	$-8.007073541 \times 10^{-2}$	-2.255944223×10^4	$1.00932845 \times 10^{-7}$	-7.60653×10^{-1}
A_4	5.5834774260×10^5	$-1.1480733696 \times 10^{10}$	1.855069328×10^5	$5.48202337 \times 10^{-4}$	$-2.742842302 \times 10^{-4}$	1.171338217×10^6		
A_5	$-6.5056457930 \times 10^5$	$8.6044663037 \times 10^{10}$	-1.163758279×10^3	$-4.09349868 \times 10^{-6}$				
A_6		$-2.5679270159 \times 10^{11}$	1.470658133	$1.91471914 \times 10^{-8}$				
A_7			$5.082303291 \times 10^{-4}$	$-5.13113688 \times 10^{-11}$				
A_8			-6.905607063×10^6	$6.02656934 \times 10^{-14}$				
A_9			3.696268789×10^4					
A_{10}			-3.493447874×10^1					
A_{11}			7.817570089×10^7					
A_{12}			-2.981428648×10^5					

Intermediate Densities.—The data in Region II of figure 2 were approximated by 35 isotherm polynomials of the form

$$P = RT\rho + \sum_{J=1}^{N} A_J \rho^{(J-1)}, \qquad (5)$$

$$A_1 = A_2 = 0 \text{ for } T > T_c.$$

The number of coefficients used varied from four at 128 K and at 300 K to a maximum of fourteen for the 156 K isotherm. The standard deviations of the 650 data points averaged about 0.02 percent in density for the various isotherms.

Melting Curve.—Experimental runs #132 and #133 included 21 values of the melting pressure at 0.1 K intervals. The measured pressures varied from 1.2 to 16 MN/m². These data were fitted with the Simon melting equation in the form

$$P = P_t + P_o[(T/T_t)^c - 1], \qquad (6)$$

with c and T_t being varied to obtain the best fit. The first row of table 6 gives the set of parameters obtained with σ being the standard deviation of the fit in MN/m². The value obtained for T_t, 54.3507 ±0.0010 K, will be used here as the best value for the triple point temperature.

The second row of table 6 shows the fit of eq (6), with the value of T_t obtained above, to the data of Mills and Grilly [13]. These data are less precise but extend in pressure from 36 to 350 MN/m². The third row of table 6 gives the parameters obtained by fitting eq (6) to both sets of data, using a relative weighting equal to $1/\sigma^2$. Table 7 illustrates this last fit.

b. Additional Data Used

Certain data from other sources were used as supplemental information for these calculations. Vapor pressures used here are based on the data of Hoge [10]. These were published in analytical form by Stewart [11], whose equation is reproduced here for convenience.

$$\ln P(\text{MN/m}^2) = A_1 + A_2T + A_3T^2 + A_4T^3 + A_5T^4 + A_6T^5 + A_7T^6 + A_8T^7. \qquad (7)$$

Values of the coefficients for eq (7) are given in table 4.

The critical temperature, 154.576 ± 0.01 K on the IPTS 1948, is taken from [14]. Densities of saturated liquid and vapor in the critical region are difficult

TABLE 5. *The second and third virial coefficients.*

Units are (cm^3/mol) and $(cm^3/mol)^2$ respectively. The quantities δB and δC are the estimated uncertainties.

Temp K	Second virial		δB	Third virial		δC
	Eq (3)	Isotherm		Eq (3)	Isotherm	
85	−267.78		30.	−21462		15000
90	−240.67			−12764		
95	−217.51			−7058		
100	−197.54		15.	−3326		4000
105	−180.20			−904		
110	−165.05			644		
115	−151.71			1609		
120	−139.91		5.	2187		1000
125	−129.41			2507		
130	−120.02			2659		
135	−111.59			2702		
140	−103.98		1.	2677		100
145	−97.08			2611		
150	−90.81	−90.81	0.25	2522	2515	40
155	−85.09			2423		
160	−79.84	−79.85	0.25	2320	2322	30
165	−75.02	−74.99		2219	2213	
170	−70.58	−70.50		2122	2107	
175	−66.48	−66.38		2031	2014	
180	−62.67	−62.58		1948	1932	
185	−59.14	−59.03		1871	1853	
190	−55.85	−55.74		1801	1784	
195	−52.77	−52.67		1738	1722	
200	−49.89	−49.80	0.30	1680	1666	30
205	−47.20			1628		
210	−44.66	−44.59		1580	1570	
215	−42.27			1537		
220	−40.02	−39.98		1498	1490	
225	−37.90			1461		
230	−35.89	−35.87		1428	1424	
235	−33.98			1397		
240	−32.17	−32.18		1368	1369	
245	−30.45			1342		
250	−28.81	−28.85		1317	1322	
255	−27.25			1294		
260	−25.77	−25.81		1273	1280	
265	−24.34			1253		
270	−22.98	−23.04		1234	1243	
275	−21.68			1217		
280	−20.44	−20.51		1201	1213	
285	−19.24			1186		
290	−18.09	−18.13		1172	1179	
295	−16.98			1160		
300	−15.92	−16.01	0.30	1149	1162	30

TABLE 6. *Parameters for the Simon melting equation for oxygen*

Data used	P_0	c	T_t	σ, MN/m²
This data only	266.27	1.775	54.3507	0.0041
Data of Mills and Grilly [13]	270.1	1.754	54.3507	.51
Both sets of data	267.21	1.769	54.3507	

to derive from PVT data and were also taken from [14]. These densities appear in the center section of table 8. The critical pressure, P_c, was calculated from (7) at the critical temperature. The thermodynamic properties calculations are based on the thermo-

TABLE 7. *Fit of the Simon equation to melting curve data*

Data in lower part are from [13].

T K	P_{exp} MN/m²	P_{calc} MN/m²	Diff MN/m²
54.50	1.303	1.300	−0.003
54.50	1.297	1.300	.003
54.60	2.170	2.172	.002
54.70	3.052	3.045	−.007
54.80	3.922	3.920	−.002
54.90	4.793	4.796	.003
55.00	5.675	5.673	−.002
55.00	5.672	5.673	.001
55.10	6.551	6.551	.000
55.20	7.426	7.431	.005
55.30	8.307	8.311	.004
55.40	9.187	9.193	.006
55.50	10.080	10.076	−.004
55.50	10.076	10.076	.000
55.60	10.954	10.961	.007
55.70	11.843	11.847	.004
55.80	12.735	12.733	−.002
55.90	13.630	13.621	−.009
56.00	14.515	14.511	−.004
56.10	15.403	15.401	−.002
56.20	16.289	16.293	.004
58.57	37.399	37.783	.384
59.79	49.386	49.111	−.275
61.92	70.036	69.317	−.719
63.93	88.781	88.881	.100
65.79	106.938	107.413	.475
67.85	128.956	128.411	−.545
69.92	150.964	150.012	−.952
71.96	172.212	171.786	−.426
74.40	199.033	198.459	−.574
76.54	223.067	222.414	−.653
77.06	227.971	228.313	.342
79.03	250.303	250.942	.639
81.04	274.814	274.481	−.333
83.39	301.594	302.576	.982
85.33	325.963	326.233	.270
87.31	351.162	350.809	−.353

dynamic functions of the ideal gas calculated by Woolley [5].

c. Derived Data

The representations of the experimental data, in the previous section, allow us to derive other useful properties.

Isochores.—In the calculation of most of the thermodynamic properties the quantities $(\partial P/\partial T)_\rho$ and $(\partial^2 P/\partial T^2)_\rho$ are needed. In Regions I and III of figure 2 these quantities are calculated from the analytic surfaces. In Region II the isotherm polynomials were used to calculate pressures at even increments of density. The pressure-temperature pairs (true isochores) thus obtained were fitted using functions of the form

$$P = \sum_{J=1}^{N} A_J T^{(3-2J)}. \tag{8}$$

A density increment of 0.0005 mol/cm³ was used. The number of terms used in eq (8) varied between 6

at the lowest densities and 3 at the highest. Between the densities 0.0290 and 0.0330 mol/cm³ the isochores were constrained to have their second derivatives, $(\partial^2 P/\partial T^2)_\rho$, match those calculated by the liquid surface, eq (4), at 128 K.

Two-Phase Boundaries.—Derived "experimental" densities of the saturated liquid and saturated vapor may be found from the intersections of the experimental isochores with the vapor pressure curve eq (7). The first several points of an experimental run are fitted with a low order polynomial, $P=P(T)$, either a quadratic or cubic. The expected uncertainty in this temperature of intersection may be calculated from the estimated uncertainty in the vapor pressure, the slopes of the two curves, quality of the fit of the polynomial, the temperature range over which the fit was made, and the length of the extrapolation to the intersection temperature. This procedure was applied to the experimental runs, and the calculated uncertainties varied from 1 millidegree in the best cases to 100 millidegrees near the critical point where the isochores and the vapor pressure curve are almost colinear.

The densities of the saturated liquid were found in this way, between 120 K and 150 K, and were smoothed and interpolated by means of a 7-term polynomial. For the saturated vapor over the same temperature range the number of experimental runs proved to be too small for this technique to be applied with good results. Therefore, the vapor densities were found from the intersection of the virial surface, eq (2), with the vapor pressure curve. The saturation densities thus obtained were computed at 1 K intervals and averaged to obtain the rectilinear diameter,

$$\rho_{RD}=\tfrac{1}{2}(\rho_{\text{sat }L}+\rho_{\text{sat }G}).$$

The resulting rectilinear diameter was fitted by means of a function of the form,

$$\rho_{RD}=A_1+A_2(T_c-T)+A_3(T_c-T)^2 \qquad (9)$$

with an average deviation of 2×10^{-6} mol/cm³. From eq (9), a value of 0.01363 mol/cm³ was obtained for the critical density, A_1. Values of the other parameters are given in table 4.

The isochore-vapor pressure intersection temperatures were considered unreliable above about 152 K because of the small angle of intersection. Densities calculated from the dielectric measurements of [14]. were used in the temperature range 150 K to T_c.

All of the saturation densities, ρ_{sat}, both liquid and vapor, were fitted with a function of the form

$$|\rho_{\text{sat}}-\rho_{RD}|=\sum_{J=1}^{3} A_J\left(\frac{T_c-T}{T_c}\right)^{(2J-1)\beta} \qquad (10)$$

with $\beta=0.353$. The fit of eq (10) is illustrated in table 8, where ΔT_{est} is the uncertainty in the intersection temperature, calculated as indicated above, and ΔT_{calc} is found from $|\rho_{\text{exp}}-\rho_{\text{calc}}|/|d\rho/dT|$.

TABLE 8. *Fit of the derived saturation density data*

Data in center section are dielectric measurements from [14]. Above the line—vapor, below—liquid.

ID	Temp. K	Density exp mol/cm³	Density calc mol/cm³	Diff. %	Delta T		Relative weight
					calc[a] K	est K	
121	138.573	0.003374	0.003376	0.07	0.013	0.005	1060
104	146.387	.005258	.005265	0.14	.023	.008	726.4
103	147.512	.005656	.005652	−.07	.011	.020	209.8
102	149.463	.006454	.006451	−.05	.007	.012	334.0
101	150.379	.006888	.006905	.25	.033	.014	217.4
100	152.695	.008478	.008505	.31	.029	.021	41.10
	150.000	.006716	.006709	−.10	.013	.000	474.7
	153.000	.008815	.008806	−.09	.008	.000	1844
	153.500	.009410	.009401	−.09	.006	.000	469.6
	153.600	.009544	.009541	−.03	.002	.000	468.8
	154.000	.010213	.010226	.13	.006	.000	462.3
	154.100	.010441	.010445	.04	.002	.000	458.8
	154.101	.010444	.010447	.03	.001	.000	458.7
	154.200	.010694	.010697	.02	.001	.000	453.1
	154.300	.010994	.010997	.03	.001	.000	204.6
	154.397	.011357	.011368	.10	.003	.000	199.9
	154.490	.011885	.011882	−.02	.000	.000	356.5
	154.500	.011904	.011956	.44	.007	.000	29.02
	154.510	.012025	.012037	.10	.001	.000	174.9
	154.523	.012182	.012156	−.21	.003	.000	49.42
	154.540	.012338	.012344	.05	.000	.000	65.35
	154.544	.012416	.012396	−.16	.001	.000	27.66
	154.546	.012450	.012424	−.22	.002	.000	35.10
	154.560	.012591	.012664	.58	.004	.000	8.40
	154.566	.012875	.012811	−.50	.002	.000	2.06
	154.566	.012763	.012811	.38	.002	.000	2.06

367-409 OL-70—8

TABLE 8. *Fit of the derived saturation density data* — Continued

Data in center section are dielectric measurements from [14]. Above the line — vapor, below — liquid.

ID	Temp. K	Density exp mol/cm³	Density calc mol/cm³	Diff. %	Delta T		Relative weight
					calc[a] K	est K	
	154.566	.014457	.014452	−.03	.000	.000	2.06
	154.566	.014429	.014452	.16	.001	.000	2.06
	154.560	.014551	.014600	.34	.002	.000	8.04
	154.546	.014819	.014842	.15	.002	.000	35.10
	154.544	.014869	.014870	.00	.000	.000	35.37
	154.540	.014932	.014923	−.06	.001	.000	65.35
	154.523	.015126	.015113	−.09	.001	.000	49.42
	154.510	.015241	.015233	−.06	.001	.000	174.9
	154.500	.015304	.015315	.07	.001	.000	29.02
	154.490	.015401	.015390	−.07	.001	.000	356.5
	154.397	.015926	.015915	−.06	.002	.000	199.9
	154.300	.016285	.016298	.08	.004	.000	204.6
	154.200	.016616	.016611	−.03	.002	.000	453.1
	154.101	.016863	.016872	.05	.004	.000	458.7
	154.100	.016882	.016875	−.04	.003	.000	458.8
	154.000	.017094	.017106	.07	.005	.000	462.3
	153.600	.017829	.017838	.05	.006	.000	468.8
	153.500	.017982	.017991	.05	.006	.000	469.6
	153.000	.018635	.018646	.06	.009	.000	1844
	150.000	.021104	.021108	.02	.007	.000	474.7
91	152.627	.019099	.019056	−.23	.042	.025	30.63
90	151.668	.019959	.019929	−.15	.037	.020	76.56
89	150.539	.020764	.020760	−.02	.006	.005	734.0
88	149.012	.021699	.021691	−.04	.015	.002	1094
87	147.447	.022516	.022503	−.06	.027	.003	1055
86	145.865	.023238	.023227	−.05	.025	.002	1123
59	143.692	.024116	.024111	−.02	.013	.004	1053
85	142.442	.024580	.024576	−.02	.012	.002	1136
82	140.910	.025118	.025110	−.03	.023	.002	1140
64	139.642	.025527	.025528	.01	.004	.002	1142
84	138.704	.025829	.025825	−.01	.012	.004	1094
83	136.892	.026372	.026373	.00	.003	.001	1157
62	134.715	.026982	.026991	.03	.034	.001	1158
65	133.556	.027300	.027306	.02	.021	.001	1158
81	131.980	.027719	.027718	−.00	.004	.002	1151
61	130.975	.027960	.027973	.05	.050	.001	1159
80	129.729	.028276	.028280	.01	.017	.001	1159
67	127.077	.028901	.028907	.02	.028	.002	1153
75	124.417	.029498	.029503	.02	.025	.002	1154
34	123.117	.029783	.029784	.00	.004	.003	1147
39	122.723	.029869	.029868	−.00	.006	.002	1155
58	121.635	.030099	.030096	−.01	.016	.001	1160
76	120.071	.030430	.030416	−.05	.068	.002	1156

[a] equal to $|\Delta\rho|/|d\rho/dT|$.

Then the densities of the saturated liquid and saturated vapor are given by

$$\rho_{\mathrm{sat}\,L} = \rho_{RD} + \sum_{J=1}^{3} A_J \left(\frac{T_c - T}{T_c}\right)^{(2J-1)\beta} \qquad (11a)$$

and

$$\rho_{\mathrm{sat}\,G} = \rho_{RD} - \sum_{J=1}^{3} A_J \left(\frac{T_c - T}{T_c}\right)^{(2J-1)\beta} \qquad (11b)$$

where the coefficients are given in table 4. Equation (11a) is used to represent the liquid densities between 128 K and the critical temperature. Between the triple point and 128 K the densities are determined by the intersection of the liquid surface, eq (4), and the vapor pressure curve. Equation (11b) is used to obtain the vapor density between 150 K and T_c, while the intersection of the virial surface and the vapor pressure curve is used at lower temperatures. The isotherm polynomials, eq (5), were constrained to agree with the saturation densities calculated by equations (11a) and (11b), where applicable.

The intersection of the liquid surface, eq (4), with the melting curve was used to obtain the density of the liquid in equilibrium with solid. This density

may be approximated either as a function of pressure or as a function of temperature by

$$\rho_{\text{melt } L} = \rho_t + 1.79 \times 10^{-5} P(\text{MN/m}^2) \qquad (12a)$$

or

$$\rho_{\text{melt } L} = \rho_t + 1.60 \times 10^{-4} (T - T_t), \qquad (12b)$$

using a value of 0.04083 mol/cm³ for ρ_t, as given in table 13.

Equation (6) may be combined with the heat of fusion, 444.8±1.3 j/mol, given by Giauque and Johnston [15], to obtain a value of 0.94±0.01 cm³/mol for the volume change upon melting at the triple point.

2.4. Comparison With Literature

The present results have been compared with some of the data published in the literature. The following survey is not comprehensive, but comparisons are made with many of the more significant contributions. Other comparisons and a critical survey of all the literature to 1966 may be found in reference [11].

The virial coefficients, calculated from eqs (3a) and (3b), are compared with the experimental values of seven other investigators in table 9. The values attributed to Michels, Schamp, and de Graaff [16] were derived from their precise P–V–T data by the author and are seen to agree well with the results of this research. The older works of reference [17] and [18] agree less well. The values of B of Nijhoff and Keesom [19] are based on fewer data points of lower precision, and show a systematic difference of about 2–3 cm³/mol from the present work. The values of B of Van Itterbeek and Van Paemel [20] and of Van Lammeren [21] were calculated from velocity of sound measurements and are based upon the high temperature data of reference [19]. They are seen to differ considerably from the present results at the lower temperatures. The data of Cath and Onnes [31] were derived in the course of gas thermometry measurements and agree reasonably well with this research. Estimates of the uncertainty in the present results are given in the columns labeled "δB" and "δC" in table 5.

Comparisons are made with the compressed liquid P–V–T data of Van Itterbeek and Verbeke [3] in figure 3. It may be seen that there are some systematic differences with respect to both temperature and pressure, and in general, the agreement is not as good as might be expected. The densities of Timrot and Borisoglebskii [1, 2] are systematically lower than ours by about 0.5 percent in the compressed liquid between 83 K and 153 K. Figure 4 shows a comparison with the data of Michels et al. [16] near room temperature.

Table 3 compares the vapor pressure measurements with eq (7) taken from reference [11], which is based upon the data of Hoge [10]. Tables 6 and 7 compare the melting pressure data with the results of Mills and Grilly [13]. In both cases the agreement is very good. In addition, 15 determinations of the vapor pressure were made at 0.1 K intervals between 75 K and 76.5 K with the quartz bourdon gage. The results fell between the curve of eq (7) and the recent curve of Muijlwijk, Moussa, and van Dijk [22], agreeing with each to within 34 N/m².

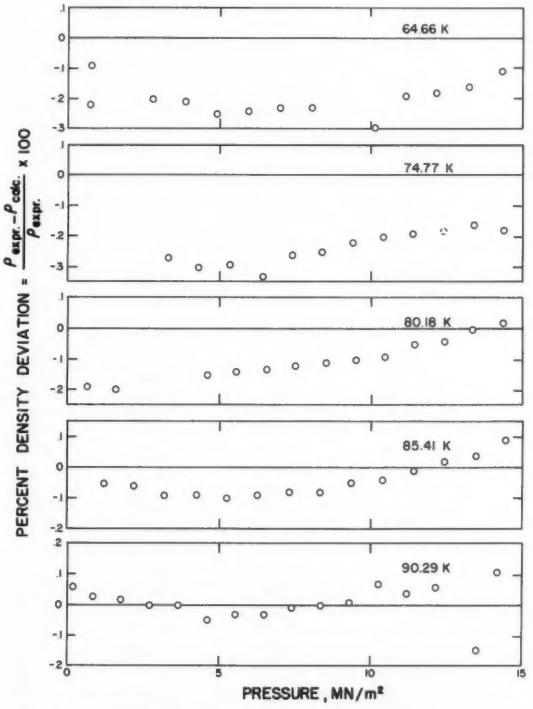

FIGURE 3. *Density deviation of the data of Van Itterbeek and Verbeke [3] from eq (4).*

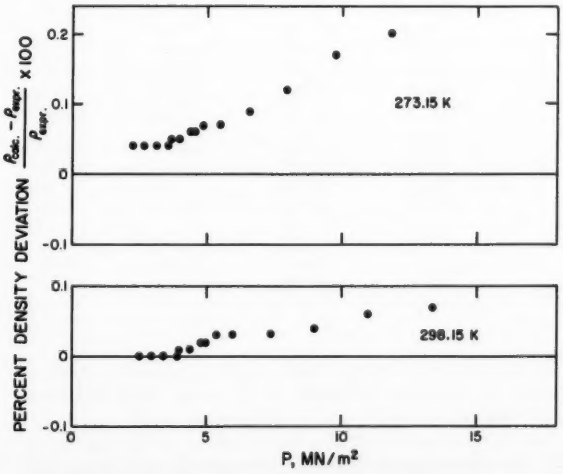

FIGURE 4. *Comparison with the data of Michels, et al. [16].*

TABLE 9. *Comparison of the calculated virial coefficients with other experimental values from the literature*

T	B_{exp}	B_{calc}	ΔB	C_{exp}	C_{calc}	ΔC	
K	cm^3/mol			$(cm^3/mol)^2$			
273.15	−21.44	−22.16	0.72	1033.0	1223.0	−190.0	Ref. [17]
298.15	−16.76	−16.31	−.45	962.0	1153.0	−191.0	
273.15	−21.67	−22.16	.49	1354.0	1223.0	131.0	Ref. [18]
298.15	−16.70	−16.31	−.39	1174.0	1153.0	21.0	
120.59	−134.90	−138.61	3.71				
127.76	−121.80	−124.11	2.31				
137.86	−104.40	−107.14	2.74				
148.20	−90.42	−93.00	2.58				
154.57	−82.66	−85.56	2.90				
156.14	−81.39	−83.85	2.46				Ref. [19]
157.14	−79.78	−82.79	3.01				
159.21	−78.26	−80.64	2.38				
163.16	−73.71	−76.75	3.04				
170.66	−67.51	−70.02	2.51				
193.15	−51.25	−53.88	2.63				
233.14	−32.99	−34.68	1.69				
83.15	−289.00	−279.02	−9.98				
93.15	−226.20	−225.69	−0.51				
103.15	−185.90	−186.36	.46				
113.15	−155.70	−156.46	.76				
123.15	−133.10	−133.16	.06				
133.15	−114.20	−114.61	.41				Ref. [31]
143.15	−99.20	−99.56	.36				
153.15	−86.20	−87.14	.94				
163.15	−75.30	−76.76	1.46				
173.15	−65.90	−67.96	2.06				
183.15	−57.80	−60.42	2.62				
193.15	−51.50	−53.88	2.38				
203.15	−46.40	−48.17	1.77				
213.15	−41.90	−43.14	1.24				
223.15	−37.40	−38.67	1.27				
233.15	−33.60	−34.67	1.07				
243.15	−30.90	−31.08	0.18				
253.15	−27.80	−27.82	.02				
263.15	−24.60	−24.86	.26				
273.15	−23.10	−22.16	−.94				
75.00	−278.00	−337.99	59.99				
80.00	−246.00	−299.82	53.82				
90.00	−208.00	−240.70	32.70				
100.00	−181.00	−197.56	16.56				Ref. [20]
110.00	−157.00	−165.06	8.06				
120.00	−136.00	−139.92	3.92				
125.00	−126.00	−129.41	3.41				
150.00	−88.00	−90.81	2.81				
200.00	−47.50	−49.89	2.39				
80.00	−278.00	−299.82	21.82				
90.00	−222.00	−240.70	18.70				
100.00	−186.00	−197.56	11.56				Ref. [21]
110.00	−159.00	−165.06	6.06				
273.15	−21.91	−22.16	0.25	1231.0	1223.0	8.0	
298.15	−16.25	−16.31	0.06	1164.0	1153.0	11.0	Ref. [16]
323.15	−11.62	−11.49	−0.13	1143.0	1115.6	27.4	

Table 10 is a comparison of the critical densities found by various authors. It is seen that different experimenters found widely divergent values.

No experimental values were found in the literature for the triple point density. In table 11 a comparison is made of various values for the triple point temperature. With the possible exception of the work of Furukawa and McCoskey, the different authors agree reasonably well considering the sources of errors in thermometry listed above. It might be mentioned, however, that Furukawa and McCoskey were the only workers who measured a melting curve, i.e.,

TABLE 10. *Comparison of values of the critical density from the literature*

Mathias and Onnes [23]	0.01344 mol/cm³
Timrot, et al. [1]	.0127
Hoge [10]	.012
Stewart [11]	.01333
This research	.01363 ± 0.00002

TABLE 11. *Comparison of values of the triple point temperature from several sources*

Hoge [10]	[a] 54.353 K
Muijlwijk, Moussa, van Dijk [22]	[b] 54.349_3
Furukawa and McCoskey [24]	[a] 54.360
This research	54.350_7

[a] Converted to NBS–1955 Temperature Scale.
[b] Using an NBS calibrated thermometer.

a curve of temperature vs. fraction melted. When only about 15 percent of their sample was liquid they found an equilibrium temperature of 54.350 K.

The calculated volume change with melting at the triple point depends primarily on which melting pressure curve is used. The results from the four published experimental melting curves are compared in table 12. The agreement with Mills and Grilly is surprisingly good when it is remembered that all their data were taken at pressures greater than 35 MN/m². The molar volume of the solid at the triple point, calculated here is 23.55 ± 0.03 cm³/mol. This value is in good agreement with the value of 23.49 ± 0.07 measured by Talkachev and Manzhelii [27] at 52.2 K, when allowance is made for thermal expansion of the solid from 52.2 K to 53.35 K.

TABLE 12. *Comparison with published values for the volume change on melting at the triple point*

Lisman and Keesom [25]	1.01 cm³/mol
Mills and Grilly [13]	0.93
Jahnke [26]	0.918 ± 0.02
This research	0.94 ± 0.01

3. Derived Thermodynamic Properties

3.1. Calculation of the Properties

a. Additional Data Used

Calculations of the thermodynamic properties of the compressed liquid make use of the heat capacity of the saturated liquid, C_{sat} from reference [6]. The expression used for C_{sat} is

$$C_{sat}=\frac{A_1}{(T_0-T)^{1/2}}+A_2+A_3T+A_4T^2 \qquad (13)$$

with $T_0=154.77$ and the coefficients given in table 4. This expression fits the data to within about 2 K of T_c.

Use was also made of new experimental measurements, reference [7], of C_v at a particular density $\rho_1(0.028687\text{mol/cm}^3)$ in the compressed liquid. This isochore intersects the vapor pressure curve at 128 K and intersects the 160 K isotherm at a pressure of about 33 MN/m². The heat capacity may be expressed as

$$C_v(\rho_1)=\sum_{J=1}^{4} A_J T^{(2-J)}, \qquad (14)$$

with the coefficients given in table 4.

b. Methods of Calculation

A high speed digital computer was used along with the surface representations for the three regions in figure 2 to calculate density from a given input of temperature and pressure. Once the density had been established the thermodynamic calculations proceeded as follows.

The following equations were used for densities less than critical at $T<160$ K and for all densities at $T\geq 160$ K:

$$H(T,\rho)=H^\circ(T)+\frac{P}{\rho}-RT+\int_0^\rho\left[\frac{P}{\rho^2}-\frac{T}{\rho^2}\left(\frac{\partial P}{\partial T}\right)_\rho\right]d\rho, \qquad (15)$$

$$S(T,\rho)=S^\circ(T)-R\ln\left(\frac{RT\rho}{P_0}\right)+\int_0^\rho\left[\frac{R}{\rho}-\frac{1}{\rho^2}\left(\frac{\partial P}{\partial T}\right)_\rho\right]d\rho, \qquad (16)$$

where $P_0=1$ atm;

$$C_v(T,\rho)=C_v^\circ(T)-T\int_0^\rho\frac{1}{\rho^2}\left(\frac{\partial^2 P}{\partial T^2}\right)_\rho d\rho. \qquad (17)$$

The values of H°, S°, and C_v° for the ideal gas at 1 atm were obtained from Woolley [5]. All integrations in Region II, figure 2 were performed numerically, using the trapezoidal rule.

For densities greater than critical and temperatures between 128 K and 160 K the properties, calculated by the equations above, at 160 K and density $\rho_1(\rho_1=0.028687$ g mole/cm³) serve as the starting point. For this particular density values of the heat capacity at constant volume, given by eq (14), were used to compute changes in the properties with temperature:

$$H(T,\rho_1)=U(160,\rho_1)+\int_{160}^{T}C_v(T,\rho_1)dT+P(T,\rho_1)/\rho_1, \qquad (18)$$

$$S(T,\rho_1)=S(160,\rho_1)+\int_{160}^{T}[C_v(T,\rho_1)/T]dT. \qquad (19)$$

Then computations were made along isotherms as follows:

$$H(T, \rho) = H(T, \rho_1) + \int_{\rho_1}^{\rho} [P - T(\partial P/\partial T)_\rho]/\rho^2 d\rho + P(T, \rho)/\rho - P(T, \rho_1)/\rho_1, \quad (20)$$

$$S(T, \rho) = S(T, \rho_1) - \int_{\rho_1}^{\rho} [(\partial P/\partial T)_\rho/\rho^2] d\rho, \quad (21)$$

$$C_v(T, \rho) = C_v(T, \rho_1) - T \int_{\rho_1}^{\rho} [(\partial^2 P/\partial T^2)_\rho/\rho^2] d\rho. \quad (22)$$

For the compressed liquid at temperatures less than 128 K the properties of the saturated liquid at 128 K ($\rho = \rho_1$) serve as the starting point. First the changes with temperature are computed along the saturation line:

$$H(T, \rho_{satL}) = H(128, \rho_{satL}) + \int_{128}^{T} C_{sat} dT + \int_{P_{sat(128)}}^{P_{sat}(T)} (1/\rho_{satL}) dP, \quad (23)$$

$$S(T, \rho_{satL}) = S(128, \rho_{satL}) + \int_{128}^{T} (C_{sat}/T) dT, \quad (24)$$

and

$$C_v(T, \rho_{satL}) = C_{sat}(T) + \frac{T}{\rho^2_{satL}} \left(\frac{d\rho_{satL}}{dT}\right) \left(\frac{\partial P}{\partial T}\right)_\rho. \quad (25)$$

Next the isothermal changes are computed using eqs (20, 21, 22) and substituting $\rho_{satL}(T)$ in place of ρ_1.

The internal energy and heat capacity at constant pressure are computed from

$$U(T, \rho) = H(T, \rho) - P/\rho, \quad (26)$$

and

$$C_p(T, \rho) = C_v(T, \rho) + (T/\rho^2)\,(\partial P/\partial T)^2_\rho/(\partial P/\partial \rho)_T. \quad (27)$$

Two other quantities have been calculated. The velocity of sound, W, is given by the relation

$$W = ((C_p/C_v)\,(\partial P/\partial \rho)_T)^{1/2}, \quad (28)$$

and the Joule-Thomson inversion curve may be defined by the locus of points where

$$T(\partial P/\partial T)_\rho = \rho(\partial P/\partial \rho)_T. \quad (29)$$

3.2. Results

Tables 13 and 14 present the results of all calculations on the saturation boundary and on selected isobars respectively. The terms isochore and isotherm derivative refer to $(\partial P/\partial T)_\rho$ and $(\partial P/\partial \rho)_T$ respectively.

The derived Joule-Thomson inversion curve is given in table 15, where δP is the uncertainty in the inversion pressure calculated from an assumed 1 percent error in either the isotherm or the isochore derivative.

Figure 5 illustrates the variation of C_p with temperature along several isobars, and Figure 6 shows the variation of C_v with density along several isotherms.

3.3. Estimate of Uncertainties in the Derived Properties

Probably the best estimate of the uncertainties in the derived properties is obtained through comparisons with experimental values for these properties published in the literature. Unfortunately, these measurements are often either nonexistent or limited in scope.

Because of the rather roundabout process, detailed in section 3.1, used to obtain the enthalpy of the liquid, it is desirable to make a comparison with liquid enthalpies obtained by other methods. This is best done by comparing heats of vaporization from various sources, in table 16. Here the second column is the difference between the enthalpies of the vapor and liquid states taken from table 13, while column four contains the change in enthalpy calculated using the Clapeyron equation. The values from reference [11]

TABLE 13. *Thermodynamic properties of oxygen on the saturation boundaries.**

T	P	V	$\left(\frac{\partial P}{\partial \rho}\right)_T$	$\left(\frac{\partial P}{\partial T}\right)_\rho$	Internal Energy	Enthalpy	Entropy	C_v	C_p	Vel. of Sound
K	MN/m²	cm³/mol	J/mol	MN/m²-K	J/mol	J/mol	J/mol-K	J/mol-K	J/mol-K	m/s
54.3507	0.00015	24.49	28792	3.945	−6189.6	−6189.6	67.00	35.65	53.27	1159
54.3507	0.00015	2974819.07	452	0.000	1120.0	1571.8	209.44	20.81	29.13	141
56	0.00025	24.63	28001	3.849	−6101.7	−6101.7	68.59	35.29	53.26	1149
56	0.00025	1876345.27	465	0.0000	1154.2	1619.7	206.23	20.81	29.13	143
58	0.00043	24.80	27058	3.736	−5995.2	−5995.2	70.46	34.86	53.25	1136
58	0.00043	1111925.72	482	0.0000	1195.6	1677.6	202.60	20.81	29.14	145
60	0.00073	24.97	26134	3.624	−5888.7	−5888.7	72.27	34.45	53.25	1124
60	0.00073	683074.11	498	0.0000	1237.0	1735.5	199.26	20.81	29.15	148
62	0.00119	25.14	25228	3.516	−5782.2	−5782.2	74.01	34.06	53.26	1110
62	0.00119	433699.56	514	0.0000	1278.2	1793.2	196.16	20.82	29.16	150
64	0.00187	25.32	24341	3.410	−5675.7	−5675.6	75.70	33.67	53.27	1097
64	0.00187	283821.73	530	0.0000	1319.3	1850.6	193.29	20.82	29.18	152

TABLE 13. *Thermodynamic properties of oxygen on the saturation boundaries.** — Continued

T	P	V	$\left(\frac{\partial P}{\partial \rho}\right)_T$	$\left(\frac{\partial P}{\partial T}\right)_\rho$	Internal Energy	Enthalpy	Entropy	C_v	C_p	Vel. of Sound
K	MN/m²	cm³/mol	J/mol	MN/m²-K	J/mol	J/mol	J/mol-K	J/mol-K	J/mol-K	m/s
66	0.00287	25.50	23471	3.306	−5569.1	−5569.0	77.34	33.30	53.29	1083
66	0.00287	190960.14	546	0.0000	1360.2	1907.7	190.63	20.83	29.21	155
68	0.00428	25.69	22619	3.205	−5462.5	−5462.4	78.94	32.94	53.31	1070
68	0.00428	131788.10	562	0.0001	1400.9	1964.5	188.16	20.84	29.25	157
70	0.00623	25.87	21784	3.106	−5355.9	−5355.7	80.48	32.59	53.34	1056
70	0.00623	93094.99	577	0.0001	1441.2	2020.9	185.87	20.85	29.30	159
72	0.00886	26.07	20966	3.009	−5249.2	−5248.9	81.98	32.26	53.38	1041
72	0.00886	67181.69	592	0.0001	1481.2	2076.6	183.73	20.87	29.35	161
74	0.01236	26.26	20164	2.914	−5142.4	−5142.0	83.45	31.93	53.43	1027
74	0.01236	49440.13	607	0.0002	1520.8	2131.8	181.74	20.89	29.43	163
76	0.01691	26.47	19379	2.822	−5035.5	−5035.0	84.87	31.61	53.49	1012
76	0.01691	37043.15	621	0.0002	1560.0	2186.2	179.88	20.91	29.51	165
78	0.02273	26.67	18610	2.732	−4928.5	−4927.9	86.26	31.31	53.56	997
78	0.02273	28215.79	634	0.0003	1598.5	2239.8	178.14	20.95	29.62	167
80	0.03006	26.88	17857	2.644	−4821.3	−4820.5	87.62	31.01	53.64	982
80	0.03006	21819.46	647	0.0004	1636.5	2292.5	176.51	20.98	29.74	169
82	0.03918	27.10	17119	2.557	−4714.0	−4713.0	88.94	30.73	53.73	967
82	0.03918	17109.05	659	0.0005	1673.8	2344.1	174.98	21.03	29.89	171
84	0.05036	27.32	16397	2.473	−4606.6	−4605.2	90.24	30.45	53.84	952
84	0.05036	13587.75	670	0.0006	1710.3	2394.5	173.54	21.08	30.06	173
86	0.06391	27.55	15689	2.391	−4498.9	−4497.1	91.50	30.18	53.96	936
86	0.06391	10918.43	680	0.0008	1745.9	2443.7	172.18	21.13	30.26	174
88	0.08015	27.78	14997	2.311	−4391.0	−4388.8	92.74	29.92	54.10	921
88	0.08015	8868.59	690	0.0010	1780.7	2491.5	170.90	21.20	30.49	176
90	0.09943	28.02	14319	2.232	−4282.8	−4280.1	93.96	29.67	54.26	905
90	0.09943	7275.38	698	0.0012	1814.5	2537.9	169.68	21.28	30.74	178
92	0.12210	28.27	13655	2.156	−4174.4	−4171.0	95.15	29.42	54.44	889
92	0.12210	6023.11	706	0.0014	1847.2	2582.6	168.53	21.36	31.04	179
94	0.14852	28.52	13005	2.081	−4065.7	−4061.4	96.32	29.18	54.64	872
94	0.14852	5028.47	712	0.0017	1878.8	2625.6	167.43	21.45	31.37	180
96	0.17909	28.79	12370	2.008	−3956.6	−3951.4	97.47	28.95	54.87	856
96	0.17909	4230.71	717	0.0021	1909.2	2666.8	166.38	21.56	31.73	182
98	0.21420	29.06	11748	1.936	−3847.1	−3840.9	98.60	28.73	55.13	839
98	0.21420	3585.00	721	0.0024	1938.2	2706.2	165.38	21.68	32.14	183
100	0.25425	29.34	11139	1.866	−3737.2	−3729.7	99.71	28.51	55.42	823
100	0.25425	3057.86	723	0.0029	1966.0	2743.4	164.42	21.80	32.60	184
102	0.29965	29.63	10544	1.797	−3626.8	−3617.9	100.81	28.30	55.74	806
102	0.29965	2624.08	724	0.0034	1992.3	2778.6	163.49	21.94	33.11	185
104	0.35083	29.93	9961	1.731	−3515.8	−3505.3	101.88	28.10	56.10	788
104	0.35083	2264.42	724	0.0040	2017.1	2811.5	162.60	22.09	33.68	186
106	0.40822	30.24	9392	1.665	−3404.3	−3392.0	102.95	27.90	56.51	771
106	0.40822	1964.12	722	0.0046	2040.3	2842.1	161.74	22.26	34.30	187
108	0.47226	30.57	8836	1.601	−3292.1	−3277.7	104.00	27.71	56.96	753
108	0.47226	1711.70	719	0.0053	2061.8	2870.1	160.91	22.44	34.99	187
110	0.54339	30.90	8292	1.538	−3179.2	−3162.4	105.03	27.52	57.47	736
110	0.54339	1498.21	714	0.0062	2081.5	2895.6	160.10	22.63	35.76	188

TABLE 13. *Thermodynamic properties of oxygen on the saturation boundaries.** —Continued

T	P	V	$\left(\frac{\partial P}{\partial \rho}\right)_T$	$\left(\frac{\partial P}{\partial T}\right)_\rho$	Internal Energy	Enthalpy	Entropy	C_v	C_p	Vel. of Sound
K	MN/m²	cm³/mol	J/mol	MN/m²-K	J/mol	J/mol	J/mol-K	J/mol-K	J/mol-K	m/s
112	0.62207	31.26	7761	1.476	−3065.5	−3046.0	106.06	27.34	58.05	718
112	0.62207	1316.57	708	0.0071	2099.4	2918.4	159.31	22.83	36.61	188
114	0.70876	31.63	7242	1.415	−2950.9	−2928.5	107.08	27.16	58.70	699
114	0.70876	1161.16	700	0.0081	2115.2	2938.2	158.53	23.05	37.55	189
116	0.80391	32.02	6736	1.356	−2835.2	−2809.5	108.09	26.99	59.43	681
116	0.80391	1027.49	690	0.0093	2129.0	2955.0	157.78	23.28	38.59	189
118	0.90801	32.42	6242	1.297	−2718.5	−2689.1	109.09	26.83	60.25	662
118	0.90801	911.95	678	0.0106	2140.6	2968.6	157.03	23.52	39.75	189
120	1.0215	32.85	5760	1.239	−2600.5	−2566.9	110.08	26.67	61.19	643
120	1.0215	811.59	664	0.0120	2149.8	2978.8	156.30	23.78	41.04	189
122	1.1450	33.31	5292	1.182	−2481.1	−2442.9	111.07	26.53	62.27	623
122	1.1450	724.02	649	0.0137	2156.4	2985.4	155.57	24.06	42.49	189
124	1.2788	33.79	4836	1.126	−2360.1	−2316.8	112.06	26.39	63.49	603
124	1.2788	647.27	631	0.0155	2160.3	2988.0	154.85	24.35	44.13	189
126	1.4236	34.31	4394	1.070	−2237.3	−2188.4	113.05	26.26	64.91	583
126	1.4236	579.72	612	0.0176	2161.2	2986.4	154.12	24.65	45.99	189
128	1.5797	34.86	3965	1.015	−2112.4	−2057.3	114.04	26.15	66.56	562
128	1.5797	520.03	590	0.0199	2158.8	2980.3	153.40	24.97	48.12	188
130	1.7478	35.45	3688	0.987	−1984.8	−1922.9	115.03	26.60	69.77	550
130	1.7478	467.05	565	0.0224	2153.0	2969.3	152.68	25.31	50.60	188
132	1.9284	36.09	3314	0.924	−1853.9	−1784.3	116.04	26.48	70.79	526
132	1.9284	419.84	538	0.0254	2143.1	2952.7	151.94	25.68	53.48	187
134	2.1219	36.79	2849	0.868	−1719.9	−1641.8	117.06	26.37	74.38	501
134	2.1219	377.60	509	0.0287	2128.8	2930.0	151.19	26.06	56.90	186
136	2.3291	37.55	2472	0.811	−1582.5	−1495.0	118.09	26.30	77.32	477
136	2.3291	339.63	478	0.0324	2109.4	2900.5	150.42	26.47	61.03	186
138	2.5504	38.40	2100	0.752	−1441.1	−1343.2	119.14	26.30	81.14	450
138	2.5504	305.34	443	0.0368	2084.2	2862.9	149.63	26.90	66.14	185
140	2.7866	39.35	1745	0.696	−1295.0	−1185.4	120.21	26.38	86.51	423
140	2.7866	274.21	406	0.0418	2052.0	2816.1	148.80	27.38	72.63	183
142	3.0383	40.43	1419	0.640	−1143.0	−1020.1	121.31	26.52	93.59	396
142	3.0383	245.75	365	0.0476	2011.3	2757.9	147.92	27.89	81.18	182
144	3.3064	41.68	1124	0.589	−983.4	−845.6	122.45	26.73	103.86	369
144	3.3064	219.53	320	0.0545	1959.8	2685.6	146.98	28.48	93.04	181
146	3.5918	43.17	875	0.532	−813.9	−658.9	123.66	27.06	114.99	341
146	3.5918	195.08	270	0.0630	1894.0	2594.7	145.95	29.14	110.71	179
148	3.8955	44.99	613	0.476	−630.4	−455.2	124.95	27.54	138.37	310
148	3.8955	171.89	215	0.0737	1807.8	2477.4	144.77	29.95	140.18	177
150	4.2190	47.38	391	0.419	−425.1	−225.2	126.39	28.28	179.31	278
150	4.2190	149.13	153	0.0881	1688.2	2317.4	143.35	31.01	200.53	176
152	4.5638	50.90	194	0.353	−179.5	52.7	128.12	29.94	283.23	240
152	4.5638	126.20	84	0.109	1512.3	2088.2	141.52	33.36	373.23	171
154	4.9320	58.46	26	0.267	200.0	488.4	130.84	33.30	1478.52	190
154	4.9320	97.80	17	0.149	1165.1	1647.5	138.37	37.02	1962.81	167
154.576	5.0427	73.37		0.200	662.3	1032.2	134.32			
154.576	5.0427	73.37		0.200	662.3	1032.2	134.32			

*The first entry for each temperature refers to the liquid phase.

TABLE 14. *Thermodynamic properties of oxygen.*

0.101325 MN/m² (1 atm) Isobar

T	V	$\left(\frac{\partial P}{\partial \rho}\right)_T$	$\left(\frac{\partial P}{\partial T}\right)_\rho$	Internal Energy	Enthalpy	Entropy	C_v	C_p	Vel. of Sound
K	cm³/mol	J/mol	MN/m²-K	J/mol	J/mol	J/mol-K	J/mol-K	J/mol-K	m/s
*54.362	24.49	28805	3.945	-6189.4	-6186.9	67.00	35.65	53.26	1160
56	24.62	28019	3.850	-6102.2	-6099.7	68.59	35.29	53.25	1149
58	24.79	27077	3.736	-5995.7	-5993.2	70.45	34.87	53.25	1137
60	24.96	26153	3.625	-5889.2	-5886.7	72.26	34.46	53.25	1124
62	25.14	25247	3.517	-5782.7	-5780.2	74.01	34.06	53.25	1111
64	25.32	24360	3.411	-5676.2	-5673.7	75.70	33.68	53.26	1097
66	25.50	23490	3.307	-5569.7	-5567.1	77.34	33.31	53.28	1084
68	25.68	22638	3.206	-5463.1	-5460.5	78.93	32.95	53.30	1070
70	25.87	21803	3.107	-5356.5	-5353.9	80.47	32.60	53.34	1056
72	26.06	20984	3.010	-5249.8	-5247.2	81.98	32.26	53.37	1042
74	26.26	20182	2.915	-5143.0	-5140.4	83.44	31.93	53.42	1027
76	26.46	19397	2.823	-5036.1	-5033.4	84.86	31.62	53.48	1013
78	26.67	18627	2.732	-4929.1	-4926.4	86.25	31.31	53.55	998
80	26.88	17872	2.644	-4821.9	-4819.2	87.61	31.02	53.63	983
82	27.10	17133	2.558	-4714.6	-4711.8	88.94	30.73	53.72	967
84	27.32	16408	2.474	-4607.0	-4604.3	90.23	30.45	53.83	952
86	27.55	15698	2.391	-4499.3	-4496.5	91.50	30.18	53.96	936
88	27.78	15002	2.311	-4391.2	-4388.4	92.74	29.92	54.10	921
90	28.02	14319	2.232	-4282.9	-4280.0	93.96	29.67	54.26	905
*90.180	28.04	14258	2.225	-4273.1	-4270.3	94.07	29.64	54.28	903
*90.180	7150.15	699	0.0012	1817.5	2542.0	169.58	21.28	30.77	178
92	7309.46	716	0.0012	1857.2	2597.9	170.19	21.25	30.66	180
94	7483.81	735	0.0011	1900.8	2659.1	170.85	21.22	30.55	182
96	7657.47	753	0.0011	1944.2	2720.1	171.49	21.19	30.46	184
98	7830.51	772	0.0011	1987.5	2780.9	172.12	21.16	30.37	186
100	8002.98	790	0.0011	2030.7	2841.6	172.73	21.14	30.29	188
102	8174.94	809	0.0010	2073.7	2902.1	173.33	21.12	30.21	190
104	8346.42	827	0.0010	2116.7	2962.4	173.92	21.10	30.15	192
106	8517.48	845	0.0010	2159.6	3022.7	174.49	21.08	30.09	194
108	8688.15	863	0.0010	2202.4	3082.8	175.05	21.06	30.03	196
110	8858.45	881	0.0010	2245.2	3142.8	175.60	21.05	29.98	198
112	9028.42	898	0.0009	2287.9	3202.7	176.14	21.03	29.93	200
114	9198.08	916	0.0009	2330.5	3262.5	176.67	21.02	29.89	202
116	9367.46	934	0.0009	2373.1	3322.3	177.19	21.01	29.85	204
118	9536.57	951	0.0009	2415.6	3381.9	177.70	21.00	29.81	205
120	9705.43	969	0.0009	2458.1	3441.5	178.20	20.99	29.77	207
122	9874.07	987	0.0009	2500.5	3501.0	178.69	20.98	29.74	209
124	10042.49	1004	0.0008	2542.9	3560.5	179.18	20.97	29.71	211
126	10210.71	1022	0.0008	2585.3	3619.9	179.65	20.96	29.68	213
128	10378.75	1039	0.0008	2627.6	3679.2	180.12	20.95	29.66	214
130	10546.61	1056	0.0008	2669.8	3738.5	180.58	20.94	29.63	216
132	10714.31	1074	0.0008	2712.1	3797.7	181.03	20.94	29.61	218
134	10881.86	1091	0.0008	2754.3	3856.9	181.47	20.93	29.59	220
136	11049.26	1108	0.0008	2796.5	3916.1	181.91	20.92	29.57	221
138	11216.52	1126	0.0007	2838.7	3975.2	182.34	20.92	29.55	223
140	11383.66	1143	0.0007	2880.8	4034.2	182.77	20.91	29.53	225
142	11550.68	1160	0.0007	2922.9	4093.3	183.19	20.91	29.51	226
144	11717.58	1177	0.0007	2965.0	4152.3	183.60	20.90	29.49	228
146	11884.38	1194	0.0007	3007.1	4211.3	184.01	20.90	29.48	229
148	12051.07	1212	0.0007	3049.1	4270.2	184.41	20 89	29.46	231
150	12217.67	1229	0.0007	3091.2	4329.1	184.80	20.89	29.45	233
152	12384.18	1246	0.0007	3133.2	4388.0	185.19	20.88	29.44	234
154	12550.61	1263	0.0007	3175.2	4446.9	185.58	20.88	29.43	236
156	12716.95	1280	0.0007	3217.2	4505.7	185.96	20.88	29.41	237
158	12883.21	1297	0.0006	3259.1	4564.5	186.33	20.87	29.40	239
160	13049.40	1314	0.0006	3301.1	4623.3	186.70	20.87	29.39	240
165	13464.57	1357	0.0006	3405.9	4770.2	187.61	20.86	29.37	244
170	13879.36	1399	0.0006	3510.7	4917.0	188.48	20.86	29.35	248
175	14293.80	1442	0.0006	3615.4	5063.7	189.33	20.85	29.33	252
180	14707.94	1484	0.0006	3720.1	5210.4	190.16	20.85	29.32	255
185	15121.80	1526	0.0006	3824.7	5356.9	190.96	20.85	29.30	259
190	15535.41	1568	0.0005	3929.3	5503.4	191.74	20.85	29.29	262
195	15948.81	1611	0.0005	4033.8	5649.8	192.50	20.85	29.28	266
200	16362.00	1653	0.0005	4138.3	5796.2	193.25	20.85	29.27	269
210	17187.85	1737	0.0005	4347.3	6088.9	194.67	20.85	29.26	276
220	18013.10	1821	0.0005	4556.3	6381.5	196.04	20.85	29.26	283
230	18837.85	1905	0.0004	4765.3	6674.1	197.34	20.86	29.26	289
240	19662.17	1989	0.0004	4974.4	6966.7	198.58	20.88	29.27	295
250	20486.13	2073	0.0004	5183.7	7259.4	199.78	20.90	29.28	301
260	21309.78	2157	0.0004	5393.1	7552.3	200.92	20.92	29.30	307
270	22133.17	2240	0.0004	5602.8	7845.4	202.03	20.95	29.32	313
280	22956.31	2324	0.0004	5812.7	8138.8	203.10	20.99	29.35	319
290	23779.26	2408	0.0004	6023.1	8432.5	204.13	21.03	29.39	324
300	24602.02	2491	0.0003	6233.8	8726.6	205.13	21.08	29.43	330

*Two-phase boundary.

TABLE 14. *Thermodynamic properties of oxygen.*—Continued

1 MN/m² Isobar

T	V	$\left(\frac{\partial P}{\partial \rho}\right)_T$	$\left(\frac{\partial P}{\partial T}\right)_\rho$	Internal Energy	Enthalpy	Entropy	C_v	C_p	Vel. of Sound
K	cm³/mol	J/mol	MN/m²-K	J/mol	J/mol	J/mol-K	J/mol-K	J/mol-K	m/s
*54.466	24.48	28917	3.946	−6187.9	−6163.4	67.03	35.65	53.23	1161
56	24.61	28182	3.857	−6106.4	−6081.8	68.51	35.32	53.22	1152
58	24.77	27241	3.744	−6000.1	−5975.3	70.38	34.90	53.21	1139
60	24.94	26319	3.633	−5893.9	−5868.9	72.18	34.49	53.21	1126
62	25.12	25416	3.524	−5787.6	−5762.5	73.93	34.09	53.21	1113
64	25.29	24531	3.418	−5681.4	−5656.1	75.62	33.71	53.21	1100
66	25.47	23663	3.315	−5575.1	−5549.6	77.25	33.34	53.23	1087
68	25.66	22813	3.214	−5468.8	−5443.2	78.84	32.98	53.25	1073
70	25.84	21980	3.115	−5362.5	−5336.6	80.39	32.64	53.27	1059
72	26.04	21164	3.018	−5256.1	−5230.0	81.89	32.30	53.31	1045
74	26.23	20364	2.924	−5149.6	−5123.4	83.35	31.98	53.35	1030
76	26.43	19581	2.832	−5043.0	−5016.6	84.77	31.66	53.40	1016
78	26.63	18813	2.741	−4936.4	−4909.7	86.16	31.36	53.46	1001
80	26.84	18062	2.654	−4829.6	−4802.7	87.51	31.06	53.54	986
82	27.06	17325	2.568	−4722.6	−4695.6	88.84	30.78	53.62	971
84	27.28	16603	2.484	−4615.5	−4588.2	90.13	30.50	53.72	956
86	27.50	15896	2.402	−4508.1	−4480.6	91.40	30.23	53.84	941
88	27.74	15203	2.321	−4400.5	−4372.8	92.64	29.97	53.97	925
90	27.97	14524	2.243	−4292.7	−4264.7	93.85	29.72	54.12	909
92	28.22	13858	2.166	−4184.5	−4156.3	95.04	29.47	54.29	893
94	28.47	13205	2.092	−4076.0	−4047.5	96.21	29.24	54.48	877
96	28.73	12566	2.018	−3967.1	−3938.3	97.36	29.00	54.70	861
98	29.00	11939	1.947	−3857.7	−3828.7	98.49	28.78	54.94	844
100	29.28	11324	1.876	−3747.8	−3718.5	99.60	28.56	55.22	827
102	29.57	10720	1.808	−3637.3	−3607.8	100.70	28.35	55.53	810
104	29.87	10129	1.740	−3526.2	−3496.3	101.78	28.14	55.89	793
106	30.18	9548	1.674	−3414.4	−3384.2	102.85	27.94	56.29	775
108	30.51	8977	1.609	−3301.7	−3271.1	103.91	27.74	56.74	758
110	30.85	8417	1.546	−3188.0	−3157.2	104.95	27.55	57.26	739
112	31.21	7867	1.483	−3073.3	−3042.1	105.99	27.36	57.85	721
114	31.59	7326	1.421	−2957.3	−2925.7	107.02	27.18	58.52	702
116	31.99	6794	1.359	−2839.9	−2807.9	108.05	27.00	59.29	683
118	32.41	6270	1.299	−2720.8	−2688.4	109.07	26.83	60.18	663
*119.633	32.77	5848	1.250	−2622.2	−2589.4	109.90	26.70	61.01	646
*119.633	828.96	667	0.0118	2148.3	2977.2	156.43	23.73	40.79	189
120	833.40	672	0.0117	2158.7	2992.1	156.56	23.68	40.59	190
122	857.19	703	0.0112	2215.0	3072.2	157.22	23.43	39.53	193
124	880.39	733	0.0108	2270.0	3150.3	157.85	23.22	38.62	195
126	903.07	762	0.0105	2323.7	3226.8	158.47	23.02	37.85	198
128	925.30	790	0.0102	2376.5	3301.8	159.06	22.85	37.17	200
130	947.14	817	0.0099	2428.4	3375.5	159.63	22.70	36.58	203
132	968.63	843	0.0096	2479.5	3448.2	160.18	22.57	36.05	205
134	989.81	869	0.0093	2530.0	3519.8	160.72	22.45	35.59	207
136	1010.71	894	0.0091	2579.8	3590.6	161.25	22.34	35.17	210
138	1031.37	918	0.0089	2629.2	3660.5	161.76	22.24	34.80	212
140	1051.80	942	0.0087	2678.0	3729.8	162.25	22.15	34.46	214
142	1072.02	966	0.0085	2726.4	3798.4	162.74	22.07	34.15	216
144	1092.06	989	0.0083	2774.4	3866.4	163.22	21.99	33.88	218
146	1111.92	1012	0.0081	2822.0	3933.9	163.68	21.92	33.62	220
148	1131.63	1035	0.0079	2869.3	4000.9	164.14	21.86	33.39	222
150	1151.19	1058	0.0078	2916.3	4067.5	164.59	21.80	33.17	224
152	1170.62	1080	0.0076	2963.0	4133.6	165.02	21.75	32.97	226
154	1189.92	1102	0.0075	3009.4	4199.4	165.45	21.70	32.79	228
156	1209.11	1123	0.0073	3055.7	4264.8	165.87	21.65	32.62	230
158	1228.19	1145	0.0072	3101.7	4329.9	166.29	21.61	32.46	232
160	1247.17	1166	0.0071	3147.5	4394.6	166.70	21.57	32.31	234
165	1294.21	1218	0.0068	3261.1	4555.3	167.69	21.48	31.99	238
170	1340.76	1270	0.0065	3373.8	4714.6	168.64	21.41	31.71	242
175	1386.86	1320	0.0063	3485.6	4872.5	169.55	21.34	31.47	247
180	1432.59	1370	0.0061	3596.7	5029.3	170.44	21.29	31.26	251
185	1477.99	1419	0.0059	3707.2	5185.2	171.29	21.24	31.08	255
190	1523.10	1468	0.0057	3817.1	5340.2	172.12	21.20	30.92	259
195	1567.94	1516	0.0055	3926.5	5494.4	172.92	21.17	30.79	262
200	1612.56	1563	0.0054	4035.5	5648.0	173.70	21.13	30.66	266
210	1701.20	1657	0.0051	4252.4	5953.6	175.19	21.09	30.46	274
220	1789.17	1750	0.0048	4468.2	6257.4	176.60	21.05	30.30	281
230	1876.58	1842	0.0046	4683.1	6559.7	177.94	21.03	30.17	287
240	1963.54	1932	0.0043	4897.3	6860.9	179.23	21.02	30.07	294
250	2050.11	2022	0.0042	5111.1	7161.2	180.45	21.02	29.99	300
260	2136.35	2111	0.0040	5324.5	7460.8	181.63	21.02	29.94	307
270	2222.31	2200	0.0038	5537.7	7760.0	182.76	21.04	29.90	313
280	2308.03	2288	0.0037	5750.9	8058.9	183.84	21.06	29.88	319
290	2393.53	2376	0.0035	5964.1	8357.6	184.89	21.09	29.86	324
300	2478.85	2464	0.0034	6177.4	8656.2	185.90	21.13	29.87	330

*Two-phase boundary.

TABLE 14. *Thermodynamic properties of oxygen.*—Continued

5 MN/m² Isobar

T	V	$\left(\frac{\partial P}{\partial \rho}\right)_T$	$\left(\frac{\partial P}{\partial T}\right)_\rho$	Internal Energy	Enthalpy	Entropy	C_v	C_p	Vel. of Sound
K	cm³/mol	J/mol	MN/m²-K	J/mol	J/mol	J/mol-K	J/mol-K	J/mol-K	m/s
*54.923	24.43	29411	3.950	−6181.2	−6059.0	67.15	35.68	53.07	1169
56	24.52	28901	3.888	−6124.5	−6001.8	68.18	35.45	53.06	1163
58	24.68	27968	3.775	−6019.2	−5895.7	70.04	35.03	53.04	1150
60	24.85	27054	3.665	−5913.9	−5789.7	71.84	34.63	53.03	1138
62	25.02	26159	3.557	−5808.7	−5683.6	73.58	34.24	53.01	1125
64	25.19	25282	3.452	−5703.6	−5577.6	75.26	33.86	53.01	1112
66	25.37	24424	3.349	−5598.4	−5471.6	76.90	33.50	53.00	1099
68	25.54	23583	3.249	−5493.3	−5365.6	78.48	33.15	53.00	1086
70	25.72	22759	3.151	−5388.2	−5259.6	80.01	32.81	53.01	1072
72	25.91	21953	3.055	−5283.1	−5153.5	81.51	32.48	53.02	1058
74	26.10	21163	2.961	−5177.9	−5047.4	82.96	32.16	53.05	1044
76	26.29	20390	2.870	−5072.8	−4941.3	84.38	31.85	53.07	1030
78	26.49	19633	2.781	−4967.6	−4835.1	85.76	31.55	53.11	1016
80	26.69	18891	2.694	−4862.3	−4728.8	87.10	31.27	53.15	1002
82	26.89	18166	2.609	−4756.9	−4622.5	88.41	30.99	53.21	987
84	27.10	17456	2.526	−4651.5	−4516.0	89.70	30.72	53.27	973
86	27.32	16760	2.445	−4545.9	−4409.3	90.95	30.45	53.34	958
88	27.54	16080	2.366	−4440.2	−4302.5	92.18	30.20	53.43	943
90	27.77	15413	2.289	−4334.4	−4195.6	93.38	29.95	53.53	928
92	28.00	14761	2.214	−4228.4	−4088.4	94.56	29.71	53.65	913
94	28.24	14123	2.140	−4122.1	−3980.9	95.71	29.48	53.78	897
96	28.48	13498	2.068	−4015.6	−3873.2	96.85	29.25	53.93	882
98	28.73	12886	1.998	−3908.8	−3765.1	97.96	29.03	54.10	866
100	28.99	12287	1.930	−3801.7	−3656.7	99.06	28.81	54.30	851
102	29.26	11700	1.863	−3694.2	−3547.9	100.13	28.60	54.51	835
104	29.54	11126	1.798	−3586.4	−3438.7	101.20	28.39	54.76	819
106	29.83	10564	1.734	−3478.0	−3328.9	102.24	28.19	55.03	803
108	30.12	10013	1.671	−3369.1	−3218.5	103.27	27.99	55.34	787
110	30.43	9474	1.610	−3259.7	−3107.5	104.29	27.79	55.68	770
112	30.75	8945	1.550	−3149.5	−2995.8	105.30	27.60	56.07	754
114	31.09	8428	1.492	−3038.7	−2883.2	106.29	27.41	56.50	737
116	31.44	7921	1.434	−2926.9	−2769.7	107.28	27.22	56.98	720
118	31.80	7425	1.377	−2814.2	−2655.2	108.26	27.04	57.53	703
120	32.19	6938	1.321	−2700.4	−2539.5	109.23	26.85	58.15	685
122	32.60	6461	1.266	−2585.4	−2422.5	110.20	26.67	58.85	667
124	33.02	5995	1.212	−2469.0	−2303.9	111.16	26.49	59.64	649
126	33.48	5537	1.158	−2351.0	−2183.6	112.13	26.32	60.55	631
128	33.96	5089	1.105	−2231.1	−2061.3	113.09	26.16	61.59	612
130	34.49	4674	1.056	−2107.3	−1934.9	114.07	26.66	63.52	590
132	35.05	4241	1.014	−1981.3	−1806.0	115.05	26.52	65.87	574
134	35.65	3844	0.9500	−1853.4	−1675.2	116.04	26.39	66.38	550
136	36.31	3434	0.9024	−1721.8	−1540.2	117.04	26.28	68.81	530
138	37.04	3036	0.8457	−1586.4	−1401.2	118.05	26.19	70.78	506
140	37.84	2650	0.7889	−1446.6	−1257.3	119.09	26.14	73.23	482
142	38.76	2272	0.7341	−1300.7	−1106.9	120.15	26.16	76.74	456
144	39.81	1901	0.6775	−1147.1	−948.1	121.26	26.23	81.35	429
146	41.06	1529	0.6208	−982.8	−777.5	122.44	26.39	88.43	400
148	42.59	1179	0.5551	−804.4	−591.5	123.70	26.65	96.78	366
150	44.60	828	0.4898	−602.3	−379.3	125.13	27.11	113.53	329
152	47.63	478	0.4124	−353.9	−115.7	126.87	28.02	150.80	283
154	54.93	105	0.2929	63.4	338.0	129.84	31.40	412.84	207
*154.355	62.15	10	0.2481	338.2	648.9	131.85	34.74	3824.02	182
*154.355	89.32	7	0.1609	1017.8	1464.5	137.14	38.11	4780.17	162
156	125.60	161	0.1073	1634.2	2262.2	142.29	31.23	206.80	183
158	142.14	264	0.0901	1864.4	2575.1	144.28	28.98	127.28	190
160	154.34	343	0.0799	2023.9	2795.6	145.67	27.73	98.79	195
165	177.91	503	0.0655	2316.3	3205.8	148.20	25.92	70.48	207
170	196.80	632	0.0571	2541.8	3525.8	150.11	24.85	58.79	216
175	213.31	743	0.0512	2735.5	3802.0	151.71	24.13	52.24	224
180	228.36	843	0.0468	2910.2	4052.0	153.12	23.62	48.01	231
185	242.38	935	0.0433	3072.3	4284.2	154.39	23.23	45.04	238
190	255.65	1020	0.0404	3225.4	4503.6	155.56	22.93	42.82	244
195	268.33	1101	0.0380	3371.6	4713.3	156.65	22.68	41.11	250
200	280.54	1178	0.0359	3512.6	4915.3	157.68	22.48	39.74	255
210	303.87	1322	0.0325	3782.6	5301.9	159.56	22.18	37.70	265
220	326.10	1457	0.0298	4040.8	5671.3	161.28	21.95	36.25	274
230	347.50	1585	0.0276	4290.6	6028.1	162.87	21.77	35.16	283
240	368.27	1707	0.0258	4534.1	6375.4	164.35	21.64	34.33	291
250	388.53	1825	0.0242	4772.7	6715.3	165.73	21.53	33.68	299
260	408.38	1939	0.0229	5007.5	7049.4	167.04	21.45	33.15	306
270	427.90	2049	0.0217	5239.2	7378.7	168.29	21.39	32.73	313
280	447.14	2157	0.0206	5468.5	7704.2	169.47	21.35	32.39	320
290	466.14	2263	0.0197	5695.9	8026.6	170.60	21.32	32.11	326
300	484.94	2367	0.0188	5921.9	8346.6	171.69	21.31	31.88	333

*Two-phase boundary.

TABLE 14. *Thermodynamic properties of oxygen.*—Continued

10 MN/m² Isobar

T	V	$\left(\frac{\partial P}{\partial \rho}\right)_T$	$\left(\frac{\partial P}{\partial T}\right)_\rho$	Internal Energy	Enthalpy	Entropy	C_v	C_p	Vel. of Sound
K	cm³/mol	J/mol	MN/m²-K	J/mol	J/mol	J/mol-K	J/mol-K	J/mol-K	m/s
*55.491	24.38	30022	3.955	−6172.5	−5928.7	67.30	35.71	52.89	1179
56	24.42	29784	3.926	−6146.0	−5901.8	67.78	35.60	52.88	1176
58	24.58	28861	3.814	−6041.9	−5796.1	69.64	35.20	52.85	1164
60	24.74	27956	3.704	−5937.8	−5690.4	71.43	34.80	52.82	1152
62	24.90	27071	3.597	−5833.8	−5584.8	73.16	34.42	52.79	1139
64	25.07	26204	3.493	−5729.9	−5479.2	74.84	34.05	52.77	1127
66	25.24	25355	3.390	−5626.1	−5373.7	76.46	33.69	52.75	1114
68	25.41	24524	3.291	−5522.3	−5268.2	78.04	33.35	52.73	1101
70	25.58	23711	3.193	−5418.6	−5162.7	79.56	33.02	52.72	1088
72	25.76	22915	3.098	−5314.9	−5057.3	81.05	32.70	52.71	1075
74	25.94	22137	3.006	−5211.3	−4951.9	82.49	32.38	52.71	1061
76	26.13	21375	2.915	−5107.7	−4846.4	83.90	32.08	52.71	1048
78	26.31	20629	2.827	−5004.1	−4741.0	85.27	31.79	52.72	1034
80	26.51	19900	2.741	−4900.6	−4635.5	86.60	31.51	52.74	1020
82	26.70	19186	2.657	−4797.0	−4530.0	87.91	31.24	52.76	1006
84	26.90	18488	2.576	−4693.4	−4424.4	89.18	30.98	52.79	992
86	27.11	17806	2.496	−4589.9	−4318.8	90.42	30.72	52.82	978
88	27.31	17138	2.418	−4486.2	−4213.1	91.64	30.47	52.87	964
90	27.53	16485	2.342	−4382.5	−4107.3	92.83	30.23	52.93	950
92	27.74	15847	2.268	−4278.8	−4001.3	93.99	30.00	52.99	935
94	27.97	15223	2.196	−4174.9	−3895.3	95.13	29.77	53.07	921
96	28.20	14613	2.126	−4071.0	−3789.0	96.25	29.55	53.16	906
98	28.43	14016	2.058	−3966.9	−3682.6	97.35	29.33	53.26	892
100	28.67	13433	1.991	−3862.7	−3576.0	98.42	29.11	53.38	877
102	28.92	12863	1.926	−3758.3	−3469.1	99.48	28.90	53.51	863
104	29.17	12305	1.863	−3653.6	−3361.9	100.52	28.70	53.66	848
106	29.43	11761	1.801	−3548.8	−3254.5	101.55	28.49	53.82	833
108	29.70	11228	1.741	−3443.6	−3146.6	102.55	28.29	54.01	818
110	29.98	10708	1.682	−3338.2	−3038.4	103.55	28.09	54.22	804
112	30.27	10199	1.625	−3232.4	−2929.7	104.53	27.89	54.45	789
114	30.56	9703	1.569	−3126.2	−2820.6	105.49	27.69	54.70	774
116	30.87	9217	1.514	−3019.6	−2710.9	106.45	27.49	54.99	759
118	31.19	8743	1.461	−2912.5	−2600.6	107.39	27.29	55.30	744
120	31.52	8280	1.408	−2804.8	−2489.6	108.32	27.09	55.65	729
122	31.87	7828	1.357	−2696.5	−2377.8	109.25	26.88	56.04	714
124	32.23	7387	1.307	−2587.5	−2265.3	110.16	26.67	56.47	699
126	32.60	6957	1.258	−2477.8	−2151.7	111.07	26.46	56.94	684
128	33.00	6537	1.210	−2367.1	−2037.2	111.97	26.25	57.47	669
130	33.41	6091	1.161	−2253.9	−1919.8	112.88	26.76	58.90	647
132	33.85	5685	1.112	−2140.1	−1801.6	113.78	26.64	59.51	630
134	34.31	5309	1.066	−2024.8	−1681.7	114.68	26.52	60.27	614
136	34.79	4941	1.019	−1908.4	−1560.4	115.58	26.39	61.00	597
138	35.31	4583	0.9747	−1790.6	−1437.5	116.48	26.26	61.92	581
140	35.86	4239	0.9307	−1671.2	−1312.6	117.38	26.15	62.93	565
142	36.44	3899	0.8875	−1550.0	−1185.6	118.28	26.05	64.15	548
144	37.07	3572	0.8434	−1427.0	−1056.3	119.18	25.97	65.36	530
146	37.74	3263	0.7974	−1301.9	−924.6	120.09	25.91	66.42	511
148	38.47	2956	0.7602	−1173.9	−789.2	121.01	25.87	68.68	495
150	39.26	2665	0.7139	−1043.4	−650.8	121.94	25.85	70.06	475
152	40.12	2384	0.6722	−909.6	−508.3	122.88	25.84	72.22	456
154	41.08	2120	0.6321	−771.8	−361.0	123.85	25.85	74.84	438
156	42.14	1863	0.5894	−630.1	−208.7	124.83	25.88	77.55	418
158	43.34	1632	0.5506	−482.9	−49.5	125.84	25.93	81.05	399
160	44.70	1413	0.5105	−330.2	116.7	126.89	26.61	85.56	377
165	49.05	952	0.4112	84.2	574.7	129.71	26.69	97.19	329
170	55.48	642	0.3220	547.9	1102.7	132.86	26.93	111.47	288
175	64.63	501	0.2483	1038.8	1685.1	136.23	26.89	116.90	261
180	75.66	496	0.1960	1493.8	2250.4	139.42	26.39	106.18	250
185	86.75	564	0.1611	1872.3	2739.8	142.10	25.74	89.82	248
190	97.07	655	0.1376	2183.6	3154.3	144.32	25.12	76.87	250
195	106.54	753	0.1209	2447.8	3513.2	146.18	24.59	67.52	254
200	115.30	851	0.1083	2679.5	3832.4	147.80	24.14	60.83	259
210	131.20	1037	0.0909	3080.3	4392.3	150.53	23.47	52.29	269
220	145.55	1211	0.0789	3429.1	4884.6	152.82	23.00	46.97	278
230	158.86	1373	0.0701	3746.4	5334.9	154.83	22.65	43.42	287
240	171.39	1525	0.0634	4042.4	5756.3	156.62	22.37	40.98	295
250	183.34	1670	0.0581	4323.1	6156.6	158.25	22.14	39.16	304
260	194.84	1807	0.0538	4592.4	6540.9	159.76	21.94	37.76	312
270	205.98	1940	0.0502	4852.9	6912.7	161.17	21.78	36.65	319
280	216.81	2068	0.0471	5106.5	7274.6	162.48	21.64	35.77	327
290	227.41	2192	0.0445	5354.5	7628.6	163.72	21.53	35.05	334
300	237.81	2312	0.0421	5598.0	7976.1	164.90	21.44	34.47	341

*Two-phase boundary.

TABLE 14. *Thermodynamic properties of oxygen.*—Continued

20 MN/m² Isobar

T	V	$\left(\frac{\partial P}{\partial \rho}\right)_T$	$\left(\frac{\partial P}{\partial T}\right)_\rho$	Internal Energy	Enthalpy	Entropy	C_v	C_p	Vel. of Sound
K	cm³/mol	J/mol	MN/m²·K	J/mol	J/mol	J/mol·K	J/mol·K	J/mol·K	m/s
*56.614	24.27	31225	3.963	−6154.6	−5669.2	67.59	35.79	52.56	1197
58	24.38	30599	3.887	−6083.9	−5596.3	68.86	35.51	52.53	1189
60	24.53	29711	3.778	−5981.9	−5491.3	70.64	35.13	52.47	1178
62	24.68	28842	3.672	−5880.1	−5386.4	72.36	34.76	52.42	1166
64	24.84	27992	3.569	−5778.4	−5281.6	74.03	34.41	52.37	1154
66	25.00	27160	3.468	−5676.9	−5176.9	75.64	34.07	52.33	1142
68	25.16	26346	3.370	−5575.5	−5072.3	77.20	33.74	52.28	1130
70	25.32	25551	3.274	−5474.2	−4967.8	78.71	33.42	52.24	1117
72	25.49	24773	3.180	−5373.0	−4863.3	80.19	33.11	52.20	1105
74	25.65	24012	3.089	−5272.0	−4759.0	81.62	32.81	52.16	1092
76	25.82	23269	3.000	−5171.1	−4654.7	83.01	32.53	52.13	1080
78	26.00	22542	2.913	−5070.4	−4550.4	84.36	32.25	52.10	1067
80	26.17	21832	2.829	−4969.7	−4446.2	85.68	31.98	52.07	1054
82	26.35	21138	2.746	−4869.2	−4342.1	86.96	31.72	52.04	1041
84	26.53	20460	2.666	−4768.7	−4238.0	88.22	31.47	52.02	1028
86	26.72	19797	2.588	−4668.4	−4134.0	89.44	31.23	52.01	1015
88	26.91	19150	2.513	−4568.1	−4029.9	90.64	30.99	52.00	1002
90	27.10	18518	2.439	−4467.9	−3925.9	91.81	30.76	51.99	989
92	27.30	17901	2.367	−4367.8	−3821.9	92.95	30.54	51.99	976
94	27.49	17298	2.297	−4267.8	−3718.0	94.07	30.32	51.99	963
96	27.70	16710	2.229	−4167.9	−3613.9	95.16	30.10	52.00	950
98	27.90	16135	2.163	−4068.0	−3509.9	96.23	29.89	52.01	937
100	28.11	15574	2.099	−3968.1	−3405.9	97.29	29.68	52.04	924
102	28.33	15027	2.036	−3868.3	−3301.8	98.32	29.48	52.06	911
104	28.55	14493	1.976	−3768.6	−3197.6	99.33	29.27	52.10	898
106	28.77	13972	1.917	−3668.8	−3093.4	100.32	29.07	52.14	885
108	29.00	13464	1.859	−3569.1	−2989.0	101.30	28.86	52.19	872
110	29.24	12968	1.804	−3469.4	−2884.6	102.25	28.66	52.25	860
112	29.48	12485	1.750	−3369.6	−2780.0	103.20	28.45	52.31	847
114	29.73	12014	1.697	−3269.8	−2675.3	104.12	28.23	52.39	835
116	29.98	11554	1.646	−3170.0	−2570.5	105.04	28.02	52.47	822
118	30.24	11106	1.597	−3070.2	−2465.4	105.93	27.79	52.56	810
120	30.50	10670	1.549	−2970.2	−2360.1	106.82	27.56	52.66	798
122	30.78	10245	1.502	−2870.2	−2254.7	107.69	27.32	52.77	786
124	31.06	9831	1.456	−2770.1	−2148.9	108.55	27.07	52.88	775
126	31.35	9428	1.412	−2669.9	−2042.9	109.40	26.81	53.01	763
128	31.65	9036	1.370	−2569.6	−1936.6	110.23	26.54	53.16	752
130	31.96	8637	1.326	−2467.7	−1828.6	111.07	27.06	54.07	734
132	32.27	8262	1.279	−2365.9	−1720.5	111.90	26.97	54.20	720
134	32.60	7889	1.237	−2263.8	−1611.8	112.71	26.87	54.48	707
136	32.94	7532	1.200	−2161.0	−1502.2	113.53	26.77	54.99	695
138	33.29	7186	1.159	−2057.9	−1392.1	114.33	26.65	55.23	682
140	33.65	6854	1.121	−1954.4	−1281.3	115.13	26.53	55.63	670
142	34.03	6538	1.079	−1850.7	−1170.2	115.91	26.41	55.71	657
144	34.42	6218	1.040	−1746.9	−1058.6	116.70	26.28	55.93	643
146	34.83	5928	1.017	−1641.9	−945.4	117.48	26.15	57.04	636
148	35.24	5644	0.9704	−1537.3	−832.4	118.24	26.04	56.71	620
150	35.68	5372	0.9374	−1432.1	−718.5	119.01	25.93	57.17	608
152	36.13	5107	0.9000	−1326.8	−604.2	119.77	25.83	57.30	595
154	36.60	4853	0.8747	−1220.5	−488.4	120.52	25.74	58.27	586
156	37.09	4627	0.8343	−1114.4	−372.5	121.27	25.65	57.94	571
158	37.60	4371	0.8127	−1007.2	−255.2	122.02	25.57	59.33	563
160	38.14	4148	0.7778	−899.7	−136.9	122.76	26.10	60.04	546
165	39.57	3630	0.7022	−627.0	164.5	124.62	25.72	60.82	518
170	41.18	3172	0.6337	−351.7	471.8	126.45	25.60	62.09	490
175	42.97	2777	0.5699	−73.8	785.6	128.27	25.53	63.32	464
180	44.97	2447	0.5119	206.1	1105.5	130.07	25.43	64.41	440
185	47.21	2180	0.4601	486.5	1430.7	131.86	25.26	65.29	420
190	49.68	1973	0.4127	764.5	1758.0	133.60	25.08	65.56	401
195	52.37	1818	0.3710	1038.1	2085.5	135.30	24.88	65.38	386
200	55.26	1709	0.3339	1304.8	2410.1	136.95	24.67	64.49	374
210	61.53	1598	0.2747	1812.4	3042.9	140.03	24.29	61.83	357
220	68.17	1594	0.2307	2279.1	3642.5	142.82	23.90	58.03	348
230	74.91	1648	0.1980	2705.1	4203.3	145.32	23.54	54.25	344
240	81.62	1736	0.1736	3095.8	4728.1	147.55	23.21	50.97	345
250	88.15	1851	0.1535	3456.3	5219.3	149.56	22.90	47.62	347
260	94.51	1971	0.1386	3793.2	5683.3	151.38	22.62	45.25	351
270	100.70	2095	0.1265	4111.0	6125.0	153.05	22.36	43.25	356
280	106.73	2220	0.1163	4413.3	6547.9	154.58	22.11	41.52	361
290	112.62	2347	0.1077	4702.7	6955.1	156.01	21.86	40.06	367
300	118.38	2469	0.1006	4981.1	7348.7	157.35	21.61	38.84	372

*Two-phase boundary.

TABLE 14. *Thermodynamic properties of oxygen.*—Continued

30 MN/m² Isobar

T	V	$\left(\frac{\partial P}{\partial \rho}\right)_T$	$\left(\frac{\partial P}{\partial T}\right)_\rho$	Internal Energy	Enthalpy	Entropy	C_v	C_p	Vel. of Sound
K	cm³/mol	J/mol	MN/m²-K	J/mol	J/mol	J/mol-K	J/mol-K	J/mol-K	m/s
*57.720	24.17	32404	3.970	−6135.9	−5410.8	67.88	35.87	52.27	1215
58	24.19	32280	3.955	−6121.8	−5396.2	68.13	35.82	52.26	1213
60	24.33	31406	3.847	−6021.7	−5291.7	69.90	35.45	52.19	1202
62	24.48	30551	3.742	−5921.8	−5187.4	71.61	35.09	52.12	1191
64	24.63	29714	3.640	−5822.0	−5083.2	73.26	34.75	52.05	1179
66	24.78	28897	3.540	−5722.4	−4979.2	74.86	34.42	51.99	1168
68	24.93	28098	3.442	−5623.1	−4875.3	76.41	34.11	51.92	1156
70	25.08	27316	3.347	−5523.9	−4771.5	77.92	33.80	51.86	1144
72	25.24	26553	3.255	−5424.9	−4667.8	79.38	33.51	51.80	1133
74	25.39	25807	3.165	−5326.0	−4564.3	80.80	33.22	51.74	1121
76	25.55	25078	3.077	−5227.4	−4460.8	82.18	32.95	51.68	1109
78	25.71	24365	2.991	−5128.9	−4357.5	83.52	32.68	51.62	1097
80	25.88	23670	2.908	−5030.6	−4254.3	84.82	32.43	51.56	1085
82	26.04	22991	2.827	−4932.5	−4151.2	86.10	32.18	51.51	1072
84	26.21	22327	2.748	−4834.6	−4048.3	87.34	31.94	51.45	1060
86	26.38	21680	2.671	−4736.8	−3945.4	88.55	31.71	51.40	1048
88	26.55	21047	2.597	−4639.2	−3842.6	89.73	31.48	51.36	1036
90	26.73	20430	2.524	−4541.8	−3739.9	90.88	31.26	51.31	1024
92	26.91	19828	2.454	−4444.5	−3637.3	92.01	31.04	51.26	1012
94	27.09	19240	2.385	−4347.4	−3534.8	93.11	30.83	51.22	999
96	27.27	18667	2.319	−4250.5	−3432.4	94.19	30.62	51.18	987
98	27.46	18108	2.254	−4153.7	−3330.1	95.25	30.42	51.15	975
100	27.64	17562	2.191	−4057.1	−3227.8	96.28	30.21	51.11	964
102	27.84	17030	2.131	−3960.7	−3125.6	97.29	30.01	51.08	952
104	28.03	16511	2.072	−3864.4	−3023.5	98.28	29.81	51.05	940
106	28.23	16005	2.014	−3768.3	−2921.4	99.26	29.61	51.02	928
108	28.43	15512	1.959	−3672.4	−2819.4	100.21	29.40	51.00	917
110	28.64	15031	1.905	−3576.6	−2717.4	101.14	29.19	50.98	906
112	28.85	14562	1.853	−3481.0	−2615.5	102.06	28.97	50.95	895
114	29.06	14105	1.803	−3385.5	−2513.6	102.97	28.75	50.93	884
116	29.28	13660	1.754	−3290.2	−2411.7	103.85	28.52	50.91	873
118	29.50	13227	1.706	−3195.0	−2309.9	104.72	28.29	50.90	862
120	29.73	12804	1.660	−3100.0	−2208.1	105.58	28.04	50.88	852
122	29.96	12393	1.616	−3005.2	−2106.3	106.42	27.77	50.86	842
124	30.20	11992	1.573	−2910.5	−2004.5	107.25	27.50	50.83	832
126	30.44	11602	1.532	−2816.0	−1902.7	108.06	27.21	50.81	823
128	30.69	11223	1.491	−2721.6	−1801.0	108.86	26.90	50.79	814
130	30.94	10917	1.450	−2626.1	−1697.9	109.66	27.43	51.41	800
132	31.20	10519	1.407	−2530.7	−1594.8	110.45	27.35	51.53	787
134	31.46	10272	1.389	−2434.4	−1490.5	111.23	27.26	52.19	784
136	31.73	9873	1.337	−2338.9	−1387.0	112.00	27.17	51.96	768
138	32.01	9515	1.297	−2243.3	−1283.1	112.76	27.07	52.08	756
140	32.29	9174	1.263	−2147.5	−1178.8	113.51	26.97	52.34	746
142	32.58	8878	1.233	−2051.3	−1073.8	114.25	26.86	52.69	738
144	32.87	8523	1.168	−1956.3	−970.1	114.98	26.76	51.68	717
146	33.18	8180	1.158	−1860.2	−864.9	115.70	26.64	52.98	713
148	33.49	7933	1.127	−1763.9	−759.1	116.42	26.52	53.10	705
150	33.82	7660	1.090	−1668.0	−653.5	117.13	26.40	53.03	693
152	34.14	7398	1.053	−1572.4	−548.1	117.83	26.27	52.82	682
154	34.48	7145	1.035	−1476.4	−441.9	118.52	26.14	53.59	677
156	34.83	6844	0.9967	−1380.8	−336.0	119.21	26.01	53.48	663
158	35.18	6674	0.9615	−1285.2	−229.7	119.88	25.90	52.99	653
160	35.54	6372	0.9238	−1190.3	−124.1	120.55	26.41	53.47	635
165	36.49	5863	0.8693	−948.6	146.3	122.21	25.99	54.32	619
170	37.51	5402	0.8055	−707.3	418.0	123.83	25.86	54.59	597
175	38.59	4974	0.7465	−466.3	691.5	125.42	25.79	54.98	576
180	39.74	4569	0.6894	−226.1	966.1	126.97	25.69	55.26	554
185	40.97	4233	0.6380	13.3	1242.3	128.48	25.54	55.40	536
190	42.27	3927	0.5910	251.2	1519.3	129.96	25.34	55.54	519
195	43.65	3665	0.5471	486.6	1796.1	131.40	25.10	55.44	503
200	45.11	3431	0.5076	718.8	2072.2	132.79	24.81	55.38	489
210	48.26	3096	0.4379	1172.7	2620.6	135.47	24.31	54.60	466
220	51.66	2888	0.3794	1610.2	3160.0	137.98	23.98	53.24	448
230	55.28	2741	0.3333	2029.0	3687.4	140.32	23.68	52.16	434
240	59.05	2693	0.2948	2429.8	4201.2	142.51	23.45	50.46	426
250	62.88	2692	0.2627	2809.8	4696.3	144.53	23.22	48.56	420
260	66.77	2701	0.2367	3170.8	5173.8	146.41	22.97	47.02	416
270	70.67	2745	0.2148	3514.9	5635.0	148.15	22.71	45.37	414
280	74.57	2816	0.1970	3844.3	6081.3	149.77	22.46	43.93	415
290	78.44	2908	0.1819	4160.3	6513.6	151.29	22.23	42.53	417
300	82.28	3005	0.1690	4464.0	6932.3	152.71	22.00	41.30	420

*Two-phase boundary.

TABLE 15. *The Joule-Thomson inversion curve*

T K	*P* MN/m²	Density mol/cm³	ΔP[a] MN/m²
125	1.58	0.02942	0.18
130	5.34	.02907	.20
135	8.76	.02869	.21
140	12.07	.02835	.23
145	15.29	.02802	.26
150	18.07	.02765	.26
155	20.73	.02729	.29
160	23.57	.02700	.29
165	25.97	.02666	.31
170	28.27	.02633	.32
175	30.46	.02600	.34
180	32.55	.02569	.35
185	34.46	.02537	.38
190	36.24	.02504	.38

[a] The uncertainty due to a 1 percent assumed uncertainty in either the isotherm or the isochore derivative.

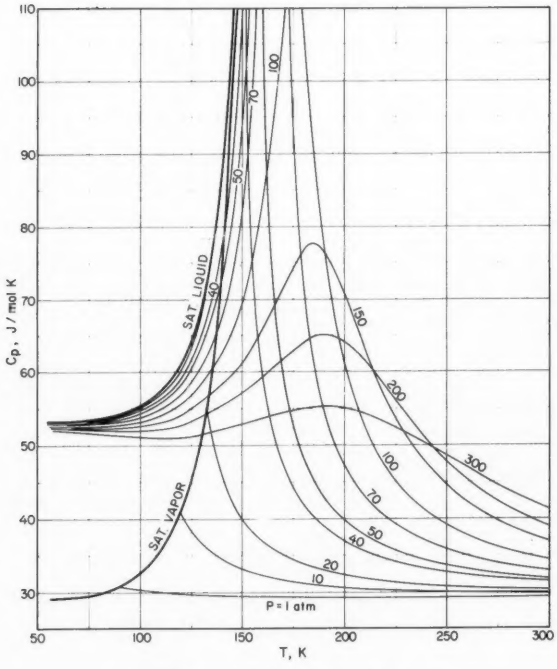

FIGURE 5. C_p *along selected isobars.*

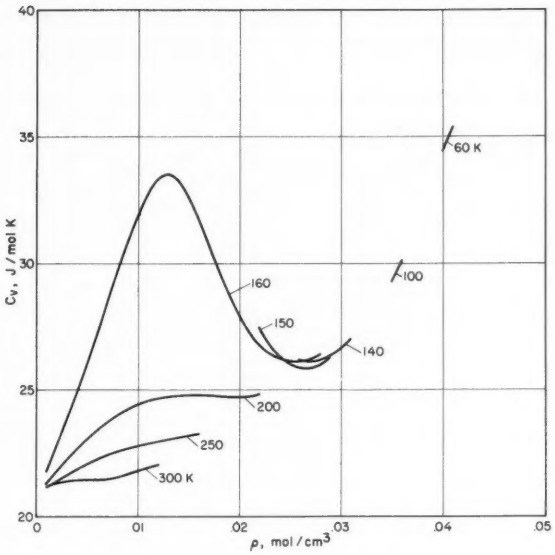

FIGURE 6. C_v *along selected isotherms.*

were also calculated by means of the Clapeyron equation, using the same pressure equation, and differ from those in column four only through the use of somewhat different values for the virial coefficients. A comparison of columns 2 and 3 indicates the degree of thermodynamic consistency in the present method of calculation. Differences between ΔH and $T\Delta S$ of 1 to 3 J/mol may be expected in these calculations. However, the first line of table 16 reveals a discrepancy of 20 J/mol at the triple point, which must be explained. The problem arises from the second term, $-R \ln (RT\rho/P_0)$, in eq (16) for the entropy of the vapor phase. The density, ρ, is found from the vapor pressure, eq (7), which is based upon Hoge's [10] value of 1.14 mm for the triple point pressure. This value is subject to a large relative uncertainty. In a more recent work Muijlwijk et al. [22], found a value of 1.097_5 mm, or a difference of 3.7 percent. Using this latter triple point pressure results in a value of 7758 J/mol for $T\Delta S$ in much better agreement with the calculated ΔH. Thus we must conclude that the triple point pressure is closer to 1.0975 mm and eq (7) should be modified accordingly. This same error would also be evident in the value of the density of the saturated vapor given in table 13.

The problem is also apparent to a lesser extent in the next three lines of table 16. This inaccuracy affects only the calculated thermodynamic properties of the saturated vapor near the triple point. Values of ΔH calculated by means of the Clapeyron equation suffer from the large relative uncertainty in the slope of the vapor pressure curve at low temperatures. The last two columns of table 16 contain some experimental measurements of the heat of vaporization.

The entropy of the liquid at the triple point, calculated by the path described in section 3.1, is 67.001 J/mol-K. The entropy for this point, calculated by Giauque and Johnston [15] from their calorimetric data on solid oxygen, is $67.095 \pm .15$ J/mol-K. Thus we see that the two experiments are consistent with the Third Law.

The calculated velocity of sound in the saturated liquid is compared with the measurements of Blagoi et al. [28], and of Van Itterbeek and Van Dael [29, 32] in figure 7. The change in the P–V–T surface representation from Region I to Region II at 128 K is apparent. Most of the scatter apparent near the critical point occurs in the calculated rather than the experimental values. The agreement is reasonable if we consider that the comparison is made along an edge of the surface representation. Similarly table 17 contains a comparison with the experimental values in the com-

TABLE 16. *Comparison of calculated and measured heats of vaporization in J/mol*

Temp.	Calculated – This Research			Ref. [11] Clapeyron equation	Ref. [15]	Ref. [24]
	Table 13		Clapeyron equation		Experimental	
	ΔH	$T\Delta S$				
54.350_7	7761	7741	7678			
60	7624	7634	7516			
68.4	7417	7413	7416	7416		7418
70	7377	7381	7379	7384		
76	7221	7220	7240	7244		7228
80	7113	7110	7131	7137		
84.1	6997	6995	7009	7017		7005
90	6818	6815	6820	6832		
90.18	6812	6809	6810	6826	6815 ± 6.8	6825
100	6473	6471	6459	6477		
110	6058	6058	6039	6061		
120	5546	5546	5532	5555		
130	4891	4893	4888	4906		
140	4002	4003	4009	4013		
150	2543	2544	2549	2578		

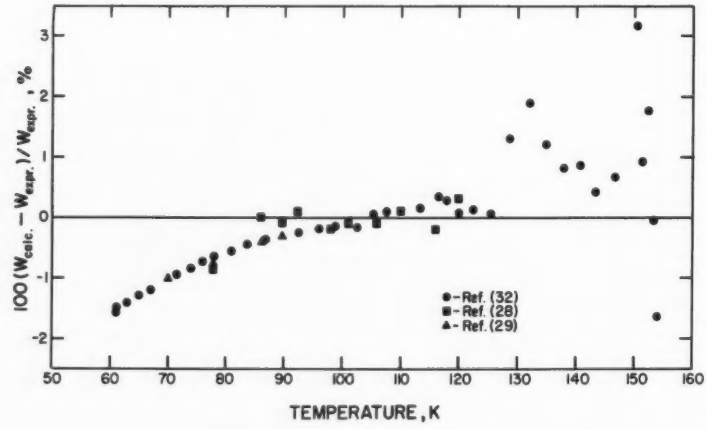

FIGURE 7. *Comparison of experimental and calculated sound velocities in the saturated liquid.*

pressed liquid. The agreement leaves something to be desired. Each isotherm from 67.5 K to 90.4 K shows the same behavior; the disagreement gets worse as the pressure goes up, reaching 2.1 percent at pressures of about 30 MN/m². An error in the elastic stretching coefficient of the sample holder, "a" in eq (1) could account for a portion of the error on each isotherm. For example, a 100 percent error in "a" would change the calculated velocities by 0.9 percent at 0.1 MN/m² and 1.2 percent at 30 MN/m² at 70 K and by 0.6 to 0.9 percent at 90 K. Another 0.5 percent might be attributed to the analytic surface used to fit the data. In addition, close examination of references [28] and [29] will reveal discrepancies of 0.2–0.4 percent between the various experimental measurements. Further experimental measurements on the velocity of sound in the compressed liquid would be very desirable. The last section of table 17 contains a comparison with the work of Van Itterbeek and Van Dael in the low density gas. Here the agreement is somewhat better and it is felt that the calculated values are more reliable than the experimental measurements.

Comparison with the measurements of C_v by Voronel, et al. [30], reveals good agreement at 160 K. The disagreement becomes quite large nearer the critical point, and this is to be expected since no mechanism causing C_v to diverge was incorporated into the P–V–T surface used here. Comparison of the calculated C_v's with the measurements of Goodwin and Weber [6] revealed generally excellent agreement over the whole P–V–T surface. Small irregularities

TABLE 17. *Comparison with experimental measurements of the velocity of sound in compressed liquid and in low density gas*

Temp K	Press MN/m^2	$100(W_{exp}-W_{calc})/W_{exp}$ Ref. [29]
67.53	29.5	2.11
	19.8	1.89
	9.7	1.62
	0.40	1.29
	34.6	2.15
73.43	24.8	1.87
	14.9	1.67
	5.0	1.40
	29.6	2.18
77.72	19.6	1.85
	9.9	1.39
	0.19	0.94
	34.2	2.22
83.83	24.8	1.81
	15.0	1.47
	5.8	1.10
	29.7	2.14
90.40	19.9	1.61
	10.1	1.06
	0.19	0.52
231.8	2.91	−0.07
248.8	5.11	.77
274.2	4.07	.35

may be seen in the 300 K isotherm for C_v in figure 6. These are probably caused by small errors in the second derivatives near the edge of the P–V–T surface.

The author is grateful to R. D. Weekley and L. J. Ericks for the preparation of the figures. He would also like to thank B. A. Younglove, D. E. Diller, and R. D. Goodwin for valuable comment and discussion. This project has been supported by the National Aeronautics and Space Administration.

4. References

[1] Timrot, D. L., and Borisoglebskii, V. P., Soviet Phys. JETP **11**, No. 6, 1248–50 (1960).
[2] Timrot, D. L., and Borisoglebskii, V. P., Office of Technical Services, Washington, D.C., Order No. 6121722 (April 1961).
[3] Van Itterbeek, A., and Verbeke, O., Cryogenics **1**, No. 2, 77–80 (1960).
[4] Van Itterbeek, A., and Verbeke, O., Cryogenics **2**, No. 2, 79–80 (1961).
[5] Woolley, H. W., J. Res. NBS **40**, 163–68 (1948) RP 1864.
[6] Goodwin, R. D., and Weber, L. A., J. Res. Nat. Bur. Stand. (U.S.), **73A**, (Phys. and Chem.) No. 1, 15–24 (Jan.–Feb. 1969).
[7] Goodwin, R. D. and Weber, L. A., J. Res. Nat. Bur. Stand. (U.S.), **73A**, (Phys. and Chem.) No. 1, 1–13 (Jan.–Feb. 1969).
[8] Goodwin, R. D., J. Res. Nat. Bur. Stand. (U.S.) 65C (Eng. and Instr.), No. 4, 231–243 (Oct.–Dec. 1961).
[9] Wassenaar, T., Thesis, Univ. Amsterdam (1952).
[10] Hoge, H. J., J. Res. NBS **44**, 321–45 (1950) RP 2081.
[11] Stewart, R. B., Thesis, Dept. Mech. Eng., Univ. Iowa (1966).
[12] Hust, J. G., and McCarty, R. D., Cryogenics, 200–06 (Aug. 1967).
[13] Mills, R. L., and Grilly, E. R., Phys. Rev. **99**, No. 2, 480–86 (1955).
[14] Weber, L. A., to be published.
[15] Giauque, W. F., and Johnston, H. L., J. Am. Chem. Soc. **51**, 2300–21 (1929).
[16] Michels, A., Schamp, H. W., and de Graaff, W., Physica **20**, 1209–14 (1954).
[17] Kuypers, H. A., and Kamerlingh Onnes, H., Comm. Leiden, nr. 165a (1923).
[18] Holborn, L., and Otto, J., Zs. f. Physik **10**, 367 (1922).
[19] Nijhoff, G. P., and Keesom, W. H., Communs. Phys. Lab. Univ. Leiden No. 179b (1925).
[20] Van Itterbeek, A., and Van Paemel, O., Physica **5**, No. 7, 593–604 (1938).
[21] Van Lammeren, J. A., Communs. Phys. Lab. Univ. Leiden Suppl. No. 77b (1935), or Physica **2**, 833 (1935).
[22] Muijlwijk, R., Moussa, M. R., and van Dijk, H. Physica **32**, 805–822 (1966).
[23] Mathias, E., and Kamerlingh Onnes, H., Communs. Phys. Lab. Univ. Leiden No. 117 (1911).
[24] Furukawa, G. T., and McCoskey, R. E., NACA Tech. Note 2969 (1953).
[25] Lisman, J. H. C., and Keesom, W. H., Physica **2**, 901–06 (1935).
[26] Jahnke, J. A., J. Chem. Phys. **47**, 336 (1967).
[27] Tolkachev, A. M., and Manzhelii, V. G., Soviet Phys. Solid State, **7**, No. 7, 1711–3 (Jan. 1966).
[28] Blagoi, Yu. P., Butko, A. E., Mikhailenko, S. A., and Yakuba, V. V., Soviet Phys.–Acoustics **12**, No. 4 (1967).
[29] Van Itterbeek, A., and Van Dael, W., Physica **28**, No. 9, 861–70 (1962).
[30] Voronel, A. V., Chashkin, Yu. R., Popov, V. A., and Simkin, V. G., Soviet Phys. JETP **18**, 568–9 (1964).
[31] Cath, P. G., and Kamerlingh Onnes, H., Comm. Leiden, nr. 156a (1922).
[32] Van Dael, W., Van Itterbeek, A., Cops, A., and Thoen, J., Physica **32**, 611–20 (1966).

(Paper 74A1–587)

367–409 OL–70—9

JOURNAL OF RESEARCH of the National Bureau of Standards—A. Physics and Chemistry
Vol. 74A, No. 1 January–February 1970

Publications of the National Bureau of Standards*

Selected Abstracts

CODASYL COBOL, *Journal of Development 1968, Nat. Bur. Stand. (U.S.), Handb. 106, 344 pages (July 1969), $2.75.*

Key words: COBOL; CODASYL; journal.

This document is a report to the COBOL community from the Conference on Data Systems Languages (CODASYL) Common Business Oriented Language (COBOL) Programming Language Committee. It is an official report documenting the development activities of CODASYL through July 1968.

Colwell, J. H., Mangum, B. W., Utton, D. B., **The low temperature magnetic properties of some hexagonal rare-earth trihalides,** *Phys. Rev.* **181,** *No. 2, 842–854 (May 10, 1969).*

Key words: Heat capacity; linear chain models; low temperature; magnetic properties; magnetic susceptibility; nuclear quadrupole resonance; rare-earth trihalides; spontaneous magnetization.

We have made measurements of the low temperature heat capacity, magnetic susceptibility, and chlorine nuclear quadrupole resonance (NQR) of $CeCl_3$, $PrCl_3$, $NdCl_3$, $SmCl_3$, and $CeBr_3$. Some measurements have been made on $PrBr_3$ and $NdBr_3$. The experimental results can be closely correlated with antiferromagnetic linear chain models. The NQR shows that long-range order occurs in $PrCl_3$ at 0.428 K. In $NdCl_3$ the NQR line disappeared at 0.50 K and the resonances produced by an internal field appeared at 0.17 K. In $CeCl_3$ the NQR resonance disappeared at 0.110 K. In $CeCl_3$ the NQR resonance disappeared at 0.110 K and no lines were found above 0.054 K. In $SmCl_3$ the NQR line disappeared at 0.21 K and no resonance was observed above 0.1. K. In $PrCl_3$ and $NdCl_3$ we have measured the internal field, which is proportional to the sublattice magnetization, at the chlorine nucleus below their Néel temperatures and have determined the magnitude and the direction of the internal field at the chlorine nucleus relative to the principal axes of the electric field gradient.

Abramowitz, S., Levin, I. W., **Raman spectrum of ONF_3,** *J. Chem. Phys.* **51,** *No. 1, 463–464 (July 1, 1969).*

Key words: Infrared trifluoramine oxide; laser, low temperature; Raman; vibrational assignment.

The Raman spectrum of a polycrystalline film of trifluoramine oxide at 78 °K has been observed. The fundamental frequencies of the bending modes $\nu_3(A_1)$ and $\nu_5(E)$ are found at 535 and 522 cm^{-1}. The doubly degenerate NF_2 stretching mode, $\nu 4$, is thought to be complicated by a resonance between ν_4 and $\nu_5 + \nu_6$.

Bates, R. G., **Inner reference electrodes and their characteristics,** *Chapter in Glass Microelectrodes,* M. Lavallee, O. F. Schanne, and N. C. Hebert, Eds., *pp. 1–24 (John Wiley and Sons, Inc., New York, N.Y., 1969).*

Key words: Glass electrode; inner solutions; pH measurement calomel electrode; reference electrodes; silver-silver chloride electrode; temperature coefficients of e.m.f.

The principles governing the selection of the most suitable electrodes and inner solutions for making electrical contact with the reference side of the glass electrode are set forth. Particular attention is given to choice of the best electrode and solution composition to minimize, or even to nullify, the temperature variation of the standard e.m.f. of the pH cell. Temperature coefficients of the e.m.f. of glass electrode pH cells of various designs are listed and other useful characteristics of inner electrodes and inner solutions are summarized.

Bates, R. G., **Medium effects and pH in nonaqueous solvents,** *Chapter in Solute-Solvent Interactions,* C. D. Ritchie and J. F. Coetzee, Eds., *pp. 45–96 (Marcel Dekker Inc., New York, N.Y., 1969).*

Key words: Acidity; ion activity; medium effect; nonaqueous solvents; pH; thermodynamics.

The nature of acidity in nonaqueous solvents of various types is discussed and the implications of acid-base behavior on the feasibility of establishing useful scales for experimental pH and acidity measurement are considered. The Brønsted concept provides a useful approach to the quantitative expression of acid-base potential in many solvent media with some acidic or basic character but is of doubtful value in aprotic or inert solvents. A general scale of acidity or electrode potential applicable to more than one solvent requires a knowledge of the medium effect of the proton or the free energy of transfer of the proton from one solvent to another. Various methods of determining medium effects for ions are considered and shown to be inadequate at the present time. The role of dielectric constant and solvation phenomena in the medium effect are discussed, and suggestions are made for the practical measurement of acidity in deuterium oxide and alcohol-water solvents.

Bennett, H. S., **Ultrasonic attenuation in Heisenberg magnets,** *Phys. Rev.* **181,** *No. 2, 978 (May 10, 1969).*

Key words: Antiferromagnet; critical fluctuations; ferromagnet; Gd; Heisenberg magnet; MnF_2; $RbMnF_3$; ultrasonic attenuation.

The microscopic theory developed by H. S. Bennett and E. Pytte to treat ultrasonic attenuation in Heisenberg magnets overestimates the critical fluctuations. It is shown that much better agreement with experiment obtains when this fact is explicitly taken into account.

Berger, M. J., Seltzer, S. M., Chappell, S. E., Humphreys, J. C., Motz, J. W., **Table of response functions for silicon electron detectors,** *Nat. Bur. Stand. (U.S.), Tech. Note 489, 62 pages (Aug. 1969), 60 cents.*

Key words: Electron; energy absorption; electron back-scattering; electron transmission; detector response function; silicon detectors.

Calculated response functions are presented which describe the pulse-height distributions produced by monoenergetic electrons incident on silicon detectors. It is assumed that the direction of incidence is perpendicular, and that the detectors are wide enough so that lateral leakage of energy is insignificant. The validity of the

calculations has been confirmed experimentally for incident energies between 0.25 MeV and 1.0 MeV and detectors with thicknesses between 0.061 mm and 3.0 mm. The calculated response functions cover a wider range of conditions, including fourteen energies between 0.15 MeV and 5.0 MeV and ten detector thicknesses between 0.05 and 10.0 mm. At energies ≥ 1 MeV, response functions are given not only for bare detectors but also for an arrangement in which the detectors are shielded on the transmission side by another detector operating in anti-coincidence.

Boyd, M. E., Larsen, S. Y., Kilpatrick, J. E., **Quantum mechanical second virial coefficient of a Lennard-Jones Gas. Helium,** *J. Chem. Phys.* **50,** *No. 9, 4034–4055 (May 1, 1969).*

Key words: Equation of state; exchange effects; helium; Lennard-Jones gas; second virial coefficient; Wigner-Kirkwood expansion.

The quantum mechanical second virial coefficients of Lennard-Jones He^3 and He^4 gases with the De Boer parameters have been obtained over the complete temperature range from near absolute zero to the classical region. A formalism separating the virial into direct (Boltzmann) and exchange (spin and quantum statistics) contributions has been employed. The calculation is based on phase shifts except at the very highest temperatures where a Wigner-Kirkwood method has been used. Examinations of the exchange term shows in detail the rapid suppression of the statistical effects with rising temperature, their contribution dropping to less than .001 cm^3 by 7 °K (He^4). Comparison of the high temperature (Boltzmann) results with those obtained by a third order Wigner-Kirkwood expansion shows excellent agreement down to about 50 °K for He^4 and 60° for He^3. The Wigner-Kirkwood expansion is shown to be unsuitable for determining the behavior of the exchange terms.

Bur, A. J., Roberts, D. E., **Rodlike and random-coil behavior of poly(*n*-butyl isocyanate) in dilute solutions,** *J. Chem. Phys.* **51,** *No. 1, 406–420 (July 1, 1969).*

Key words: Dielectric constant; dielectric relaxation time; dipole moment; Kratky-Porod worm-like model; molecular relaxation in dilute solution; poly(butyl-isocyanate); polymer chain configuration; polypeptides; rodlike molecules.

The polymer chain configuration, molecular relaxation and the dipole moment of poly(*n*-butyl isocyanate), $(-CO-NR-)_n$ where $R=C_4H_9$, have been studied by dielectric measurements of the polymer in dilute solution. The complex dielectric constant, $\epsilon^* = \epsilon' - j\epsilon''$, was measured at room temperature over a frequency range 10^{-1} Hz to 1×10^6 Hz for fractionated samples whose molecular weights cover a very broad range, 20×10^3 to 10×10^6. From observation of the dielectric relaxation time as a function of molecular weight we deduce that the low molecular weight molecule ($M_w < 80 \times 10^3$) is rodlike and helical. Upon increasing the molecular weight, this rodlike conformation can not be sustained and chain flexibility accumulates with the addition of each monomer unit to the chain. Finally at high molecular weight, $M_w > 10^6$, the polymer chain configuration can be described as random coil. The relaxation time and dipole moment measurements indicate that there is a one-to-one correspondence between the end-to-end distance and the dipole moment of the poly(*n*-butyl isocyanate) (PBIC) molecule. Using the dipole moment data alone, we are able to show that the PBIC chain configuration as a function of molecular weight can be described by the Kratky-Porod worm-like model. The relationship between PBIC and biological molecules, especially the polypeptides, is discussed.

Dehl, R. E., Hoeve, C. A. J., **Broadline NMR study of H_2O and D_2O in collagen fibers,** *J. Chem. Phys.* **50,** *No. 8, 3245–3251 (1969).*

Key words: Anisotropic molecular motion; Broadline NMR; D_2O in collagen; H_2O in collagen; proton exchange; quadrupole splitting.

The deuterium NMR spectra of D_2O absorbed in parallel collagen fibers have been recorded for samples containing four different percentages of D_2O. In all cases, the spectra consisted of a pair of lines, the separation of which is given by $K(3\cos^2\theta - 1)$, where K is small compared to the rigid-lattice value and decreases with increasing moisture content of the fibers, and θ is the angle between the fiber axis and the magnetic field. The splitting is ascribed to quadrupole perturbation of the Zeeman levels of deuterium, caused by slightly anisotropic but rapid reorientation of D_2O molecules in the fiber lattice. Contrary to the interpretation by others, we have concluded from a comparison of the spectra of D_2O and H_2O in collagen (1) that the center line in the H_2O spectra is not due to water, and (2) that line broadening in the H_2O spectra, both at high temperatures and in the presence of added salts, is due to proton exchange between the water molecules. Molecular motion causes both H_2O and D_2O splittings to be reduced to approximately the same fraction of their respective rigid-lattice splittings.

DeWit, R., **Differential geometry of the nonlinear continuum theory of dislocation** (*Proc. IUTAM Conf. Stuttgart, Germany, Aug. 28–Sept. 2, 1967*), *Chapter in Mechanics of Generalized Continua, pp. 251–261 (Springer-Verlag, Berlin, Germany, 1968).*

Key words: Affine connection; continuum; defect; deformation; dislocation; non-linear; non-Riemmannian geometry; torsion.

The differential geometric aspects of the limited nonlinear continuum theory of crystal dislocations are developed in terms of a non-Riemmannian geometry with vanishing Riemann-Christoffel curvature. The emphasis is on a general notation and a covariant formulaiton The emphasis is on a general notation and a covariant formulation of the theory. Comparisons are made with the works of KRÖNER and ERINGEN. The drawback of non-distant parallelism in passing to the general theory with non-vanishing curvature are discussed.

Dibeler, V. H., Walker, J. A., **Mass spectrometric study of photoionization, XIV. Nitrogen trifluoride and trifluoramine oxide,** *Inorg. Chem.* **8,** *1728–1733 (1969).*

Key words: Bond dissociation energies; heats of formation; ionization energies; mass spectra; NF_3; ONF_3; vacuum ultraviolet.

Photoionization yield curves for the NF_3, NF_2^+, and NF^+ ions of nitrogen trifluoride and the ONF_3^+, ONF_2^+, and NO^+ ions of trifluoramine oxide were obtained from threshold to 600A. Ionization energies were used to calculate heats of formation of ions, ionization energies of radicals, and bond dissociation energies. The high precision of the photoionization measurements were not fully utilized because of uncertainties in, or lack of, supporting thermal and spectral data. The following bond dissociation energies (in eV) were derived: $D(NF_2-F)=2.43$, $D(NF-F)=3.6$, and $D(NF)=2.3$. The heat of formation, ΔHf_0° $(ONF_3)=-2.87$ eV (-66 kcal mol^{-1}) was derived from ionization threshold data and used to estimate $D(O-NF_3)=4.1$ eV, $D(ONF_2-F)=1.9$ eV, and related thermodynamic properties.

Dickson, R. W., Wachtman, J. B., Jr., Copley, S. M., **Elastic constants of single crystal Ni_3Al from 10 to 850 °C,** *J. Appl. Phys.* **40,** *No. 5, 2276–2279 (Apr. 1969).*

Key words: Aluminum; elastic constants; elastic moduli; nickel; single crystals; superalloy.

The elastic constants of single-crystal Ni_3Al were determined 10 to 850 °C by a resonance technique. The values of the compliance and their standard errors at 25 °C are $s_{11}=0.927\pm0.015$, $s_{44}=0.825\pm0.027$ and $s_{12}=-0.319\pm0.050$ in units of 10^{-11} m^2/N.

Frederikse, H. P. R., Hosler, W. R., Casella, R. C., **Piezoresistive effects in semiconducting strontium titanate, Proc. Ninth Intern. Conf. Physics of Semiconductors,** *Moscow, USSR, July 23–29, 1968, pp. 1175–1180 (NAUKA, Leningrad, USSR, 1968).*

Key words: Piezoresistive effects; semiconductors; strontium titanate.

Piezoresistive effects in doped $SrTiO_3$ measured at 300, 77, and 4 K are interpreted in terms of a many-valleyed energy band model [spheroids along ⟨100⟩ direction]. Low temperature saturation is explained by assuming domain flipping under stress.

Hanley, H. J. M., Klein, M., **Selection of the intermolecular potential function, III. From the isotopic thermal diffusion factor,** *J. Chem. Phys.* **50,** *No. 11, 4675–4770 (June 1, 1969).*

Key words: Fitting of experimental data; isotopic thermal diffusion coefficient; potential function families; sensitivity of coefficient.

A method developed previously to evaluate quantitatively the relationship between intermolecular potential functions and macroscopic properties is extended to the isotopic thermal diffusion factor. As before, the relationship between function families has been clarified. In particular, an insensitive temperature range, here about $2 < T^*_{(\delta)_p} < 4$, was found in which the data do not permit the selection of a function. The function families studied were the m–6, Kihara, and exp–6. A quantitative evaluation of the sensitivity of the thermal diffusion coefficient to the potential function is presented.

Herbert, R. L., Tryon, M., Wilson, W. K., **Differential thermal analysis of some papers and carbohydrate materials,** *Tappi* **52,** *No. 6, 1183–1188 (June 1969).*

Key words: Carbohydrate materials; differential thermal analysis; papers.

A study of the thermal degradation of various types of papers by differential thermal analysis (DTA) showed two distinct endothermic peaks, one at 135–155 °C, indicating loss of sorbed moisture, and the other at 310–365 °C, indicating massive decomposition. When the papers are ranked in order of decreasing temperature of the decomposition endotherm, and in decreasing pH values, a high correlation is indicated. Data on the DTA of several carbohydrate compounds related to cellulose also are presented.

Herron, J. T., Huie, R. E., **Rates of reaction of atomic oxygen (O^3P). Experimental method and results for some C_1 to C_5 chloroalkanes and bromoalkanes,** *J. Phys. Chem.* **75,** *No. 5, 1326–1335 (May 1969).*

Key words: Atomic oxygen; bromoalkane; chemical kinetics; chloroalkane; mass spectrometry; organic compounds; rate constant.

A method for measuring rate constants for the reactions of atomic oxygen (^3P) with organic compounds is described. Rate constants and Arrhenius parameters are reported for the reactions of atomic oxygen with twelve chloroalkanes and bromoalkanes from 336 to 622 K.

Horn, L., **Thermal gradient effects on thirteen flush mounted pressure transducers,** *Nat. Bur. Stand. (U.S.), Tech. Note 490, 23 pages (Aug. 1969), 30 cents.*

Key words: Pressure measurement errors; pressure transducers; response; temperature; thermal gradients; zero shift.

Thirteen different flush mounted pressure transducers of seven manufacturers were tested by creating a thermal gradient in them and recording the resultant zero shifts. Photographs of typical outputs are shown and the results are compared. A typical recording shows these general characteristics; 1. a very rapid change in output reaching a peak in a second or less, 2. a more gradual shift which reaches a peak in a time which may be a few seconds or more than a minute, and 3. a shift in reading which remains as long as the gradient is maintained. Examples were found in which each of these were positive or negative. The magnitude in a few cases was small, in many was a large fraction of its range, and in one case well in excess of the full scale range.

Hubbell, J. H., **Gamma-ray cross-section evaluation and compilation,** *Proc. Special Sessions on Gamma-Ray Production and Transport and on Civil Defense Shielding, Winter Meeting of the American Nuclear Society, Nov. 5–9, 1967, Chicago, Ill., A. E. Straker, Ed., ANS-SD-7, AEC TID-4500 Series, pp. 71–77, 82–100 (Aug. 1969).*

Key words: Compilations; energy absorption coefficients; gamma-ray coefficients; photon attenuation coefficients; photon cross sections; x-ray attenuation coefficients.

A brief history of compilation activity in the field of photon attenuation coefficients is given. Available experimental attenuation coefficient data are reviewed for $Z = 1$ to 100 and photon energies 10 eV to 100 GeV with indications given of gaps and uncertainties. Mention is made of recent and in-progress compilations at NBS, LRL (Livermore) and elsewhere, and of the existence of an NSRDS (National Standard Reference Data System) "X-ray attenuation coefficient information center" at the NBS.

Hubbell, J. H., **Photon cross sections, attenuation coefficients, and energy absorption coefficients from 10 keV to 100 GeV,** *Nat. Stand. Ref. Data Ser., Nat. Bur. Stand. (U.S.), 29, 85 pages (Aug. 1969), 75 cents.*

Key words: Attenuation coefficient; Compton scattering; cross section; energy absorption coefficient; gamma rays; pair production; photoelectric absorption; photons; x-rays.

This report updates and extends previous NBS tabulations. Section 1 contains the information of most immediate practical use: (a) a tabulation of the attenuation coefficient for 23 elements ($_1$H to $_{92}$U) between 10 keV and 100 GeV and (b) a tabulation of the energy absorption coefficient for air, water, and 18 elements between 10 keV and 10 MeV, and for air, water, and 7 elements up to 100 MeV. Section 2 contains detailed information on the predominant processes (photoelectric absorption, Compton scattering and pair production) and a brief discussion of other processes which combine to give the attenuation coefficient. Theoretical and experimental data are reviewed, and auxiliary tables and approximation formulas are given. Section 3 contains tabulations of cross sections for the predominant processes between 10 keV and 100 GeV for 23 elements and for 13 compounds and mixutres.

Hust, J. G., Powell, R. L., **Thermal conductivity of aerospace alloys at cryogenic temperatures** *(Proc. 8th Conf. Thermal Conductivity, Purdue University, West Lafayette, Ind., Oct. 7–10, 1968), Chapter in Thermal Conductivity, C. Y. Ho and R. E. Taylor, Eds., pp. 197–208 (Plenum Press Inc., New York, N.Y., 1969).*

Key words: Aluminum alloy; electrical resistivity; Lorenz ratio; nickel alloy; thermal conductivity; thermopower; titanium alloy.

The apparatus described at the last Thermal Conductivity Conference has been used to determine the thermal conductivity, electrical resistivity, Lorenz ratio, and thermopower of several aerospace alloys between 4 and 300 K: titanium A–110 AT, Inconel 718*, Hastelloy X*, and aluminum 7039. These data are presented graphically. By utilizing detailed numerical and theoretical analyses, we have been able to separate the electronic and lattice contributions to the total thermal conductivity. Various scattering mechanisms have also been resolved for both types of conduction. The first three alloys are predominantly lattice conductors at low temperatures, with total Lorenz numbers as high as $15V^2/K^2$ near 20 K.

Jacox, M. E., Milligan, D. E., **Matrix-isolation study of the vacuum-ultraviolet photolysis of methyl fluoride. The infrared spectra of the free radicals CF, HCF, and H_2CF,** *J. Chem. Phys.* **50,** *No. 8, 3252–3262 (Apr. 15, 1969).*

Key words: Cl_2 reactions; $CoCl_2$; $CrCl_2$; emission spectrum; $FeCl_2$; infrared spectrum; matrix isolation; $MnCl_2$; molecular orbitals; $NiCl_2$; transition-metal reactions; ultraviolet spectrum.

Individual molecules of $CrCl_2$, $MnCl_2$, $FeCl_2$, $CoCl_2$, and $NiCl_2$ have been isolated in an argon matrix at 14 K in sufficient concentration for infrared and ultraviolet spectroscopic study not only by using the conventional effusion cell as a source of the MCl_2 species, but also by trapping the products of the reaction of chlorine with the hot transition-metal surface. Studies of the infrared spectra of all of these species in the 250–4000-cm^{-1} spectral range are consistent with a linear structure. Ultraviolet absorptions in the 2000–5500-Å spectral range are in good agreement with the previously reported gas-phase absorptions. However, the absorption observed for matrix-isolated $NiCl_2$ between 4400 and 5000 Å must be attributed to three different electronic transitions, one of which exhibits extensive band structure. A molecular-orbital treatment involving participation of the 3d nickel electrons in the bonding of the molecule predicts the occurrence of several transitions in this energy range and provides a framework for understanding the appearance of extensive vibrational structure in several of the electronic transitions of $NiCl_2$.

Janz, G. J., Dijkhuis, Chr. G. M., **Molten salts: Volume 2, Section 1. Electrochemistry of molten salts: Gibbs free energies and excess free energies from equilibrium-type cells,** *Natl. Stand. Ref. Data Ser., Nat. Bur. Stand. (U.S.), 28, 116 pages (Aug. 1969).*

Key words: Critically evaluated data; equilibrium electrochemical cells; excess entropies; excess Gibbs free energies; Gibbs free energies; molten salt mixtures; molten salts; surface tension; thermodynamics of molten salts.

The critical evaluation of excess free energies of binary molten salt mixtures with a common ion from equilibrium-type electrochemical cells is described in this report. For this purpose calculations using the original emf data were systematically undertaken to establish comparisons of free energy values of various workers that would be significant. The reversibility of electrodes is investigated by comparing the electromotive force of cells with a single molten salt as liquid electrolyte with thermochemical data.

Janz, G. J., Lakahminarayanan, G. R., Tomkins, R. P. T., Wong, J., **Molten salts: Volume 2, Section 2. Surface tension data,** *Nat. Stand. Ref. Data Ser., Nat. Bur. Stand. (U.S.), 28, 116 pages (Aug. 1969).*

Key words: Critically evaluated data; equilibrium electrochemical cells; excess entropies; excess Gibbs free energies; Gibbs free energies; molten salt mixtures; molten salts; surface tension; thermodynamics of molten salts.

Data on the surface tensions of single salt melts have been systematically collected and evaluated. Results are given for 106 inorganic compounds over a range of temperatures where available.

Jones, M. C., Palmer, D. C., **A technique for the measurement of spectral reflectances at low temperatures in the infrared and far infrared** *(Proc. AIAA Third Thermophysics Conf., Los Angeles, Calif., June 24–26, 1968), Chapter in Progress in Astronautics and Aeronautics. Vol. 21, Thermal Design Principles of Spacecraft and Entry Bodies, pp. 543–557 (Academic Press Inc., New York, N.Y., 1969).*

Key words: Infrared; measurement; low-temperature; spectra reflectance; stainless steel; technique.

An experimental technique is described for the measurement of normal, spectral, specular reflectance of materials at temperatures from room temperature down to a few degrees above liquid helium temperature. The reflectance of samples is measured by comparison with reference samples of ultra-high-vacuum deposited gold on glass substrates. The difficulty of maintaining sufficient parallelism between sample and reference has been overcome; so too the problem of excessive delay between recording sample and reference has been reduced. Experimental details are given and, in illustration of the technique, the reflectance of electropolished stainless steel is presented for the wavelength range 3 μm to 300 μm at 297 K, 77 K, and 10.5 K.

Kuriyama, M., Miyakawa, T., **Theory of x-ray diffraction by a vibrating crystal,** *J. Appl. Phys.* **40,** *No. 4, 1697–1702 (Mar. 15, 1969).*

Key words: Dynamical diffraction; extinction; kinematical diffraction; piezoelectricity; theory; thickness vibration; vibrational modes; X-ray diffraction.

The scattering amplitude for X-ray diffraction by a vibrating crystal is obtained. The Bragg diffracted propagators for the perfect crystal are replaced by new propagators in which the Fourier transform of the polarizability of the crystal is multiplied by $J_0(\mathbf{H} \cdot \Delta_q)$ for the vibrational amplitude Δ_q, as is corrected by the Debye-Waller factor in the thermal problem. The scattering amplitude contains not only dynamical scattering but kinematical scattering.
The case of ideal thickness vibration is studied in detail. The real part of the perturbed scattering amplitude is proportional to $\sin \mathbf{H} \cdot \mathbf{A}_q$ multiplied by the H-th Fourier transform of the polarizability. The transient process from dynamical to kinematical scattering, that is, a decrease in extinction, is clearly demonstrated in terms of the vibrational amplitude.

Levin, I. W., Abramowitz, S., **Vibrational spectra and force field for ruthenium tetroxide,** *J. Chem. Phys.* **50,** *No. 11, 4860 (June 1, 1969).*

Key words: Coriolis constant; force field; infrared; isotopic shift; ruthenium tetroxide; vibrational amplitude; vibrational spectra.

Measurement of the infrared gas-phase spectrum of the ν_3 vibration for RuO_4 provides values for both the Coriolis zeta constant ζ_3 and the isotopic frequency shift $\Delta\nu_3$ for the $^{101}Ru - {}^{102}Ru$ exchange. These data, in addition to the vibrational amplitudes $l(Ru-O)$ and $l(O-O)$, serve as constraints in specifying unique force fields for the F_2 symmetry species of RuO_4. Agreement among the sets of force constants separately determined by the supplemental information confirms the potential function for this system.

McNesby, J. R., **The photochemistry of Jupiter above 1200 Å,** *J. Atmospheric Sci.* **26,** *No. 3, 594–599 (May 1969).*

Key words: Ammonia; Jupiter; methane; photochemistry; vacuum ultraviolet.

Jovian photochemistry is shown to consist of four zones: (1) Photolysis of methane at 1216 Å and a total pressure of about 10^{-6} atmospheres and 130 km above the ammonia cloud top; (2) Photolysis of ammonia at 1700–2200 A and a total pressure of about 10^{-4} atmospheres at 100 km; (3) Photolysis of both methane and ammonia at 1350–1450 A at 100 km; and (4) Photolysis of ammonia at 1450–1700 A around 10^{-2} atmospheres at 60 km. No photolysis occurs below this level. The large excess of hydrogen suggests that all radicals ultimately react with hydrogen, the net result being production of H atoms. It is concluded that complex C–H–N molecules are not formed in Jovian photochemistry because of the reducing atmosphere. Methane and ammonia persist in the atmosphere because there is no mechanism available for their disappearance.

Madey, T. E., Yates, J. T., Jr., **The measurement of sticking coefficients at high temperature using the isotopic mixing method,** *(Proc. Sixth Intern. Symp. Rarefied Gas Dynamics, Cambridge, Mass., July 22–26, 1968), Chapter in The Measurement of Sticking Coefficients at High Temperatures Using the Isotopic Mixing Method II, 1345–1348 (Academic Press Inc., New York, N.Y., 1969).*

Key words: Carbon monoxide; high temperature; isotopic mixing; molybdenum; monoxide; nitrogen; rhenium; sticking coefficient; tungsten.

The reactive sticking coefficients for CO on Re and N_2 and CO on W have been determined at high temperatures and low coverages by studying the surface reactions: $^{14}N_2 + {}^{15}N_2 \quad 2\,{}^{14}N{}^{15}N$ and $^{12}C^{18}O + {}^{13}C^{16}O \quad {}^{12}C^{16}O + {}^{13}C^{18}O$. At $T > 1500$ K, is nearly unity for CO on W and Re; ~ .01 for N_2 on W.

Melmed, A. J., **Single-specimen FEM–LEED studies: carbon on tungsten,** *J. Appl. Phys.* **40,** *No. 5, 2330–2334 (Apr. 1969).*

Key words: Field emission microscopy; low-energy electron diffraction; surface study; carbon on tungsten.

Field-electron microscopy and low-energy-electron diffraction can be used in a complementary manner. A method of making such a direct combination on a single specimen is described and applied to a study of the problem of carbon contamination of tungsten surfaces. It is shown that, within the sensitivity of the apparatus used, carbon may be present and undetected by LEED on a (non-perfect) (011)-oriented W LEED specimen.

Miller, K. J., Mielczarek, S. R., Krauss, M., **Energy surface and generalized oscillator strength of the $^1A''$ Rydberg state of H_2O,** *J. Chem. Phys.* **51,** *No. 1, 26–32 (July 1969).*

Key words: Born approximation; energy surface; generalized oscillator strength; H_2O; Hartree-Fock; Rydberg.

The energies and wave functions of the lowest singlet and triplet Rydberg states in H_2O were calculated in the expansion basis self-consistent field procedure for a single configuration. A portion of the energy surface of the $^1A''$ Rydberg state for an OHO angle of 105° was determined that shows the asymmetric dissociation of this state into ground state $H(^2S)$ and $OH(^2H)$ fragments. The energy along the reaction coordinate is almost separable into a repulsion depending only on the center of mass separation and an attractive

potential that depends only on the OH internuclear separation. For the C_{2v} conformation a large basis set was used to approach the Hartree-Fock limit. Using these functions a minimum was calculated in the generalized oscillator strength for the $^1A_1 \rightarrow {}^1B_1$ transition as a function of the momentum transfer function or the electron scattering angle. This behavior was then confirmed experimentally for an energy loss of 7.4 eV with an incident electron energy of 500 eV. Such a minimum is a general characteristic of Rydberg transitions and is not an essentially molecular phenomena. The good agreement between experiment and theory indicates a reasonable fit to the Rydberg wave function by the approximate Hartree-Fock calculation.

Newton, C. J., Ruff, A. W., Jr., **X-ray studies of plastically deformed silver alloys—effects due to oxygen, hydrogen, and tin solutes,** *Advan. X-Ray Anal.* **12,** *316–328 (1969).*

Key words: Domains; hydrogen; oxygen; silver alloys; stacking fault; x-ray diffraction.

Solid specimens of silver were changed at different temperatures in atmospheres of oxygen and of hydrogen. X-ray diffraction line profiles were obtained using powders filed from the treated specimens. Fourier analysis of the diffraction lines was conducted following the method of Warren. The effective particle sizes and root-mean-square strains were obtained from the line shape analysis. Stacking fault and twin fault probabilities were determined from peak-position and center-of-gravity displacements, respectively. For the purpose of comparison, two vacuum-melted silver samples and two different silver-tin alloys (4 at .% and 10.3 at .% tin) were studied. The stacking fault and twin fault probabilities were observed to be nearly unaffected by charging in either oxygen or hydrogen. These results are consistent with recent direct determinations of the effect of oxygen on the stacking fault energy of silver. In contrast, the rms strains and particle sizes changed significantly after charging in oxygen. A decrease in the root-mean-square strain and a corresponding increase in the particle size was found. These effects were opposite to those obtained by adding substitutional solute to silver, confirmed in the present study of two silver-tin alloys. These findings are interpreted to indicate the effect of oxygen clustered with impurities on the dislocations and stacking faults in silver.

Pella, P. A., DeVoe, J. R., Snediker, D. K., **Problems in using Mössbauer spectrometry for quantitative analysis: application to tin,** *Anal. Chem.* **41,** *No. 1, 46–50 (Jan. 1969).*

Key words: High resolution detector; Mössbauer; quantitative analysis; source-sample-detector geometry; tin compounds; use of filters.

Initial studies for the application of Mössbauer spectroscopy to the quantitative analysis of tin compounds are described. The effect of variables such as drift in detector response, sample thickness and sample concentration on the spectral parameters was studied using Pd_3Sn^{119m} as a source and synthetic samples of SnO_2 in an Al_2O_3 matrix. Under controlled conditions, the reproducibility of the spectral parameters were studied for sample sizes from 3 to 122 mg of SnO_2 with a relative standard deviation (of a single measurement) for 3 replicates of 0.5 to 5% over this range of sample size. The data were well approximated by an exponential absorption law. Such factors as source-sample-detector geometry, use of filters, and a high resolution detector were considered in an effort to optimize the ratio of the resonant absorption intensity to the total transmitted intensity.

Rains, T. C., **Chemical interferences in condensed phase,** *Chapter 12 in Flame Emission and Atomic Absorption Spectrometry, J. A. Dean and T. C. Rains, Ed., 1, 349–379 (Marcel Dekker Inc., New York, N.Y., June 1969).*

Key words: Atomic absorption; atomic fluorescence; flame emission; flame temperature; interference; oxidant-fuel; protective chelation; releasing agent.

In flame emission, atomic absorption or atomic fluorescence spectrometry, condensed phase type of interference is observed to occur for many analytes. The degree of interference on the analyte depends upon the interferent and the various parameters associated with the production of free atoms in the flame gas. Proposed mechanisms for the interference of PO_4^{3-}, SO_4^{2-} and Al^{3+} on the alkaline-earth metals are discussed together with methods for their elimination or control. The effect of flame temperature, choice of oxidant-fuel, nebulizer-burner systems and the use of releasing or protective chelating agents are reviewed as a method to minimize the condensed phase type of interference.

Rubin, R. J., **Transmission properties of an isotopically disordered one-dimensional harmonic crystal,** *J. Math. Phys.* **9,** *No. 12, 2252–2266 (Dec. 1968).*

Key words: Crystal dynamics; defects; disordered crystals; wave propogation in stochastic media; multiple scattering.

The amplitude $T_N(w)$ of a wave of frequency w which is transmitted by a disordered array of N isotopic defects in a one-dimensional crystal has been investigated in the limit in which $N \rightarrow \infty$ while the overall concentration of the defects in the array remains fixed. The transmitted amplitude $T_N(w)$ is proportional to the reciprocal of the magnitude of an Nth order determinant whose elements depend explicitly upon the spacings between defects, the incident frequency w, and the relative mass difference $Q=(M-m)/m$ between the defect particles and the particles of the host crystal. $T_N(w)$ is represented as $\exp[-N\alpha_N(w, Q, c)]$ where C is the overall fractional concentration of defects; and two types of estimates of $\alpha_N(w, Q, c)$ are obtained. First, assuming that the spacings between nearest-neighbor pairs of defects are independent random variables, upper and lower bounds are obtained on $\alpha_N(w, Q, c)$ which are independent of N. Provided that c is sufficiently small, the lower bound is positive. Second, Monte Carlo estimates of $\alpha_N(w, Q, c)$ are obtained in the cases $Q=1, C=0$, and $Q=1, C=0.5$ for arrays of 3×10^4 defects. These Monte Carlo estimates are compared with the previously obtained bounds. It is also shown that at the special frequencies of Matsuda and for $Q \geq Q_{crit}$, the limiting value of $\alpha_N(w, Q, c)$ is positive in the entire concentration range $0<C<1$. Explicit upper and lower bounds are obtained on $\alpha[\sin(\pi/4), 1, C]$.

Ruff, A. W., Jr., Ives, L. K., **Stacking fault energy determinations in HCP silver-tin alloys,** *Acta Met.* **17,** *1045–1055 (Aug. 1969).*

Key words: Dislocation; dislocation double ribbons; dislocation nodes; hep alloys; silver-tin alloys; stacking fault energy.

Measurements of the intrinsic stacking fault energy as a function of tin solute concentration are reported through the range of the intermediate hexagonal ζ-phase. Four different alloy compositions in the range 12 to 17 atomic percent tin were studied. Extended dislocation nodes and dislocation double ribbons were observed and measured in order to determine the stacking fault energy. The stacking fault energy values obtained from measurements on these two configurations were in good agreement and indicated that the magnitude of the stacking fault energy increased linearly with solute concentration in the hcp phase. These results are compared with those of the cubic α-phase alloys. The dislocation configurations in the hexagonal alloys are briefly described.

Scheer, M. D., Fine, J., **The electron affinity of lithium,** *J. Chem. Phys.* **50,** *No. 10, 4343–4347 (May 15, 1969).*

Key words: Electron affinity; lithium; mass spectrometry; positive and negative surface ionization.

The positive and negative surface ionization of a lithium atom beam on a thin, heated, molybdenum ribbon was studied using a specially designed mass spectrometer. At a constant incident beam flux, Li^+ yields were determined as a function of surface temperature in the 1400 to 2100 K range. Using 5.39 eV for the first lithium ionization potential (I), this data yielded an average positive ion work function ($\bar{\phi}_+$) of 4.38 eV with a standard deviation of 0.01 eV. The $[Li^+/Li^-]$ ratio was then determined at beam intensities and surface temperatures made sufficiently large to give measurable Li^- yields. From the above values for I, $\bar{\phi}_+$, $\bar{T}$, and $[Li^+/Li^-]$, it was found that $A(Li)=\bar{\phi}_- - 3.35$ eV with a standard deviation of 0.05 eV. The quantity ϕ_- is an average negative ion work function. This could not be measured with any precision because of the very small

Li^- yields. A recent determination of the single plane work functions of molybdenum shows a variation from 4.0 eV for the (116) plane to 5.0 eV for a (110) surface. Since the negative ion work function average accentuates the low work function patches, the maximum uncertainty in $\bar{\phi}_-$ is given by $4.0 < \bar{\phi}_- < 4.4$ eV. Consequently, the electron affinity of lithium is bounded by the following values: $0.65 < A(\text{Li}) < 1.05$ eV. From previously reported measurements of the polycrystalline work function of molybdenum, it is concluded that A(Li) is more likely to be near the upper rather than the lower limit of this range of uncertainty.

Seidel, G. P., **Neutron radiation hardening of polycrystalline iron,** *Radiation Effects* **1,** *177–190 (1969).*

Key words: Annealing; impurities; iron; radiation hardening; strain ageing yield stress.

The dependence of the yield stress of vacuum-annealed and hydrogen purified iron polycrystals as a function of neutron dose and annealing temperature and the influence of these parameters on the effect of static strain-ageing has been investigated. The radiation hardening was found to depend sensitively on the interstitial impurities N and C. This is explained by both a nucleation of precipitation and a trapping of the impurities at radiation produced intrinsic defects. The radiation enhanced precipitation predominates in impurer iron and at low doses can be abolished through annealing below 190 °C. The trapping becomes effective at higher doses or in purer iron. Below 400 °C two recovery stages for the yield stress are observed (between 200 and 260 °C and between 320 and 400 °C), which can be explained by the detrapping of N and C respectively. The static strain-ageing was found to be reduced by neutron irradiation. It reappears after annealing at temperatures, at which the precipitates are thought to be redissolved and the C and N atoms to be detrapped.

Shirley, J. H., **Validity of the semiclassical approximation in maser theory,** *Phys. Rev.* **181,** *No. 2, 600–609 (May 10, 1969).*

Key words: Correlations; laser; maser; phase fluctuations; semiclassical.

A simple model of a maser or laser consisting of a single mode field coupled to N identical two-level atoms is considered. The semiclassical approximation is equivalent to neglecting the statistical correlations between the atoms and the field. The accuracy of this approximation is investigated by writing equations of motion for the correlations. To obtain a complete, self-consistent set of equations, it is necessary to include correlations of the field with itself (related to the coherence of the field) and correlations between different atoms. Relaxations and an energy source are introduced phenomenologically into the equations of motion. They are then solved for the case of steady state oscillation. It is found that the correlations are smaller than the terms kept in the semiclassical theory by the order of one over the number of photons present in the field, larger if thermal photons abound, but smaller if the field relaxation is dominant. Expressions are also found for the amplitude and phase fluctuations of the field. The latter yield a linewidth for the maser oscillator in agreement with earlier calculations, but obtained by a different method.

Swanson, H. E., McMurdie, H. F., Morris, M. C., Evans, E. H., **Standard x-ray diffraction powder patterns,** *Nat. Bur. Stand. (U.S.), Monogr. 25, Section 7, 188 pages (Sept. 1969),* ***$1.50.***

Key words: Crystal structure; integrated intensities; peak intensities; reference intensities; lattice constants; powder patterns; standard; x-ray diffraction.

Standard x-ray diffraction powder patterns are presented for 81 substances. Forty-five of these patterns represent experimental data and 36 are calculated. The experimental x-ray powder diffraction patterns were obtained with a Geiger or proportional counter x-ray diffractometer, using samples of high purity. All d-values were assigned Miller indices determined by comparison with computed interplanar spacings and from consideration of space group extinctions. The densities and lattice constants were calculated, and the refractive indices were measured whenever possible. The calculated x-ray powder diffraction patterns were computed from published crystal structure data. Both peak height and integrated intensities are reported for the calculated patterns.

Weir, C. E., Piermarini, G. J., Block, S., **Single crystal x-ray diffraction at high pressure,** *Proc. American Crystallographic Association High Pressure X-ray Diffraction Symposium, Seattle, Washington, Mar. 23–29, 1969, 5, 105–111 (1969).*

Key words: High pressure; single crystal; x-ray diffraction.

Apparatus and techniques used for single crystal x-ray diffraction at high pressures are described briefly. The three types of determinations carried out successfully are discussed. These are: 1—compressibility measurements; 2—unit cell and space group determinations on high pressure phases; and 3—a structure determination.

Weisman, I. D., Bennett, L. H., **Quadrupolar echoes in solids,** *Phys. Rev.* **181,** *No. 3, 1341–1350 (May 15, 1969).*

Key words: KI, NiAl; nuclear magnetic resonance; pulsed nuclear resonance; quadrupolar interactions; spin echoes.

In a classic paper, Solomon showed that the presence of inhomogeneous, first order quadrupolar interactions leads to the formation of extra "allowed" spin echoes in nuclei for which the spin $I=5/2$. We demonstrate (both theoretically and experimentally) that shifting the rf phase of the second pulse by 90° (in a spin 5/2 system) enhances the allowed echoes by a factor of almost 5 in amplitude over the unshifted case. Using the density matrix formulation (and assuming no magnetic inhomogeneities), we have derived, for a 90° phase shift, the amplitude and shape dependence on the second pulse turning angle of the $3\tau/2$, 2τ and 3τ echoes. Experimental echo amplitudes and shapes (for both 0° and 90° phase shifts) were obtained, at room temperature, on ^{127}I in a fused sample of KI and these show quite good agreement with the calculations. Due to the enhancement, this technique affords a much easier separation of the respective distributions arising from the $3/2 \leftrightarrow 5/2$ and from the $1/2 \leftrightarrow 3/2$ satellite transitions than is possible in the unshifted case. Another feature of the phase shifted case is that, in favorable circumstances, the 3τ echo may be observed although the 2τ echo is obscured by the receiver recovery time. Preliminary data on quadrupole distributions at Al sites in NiAl intermetallic compounds are presented.

Weiss, B-Z., Meyerson, M. R., **Effect of chromium diffusion coatings on fatigue in iron,** *Trans Met. Soc. AIME* **245,** *1633–1643 (July 1969).*

Key words: Armco Iron; chromium diffusion coatings; fatigue; crack formation; crack propagation.

Chromium diffusion coatings on commercial Armco Iron lead to structural, compositional, and stress distributional changes in the outer layers. These changes affect the mechanism of fatigue crack formation. In chromized samples, the crack initiates below the Cr-rich zone after only a limited portion of the total lifetime (5% to 10%). The crack formation was observed at the grain boundaries, where precipitated Cr-carbides were found. Residual tensile stresses and a stress concentration caused by the carbides are considered as accelerating factors. In uncoated samples, the cracks form at slip boundaries after 40% to 50% of total lifetime. The propagation process in coated samples is slower than in uncoated samples, as a result of the moderate rate of propagation until such time as the crack proceeds completely through the coating. At best, the Cr-diffusion causes little if any increase in fatigue life, and in certain cases a severe deterioration in fatigue life is observed.

Woo, S. B., Branscomb, L. M., Beaty, E. C., **Sunlight photodetachment rate of ground state O_2^-,** *J. Geophys. Res. Space Physics* **74,** *No. 11, 2933–2940 (June 1, 1969).*

Key words: Drift tube; ion mobility; O_2^-; oxygen negative ion; photoionization; photodetachment.

Swarm, instead of the usual crossed-beam, technique is used to measure the sunlight photodetachment rate of O_2^-. The advantage of this technique is that the molecular negative ions can be relaxed

through approximately 10^6 collisions at thermal energy to ground vibrational and electronic state, before being introduced to the photodetachment chamber. Consequently, one can be confident of the applicability of data to the mesophere where the molecular negative ions are thought to be in thermal equilibrium with the temperature of the neutral gas. The measured absolute sunlight photodetachment rate of O_2^- is 0.3 ± 0.1 per ion per second. This value is obtained through a relative measurement, calibrating against the 1.44 s^{-1} absolute sunlight photodetachment value of O^-, reported by Branscomb. A preliminary absolute solar-spectrum photodetachment rate of O_3^- is reported. This value is 0.06 per ion per second, believed good to a factor of two.

Yakowitz, H., Michaelis, R. E., Vieth, D. L., **Homogeneity characterization of NBS spectrometric standards. IV: Preparation and microprobe characterization of W-20% Mo alloy fabricated by powder metallurgical methods** (*Proc. 17th Annual Conf., Applications of X-ray Analysis, Estes Park, Colo., Aug. 21–23, 1968*), *Chapter in Advances in X-ray Analysis, C. S. Barett, G. R. Mallett, and J. B. Newkirk, eds., 12, 418–438 (Plenum Press Inc., New York, N.Y., 1969).*

Key words: Homogeneity testing; microprobe analysis; powder metallurgy; NBS standards; metallography; tungsten-Molybdenum alloys.

A significant problem of the National Bureau of Standards Standard Reference Materials program is the provision of standards suitable in homogeneity for use with microanalytical techniques such as the spark source mass spectrograph and the electron probe microanalyzer. An interim approach to the problem has been the extended homogeneity characterization of selected existing standards. This paper describes the preparation and evaluation of the first NBS standard tested specifically from the beginning for application to electron probe microanalyzers. The standard designated SRM 480 is a tungsten-20 weight percent molybdenum alloy prepared by a powder metallurgy process. Based on the results of about 1500 determinations for both tungsten and molybdenum by electron probe microanalysis, the material was found to be of high homogeneity at about the micrometer level of spatial resolution. The coefficient of variation for molybdenum was 2.5% and that for tungsten 1.5%. Correction of relative intensity ratios to obtain concentrations is discussed in terms of input parameter uncertainties such as mass absorption coefficients, and electron backscatter factors. The result of studies for atomic number correction and effects on operating voltage on the microprobe absorption correction, will be given. It is concluded that SRM 480 should be a valuable addition to any microprobe laboratory doing quantitative analyses.

Young, D. S., Mears, T. W., **Measurement and standard reference materials in clinical chemistry,** *Clin. Chem.* **14,** *No. 10, 929–943 (Oct. 1968).*

Key words: Clinical, medicine; measurement; standard reference materials.

The concept of the measurement system based upon the four parameters—length (meter), mass (kilogram), time (second), and temperature (Kelvin)—is developed. The proper daily operation of an analytical laboratory depends on these basic measurements, and several derived from them, e.g., the liter. An additional component of chemical measurement which directly influences accuracy is the purity of the standards and reagents employed. The Standard Reference Materials program of the National Bureau of Standards provides a central source of guaranteed high-purity reference materials which are available to all. The reliability of chemical measurements will increase as new Standard Reference Materials such as cholesterol, uric acid, urea, and creatinine are utilized to standardize methods and instruments in the clinical laboratories of this country.

Other NBS Publications

J. Res. Nat. Bur. Stand. (U.S.), 73B (Math. Sci.), No. 4 (Oct.–Dec. 1969), $1.25.

Temperature renormalization in the non-linear Vlasov problem. W. L. Sadowski and Z. G. Ruthberg.

Selective excitation of harmonics in a collisionless plasma by two counterstreaming electron beams. W. L. Sadowski and Z. G. Ruthberg.

Simultaneous contractification. A. J. Goldman and P. R. Meyers.

A theorem on convex hulls. W. A. Horn.

The partitioning of interaction in analysis of variance. J. Mandel.

Highly restricted partitions. H. Gupta.

J. Res. Nat. Bur. Stand. (U.S.), 73C (Engr. and Instr.), Nos. 3 and 4 (July–Dec. 1969), $1.25.

Design features of a precision ac-dc converter. L. A. Marzetta and D. R. Flach.

An improved high-precision calibration procedure for reference standard hydrometers. H. A. Bowman and W. H. Gallagher.

The nuclear quadrupole resonance magnetometer: A new method for the precision measurement of the magnitude and direction of magnetic fields. M. Linzer.

Optical FM system for measuring mechanical shock. L. D. Ballard, W. S. Epstein, E. R. Smith, and S. Edelman.

Austin, A. V., Management and the metric system, Defense Management J. **5,** No. 2, 27–34 (1969).

Bates, R. G., Editor, Electrochemical Analysis Section, summary of activities July 1968 to June 1969, Nat. Bur. Stand. (U.S.), Tech. Note 503, 99 pages (Aug. 1969), $1.00.

Beatty, R. W., Yates, B. C., A graph of return loss versus frequency for quarter-wavelength short-circuited waveguide impedance standards, IEEE Trans. Microwave Theory Tech. **MTT-17,** No. 5, 282–284 (May 1969).

Bender, P. L., Optical orientation experiments at Princeton, Chapter in Polarisation Matiere et Rayonnement, Volume Jubilaire en L'Honneur D'Alfred Kastler, pp. 436–441 (Presses Universitaires de France, Paris, 1969).

Boone, T. H., Skoda, L. F., Cullen, W. C., Laboratory-field comparisons of built-up roofing membranes, Roofing Siding Insul. Mag. **46,** No. 4, 28–33 (Apr. 1969).

Brower, W. S., Robbins, C. R., Growth of $CaTiSiO_5$ by the Czochralski method, J. Crystal Growth **5,** 233–234 (1969).

Butterfield, M. A., OCR standards today, Chapter 37 in Optical Character Recognition and the Years Ahead, pp. 318–335 (Business Press, Elmhurst, Ill., July 1969).

Cahill, K. E., Regularization of the P representation, Phys. Rev. **180,** No. 5, 1244–1255 (Apr. 25, 1969).

Champion, C. E., Marinenko, G., Errors in coulometric chloride titrations due to photodecomposition of silver chloride, Anal. Chem. **41,** No. 1, 205–207 (Jan. 1969).

Cook, A. R., Matarrese, L. M., Zero-field EPR of Fe^{3+} in quartz, J. Chem. Phys. **50,** No. 6, 2361–2364 (Mar. 15, 1969).

Coriell, S. R., Hardy, S. C., Morphology of unstable ice cylinders, J. Appl. Phys. **40,** No. 4, 1652–1655 (Mar. 1969).

Crawford, B. H., Nimeroff, I., Radiation sources and their power supplies, Chapter in Techniques of Photostimulation in Biology, (North-Holland Publ. Co., Amsterdam, The Netherlands) pp. 19–48 (1968).

Crissman, J. M., Mechanical relaxation in polypropylene as a function of polymorphism and degree of lamellar orientation, J. Poly. Sci. **7,** Part A2, 389–404 (1969).

Cushen, W. E., Systems analysis activities at the Technical Analysis Division of the National Bureau of Standards, C-E Newsletter **4,** No. 3, 4–5 (June 1969).

Deslattes, R. D., Paretzkin, B., A small set of reference crystals for double-crystal topography, J. Appl. Cryst. **1,** Part 3, 176–178 (Sept. 1968).

DeRis, J. N., Spread of a laminar diffusion flame, Proc. Conf. Twelfth Symp. (International) on Combustion, Poitiers, France, July 17, 1968, pp. 241–252 (Combustion Institute, Pittsburgh, Pa., 1969).

Diamond, J. J., Editor, Bibliography on the high temperature chemistry and physics of materials, April, May, June 1969, Nat. Bur. Stand. (U.S.), Spec. Publ. 315-2, 74 pages (July 1969), 75 cents.

DiMarzio, E. A., Guttman, C. M., Separation by flow, J. Polymer Sci. Polymer Letters **7,** 267–272 (1969).

Dodd, J. N., Enemark, E., Gallagher, A., Quenching of cesium resonance radiation by helium, J. Chem. Phys. **50,** No. 11, 4838–4842 (June 1, 1969).

Domen, S. R., Heat loss compensated calorimeter, Nature **222,** No. 5198, 1061 (June 14, 1969).

Durst, R. A., Determination of fluoride by analate additions potentiometry, Mikrochim. Acta, pp. 611–614 (1969).

Ehrlich, M., Proposed National Bureau of Standards Program for the calibration of instruments used in high-energy electron and x-ray beams (Proc. Conf. High-Energy Radiation Therapy Dosimetry, New York, N.Y., June 1967), Annal. N. Y. Acad. Sci. 161, No. **1,** 139–145 (July 3, 1969).

Flynn, D. R., O'Hagan, M. E., Measurements of the thermal conductivity and electrical resistivity of platinum from 100 to 900 °C, Engelhard Indust. Tech. Bull. **8,** No. 4, 117–147 (Mar. 1968).

Flynn, D. R., Watson, T. W., Measurement of the thermal conductivity of soils to high temperature, Atomic Energy Report SC–CR–69–3059 (Apr. 1969).

Frederick, N. Y., A new high-frequency current standard, IEEE Trans. Instr. Meas. **IM–17,** No. 4, 285–290 (Dec. 1968).

Franklin, A. D., Editor, ARPA–NBS program of research on high temperature materials, Period covered, July 1 to December 31, 1968, Nat. Bur. Stand. (U.S.), Tech. Note 494, 28 pages (Sept. 1969), 35 cents.

Greenfeld, S. H., A study of the variables involved in the saturating of roofing felts, Nat. Bur. Stand. (U.S.), Bldg. Sci. Ser. **19,** 18 pages (June 1969), 30 cents.

Greenfeld, S. H., Hail resistance of roofing products, Nat. Bur. Stand. (U.S.), Bldg. Sci. Ser. **23,** 11 pages (Aug. 1969), 25 cents.

Grenley, D. G., Study of the effect of certain modified mortars on compressive and flexural strength of masonry (Proc. Intern. Conf. Masonry Structural Systems, University of Texas, Austin, Texas, Nov. 30–Dec. 2, 1967), Chapter in Designing Engineering and Constructing with Masonry Products, F. B. Johnson, Ed., Paper 5, pp. 28–33 (Gulf Publ. Co., Houston, Texas, May 1969).

Grenley, D. G., Cattaneo, L. E., Pfrang, E. O., Effect of edge load on flexural strength of clay masonry systems utilizing improved mortars (Proc. Intern. Conf. Masonry Structural Systems, University of Texas, Austin, Texas, Nov. 30–Dec. 2, 1967), Chapter in Designing Engineering and Constructing with Masonry Products, F. B. Johnson, Ed., Paper 17, pp. 119–128 (Gulf Publ. Co., Houston, Texas, May 1969).

Hanley, H. J. M., Childs, G. E., Dilute gas viscosities at low temperatures, J. Chem. Phys. **50,** No. 10, 4600–4601 (May 5, 1969).

Hiza, M. J., Duncan, A. G., Comments on "Intermolecular forces: thermal diffusion and diffusion in He-Kr and H_2-Kr", Phys. Fluids **12,** No. 7, 1531–1532 (July 1969).

Hoer, C. A., Smith, W. L., A 1-MHz binary inductive voltage divider with ratios of 2^n to 1 or $6n$ dB, IEEE Trans. Instr. Meas. **IM–17,** No. 4, 278–284 (Dec. 1968).

Hoffman, J. D., Lauritzen, J. I., Jr., Passaglia, E., Ross, G. S., Frolen, L. J., Weeks, J. J., Kinetics of polymer crystallization from solution and the melt, Kolloid-Z. Polymere **231,** 564 (1969).

Hudson, R. P., The CMN temperature scale, Proc. XI Conf. Low Temperature Physics, St. Andrews, Scotland, Aug. 21–28, 1968, I, 501–504, Paper D1.8 (University of St. Andrews, Scotland, 1968).

Huget, E. F., Brauer, G. M., Kumpula, J. W., Civjan, S., A filled cold-curing acrylic resin as a splinting material, J. Am. Dent. Assoc. **79,** 645–648 (Sept. 1969).

Jackson, J. L., Lifson, S., Coriell, S. R., Association times of counterions to polyelectrolytes in solution, J. Chem. Phys. **50,** No. 11, 5045 (June 1, 1969).

Janz, G. J., Dijkhuis, Chr. G. M., Molten salts: Volume 2. Section 1. Electrochemistry of molten salts: Gibbs free energies and excess free energies from equilibrium-type cells (Combined with Section 2), Nat. Stand. Ref. Data Ser., Nat. Bur. Stand. (U.S.), 28, 116 pages (Aug. 1969), $2.75.

Janz, G. J., Lakshminarayanan, G. R., Tomkins, R. P. T., Wond, J., Molten salts: Volume 2. Section 2. Surface tension data (Combined with Section 1), Nat. Stand, Ref. Data Ser., Nat. Bur. Stand. (U.S.), 28, 116 pages (Aug. 1969), $2.75.

Jones, E., Yelon, W. B., Edelman, S., Piezoelectric shakers for wide-frequency calibration of vibration pickups, J. Acoust. Soc. Am. **45,** No. 6, 1556–1559 (June 1969).

Kasen, M. B., A method for producing small grain size in superpurity aluminum, Trans. Met. Soc. AIME **245,** No. 7, 1660–1661 (July 1969).

Keller, R. A., Intersystem crossing from excited triplet states into the singlet manifold (Proc. Intern. Conf. Molecular Luminescence, Loyola Univ., Chicago, Ill, Aug. 20–23, 1968), Chapter in Molecular Luminescence, E. C. Lim, Ed., pp. 453–468 (W. A. Benjamin Inc., New York, N.Y., 1969).

Klein, R., Scheer, M. D., Reaction of $O(^3P)$ with 2-methyl-2-pentene at low temperatures and its implication for the transition state, J. Phys. Chem. **73,** 1598–1599 (1969).

Klose, J. Z., Transition probabilities and mean lives of the $2S_7$ laser level in neon I, J. Quant. Spec. Rad. Trans. **9,** No. 6, 881–883 (June 1969).

Ku, H. H., Kullback, S., Approximating discrete probability distributions, IEEE Trans. Info, Theory **IT–15,** No. 4, 444–447 (July 1969).

Koonce, C. S., Tunneling into low carrier density superconductors, Phys. Rev. **182,** No. 2, 5407 (June 10, 1969).

Kusuda, T., Proposed procedures for determining building heating and cooling loads for energy calculations, ASHRAE Symposium Bulletin, pp. 1–75 (1969).

Kusuda, T., Thermal response factors for multi-layer structures of various heat conduction systems, ASHRAE J. **75,** No. 2108, 1–25 (Jan. 1969).

LaFleur, P. D., Activation Analysis Section at the National Bureau of Standards, Washington, D.C., U.S.A., Laboratory of the Issue, J. Radioanalytical Chem. **3,** No. 1–2, 127–133 (July 1969).

Lamb, V. A., Electroplating with current pulses in the microsecond range, Plating **56,** No. 8, 909–913 (Aug. 1969).

Lehner, J., Newman, M., On Reimann surfaces with maximal automorphism groups, Glasgow Math. J. **8,** Part 2, 102–112 (July 1967).

Leiss, J. E., Penner, S., Rose, J. E., Broberg, J. B., Transient beam loading in electron linear accelerators (Proc. 1969 Particle Accelerator Conf., Washington, D.C., March 5–7, 1969), IEEE Trans. Nucl. Sci. **NS–16,** Part I, No. 3, 1027–1030 (June 1969).

Mangum, B. W., Soulen, R. J., Utton, D. B., Magnetic ordering in cerium trichloride at low temperatures, Proc. XI Conf. Low Temperature Physics, St. Andrews, Scotland, Aug. 21–28, 1968, 2, 1361–1363, Paper C10.9 (University of St. Andrews, Scotland, 1968).

Mangum, B. W., Thornton, D. D., Nuclear relaxation measurements of ^{35}Cl in $PrCl_3$, Phys. Rev. Letters **22,** No. 21, 1105–1107 (May 26, 1969).

Marcus, M., Newman, M., Doubly stochastic associated matrices, Duke Math. J. **34,** No. 3, 591–598 (Sept. 1967).

Margoshes, M., Rasberry, S. D., Fitting of analytical functions with digital computers in spectrochemical analysis, Anal. Chem. **41,** 1163–1172 (Aug. 1969).

Marinenko, G., Champion, C. E., Difference between the inflection point and the equivalence point in coulometric titrations of weak acids, Anal. Chem. **41,** No. 10, 1208–1211 (Aug. 1969).

Martin, W. C., Tech, J. L., Wilson, M., Note on the $3p^54s3d$ configuration in neutral potassium (K I), Phys. Rev. **181,** No. 1, 66–69 (May 5, 1969).

Matarrese, L. M., Wells, J. S., Peterson, R. L., EPR spectrum of Fe^{3+} in synthetic brown quartz, J. Chem. Phys. **50,** No. 6, 2350–2360 (Mar. 15, 1969).

May, L., Spkjkerman, J. J., On the relationship between Mössbauer spectroscopy and the nuclear magnetic resonance of organotin compounds, J. Chem. Phys. Letter to the Editor **46,** No. 8, 3272–3273 (Apr. 15, 1967).

Menis, O., Rains, T. C., Determination of arsenic by atomic absorption spectrometry with an electrodeless discharge lamp as a source of radiation, Anal. Chem. **41,** No. 7, 952–954 (June 1969).

Menke, J. L., Beam monitoring at the NBS linac-energy, positioning, current, charge (Proc. 1969 Particle Accelerator Conf., Washington, D.C., March 5–7, 1969), IEEE Trans. Nucl. Sci. **NS–16,** Part I, No. 3, 921–922 (June 1969).

Milton, J. B., Standard time and frequency: Its generation, control, and dissemination from the National Bureau of Standards Time and Frequency Division, Nat. Bur. Stand. (U.S.), Tech. Note 379, 27 pages (Aug. 1969), 35 cents.

Mullen, L. O., Sullivan, D. B., Fabrication of tunnel junctions on niobium films, J. Appl. Phys. **40,** No. 5, 2115–2117 (April 1969).

Nargolwalla, S. S., Przybylowicz, E. P., Suddueth, J. E., Birkhead, S. L., Solution of blank problems in 14-MeV neutron activation analysis for trace oxygen, Anal. Chem. **41,** No. 1, 168–170 (Jan. 1969).

Newman, M., A diophantine equation, J. London Math. Soc. **43,** 105–107 (1968).

Newman, M., Some results on roots of unity, with an application to a diophantine problem, Aequat. Math. **2,** No. 2/3, 163–166 (Nov. 28, 1967).

Nimeroff, I., Schleter, J. C., Professor Harry J. Keegan: colorimetrist's spectrophotometrist, J. Appl. Opt. **8,** No. 4, 757–761 (Apr. 1969).
O'Connell, J., An isospin sum rule for photonuclear reactions, Phys. Rev. Letters **22,** No. 24, 1314–1316 (June 16, 1969).
Odom, J. V., Problems of metric conversion, ASTME Vectors **4,** No. 4, 17–19 (July/Aug. 1969).
Pfeiffer, E. R., Schooley, J. F., Superconducting transition temperatures of Nb-doped $SrTiO_3$, Phys. Letters **29A,** No. 10, 589–590 (Aug. 11, 1969).
Powell, C. J., Analysis of optican- and inelastic-electron-scattering data. Parametric calculations, J. Opt. Soc. Am. **59,** No. 6, 738–743 (June 1969).
Radziemski, L. J., Jr., Kaufman, V., Wavelengths, energy levels, and analysis of neutral atomic chlorine (Cl I), J. Opt. Soc. Am. **59,** No. 4, 424–443 (Apr. 1969).
Rains, T. C., Chemical aspects of atomic absorption, Am. Soc. Testing Mater. Spec. Tech. Publ. 443, 19–36 (1969).
Rains, T. C., Menis, O., High-precision flame emission spectrometry, Spectroscopy Letters **2,** No. 1, 1–7 (1969).
Reeve, G. R., A heterodyne near-zone field-strength meter, IEEE Trans. Instr. Meas. **IM-18,** No. 1, 32–37 (Mar. 1969).
Robbins, R. F., Weitzel, D. H., An automated resilience apparatus for polymer studies from −196 to +180 °C, Rev. Sci. Instr. **40,** No. 8, 1014–1017 (Aug. 1969).
Ryan, J. V., Federal government's role and activities in consumer safety. The role of the Fabric Flammability Section, Proc. Spring Workshop, Home Conf., 5 pages, National Safety Council, General Session, Washington, D.C., May 26, 1969.
Santone, L. C., Application of systems analysis to urban problems, International City Management Association, The Municipal Yearbook, pp. 225–232 (1969).
Scheer, M. D., Fine, J., The desorption kinetics of Cl^- and I^- on Mo and Ta as determined by the pulsed-beam method (Proc. Sixth Intern. Symp. Rarefied Gas Dynamics, Cambridge, Mass., July 22–26, 1968), Chapter in The Measurement of Sticking Coefficients at High Temperatures Using the Isotopic Mixing Method II, 1469–1477 (Academic Press Inc., New York, N.Y., 1969).
Simpson, J. A., Electron impact spectrometry for gas phase chemical analysis, Mater. Res. Stand. **9,** No. 8, 13–16 (Aug. 1969).
Sitterly, C. M., Forbidden transitions in atoms: catalogs and identifications, Mem. Soc. Roy. Sci. Liege **V,** No. 16, 17–29 (1969).
Stiehler, R. D., History of measurement and the SI units, Mater. Res. Std. **9,** No. 6, 14–18 (June 1969).
Strobridge, T. R., Refrigeration for superconducting and cryogenic systems (Proc. 1969 Particle Acceleration Conf., Washington, D.C., March 5–7, 1969), IEEE Trans. Nuclear Sci. **NS-16,** Part I, No. 3, 1104–1108 (June 1969).
Swartzendruber, L. J., Bennett, L. H., Watson, R. E., Dilute ^{57}Fe Mössbauer studies in Cu-Ni alloys, J. Appl. Phys. **40,** No. 3, 1489–1490 (Mar. 1, 1969).
Tate, D. R., Gravity measurements and the standards laboratory, Nat. Bur. Stand. (U.S.), Tech. Note 491, 10 pages (Aug. 1969), 25 cents.
Tate, E. L., Variations on a theme: government and library cooperation, D.C., Libraries **39,** No. 3, 53–55 (1968).
Verdier, P. H., A simulation model for the study of the motion of random-coil polymer chains, J. Computational Phys. **4,** No. 2, 204–210 (1969).
Viezbicke, P. P., Jr., Interactions between nested receiving rhombic antennas, IEEE Trans. Ant. Prop. **AP-17,** No. 1, 16–23 (Jan. 1969).
Waddell, W. J., Bates, R. G., Intracellular pH, Physiol. Rev. 49, No. 2, 289–329 (1969).
Wagman, D. D., Elements of chemical thermodynamics: Introduction to thermal methods, Chapter 86 in Treatise on Analytical Chemistry, Part I, Theory and Practice, I. M. Kolthoff, P. J. Elving, and E. B. Sandell, Ed., 8, 4909–4936 (Interscience Publ. Inc., New York, N.Y., 1968).
Watson, R. E., Bennett, L. H., Freeman, A. J., Comments on "origin of solvent Knight shifts in alloys", Phys. Rev. **179,** 590–592 (Mar. 10, 1969).
Wolcott, N. M., Falge, R. L., Bennett, L. H., Magnetic behavior of intermetallic compounds of beryllium, J. Appl. Phys. **40,** No. 3, 1377–1378 (Mar. 1, 1969).

**Publications for which a price is indicated are available by purchase from the Superintendent of Documents, U.S. Government Printing Office, Washington, D.C. 20402 (foreign postage, one-fourth additional). The NBS non-periodical series are also available from the Clearinghouse for Federal Scientific and Technical Information, Springfield, Va. 22121. Reprints from outside journals and the NBS Journal of Research may often be obtained directly from the authors.*

U.S. GOVERNMENT PRINTING OFFICE : 1970 OL—367–409

UNIVERSITY MICROFILMS INC
ATTN SERIALS SECTION
300 NORTH ZEEB RD
ANN ARBOR MICH 48106

UNITED STATES
GOVERNMENT PRINTING OFFICE
DIVISION OF PUBLIC DOCUMENTS
WASHINGTON, D.C. 20402

OFFICIAL BUSINESS

POSTAGE AND FEES PAID
U.S. GOVERNMENT PRINTING OFFICE

JOURNAL OF RESEARCH of the National Bureau of Standards
A. Physics and Chemistry

Vol. 74A, No. 1 Jan.–Feb. 1970

Contents

Page

Standardization of cesium-137 gamma-ray sources in terms of exposure units (Roentgens). T. P. Loftus. 1

Calculations of Zn II $3d^9 4s5s$ and Ag I $4d^9 5s6s$, and some new levels in these spectra. William C. Martin and Jack Sugar. 7

New vacuum ultraviolet wavelengths and revised energy levels in the second spectrum of zinc (Zn II). William C. Martin and Victor Kaufman. 11

CIE 1960 UCS diagram and the Müller theory of color vision. Deane B. Judd and Gary T. Yonemura. 23

Blemish formation in processed microfilm. II. C. I. Pope. 31

Positive and negative ion sublimation from transition metal surfaces: A review of some recent results. Milton D. Scheer. 37

Generation of controlled low pressures of nitrogen by means of dissociation equilibria. Ronald H. Orcutt. 45

Temperature coefficient of the bismuth I-II transition pressure. James C. Houck. 51

Isothermal diffusion in the dilute range of the system $Ca(OH)_2$-H_3PO_4-H_2O—Theory. E. C. Moreno, P. R. Patel, and W. E. Brown. 55

High-speed (subsecond) measurement of heat capacity, electrical resistivity, and thermal radiation properties of molybdenum in the range 1900 to 2800 K. A. Cezairliyan, M. S. Morse, H. A. Berman, and C. W. Beckett. 65

P-V-T, thermodynamic and related properties of oxygen from the triple point to 300 K at pressures to 33 MN/m^2. L. A. Weber. 93

Publications of the National Bureau of Standards. 131

Library of Congress Catalog Card Number: 62–37059

For sale by the Superintendent of Documents, U.S. Government Printing Office, Washington, D.C. 20402. (Order by SD Catalog No. C 13.22/sec.A:74/1). Single copy price varies. This issue $1.75. Subscription price $9.50 a year; $2.25 additional for foreign mailing.

UNITED STATES GOVERNMENT PRINTING OFFICE, WASHINGTON : 1970